INVESTIGATION OF ZERO-TEMPERATURE TRANSVERSE-FIELD ISING MODELS WITH LONG-RANGE INTERACTIONS

Untersuchung langreichweitiger Isingmodelle im transversalen Feld bei Temperatur $T = 0\,\mathrm{K}$

Der Naturwissenschaftlichen Fakultät
der Friedrich-Alexander-Universität Erlangen-Nürnberg

zur Erlangung des

Doktorgrades dr. rer. nat.

vorgelegt von

sebastian fey

Als Dissertation genehmigt
von der Naturwissenschaftlichen Fakultät
der Friedrich-Alexander-Universität Erlangen-Nürnberg

Tag der mündlichen Prüfung:	2020-05-07
Vorsitzender des Promotionsorgans:	Prof. Dr. Hanno Sahlmann
Gutachter:	Prof. Dr. Kai P. Schmidt
	Prof. Dr. Martin Eckstein

ABSTRACT

In this thesis I aim to investigate ground-state properties of a quantum-mechanical long-range interacting spin model at temperature $T = 0\,\mathrm{K}$. Paradigmatic models such as the Ising model are mostly limited to nearest-neighbor interactions. However, their long-range counterparts often display a drastically different behavior. Long-range interactions can induce an effective dimensionality into the system, leading to continuously varying critical exponents of quantum phase transitions in ferromagnetic systems and the appearance of multiplicative logarithmic corrections. For antiferromagnetic interactions frustration can result in the appearance of new phases. During the last decades several studies of such models have been performed with various methods. Exact diagonalization and Quantum Monte-Carlo calculations are yet limited to finite system sizes. Density-matrix renormalization-group methods allow handling infinite sizes but results are only available for (quasi-)one-dimensional models.

In this thesis, a method is presented which allows the computation of quantitative results for gapped quantum-many-body systems with long-range interactions in the bulk limit based on a perturbative approach. Perturbative continuous unitary transformations are combined with Monte-Carlo methods for an evaluation of nested infinite sums and Padé extrapolations to extract critical behavior. Long-range-interacting Ising models in a transverse magnetic field were analyzed, where the interaction decays algebraically as $r^{-\alpha}$ with inter-spin distance r. The investigation of low-energy excitation gaps was used to determine phase diagrams and critical exponents for multiple different lattice geometries.

For ferromagnetic spin-spin interactions a phase transition from a polarized paramagnetic phase in the high-field limit to an ordered phase, which breaks the $\mathbb{Z}_2$ symmetry, was found in all cases. Depending on α renormalization-group calculations predict three different regimes. For small α mean-field criticality is expected while for large values systems are supposed to display nearest-neighbor exponents. Continuously-varying critical exponents that are expected to exist in between could be confirmed in this thesis. In one and two dimensions multiplicative logarithmic corrections were found that are expected for the nearest-neighbor model only on the cubic lattice in three dimensions. This strengthens the interpretation of the long-range model as having similar properties as the short-range-interacting model in an effective dimension.

While in this thesis frustration effects induced by an antiferromagnetic interaction were already found for bipartite lattices, these are especially interesting for models that are already highly frustrated in the nearest-neighbor case. For the Ising model on the

triangular lattice additional stripe-ordered phases were found, leading to an increased complexity of the ground-state phase diagram. After mapping the triangular lattice to a finite cylinder, indications for infinite-order phase transitions appeared that require further studies in the future.

ZUSAMMENFASSUNG

Das Ziel der vorliegenden Arbeit ist die Untersuchung der Grundzustandseigenschaften langreichweitiger quantenmechanischer Spinmodelle bei einer Temperatur $T = 0\,\mathrm{K}$. Lehrbuchbeispiele für die theoretische Beschreibung magnetischer Quantensysteme wie das Isingmodell sind meist auf kurzreichweitige Wechselwirkungen beschränkt. Ihre langreichweitigen Gegenstücke zeigen jedoch häufig ein drastisch unterschiedliches Verhalten. Im Allgemeinen führen sie zu einer effektiven Dimensionalität der Systeme und erlauben so bei ferromagnetischen Modellen eine kontinuierliche Variierung kritischer Exponenten von Quantenphasenübergängen und das Auftreten logarithmischer Korrekturen. Bei antiferromagnetischen Wechselwirkungen kommen Frustrationseffekte zum Tragen, die die Enstehung neuer Phasen befördern können. In den letzten Jahrzehnten gab es deshalb immer wieder Untersuchungen solcher Modelle mit verschiedenen Methoden. In Beispielen wie der exakten Diagonalisierung und Quanten-Monte-Carlo Rechnungen sind die untersuchten Systeme jedoch stets auf endliche Systemgrößen beschränkt. Dichtematrix-Renormalisierungsgruppen erlauben zwar die Untersuchung unendlicher Systeme, konnten jedoch bisher nur (quasi-)eindimensionale Modelle behandeln.

In der vorliegenden Arbeit wird eine Methode vorgestellt, die quantitative Ergebnisse für unendlich große lückenbehaftete Quantenvielteilchensysteme mit langreichweitigen Wechselwirkungen liefern kann, beruhend auf einem störungstheoretischen Ansatz. Perturbative kontinuierliche unitäre Transformationen wurden komplementiert mit Monte-Carlo Methoden zur Auswertung verschachtelter unendlicher Summen und Padé Extrapolationen, um das kritische Verhalten zu bestimmen. Es wurden langreichweitige Isingmodelle in einem transversalen Magnetfeld analysiert, deren Spin-Spin-Wechselwirkungen algebraisch mit dem Abstand r wie $r^{-\alpha}$ abfallen. Zur Bestimmung von Phasendiagrammen und kritischen Exponenten für diverse Gittergeometrien wurden dazu hauptsächlich die Energielücken von Niedrigenergieanregungen im Hochfeldlimes studiert.

Für ferromagnetische Spin-Spin-Wechselwirkungen konnten in allen betrachteten Fällen Quantenphasenübergänge zwischen einer ungeordneten paramagnetischen Phase, in der die einzelnen Spins parallel zum Magnetfeld polarisiert sind, und einer geordneten Phase, die die $\mathbb{Z}_2$-Symmetrie bricht, gefunden werden. Renormierungsgruppenbasierte

Rechnungen sagen drei Bereiche unterschiedlicher Kritikalität voraus. Für kleine Werte von α wird eine der Molekularfeldtheorie entsprechende Kritikalität, im Bereich großer α Nächste-Nachbar-Kritikalität erwartet. Die dazwischen prognostizierten, kontinuierlich variierenden kritischen Exponenten konnten im Rahmen der hier präsentierten Methode bestätigt werden. Zudem fanden sich auch in ein und zwei Dimensionen multiplikative logarithmische Korrekturen, die für das kurzreichweitige Quantenmodell erst für ein dreidimensionales kubisches Gitter erwartet werden. Dies bestätigt die Interpretation des Modells mit langreichweiten Wechselwirkungen als ein kurzreichweitiges Modell in einer effektiven Dimension.

Während in der vorliegenden Arbeit Effekte der Frustration durch eine antiferromagnetische Wechselwirkung schon bei bipartiten Gittern sichtbar wurden, sind diese besonders interessant für Gitter, bei denen das Isingmodell mit Nächster-Nachbar-Wechselwirkung bereits frustriert ist. Bei der Untersuchung des Isingmodells auf dem Dreiecksgitter konnten deutliche Hinweise für eine größere Reichhaltigkeit des Phasendiagramms mit der Existenz zusätzlicher Streifenphasen gefunden werden, die durch das Einführen langreichweitiger Wechselwirkung bedingt ist. Für Dreiecksgitter, abgebildet auf einen endlichen Zylinder, wurden zudem Hinweise auf mögliche exotische Quantenphasenübergänge unendlicher Ordnung gefunden, die jedoch weitere zukünftige Untersuchungen erfordern.

CONTENTS

1 INTRODUCTION 1
1.1 Quantum phase transitions . . . 5
1.2 Long-range-interacting systems . . . 11
1.3 Research on additive long-range systems . . . 12
1.3.1 Classical model . . . 14
1.3.2 Quantum model . . . 15
1.3.3 Experimental systems . . . 19
2 THE ISING MODEL 21
2.1 Criticality of the classical Ising model . . . 22
2.2 Ising model in a transverse field . . . 22
2.2.1 Ground states . . . 23
2.2.2 Elementary excitations in the Ising model . . . 27
2.2.3 Elementary excitations in the polarized phase . . . 29
2.2.4 Exact solution (nearest-neighbor chain) . . . 30
2.2.5 Quantum-classical analogy . . . 32
2.3 Long-range Ising model . . . 34
2.3.1 Nearest-neighbor limit . . . 35
2.3.2 Uniform-interaction limit . . . 35
2.3.3 Excitations in the LRIM . . . 37
3 METHODS 43
3.1 Continuous Unitary Transformations . . . 46
3.1.1 Perturbative Continuous Unitary Transformations . . . 49
3.1.2 High-field limit . . . 53
3.1.3 Linked-cluster expansion . . . 53
3.1.4 Graphs . . . 54
3.1.5 White-graph expansion . . . 57
3.1.6 Embedding PCUT results for a long-range model . . . 57
3.2 Computation of nested infinite sums . . . 59
3.2.1 Exact solutions . . . 59
3.2.2 The structure of the nested sums . . . 59
3.2.3 Convergence analysis of partial nested multi sums . . . 61
3.2.4 Monte-Carlo sampling . . . 66
3.3 Extrapolation techniques . . . 82
3.3.1 Padé extrapolations . . . 83
3.3.2 DLog Padé extrapolations . . . 85

3.4 Calculation flow . . . 86
3.5 Mean-field calculations . . . 88
3.5.1 Square lattice . . . 90
3.5.2 Triangular lattice . . . 92
4 PHASE TRANSITIONS IN THE LRTFIM 97
4.1 1D Ising chain . . . 98
4.1.1 Ground-state energy . . . 98
4.1.2 Dispersion . . . 99
4.1.3 Ferromagnetic interaction . . . 101
4.1.4 Antiferromagnetic interaction . . . 103
4.1.5 General remarks . . . 105
4.2 Hypercubic lattices . . . 106
4.2.1 Square lattice . . . 106
4.2.2 Cubic lattice . . . 111
4.3 Triangular lattice . . . 113
4.3.1 Dispersion . . . 113
4.3.2 Ferromagnetic interaction . . . 115
4.3.3 Antiferromagnetic interaction . . . 117
4.4 Cylindrical triangular lattice . . . 118
4.4.1 Geometry . . . 120
4.4.2 Pure LRIM . . . 120
4.4.3 XC(6) . . . 124
4.4.4 XC(4) . . . 127
4.4.5 Physics of the LRTFIM on the XC(n) lattice . . . 129
5 FINAL REMARKS 131
APPENDICES 137
A Own publications and contributions of the authors . . . 137
A.1 Critical behavior of quantum magnets with long-range interactions in the thermodynamic limit . . . 137
A.2 Quantum Criticality of Two-Dimensional Quantum Magnets with Long-Range Interactions . . . 138
A.3 Quantum criticality of the transverse-field Ising model with long-range interactions on triangular-lattice cylinders . . . 138
B Definitions . . . 139
B.1 Pauli matrices . . . 139
B.2 Mathematical functions and series . . . 139
C Algorithms . . . 140
C.1 Adjacency-number-calculation algorithm . . . 140
C.2 Double-sided zeta distribution . . . 142

C.3 Deprecated Markov-Chain Monte-Carlo moves 143
D Wave vectors of magnetic orders 147
D.1 Columnar (zigzag-striped) phase on the triangular lattice 148
D.2 Further magnetic structures 150
E Low-field expansion of the triangular-lattice cylinder 150
E.1 Stripe-ordered phases 150
F Data 153
F.1 Series coefficients 153
F.2 Critical values and exponents 164
F.3 Dispersion data points 169

BIBLIOGRAPHY 171

LIST OF FIGURES

Figure 1.1 Schematic setup of cold-ion trap and experimental image of top view. . . . 3
Figure 1.2 Algebraical decay of interactions in an ion trap. . . . 4
Figure 1.3 Qualitative phase diagram illustrating a quantum-critical point. 7
Figure 1.4 An overview of different additive and non-additive systems in the α-d-plane. . . . 13

Figure 2.1 Ferromagnetic to antiferromagnetic mapping of the 1D spin chain. . . . 23
Figure 2.2 Ground states in the Ising model . . . 25
Figure 2.3 Illustration of a ground state and dimer model on the frustrated IM on a triangular lattice. . . . 26
Figure 2.4 The maximally-flippable state on the triangular lattice. . . . 27
Figure 2.5 Illustration of the Suzuki-Trotter mapping. . . . 33
Figure 2.6 Lower part of the energy spectra of the LRIM. . . . 37
Figure 2.7 Low excitations of the ferromagnetic LRIM on a 1D chain. . . . 40
Figure 2.8 Low excitations of the antiferromagnetic LRIM on a 1D chain. 41

Figure 3.1 Qualitative phase diagram illustrating a quantum-critical point. 44
Figure 3.2 Illustration of the PCUT method. . . . 50
Figure 3.3 Illustration of the adjacency-matrix and adjacency-number construction . . . 55
Figure 3.4 Iterative scheme for generating graphs. . . . 56
Figure 3.5 Illustration of graph $\mathcal{G}_{51}$ and $\mathcal{G}_{60}$ . . . 60
Figure 3.6 A comparison of the Wynn extrapolation values and the scaling of partial sums. . . . 67
Figure 3.7 Randomly sampled circle. . . . 68
Figure 3.8 Illustration of a rift move. . . . 72
Figure 3.9 Multi-site rift moves in 1D . . . 74
Figure 3.10 Illustration of a shift move. . . . 75
Figure 3.11 A comparison of different choices for the weight $\pi(a)$ for the Monte-Carlo summation. . . . 76
Figure 3.12 Relative error of the running average of the MCMC. . . . 77
Figure 3.13 One-dimensional two-site unit-cell chain . . . 80

Figure 3.14 A comparison of the dispersion of the LRTFIM on a 1D chain with one and two sites per unit cell. 81
Figure 3.15 DLogPadé families of λ_c. 84
Figure 3.16 Flow diagram of methods for LCE of the LRTFIM. 87
Figure 3.17 Magnetic orders on the triangular lattice 93

Figure 4.1 Analytic dispersion of the 1D LRTFIM chain in $\mathcal{O}(2)$. 99
Figure 4.2 Dispersion of the 1D long-range transverse-field Ising model (LRTFIM) chain for $\alpha = 2$. 100
Figure 4.3 The one-QP gap $\Delta_{f/af}$ of the 1D LRTFIM chain as a function of λ for ferro-/antiferromagnetic Ising interactions. 101
Figure 4.4 Phase diagram and critical exponents of the ferromagnetic 1D LRTFIM chain. 102
Figure 4.5 Phase diagram and critical exponents of the antiferromagnetic 1D LRTFIM chain. 105
Figure 4.6 Square lattice vectors. 107
Figure 4.7 Dispersion of the antiferromagnetic LRTFIM on a square lattice. 108
Figure 4.8 Phase diagram and critical exponents of the ferromagnetic 2D LRTFIM on a square lattice. 109
Figure 4.9 Phase diagram and critical exponents of the antiferromagnetic 2D LRTFIM on a square lattice. 111
Figure 4.10 Phase diagram and critical exponents of the ferromagnetic 3D LRTFIM on a cubic lattice. 112
Figure 4.11 Phase diagram and critical exponents of the antiferromagnetic 3D LRTFIM on a cubic lattice. 113
Figure 4.13 The one-QP dispersion of the antiferromagnetic LRTFIM on the triangular lattice. 115
Figure 4.14 Phase diagram and critical exponents of the ferromagnetic 2D LRTFIM on a triangular lattice. 116
Figure 4.15 Comparison of the critical exponents of the ferromagnetic LRTFIM on the square and triangular lattice. 117
Figure 4.16 Phase diagram and critical exponents of the antiferromagnetic 2D LRTFIM on a triangular lattice. 119
Figure 4.17 Illustration of the XC(n) cylinder geometry for $n = 6$. 120
Figure 4.18 Illustration of different stripe orders. 121
Figure 4.19 LRIM stripe energies for XC(4) and XC(6). 121
Figure 4.20 Maximally flippable state and clock order of the XC(6) lattice. 124
Figure 4.21 Ground-state phase diagram of the XC(6) cylinder. 125
Figure 4.22 Determination of the phase boundaries of the XC(6) lattice. . 126
Figure 4.23 Maximally flippable state and clock order of the XC(4) lattice. 127

Figure 4.24 Ground-state phase diagram of the XC(4) cylinder. 128

Figure C.1 Overview of graphs, adjacency number and symmetry in order four. 141
Figure C.2 Plot of the sampled double-sided zeta distribution 143
Figure C.3 Rift moves in 2D 144
Figure C.4 Illustration of optimized antiferromagnetic summation 145
Figure D.1 Columnar magnetic orders on the triangular lattice 148
Figure E.1 Bare series of the ground-state energy per site $e_0^{\perp,(n)}$. 151

LIST OF TABLES

Table 1.1 Definition of critical exponents of QPTs in magnetic systems . . 8
Table 1.2 Overview of critical exponents of different universality classes . 10

Table 4.1 Critical decay exponents α_c for a phase transition between orthogonal ($\alpha > \alpha_c$) and zigzag ($\alpha < \alpha_c$) stripes. 122

Table F.1 Coefficients c_r of the ground-state energy per site e_0 for each order r in the LRTFIM on the one-dimensional chain. The first order is exactly zero. 153
Table F.2 Coefficients c_r of $\Delta_{\text{ch, f}}$ for each order r in the ferromagnetic LRTFIM on the one-dimensional chain ($k = 0$). 154
Table F.3 Coefficients c_r of $\Delta_{\text{ch, af}}$ for each order r in the antiferromagnetic LRTFIM on the one-dimensional chain ($k = \pi$). 155
Table F.4 Coefficients c_r of the ground-state energy per site e_0 for each order r in the LRTFIM on the two-dimensional square lattice. The first order is exactly zero. 156
Table F.5 Coefficients c_r of $\Delta_{\text{sq, f}}$ for each order r in the ferromagnetic LRTFIM on the two-dimensional square lattice ($\boldsymbol{k} = \mathbf{0}$). 157
Table F.6 Coefficients c_r of $\Delta_{\text{sq, af}}$ for each order r in the antiferromagnetic LRTFIM on the two-dimensional square lattice ($\boldsymbol{k} = (\pi, \pi)^T$). 158
Table F.7 Coefficients c_r of the ground-state energy per site e_0 for each order r in the LRTFIM on the two-dimensional triangular lattice. The first order is exactly zero. 159
Table F.8 Coefficients c_r of $\Delta_{\text{tr, f}}$ for each order r in the ferromagnetic LRTFIM on the two-dimensional triangular lattice ($\boldsymbol{k} = \mathbf{0}$). . . . 160
Table F.9 Coefficients c_r of $\Delta_{\text{tr, af}}$ for each order r in the antiferromagnetic LRTFIM on the two-dimensional triangular lattice ($\boldsymbol{k} = (2\pi/3, -2\pi/3)^T$). 161
Table F.10 Coefficients c_r of $\Delta_{\text{cub, f}}$ for each order r in the ferromagnetic LRTFIM on the three-dimensional cubic lattice ($\boldsymbol{k} = \mathbf{0}$). 162
Table F.11 Coefficients c_r of $\Delta_{\text{cub, af}}$ for each order r in the antiferromagnetic LRTFIM on the three-dimensional cubic lattice ($\boldsymbol{k} = (\pi, \pi, \pi)^T$). 163

Table F.12 Critical values and exponents of the ferromagnetic LRTFIM on the 1D chain. 164
Table F.13 Critical values and exponents of the antiferromagnetic LRTFIM on the 1D chain. 165
Table F.14 Critical values and exponents of the ferromagnetic LRTFIM on the 2D square lattice. 166
Table F.15 Critical values and exponents of the antiferromagnetic LRTFIM on the 2D square lattice. 166
Table F.16 Critical values and exponents of the ferromagnetic LRTFIM on the 2D triangular lattice. 167
Table F.17 Critical values and exponents of the antiferromagnetic LRTFIM on the 2D triangular lattice. 167
Table F.18 Critical values and exponents of the ferromagnetic LRTFIM on the 3D cubic lattice. 168
Table F.19 Critical values and exponents of the antiferromagnetic LRTFIM on the 3D cubic lattice. 168
Table F.20 Data points of the antiferromagnetic 2D square lattice dispersion. 169
Table F.21 Data points of the antiferromagnetic 2D triangular lattice dispersion. 169

ACRONYMS

CMF	cluster mean field
CUT	continuous unitary transformation
DEEPCUT	directly evaluated EPCUT
DMRG	density-matrix renormalization group
DTWA	discrete truncated Wigner approximation
DW	domain wall
ED	exact diagonalization
EPCUT	enhanced PCUT
GCUT	graph CUT
iDMRG	infinite-size density matrix renormalization group
IM	Ising model
TFIM	transverse-field Ising model
LCE	linked-cluster expansion
LRIM	long-range Ising model
LRTFIM	long-range transverse-field Ising model
KT	Kosterlitz-Thouless
MF	mean field
MC	Monte Carlo
MCMC	Markov-chain Monte Carlo
MPS	matrix product states
n/a	not available

***n*D**	*n*-dimensional
NN	nearest-neighbor
PCUT	perturbative CUT
QCP	quantum-critical point
QDM	quantum dimer model
QMC	Quantum Monte Carlo
QP	quasiparticle
QPT	quantum phase transition
RG	renormalization-group
RNG	random-number generator
SCUT	self-similar CUT
TF	transverse field
w/, w/o	with, without

1

INTRODUCTION

Phase transitions can be found everywhere in nature: Whether the transition of water ice to liquid water in the alps during spring time, the explosion of a supernova in a far-away galaxy, or the tipping point in a climate system destroying the Antarctic ice sheets or in economics just at the beginning of a financial crisis. But let us focus more on the kind of transitions that are important in physics: Here, a phase describes a state of matter with uniform physical properties such as the liquid or solid phase of water and is determined by the current equilibrium state of a system. Not only the density but also magnetic or chemical properties may determine a phase and separate it from others. Although research is still continuing, in many cases classical phase transitions are well understood theoretically and can be modeled with good agreement compared to the experimental observations using Landau's theory [Lan37]. The theory tries to describe continuous phase transitions in a general form – ignoring any microscopic details – by writing the free energy as a Taylor expansion of an order parameter around a critical point. The order parameter is a quantity, for example the magnetization or density of a sample, which indicates the appearance or disappearance of the corresponding phase. In one of the phases the order parameter is exactly zero. When the system parameters are tuned, e. g., when the temperature is lowered, the system switches to a new phase and the order parameter becomes finite at this *critical point*.

Quantum phase transitions (QPTs) stand in contrast to classical phase transitions where one main difference lies in the parameter driving the transition. Classically, tuning the temperature T and introducing *thermal* fluctuations drives the system from one phase to another. QPTs, however, occur at exactly $T = 0$. Parameters such as magnetic field or pressure which might introduce a modification of spin-exchange-interaction strengths introduce *quantum* fluctuations and determine the resulting quantum phase.

A very intriguing feature of phase transitions is a property called "universality". Quantum and thermal phase transitions can be sorted into several universality classes which share common properties at the phase transition point. These properties, such as critical exponents, need to be calculated only for one of the models in a single class. If, for a new model, the dimension, the symmetry of the order parameter, and the degrees of freedom lead to the same universality class as for a known system there is no need for a repeated calculation of the universality classes critical exponents. Consequently, the behavior of complicated models at the phase transition can often be studied by considering a simpler model in the same universality class.

The universality scheme is derived under the assumption that the studied systems consist of infinitely extended periodic copies of smaller building blocks. The microscopic behavior of the small subsystems and their collective interactions determine the properties of the macroscopic system. The fact that the number of microscopic states grows exponentially with the system size results in highly nontrivial problems. For many models the interaction between the smaller parts of the macroscopic system is assumed to decay very quickly such that it can be described with sufficient accuracy by nearest- or maybe next-nearest-neighbor interactions. In these situations the total energy of two subsystems can be understood by studying the contact region of those subsystems and the systems are called *short-range* [Cam+14]. This approximation of real systems often proves helpful in the numerical investigation of those systems since they become more accessible for calculations to one of the many different algorithms developed in the past.

If we look at *long-range* systems, where the interaction decays algebraically with the inter-particle distance r between the small constituting elements as $V(r) \propto r^{-\alpha}$, with $\alpha \geq 0$, we leave this approximation behind. It is well known that the universality class of a system can change if interactions are varied between a very short-ranging exchange and a strong coupling of elements such as, e. g., spins, atoms, or molecules which are far apart [Fis67]. The introduction of the parameter α which allows the continuous tuning of the interaction strength depending on a distance makes it possible to study the dependence of critical exponents on the interaction range.

Long-range interactions are not only interesting from a theoretical point of view but can also be of relevance for existing systems. There are dipolar interactions between spins in spin-ice materials which give rise to magnetic monopoles [CMS08], effective long-range magnetic interactions between zig-zag edges in graphene [KW17], and most closely related to the specific model introduced later in this thesis: trapped cold-ion systems in quantum optics for which the algebraic decay of interactions in the long-range transverse-field Ising model, which is introduced in the next chapter, on the triangular lattice can be continuously tuned over a wide parameter range [Bri+12; Isl+13; Boh+16; YJZ19]. But also in non-magnetic systems such as gravitational systems, two-dimensional hydrodynamics, and two-dimensional elasticity long-range interactions can play a relevant role [CDR09].

A special interest should be given to trapped cold-ion systems for two reasons. For one, in the past, there has been some success in implementing a two-dimensional Ising model (IM) with algebraically decaying interactions between spins-1/2 on a triangular lattice. A spin-1/2 describes a particle with a spin $s = 1/2$, the z-component of which is often referred to as *spin up* ($\uparrow$) for $s_z = +1/2$ and *spin down* ($\downarrow$) for $s_z = -1/2$. Basic examples of such particles are electrons and protons. In [Bri+12] the spins of the valence electrons of trapped Beryllium ions Be_9^+ were coupled to realize the model. This is no easy task as several goals needed to be achieved, such as controlling the location (the lattice

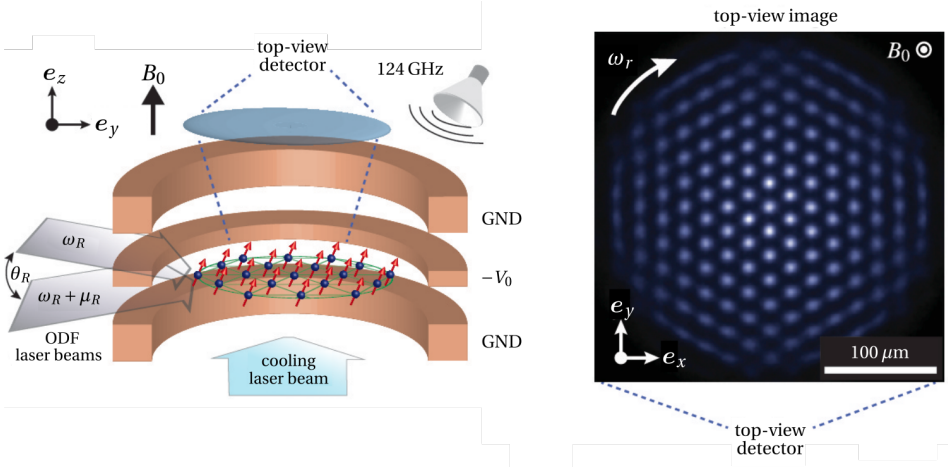

Figure 1.1: (Left) A schematic view of ions in a cold-ion trap. The ions are trapped in a quadrupolar electric potential and a magnetic field and arrange in a Coulomb lattice. The laser-cooled ions are coupled by an optical dipole force (ODF) via two detuned, angled laser beams. (Right) A triangular lattice structure emerges and can be measured in the detector. Adapted from [Bri+12].

spacing and geometry) of the spins in a deterministic way, cooling the ions, engineering the spin-spin interaction, and reading out the spin states with high fidelity. The control and readout of single ions was already demonstrated with atomic clocks in 2008 where the frequency ratio of two different atomic clocks was studied with an extremely high precision of 4.3×10^{-17} Hz [Ros+08]. Building on the previous knowledge Britton *et al.* [Bri+12] tackled the remaining points and impressively demonstrated the setup of a cold-ion trap with hundreds of spins, illustrated in Figure 1.1, where they were able to implement algebraically decaying Ising interactions. They used a Penning trap where the combination of a strong, homogeneous magnetic field $\boldsymbol{B} = B_0 \boldsymbol{e}_z$ ($B_0 = 4.46\,\mathrm{T}$) and a static quadrupolar electric potential restricted the position of the ions to a Coulomb crystal. Here, the electric field traps the ions axially (along the direction $\boldsymbol{e}_z$ of the magnetic field) and a rotation of the ions in combination with the static magnetic field forces a radial limitation on the ions due to the Lorentz force $q\boldsymbol{v} \times \boldsymbol{B}$, with charge q and velocity $\boldsymbol{v}$ of the ion. These parameters allow the control of the geometry where, after laser cooling, different Coulomb crystals can form depending on the ion density [Mit+98]. Confining the ions and therefore the valence-electron spins of the ions in such a way results in a coupling of the spins' motional degrees of freedom. Britton *et al.* used the coupling to induce the spin-spin interactions with a "spin-dependent optical dipole force" [Bri+12]. Two off-resonant laser beams shining on the ion plane in different angles and multiple scattering of the incoming photons force small displacements of the ions which in

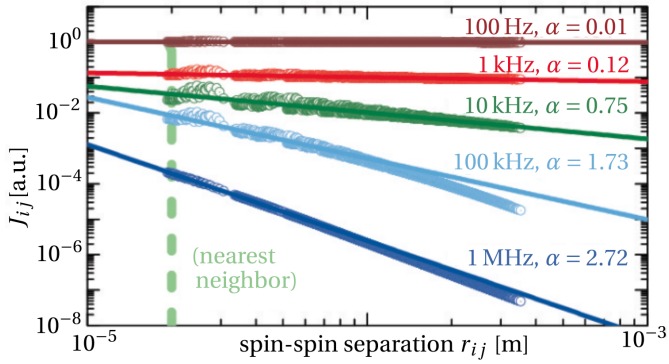

Figure 1.2: Demonstration of the algebraical decay of Ising interactions induced by a coupling of mechanical modes in an ion trap. For different mismatches in the laser detuning frequency different decay exponents can be realized. Circles are calculated from the Coulomb potential energy and the resulting optical dipole force while solid lines represent a power-law fit to the values. Adapted from [Bri+12].

turn results in a modified Coulomb potential. They have shown that this effectively results in an algebraically decaying interaction dependent on the motional modes and on the difference in laser frequency, which can be tuned to control the decay exponent α (cf. Figure 1.2) [Bri+12]. The algebraic decay of the long-range Ising interactions can be tuned continuously between $\alpha = 0$ (unweighted all-to-all interactions) and $\alpha = 3$ (dipole-dipole interactions) [Bri+12; YJZ19].

While this is already an impressive demonstration of realizing the Ising model with long-range interactions, it has to be seen in a bigger picture, which directly leads to the second point. Nowadays, a large focus is set on quantum computers, due to their massive speedup compared to classical computers in certain areas and their Turing completeness. Unfortunately, these are still quite limited, e. g., Google only recently tested a state-of-the-art quantum computer consisting of 53 qubits [Aru+19]. Using quantum computers, the theoretical study of physical many-body systems would also profit immensely. Until their useful realization, however, their might be a different pathway in *quantum simulation* which can exploit quantum supremacy, too, while possibly being simpler in its practical implementation [Fri+08; Isl+11; Bri+12; Har+18; YJZ19]. The implementation of a long-range transverse-field Ising model as one of the first quantum systems to be simulated by a cold-ion system would be impressive and promising. The Ising model has been and still is one of the most paradigmatic models to test new algorithms and techniques and therefore is a good candidate for an implementation in such a test bed. In order to verify and benchmark results from these early systems theoretical reference results are needed.

The goal of the presented thesis is to study the interplay between long-range interactions and quantum fluctuations induced by a transverse field on various different lattice geometries in several dimensions. It turns out that driving the parameter α that determines the decay of the interaction can be understood in terms of an effective spatial dimension [DTC15]. An antiferromagnetic interaction can lead to frustration effects even in the 1D model. Additionally, exotic Kosterlitz-Thouless transitions and unusual logarithmic corrections to the critical behavior were found [FS16; FKS19; Koz+19].

In the next section, I briefly recapitulate the general properties of quantum phase transitions including critical exponents and scaling relations with a special focus on magnetic systems such as the Ising model studied here. Afterwards, a short discussion of long-range-interacting systems is given. Finally, I give an overview over the history and present current results for the nearest-neighbor and long-range Ising model.

In the next chapter the Ising model is thoroughly introduced and some of its historic relevance presented. A well-known exact solution for the nearest-neighbor model is reviewed before the focus shifts to the long-range model studied in this thesis.

In Chapter 3, I discuss several methods and algorithms used to derive the results which are presented in the chapter afterwards.

Throughout the thesis, I use the common and convenient convention to set $\hbar = 1$.

1.1 QUANTUM PHASE TRANSITIONS

Most parts of this section are inspired by various books [Sim97; Sac11; Dut+15; Fen19], while the content should be found in nearly every textbook on the topic of quantum phase transitions. For a more detailed description I refer the reader to those sources.

Consider a classical translational-invariant system supporting a phase transition at a critical temperature T_c. We differentiate between two types of phase transitions:

First-order phase transitions show a jump in the first derivative of the ground-state energy and the order parameter between the two phases, while the correlation length ξ – the typical length scale of the microscopic degrees of freedom's correlation – remains finite.

A second-order (or continuous) phase transition has a smooth ground-state energy. At the phase transition the correlation length becomes infinite. The phases on both sides of the transition approach the same state at the critical point which results in a unique global critical phase and a smooth behavior of the order parameter. For second-order phase transitions several critical exponents can be associated with such a critical point: If we call the order parameter of a phase O[1], it has the thermal expectation value $\langle O(\boldsymbol{r})\rangle = 0$

1 A typical order parameter for ferromagnetic systems is the magnetization and for Néel-ordered antiferromagnets the staggered magnetization.

in the unordered phase for $T \geq T_c$ and $\langle O(\boldsymbol{r}) \rangle \neq 0$ in the ordered phase below the critical temperature. For a second-order phase transition the expected value behaves as

$$\langle O(\boldsymbol{r}) \rangle \propto (T_c - T)^{\beta} \tag{1.1}$$

close to the critical point. The function is continuous but not necessarily analytical: A continuous order parameter does not require its derivative to be continuous. While this equation defines the critical exponent β, in classical phase transitions five other universal exponents can be defined for the correlation length, the heat capacity, etc. The idea of a universal critical behavior goes back to Landau in 1937, who set up an effective theory of phase transitions [Lan37]. The theory is based on the system's description by the order parameter and only describes the critical behavior. Quantitative results for, e. g., the critical temperature T_c or other non-universal numbers can certainly not be expected from the theory.

The existence of universality might be surprising at a first glance but might become more convincing when looking at an example supported by experimental evidence. Theoretical investigations on the criticality of the liquid-gaseous transition line of water and on the 3D-Ising critical point revealed that the order parameter of the systems on the temperature behaves as

$$\rho - \rho_c \propto (T_c - T)^{\beta} \quad \text{and} \quad M \propto (T_c - T)^{\beta}\,, \tag{1.2}$$

where ρ (ρ_c) is the (critical) density and M is the magnetization, with the *same* exponent $\beta \approx 0.3285(7)$[WIH12] (gas-liquid) and $\beta \approx 0.326\,432(27)$[ES+14] (3D-Ising)[2], respectively. The values have also been measured experimentally for ^{3}He ($\beta \approx 0.321(6)$) [PDM79] or sulphurhexafluoride SF_6 ($\beta \approx 0.327(3)$) [LKG77] and for the 3D Ising antiferromagnet $DyAlO_3$ ($\beta \approx 0.311(5)$) [HVUH71]. Although the systems are decidedly different from a microscopic point of view, both can be attributed to the same universality class. The role of the density in the water system relates to the magnetization, while the pressure is replaced by the magnetic field. [Fis67]

The universal properties resulting from global properties such as the symmetry and dimension of the system are captured in Landau's effective theory and make it a useful tool to describe and determine universal critical properties. On the other hand, however, it only describes the universal behavior. If quantitative universal and non-universal properties are sought, different approaches must be taken.

A few years after the introduction by Landau the theory was extended in a joint paper by Ginzburg and Landau [GL50] in the attempt to find an effective theory for the superconducting phase which is known today as the *Ginzburg-Landau* theory.

2 The 3D-Ising exponent is derived from the results by El-Showk [ES+14] using the scaling relations in Equation (1.13).

For quantum-mechanical systems the role of the temperature T as the driving parameter of the phase transition is replaced by a different (non-thermal) parameter such as magnetic field or pressure-induced changes in exchange-interaction strength J. More specifically, in quantum systems the *competition* of the different non-commuting interactions in the Hamiltonian factor into the resulting phase[3]. If only a single interaction is present, e. g., in the Heisenberg Hamiltonian $\hat{H} = J \sum_{\langle i,j \rangle} \hat{\boldsymbol{S}}_i \hat{\boldsymbol{S}}_j$, different quantum phases can also be obtained by tuning the parameter J from negative to positive values. However, a relationship between the quantum and classical phase transition exists. As outlined later in Section 2.2.5, a mapping from a d-dimensional quantum system to a $(d+1)$-dimensional classical system can be found.

Although quantum phase transitions occur at $T = 0$ remnants of the transition might be found in experiments for $T > 0$ around the quantum-critical point (QCP) and have an influence on the low-temperature physics [Sac11; Dut+15]. The interplay of temperature and the parameter driving the quantum phase transition sets up a playground of quantum and classical criticality as illustrated in Figure 1.3.

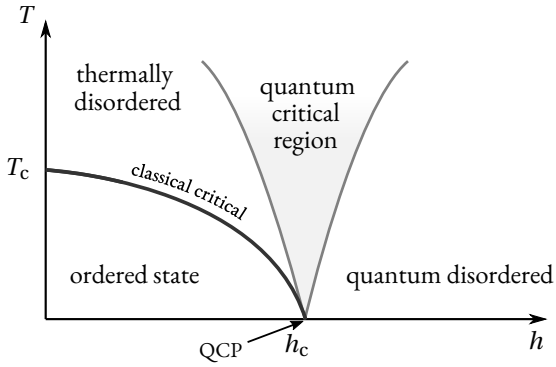

Figure 1.3: The phase diagram is divided into several areas by the interplay of thermal and quantum fluctuations. The thick black line represents the classical thermal phase transition line with the respective critical exponents and separates the ordered from the thermally disordered phase. This can be found, e. g., in transverse Ising models in dimensions $d > 1$ while for the one-dimensional model the line is absent as it has no classical thermal phase transition. For temperature $T = 0$, at the quantum-critical point, quantum fluctuations controlled by the parameter h drive the system from the ordered to the quantum-disordered state. In the shaded area above the QCP both thermal and quantum fluctuations influence the system's behavior.

There are several thermodynamic quantities diverging at the QCP, each with its respective critical exponent. An overview over the quantities and their critical exponents

3 At $T = 0$ the system relaxes to its ground state which does not need to be unique as degeneracy may be present (see, e. g., the Ising model on a triangular lattice without a field in Section 4.3.3).

Table 1.1: Definition of critical exponents of QPTs in magnetic systems [Sac11; Dut+15]. h_l is a longitudinal magnetic field while h denotes the transverse field with the critical value h_c.

QUANTITY	EXP.	DEFINITION	CONDITIONS
Correlation length ξ	ν	$\xi \propto \lvert h - h_\mathrm{c}\rvert^{-\nu}$	$h \to h_\mathrm{c}$, $h_\mathrm{l} = 0$
Specific heat C	α	$C \propto \lvert h - h_\mathrm{c}\rvert^{-\alpha}$	$h \to h_\mathrm{c}$, $h_\mathrm{l} = 0$
Order parameter m_x	β	$m_x \propto (h - h_\mathrm{c})^{\beta}$	$h \to h_\mathrm{c}$ from below $h_\mathrm{l} = 0$
Susceptibility χ	γ	$\chi \propto \lvert h - h_\mathrm{c}\rvert^{-\gamma}$	$h \to h_\mathrm{c}$, $h_\mathrm{l} = 0$
Critical isotherm	δ	$h_\mathrm{l} \propto \lvert m_x\rvert^{\delta} \operatorname{sgn} m_x$	$h_\mathrm{l} \to 0$, $h = h_\mathrm{c}$
Correlation function G	η	$G(r) \propto \lvert r\rvert^{-d+2-\eta}$	$h = h_\mathrm{c}$, $h_\mathrm{l} = 0$
Correlation time ξ_τ	z	$\xi_\tau \propto \xi^z$	$h \to h_\mathrm{c}$, $h_\mathrm{l} = 0$

is given in Table 1.1. If we pick out a few important entries, we find the correlation length, which is defined by the exponential decay of the equal-time two-point correlation function in the ground state at the QCP. The correlation function of the observable $\hat{O}$ between two points with distance $\boldsymbol{r}$ and its norm $r = |\boldsymbol{r}|$ is given as

$$G(r) = \left\langle \hat{O}(\mathbf{0}, t)\hat{O}(\boldsymbol{r}, t)\right\rangle = \frac{1}{r^{d-2+\eta}} \mathrm{e}^{-r/\xi} \,, \tag{1.3}$$

where d is the dimension of the system and η is called Fisher-exponent. As already discussed in the short description of Landau's effective theory, the order parameter itself follows

$$\langle O\rangle \propto \begin{cases} |h_\mathrm{c} - h|^{\beta} & \text{for } h < h_\mathrm{c} \\ 0 & \text{otherwise,} \end{cases} \tag{1.4}$$

where h is a transverse field in magnetic systems and defines the exponent β. The subscript "c" always indicates values at the critical point, such as the critical field h_c.

In this thesis I study the critical properties of quantum phase transitions by investigating the energy gap $\Delta(h)$ between the ground and lowest-lying excited state of quantum mechanical systems. For a second-order phase transition the gap is expected to behave as

$$\Delta \propto |h - h_\mathrm{c}|^{z\nu} \tag{1.5}$$

and defines the product of exponents z and ν. The latter determines the divergence of the correlation length

$$\xi \propto |h - h_\mathrm{c}|^{-\nu} \,, \tag{1.6}$$

while z is the dynamical critical exponent relating the correlation length to the correlation time

$$\xi_\tau \propto \xi^z \propto |h - h_\mathrm{c}|^{-z\nu} . \tag{1.7}$$

The time scale ξ_τ is similarly defined to ξ and also diverges at the QCP. It illustrates the connection of temporal and spatial dimensions in quantum phase transitions.

There are cases in which these descriptions fail and additional corrections need to be considered. One such case is the transverse-field Ising model (TFIM) at the upper critical dimension $d_\mathrm{u} = 3$ (or, respectively, the classical IM at $d_\mathrm{u}^\mathrm{c} = 4$) where multiplicative logarithmic corrections are present, e. g., in the gap

$$\Delta \propto |h - h_\mathrm{c}|^{z\nu} \ln\left(1 - \frac{h}{h_\mathrm{c}}\right)^p \tag{1.8}$$

with the logarithmic critical exponent p [LK69; BLGZJ73; WR73; WOH94; Coe+16]. Other quantities also contain such corrections – for example, in the classical Ising model in four dimensions the functional form for several quantities are given by

$$C \propto (\ln|t|)^{1/3} \qquad \text{(specific heat)} \tag{1.9}$$

$$\chi \propto |t|^{-1}(\ln|t|)^{1/3} \qquad \text{(susceptibility)} \tag{1.10}$$

$$M \propto |t|^{1/2}(\ln|t|)^{1/3} \ \ (\text{for } t \to 0^+) \qquad \text{(spontaneous magnetization)} \tag{1.11}$$

$$\Delta \propto \chi^{-1/2} \propto |t|^{1/2}(\ln|t|)^{-1/6} \qquad \text{(energy gap)} \tag{1.12}$$

where $t = 1 - T/T_\mathrm{c}$ is the reduced temperature [WOH94].

The different exponents are not completely independent of each other. The dependency results in the fact that only a few are necessary to determine the universality class of the system. These (hyper)scaling relations [Sac11; SIC12; Dut+15] are given as

$$\gamma = (2 - \eta)\nu , \qquad 2\beta = (d - 2 + \eta)\nu , \tag{1.13}$$

$$\alpha = 2 - \gamma\frac{\delta + 1}{\delta - 1} , \qquad \delta = \frac{\beta + \gamma}{\beta} , \tag{1.14}$$

$$2 = \alpha + 2\beta + \gamma , \qquad 2 - \alpha = \nu(d + z) \quad (d < d_\mathrm{u}) , \tag{1.15}$$

where d_u is the upper critical dimension [Dut+15]. In higher dimensions $d > d_\mathrm{u}$ mean-field exponents are present [Fen19]. For transverse Ising systems the dynamical critical exponent $z = 1$, such that Equation (1.15) suggests the equivalence of the quantum model in d dimensions and the classical model in $d + 1$ dimensions [SIC12].

Also, a lower critical dimension exists and is defined to be the highest integer dimension for which the critical temperature $T_\mathrm{c} = 0$, i. e. no phase transition exists for finite

Table 1.2: An overview of known values for the critical exponents of the QPT in different systems. Values marked with an asterisk (*) are derived via scaling relations.

	MF	(1 + 1)D ISING	(2 + 1)D ISING	(2 + 1)D XY	(1 + 1)D XY
ν	1/2	1	.629 99(5)	.671 55(27)	.82(2)
α	0	0*	0.101(4)	.0146(8)	[−.96(6)*]
β	1/2	1/8	.326 432(27)*	.3485(2)	.111(8)
γ	1	7/4	1.241	1.3177(5)	1.41(4)*
δ	3	15	4.28	4.780(2)	6.0(6)*
η	0*	1/4*	.036 31(3)	.0380(4)	.272(15)
z	1	1	2.04(3)	.956(1)*	2.61(6)
	[Sta87]	[Fis74; PHA91]	[LGZJ80; PHA91] [GE94; Lan94; ES+14]	[Cam+01]	[OI03]

temperatures. For example, in the classical one-dimensional Ising chain the magnetization m acts as the order parameter of the system. At any finite temperature m vanishes if the longitudinal field $h_\mathrm{l} \to 0$ while for $d > 1$ a finite temperature phase transition exists [Pei36]. For classical Ising models the upper critical dimension $d_\mathrm{u}^\mathrm{c} = 4$ and the lower critical dimension $d_\mathrm{l}^\mathrm{c} = 1$ [Dut+15]. For long-range interactions different upper and lower critical dimensions are found as discussed in Section 1.3.2.

Only two of the critical exponents are independent and therefore suffice to determine the universality class of a system [Dut+15]. To get a feeling for some typical values the exponents of some universality classes, which play an important role later on, are listed in Table 1.2.

In the last decades, systems were found where Landau's theory was not easily applicable. The theory depends on the selection of a local parameter in terms of which the free energy near the critical point is then described. For systems with a topological order no local order parameter can be defined. An example which will become important later on is the classical (1 + 1)D-XY model. It consists of spins located on the vertices of a square lattice and interacting with their nearest-neighbors in the xy-plane. With increasing temperature vortex-antivortex pairs are induced and unbind at the critical temperature T_KT. It is found that, approaching T_KT from above, the correlation length diverges not algebraically as for typical phase transitions but exponentially with the reduced temperature $(T - T_\mathrm{KT})/T_\mathrm{KT}$. This untypical behavior indicates that the phase transition is neither first-order nor continuous but lies in a separate class, which is called the Kosterlitz-Thouless (KT) type. In contrast to the previous kinds, it is not possible to describe the phase transition by a local order parameter. [Kos74]

1.2 LONG-RANGE-INTERACTING SYSTEMS

In this thesis, I consider systems where long-range interactions exist between pairs of spins. The typical potential for a two-body long-range interaction decays – at least for large distances r – algebraically as

$$V(r) \propto \frac{1}{r^\alpha}, \quad \text{with} \quad \alpha \in \mathbb{R}_0^+ . \tag{1.16}$$

Systems with such long-range interactions can generally be separated in two groups depending on the ratio of the parameter α to the dimensionality of the system. For reasons I am going to discuss immediately, systems with $\alpha \leq d$ are *non-additive* in contrast to *additive* systems for $\alpha > d$. An introduction to the physics of classical non-additive systems has been given by Dauxois [Dau+02] and a nice review of the properties of solvable classical non-additive systems was compiled by Campa *et al.* [CDR09]. Some of the thoughts presented here are taken from these publications which should be checked for a more extensive review. In contrast to the definition presented in these publications, which define a system to be short-range if $\alpha > d$ and long-range otherwise, I use the terminology "long-range" also for systems with $\alpha > d$ – in fact for any $\alpha < \infty$. The reasons are that for one, the interaction spans an infinite, and therefore rather long, distance and consequently no characteristic length scale is given. Second, these, compared to nearest-neighbor, much extended interaction allows for unconventional features such as frustration effects and continuously varying critical exponents as discussed later [Fis67; DB01; LB02].

Before dwelling on the additivity of a system, let me quickly introduce the concept of *extensivity*. In an extensive system variables such as the energy E and entropy S are proportional to the system size N. Intensive properties can be derived from the extensive quantities such as, e. g., the ground-state energy per site $e_0 = E/N$. If we consider the classical Ising Hamiltonian with long-range interactions on an arbitrary geometry in d dimensions

$$H_{\mathrm{IM}} = J \sum_{\boldsymbol{i} \neq \boldsymbol{j}}^{N} \frac{1}{|\boldsymbol{i} - \boldsymbol{j}|^\alpha} S_{\boldsymbol{i}} S_{\boldsymbol{j}} , \tag{1.17}$$

we find that for values of $\alpha \leq d$ the energy becomes superextensive. A rescaling of the interaction as

$$J \to \frac{J}{N^{1-\alpha}} \tag{1.18}$$

is necessary to ensure the extensivity of the systems energy even for values of $\alpha \leq d$. The rescaling is known as the "Kac prescription" [KUH63; CDR09] and will reappear below.

While such a rescaling is possible to fix problems with the extensivity, the situation is different for *additivity*. If a system is divided into two parts, the total energy is given by the energy of the subpart energies E_1 and E_2 and the interaction energy between the parts E_{int} as $E = E_1 + E_2 + E_{\text{int}}$. For *additive* systems the ratio of the interaction energy to the sum of subsystem energies $E_{\text{int}}/(E_1 + E_2)$ vanishes in the thermodynamic limit, such that $E \approx E_1 + E_2$ can be assumed. This property holds for a system with $\alpha > d$, but – even for a rescaled interaction – cannot be restored for smaller values of α. [CDR09]

For frustrated systems it is an open question if the additivity of the system is preserved for long-range interactions. In Section 2.3.3 we show that even down to $\alpha = 0$ an evaluation of excitation energies remains possible in the 1D Ising model with long-range interactions. However, it is unclear if this statement can be generalized to arbitrary frustrated systems.

Non-additive systems seem to be exotic at a first glance, but there are more common instances than one might think. Probably, the most prominent examples for non-additive systems have gravitational or Coulomb interactions. But more examples exist such as those exemplarily presented in [Dau+02; CDR09]. An overview over several models in the α-d-plane is given in Figure 1.4. In this thesis, however, we focus on the shaded upper part of the illustration which contains additive systems with $\alpha > d$.

1.3 CURRENT STATE OF RESEARCH ON ADDITIVE LONG-RANGE-INTERACTING MANY-BODY SYSTEMS

For a lot of interacting many-body systems the approximation that interactions decay fast enough to allow a limitation to local such as, e. g., nearest-neighbor interactions is valid. Nevertheless, there are cases such as those listed in the beginning of the chapter which require a description of interactions of further-distant microscopic degrees of freedom in the respective Hamiltonian. In many real systems a dipole-dipole or van der Waals force is present. Naturally, the theoretical treatment of such systems comes with the price of calculations which are algorithmically more difficult and numerically more demanding than those originally developed for locally interacting systems.

The fact that the nature of a critical point is influenced by the range of interactions is no recent insight [Fis67]. Early work on the classical phase transition in the spherical model of a ferromagnet with algebraically decaying interaction energy

$$J_{ij} = \frac{J}{|i-j|^{\alpha}}\,, \quad \text{with} \quad \alpha \in \mathbb{R}_0^+ \tag{1.19}$$

between the spins on sites i and j [Joy66] encouraged Nagle and Bonner to publish a study of the classical 1D Ising chain with additional algebraically decaying ferromagnetic interactions in 1970 [NB70]. They already recognized the appearance of the Riemann

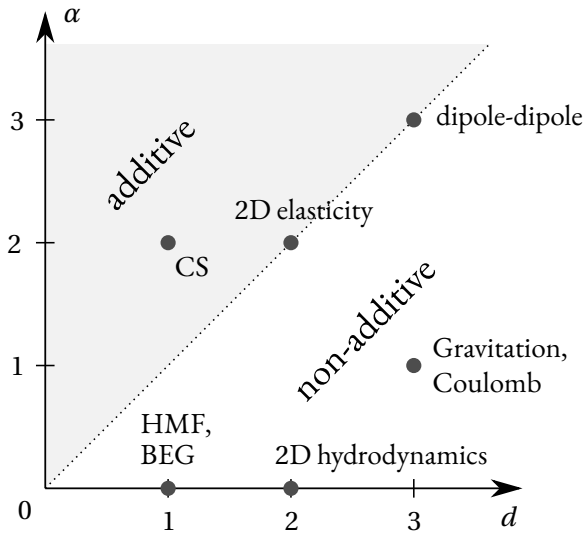

Figure 1.4: An overview of different additive and non-additive systems in the α-d-plane. The Hamiltonian Mean Field (HMF) and Blume-Emery-Griffith (BEG) model, the gravitational, 2D hydrodynamics, 2D elasticity, and dipole systems are discussed as classical non-additive systems in [CDR09]. The shaded area represents additive systems and will be studied for the Ising model with long-range interactions in a transverse field in this thesis. The Calogero–Sutherland (CS) model [Cal71; Sut71] is shown as an example for an additive system. Adapted from [CDR09].

ζ-functions in the energy summations and the need for a rescaling of the interaction for $0 \leq \alpha \leq d$ in dimension d which will also become apparent in the results later on. The fact that, using symmetries of the classical system, they were able to compute series expansions for up to 20 spins-1/2 for the classical model gives a feeling of the available computational power at that time.

Fisher *et al.* derived critical exponents γ and η for a long-range-interacting system with an n-vector order parameter in d dimensions using the ϵ-expansion of the renormalization-group (RG) technique [FMN72] only shortly after the calculation of these quantities for the short-range Heisenberg model [Wil72].

Different asymptotics of decaying interactions were studied as well. The anisotropic Heisenberg model with a Kac potential[4] drew the interest of Pearce and Thompson in 1975 [PT75]. In semiconductors exponentially decaying long-range forces between

4 The Kac potential allows the interaction up to a defined distance which should be considerably larger than the lattice spacing but can be a lot smaller than the system size.

atoms were derived around the same time and effects of the long-range interaction on the dispersion modes were found [SH76].

Today, the interest in the properties of long-range interacting systems is unabated. The possibility of an experimental realization of models with a tunable interaction [Bri+12; YJZ19] and resulting from this the availability of experimental data on such systems is motivating researchers in the field to study both static and dynamic properties for a variety of quantum-mechanical models. Especially the research on the influence of frustration in long-range models is currently still at the beginning. One of the most prominent candidates in current studies is the Ising model with long-range interactions. Starting from the classical short-ranged Ising model, the long-range counterpart will be derived step-by-step in the next chapter.

1.3.1 *Classical model*

In the past, several analytical and numerical works have been presented on the classical Ising model [Isi25]. The temperature-driven phase transition has been studied mostly for a ferromagnetically interacting system in different dimensions. In the one-dimensional Ising model, which has no classical phase transition for the nearest-neighbor model, but where long-range interactions allow a phase transition [Dys69] a Kosterlitz-Thouless type of phase transition exists for a spin-spin interaction decaying with distance r as $1/r^2$. This has been found by Anderson in 1971 [AY71] and later been confirmed analytically and numerically several times [FS82; LM01; San03].

In 2002 Luijten and Blöte studied the classical ferromagnetic Ising model in arbitrary dimension d to determine better numerical estimates for the boundaries of nearest-neighbor, mean-field, and continuously varying criticality [Fis67; LB02]. This has been the first numerical investigation since all previous work, which has lead to contradicting results, has been using the RG approach with an ϵ-expansion [Fis67; Sak73; Ent82]. The RG calculations predicted three regimes in the classical long-range Ising model: A classical regime for

$$0 < (\alpha - d) < d/2 \,, \tag{1.20}$$

an intermediate regime for

$$d/2 < (\alpha - d) < 2 \,, \tag{1.21}$$

with $\alpha \in \mathbb{R}$ defined as the decay exponent of the interaction decaying algebraically as $1/r^\alpha$ with distance r (cf. Section 2.3), and the short-range regime for larger values. The large-α regime can be intuitively understood as the nearest-neighbor case is obtained in the limit $\alpha \to \infty$.

Luijten's results have been further improved on a 2D system by using larger system sizes of up to 5120×5120 sites [Pic12] and later in 3D [BPR13]. They found the critical exponent $\eta = 2 + d - \alpha$ in the classical and intermediate regime up to $(\alpha - d) \approx 3.5$ and $\eta \approx .25$ in the short-range regime for $\alpha - d > 2$. For values of α between these limits deviations from the RG results were found suggesting that further contributions need to be taken into account due to the long-range interactions [Pic12].

These studies of the classical Ising model focus on a ferromagnetic interaction where varying critical exponents were found. Exotic phenomena and interesting properties are often introduced in the systems by frustration which is a result of competing interactions but in many situations it is simply induced geometrically by an *antiferromagnetic* interaction. For the Ising model examples are found, e. g., on the nearest-neighbor triangular or the pyrochlore[5] lattice [Lie86; MS01; Moe01]. Even more interesting is the investigation of the interplay of these interactions with quantum fluctuations introduced by a magnetic field. On the one hand, on the triangular lattice an order-by-disorder mechanism induces a second-order phase transition in the 3D-XY universality class from a symmetry-broken ground state to a paramagnet [Bla+84; MS01; IM03; Pow+13]. On the other hand, on the pyrochlore lattice, a disorder-by-disorder mechanism drives a first-order phase transition to a quantum-disordered Coulomb phase [HFB04; Bal10; Sha+12; RBS16].

1.3.2 *Quantum model*

The study of quantum-mechanical systems with long-range interactions at $T = 0$ is even more involved than the classical pendant although we should remember that d-dimensional quantum phase transitions can be identified with the classical thermal phase transitions in $(d + 1)$ dimensions [Suz76]. Here, the Ising model with long-range interactions in a *transverse magnetic field*, which is the main subject investigated in this thesis, is the paradigmatic example and has been studied by several groups. A clear trend regarding the dimensionality of the theoretical studies can be seen: While there are several publications available for the one-dimensional Ising chain (investigating various properties as discussed below), for two dimensional systems only a handful of papers exist. In three dimensions, to my knowledge, the only theoretical results are presented here.

For a general dimension d the zero-temperature transitions of the quantum model with ferromagnetic interactions were already studied in 2001 by Dutta and Bhattacharjee using RG equations [DB01]. They were able to confirm the continuously varying critical exponents and the Kosterlitz-Thouless transition already discussed above for the classical

5 The pyrochlore lattice consists of corner-sharing tetrahedrons which results in a structure similar to the one formed by the hydrogen atoms in water ice [CMS08].

system. They were also able to derive exact boundaries for the three different regimes of criticality in the quantum model. With a lower critical dimension $d_l = (\alpha - d)/2$ and an upper critical dimension $d_u = 3(\alpha - d)/2$ the range of medium long-range interactions

$$\frac{5}{3}d < \alpha < 3d\,, \tag{1.22}$$

where the model displays continuously varying critical exponents, was derived. For smaller values of α mean-field behavior is expected while for larger α nearest-neighbor criticality is present. The upper critical was also previously calculated [Sak73].

Two years later, Sandvik proposed a Quantum Monte Carlo (QMC) algorithm with local, classical- and quantum-cluster updates which avoids the interaction summations for the transverse Ising model in one dimension with arbitrary interactions. He derived results for the magnetization for ferromagnetic interactions decaying as $1/r^2$ at finite temperatures T [San03].

In 2012 a first α-dependent phase diagram of the one-dimensional Ising chain with tunable antiferromagnetic long-range interactions was studied by Koffel *et al.* using matrix product states (MPS) for finite chains of up to 150 spins with open boundary conditions [KLT12]. The group found two gapped phases – Néel-ordered and polarized (or paramagnetic) – connected via a second-order phase transition and derived critical exponents between those phases dependent on the long-range-interaction parameter α. For a ferromagnetically interacting system, about a year later critical values along with the critical exponent z of the ferromagnet-to-paramagnet transition were computed by Knap *et al.* using the finite-temperature Lanczos exact diagonalization (ED) method [Kna+13]. The calculations were carried out on small open clusters of up to 22 spins which is of the same order of magnitude as the size of several experiments with trapped ion chains for a ferromagnetic[6] [Isl+11] and antiferromagnetic interaction [Lan+11; Isl+13; Ric+13]. For a system size of 100 spins the phase diagram of the 1D antiferromagnetic long-range Ising chain was calculated again, using density-matrix renormalization group (DMRG) methods, by Vodola *et al.* [Vod+15]. They found the existence of localized gapped excited states in the paramagnetic phase for the non-additive system $\alpha \lessapprox 1$. Also using DMRG, Sun computed values for the critical field along with the critical exponent of the correlation length ν by a finite size scaling for system sizes up to 240 sites – to extract results in the $N \to \infty$ limit – for several values of $\alpha \in (0, 3]$ [Sun17]. He found that in the investigated range the critical exponent ν takes a value close to the nearest-neighbor value $\nu = 1$. For both ferro- and antiferromagnetic interactions the phase diagram was calculated again by studying the quantum Fisher information to detect the multipartite entanglement among the N spins. A finite-size scaling of the results for

6 The first experimental papers regarding quantum simulation with cold ions demonstrated the approach with two to three ions which I don't list as results for an ion *chain* but rather as an elementary building block and a principal demonstration of the technique [Fri+08; Kim+09; Kim+10; Edw+10].

$N \in [10, 120]$ was performed [GLP19] which were in good agreement with previously calculated results [KLT12; Kna+13; FS16].

Non-equilibrium properties were studied for the 1D model as well. The energetically lowest excitations in the low-field limit for the nearest-neighbor model with ferromagnetic interactions are single domain walls splitting the system in two ferromagnetically ordered parts (cf. Section 2.2.2). When the parameter α is decreased the energy of single-spin-flip excitations with a background of ferromagnetically aligned spins becomes the lowest excitation for a critical $\alpha_c \approx 2.3$, depending on the ratio of magnetic field and interaction strength J/h [Van+18; Rit19].

By using MPS techniques for system sizes up to 200 spins to study the non-equilibrium evolution of states with the magnetic field the domain-wall excitations were found to localize spatially with decreasing α in the unordered long-range system [Ler+19]. However, note that it is explicitly mentioned that this feature is found only for values of $\alpha < 2$ where we expect that single spin flips are already the relevant low-energy excitations.

Liu *et al.* found that the long-range interactions lead to a confinement of domain walls consequently resulting in pairs of domain walls as the low-energy quasiparticles and studied their dynamics under a quantum quench [Liu+19]. The dynamics of the system has also been studied with quantum quenches for a ferro- [Pap+18] and an antiferromagnetic interaction [Buy+16] and also in the classical case [CLP19].

Only recently, dynamical QPTs, which allow the classification of criticality out of equilibrium [HPK13], were investigated by Defenu *et al.* [DEH19]. They found that with removing the coupling between domain walls using a truncated Jordan-Wigner transformation to map the Ising model on a long-range Kitaev chain no anomalous dynamic criticality is present anymore. Although I mainly focus on additive systems in this section, let me still cite an interesting observation for dynamics in a non-additive quantum system. Mori studied prethermalization[7] effects in the transverse model with an additional longitudinal field and an Ising interaction between spins i and j that is rescaled with system size as

$$J_{ij} = \frac{J}{N^{1-\alpha}} \frac{1}{r_{ij}^{\alpha}} \tag{1.23}$$

such that it is normalized as

$$\sum_{i \neq j} J_{ij} = \frac{J}{N^{1-\alpha}} \sum_{i \neq j}^{N} \frac{1}{r_{ij}^{\alpha}} = 1 \tag{1.24}$$

7 Thermalization describes the case where the equilibration of a local observable under the unitary evolution of an initial state yields its thermal expectation value. This may happen with an intermediate step for the expectation value which is then called *prethermalization*. [BBW04]

for an N-spin chain [Mor19]. As already mentioned above, this scaling is known as the Kac prescription [KUH63; CDR09; Mor19] and allows calculations in the otherwise energetically instable regime of $\alpha \leq 1$ on which the paper is focused. Prethermalization effects were found for all finite transverse fields h and for $\alpha < 1/2$ if $h = 0$.

There are fewer publications available for two-dimensional models with long-range interactions. This should not come as a big surprise since the higher dimension adds some complexity, e. g., in the evaluation of the interactions. On the brink to two dimensions a quasi-one-dimensional infinite cylinder with a triangular lattice structure was studied by Saadatmand *et al.* in 2018 using DMRG algorithms [SBM18]. The goal was to determine the phase diagram of the two-dimensional triangular lattice, although we argue in [Koz+19] why the cylinder results cannot simply be mapped to the two-dimensional lattice. We find indications for a much complexer phase diagram potentially with infinite-order phase transitions. I will be elaborate on this later in Section 4.4.

Compared to the ferromagnetic case, properties of the quantum Ising model with antiferromagnetic interactions are especially difficult to calculate on a triangular lattice. Here, the ground state is highly degenerate in the field-free nearest-neighbor Ising limit since the energy of the local triangles cannot be minimized by an antiparallel alignment of neighboring spins. This problem is not mitigated by adding antiferromagnetic long-range interactions. However, applying a transverse field breaks this degeneracy. An order-by-disorder scenario is expected where the field-driven phase transition is within the 3D-XY universality class [MS01].

The transverse Ising model with long-range interactions on a triangular lattice in two dimensions was also studied using QMC simulations by Humeniuk in 2016 who confirmed the order-by-disorder transition already present in the nearest-neighbor case for antiferromagnetic interactions [Hum16; MS01]. There are, however, several issues regarding the publication: On the one hand, the data is very scarce with only one critical point for $\alpha = 3$ presented. On the other hand there are errors in the evaluation of the results where the assumption of wrong critical exponents lead to a wrong scaling for the data collapse[8]. Surprisingly enough the data points are still close to the results we obtained and published in our first paper in 2019 [FKS19] and which are discussed in Chapter 4.

On a square lattice no equilibrium results for general α and an arbitrary interaction sign has been published except for our own results on the QPT phase diagrams and criticality of the ferro- and antiferromagnetic square lattice [FKS19] which are also presented in Chapter 4. For a dipolar ($\alpha = 3$) ferromagnetic Ising interaction already in 2004 Chakraborty *et al.* used QMC techniques to compute a phase diagram in the temperature-field plane [Cha+04]. Their goal was to establish the model as a good representation for $LiHoF_4$ which is used as a model system for precisely controlling classical and quan-

8 S. Humeniuk, private communication via e-mail (2018-03-20).

tum phase transitions. Comparing their results to experimental data from [BRA96], they found a good agreement at larger temperatures ($T \approx 1.6\,\mathrm{K}$) but larger deviation for lower temperatures where quantum effects become more pronounced. The frustrating effects of an antiferromagnetic interaction on the square lattice were studied for nearest- and next-nearest-neighbor interactions in 2019 using cluster mean field (CMF) theory [KSZ19]. Although, this did not incorporate true long-range interactions it shows how taking frustrating effects by longer-ranging antiferromagnetic interactions into account can influence the phase diagram even on a bipartite lattice.

In Chapter 4 I will also present results on the long-range interacting Ising model on a three-dimensional cubic lattice. The ferromagnetic nearest-neighbor model is already expected to show mean-field criticality such that *a priori* no continuously varying exponents should be expected here.

Different models with long-range interactions were studied as well and showcase the interest in and topicality of the physics of long-range-interacting systems. Continuously varying critical exponents were also found in the ferromagnetic Heisenberg spin chain using various methods [LAB05]. The interplay of frustrated $J_1 - J_2$ interactions and additional unfrustrated long-range interactions in the Heisenberg spin chain can lead to a first-order phase transition between a Néel state and a "state with coexisting dimerization and critical spin correlations" [San10]. The entanglement in the Heisenberg chain was later studied by Roy and Dhar [RD19]. The dynamics of the XY model on the square lattice was investigated in 2015 by Schachenmayer *et al.* with a semiclassical approach using discrete truncated Wigner approximation (DTWA) in which the time evolution is replaced by a sampling of classical trajectories [SPR15]. Spatial and time-dependent correlations were computed to investigate the influence of the interactions on the dynamics. For $\alpha = 3$ a jump in the speed of correlation propagation was found. In 2015, Mahmoudian *et al.* studied the ordering effects for spinless electrons on a triangular lattice with repulsive long-range Coulomb interactions [Mah+15].

To some point, these studies are certainly performed out of a theoretical interest, to see how far currently existing methods can be pushed and further developed to incorporate more and more difficult problems. But also experimental setups cannot always be approximated to contain only short-range interactions and require therefore the consideration of long-range interactions.

1.3.3 *Experimental systems*

To show the relevance of the theoretical studies for real-world problems I list some of the experimental setups I mentioned before, but also list additional cases in which long-range interactions play an important role.

Polar molecules in optical lattices were argued to be described by an extended dipolar XXZ model – the "t-J-V-W model" – with a dipolar interaction in one dimension [Gor+11]. On a 2D square lattice, the study of only the dipolar spin-1/2 XXZ model using spin-wave theory reveals a long-range order even at a finite temperature [Pet+12].

The transverse-field Ising model on a cubic lattice was used to describe ferroelectric films ("layers of pseudo-spins with different kinds of interactions") [WZZ97]. In spin-orbit-coupled superconductors the interaction of magnetic impurities decays as $1/r^2$ [Mal18]. The interest in using chains of Rydberg atoms as quantum simulators requires a profound knowledge of the underlying system which has a density-density van der Waals interaction between two atoms falling off as $1/r^6$ [RL19].

Generally speaking, quantum simulators attract a lot of interest and are therefore a large driving force behind the studies of cold-ion systems[9]. Those have been realized in a large variety from very few [Fri+08; Kim+09; Kim+10; Edw+10] to several [Isl+11; Lan+11; Ric+14; Jur+14] up to hundreds of ions [Bri+12; Boh+16]. Properties such as dynamics and phase transitions, which often have also been studied theoretically, are investigated by those and more groups [Gre+02; SPS12; Wor+13; YJZ19] trying to find a good and reliable foundation for simulating complex quantum systems that are demanding or impossible to treat even with modern (classical) computers.

Dipolar interactions can also be found in, e. g., the already mentioned $LiHoF_4$ [BRA96], spin-ice pyrochlore materials $Ho_2Ti_2O_7$ and $Dy_2Ti_2O_7$ which have frustrated antiferromagnetic interactions [BG01; CMS08], bosonic gases [Lah+09] as well as even more exotic frustrated clusters of triangular-ordered magnetic islands which are explored for data storage and have "similarities to the classical triangular Ising antiferromagnet" [Men+09].

Long-range interactions have also been observed in cavity quantum electrodynamics [SM14]. Here, atoms located between two mirrors self-organize into a pattern if a laser beam resonates in the cavity [Asb+05]. The scattering of incoming light is used for cooling the ions if a coherent scattering exists where the incoming frequency is smaller than the outgoing $\omega_{\text{in}} < \omega_{\text{out}}$ [SHM13]. Effective long-range interactions are then mediated by multiple scattering of photons within the cavity [CDR09].

9 There are also approaches to using cold-ion systems as quantum *computers* [Nam+19].

2

THE ISING MODEL

When Wilhelm Lenz presented his student Ernst Ising with the problem of investigating a model supposed to describe the ferromagnetic properties of condensed matter systems such as, e. g., a macroscopic magnetization or phase transitions [Len21], probably nobody expected this model to become one of the most studied systems. This is even more surprising considering the initial setback. In his thesis Ising solved the one-dimensional model which is today known as Ising model (IM) in 1924 and found that there is no spontaneous magnetization possible in such a system [Isi25]. But without the symmetry breaking a macroscopic magnetization of a material cannot be explained. In his paper Ising actually argued that not even an extension to a spatial model would change the result:

> » Auch bei einem räumlichen Modell [...] gelangt man nicht zu einem anderen Ergebnis. « (Ising [Isi25])

It was only several years later, in 1944, that Lars Onsager approached the much more difficult two-dimensional problem and was able to derive an analytic solution of the model [Ons44]. He found that, in contrast to Ising's statement, the Ising model in two dimensions is indeed able to predict a phase transition between a ferromagnetic $\mathbb{Z}_2$-symmetry-broken and a thermally disordered phase with no broken symmetry. In higher dimensions $d > d_{\mathrm{u}}^{\mathrm{c}}$, with the upper critical dimension $d_{\mathrm{u}}^{\mathrm{c}} = 4$, the phase transition of the model can be described by MF theory [Dut+15].

The Mermin-Wagner theorem which states that no spontaneous symmetry breaking can be found in sufficiently short-ranged models[1] with a continuous symmetry in one or two dimensions at finite temperature is not applicable to the Ising model, since a *discrete* spin symmetry is at the heart of the model [MW66]. However, current studies indicate that the statement also holds for one-dimensional short-range models with a discrete symmetry in many cases [CS04]. In hindsight, knowing this current research, it does not come as a surprise that Ernst Ising and his thesis supervisor Wilhelm Lenz were bound to fail in describing the phase transition of ferromagnetic solid state systems by a one-dimensional model.

To get more concrete, let me write down an expression for the original model. In Reference [Isi25] Ising only describes the model verbally and argumentatively calculates

1 In this context, sufficiently short ranged means that $\sum_{\boldsymbol{R}} \left[|\boldsymbol{R}|^2 |J(\boldsymbol{R})| \right]$ converges [MW66], which in 1D requires a potential to decay faster than $1/r$.

the partition function. However, the corresponding Hamiltonian of the model can be written as

$$\hat{H}_{\mathrm{IM}} = -J \sum_{\langle \boldsymbol{i}, \boldsymbol{j} \rangle} \sigma_{\boldsymbol{i}}^{x} \sigma_{\boldsymbol{j}}^{x} , \quad J \in \mathbb{R} , \tag{2.1}$$

using the Pauli matrices $\sigma_{\boldsymbol{i}}^{x}$ (for a definition see Appendix B.1) and $J > 0$ for a ferromagnetic interaction. In the original paper $\boldsymbol{i}$ and $\boldsymbol{j}$ denote positions of N spins in *one* dimension; for higher-dimensional lattices, however, they are indeed vectors. The expression $\langle \boldsymbol{i}, \boldsymbol{j} \rangle$ means that all pairs of nearest-neighbor spins on positions $\boldsymbol{i}$ and $\boldsymbol{j}$ are included in the sum. The initial idea was the following [Isi25]: Elementary magnets can only have one of two values. They do not have a dipolar magnetic interaction in the solid body but their interaction range is limited to their very neighbors resulting in a maximally short-ranged exchange interaction.

2.1 CRITICALITY OF THE CLASSICAL ISING MODEL

In one dimension no classical thermal phase transition is present in the IM. However, the higher-dimensional systems show second-order phase transitions and the Ising model is often used as a paradigmatic representative of the respective universality class. Consequently, these are often named dD-Ising universality for the d-dimensional Ising model on a hypercubic lattice. The critical exponents of these classes are listed in the previous chapter in Table 1.2.

The universal properties of the classical Ising models are also present in the corresponding quantum model in $d - 1$ dimensions. The existence of a quantum-to-classical mapping has been proven in the past and is discussed in Section 2.2.5.

2.2 ISING MODEL IN A TRANSVERSE FIELD

While the original model aims to describe spontaneous magnetization when the temperature is lowered, for the study of quantum-mechanical phase transitions the model is often extended by a, relative to the Ising interactions, transverse magnetic field with strength h

$$\hat{H}_{\mathrm{TF}} = -h \sum_{\boldsymbol{i}} \sigma_{\boldsymbol{i}}^{z} , \quad h \in \mathbb{R} . \tag{2.2}$$

This field introduces quantum fluctuations, i. e. a flipping between the two states of the spins-1/2, in the system which allow for phase transitions if they reach a certain critical amplitude. The effect of those quantum fluctuations is similar to thermal fluctuations

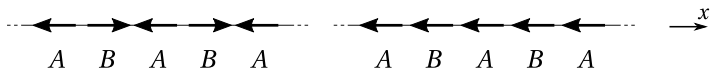

Figure 2.1: Flipping every second spin on a bipartite lattice with sublattices A and B maps the Néel ground state (left) of the antiferromagnetic Hamiltonian (2.3) to the ferromagnetic ground state (right).

introduced by the temperature in classical systems. The complete resulting transverse-field Ising model (TFIM) Hamiltonian reads

$$\hat{H}_{\mathrm{TFIM}} = \hat{H}_{\mathrm{TF}} + \hat{H}_{\mathrm{IM}} = -h\sum_{\boldsymbol{i}} \sigma_{\boldsymbol{i}}^{z} - J \sum_{\langle \boldsymbol{i},\boldsymbol{j}\rangle} \sigma_{\boldsymbol{i}}^{x}\sigma_{\boldsymbol{j}}^{x} \,. \tag{2.3}$$

This is one of the most important microscopic models. For any lattice in any dimension d, the unfrustrated ferromagnetic system allows for quantum phase transitions between a quantum paramagnet and a $\mathbb{Z}_2$-symmetry-broken phase. For bipartite lattices, with the two sublattices labeled A and B, a mapping from the antiferromagnetic interaction $J<0$ to a ferromagnetic interaction $J>0$ can be found. To this end, the spin quantization axis is rotated by π about the z-axis, which refers to the transformation

$$\sigma_{\boldsymbol{i}}^{x} \to -\sigma_{\boldsymbol{i}}^{x} \,, \quad \sigma_{\boldsymbol{i}}^{y} \to -\sigma_{\boldsymbol{i}}^{y} \,, \quad \text{and} \quad \sigma_{\boldsymbol{i}}^{z} \to \sigma_{\boldsymbol{i}}^{z} \,, \quad \text{for} \quad \boldsymbol{i} \in B \,. \tag{2.4}$$

Considering the 1D Ising chain as an example the lattice is separated into two sublattices A and B as illustrated in Figure 2.1. Applying the transformation the Hamiltonian becomes

$$\hat{H}_{\mathrm{TFIM}}^{\mathrm{chain}} = -h\sum_{i} \sigma_{i}^{z} - J \sum_{\langle i,j\rangle} (-1)^{i+j} \sigma_{i}^{x}\sigma_{j}^{x} \,. \tag{2.5}$$

This effectively maps the antiferromagnetic ground state to the ferromagnetic ground state as discussed below.

2.2.1 *Ground states*

If we consider the TFIM Hamiltonian in Equation (2.3) on bipartite lattices we find two phases at the extreme ends of the axis J/h.

A. Setting $h=0$ the original Ising model is restored. Now, there are two possibilities: For a positive value of the interaction J we can easily follow Ising's line of argument [Isi25] and see that a parallel alignment along the x-axis for neighboring spins (and therefore all spins) is preferred. Each parallel neighbor pair adds $-J$ to the energy and the total ground-state energy of the system is given by

$$E_0^{\mathrm{f}} = \left\langle \psi_0^{\mathrm{f}} \middle| \lim_{h\to 0} \hat{H}_{\mathrm{TFIM}} \middle| \psi_0^{\mathrm{f}} \right\rangle = -NJ \,, \quad \text{for} \quad J>0 \,. \tag{2.6}$$

These states $|\psi_0^{\mathrm{f}}\rangle$ are illustrated in Figures 2.2a and 2.2b on a square lattice.

Changing the sign of J yields a Néel state as the lowest-energy state where neighboring spins are aligned antiparallel. Considering the changed sign of J, the state has the same energy as the ferromagnetic state

$$E_0^{\mathrm{af}} = \left\langle \psi_0^{\mathrm{af}} \middle| \lim_{h\to 0} \hat{H}_{\mathrm{TFIM}} \middle| \psi_0^{\mathrm{af}} \right\rangle = NJ\,, \quad \text{for} \quad J<0\,. \tag{2.7}$$

The states $|\psi_0^{\mathrm{af}}\rangle$ are illustrated in Figures 2.2c and 2.2d on a square lattice. As discussed at the end of the previous section the antiferromagnetic Hamiltonian can be mapped to a ferromagnetic one for such bipartite lattices. Rotating every second spin of the Néel state by π effectively yields the ferromagnetic ground state as illustrated in Figure 2.1 for a one-dimensional spin chain.

In this phase the $\mathbb{Z}_2$ symmetry of the Hamiltonian is spontaneously broken: In each case there are two spin configurations with the same energy. If every single spin is locally rotated by 180° there is no change in energy. However, when entering the phase from a different phase, the system has to decide for one of the two configurations and the symmetry is spontaneously broken.

B. Now, we turn to the case of a vanishing Ising exchange interaction between the spins and assume $h>0$. If we set $J=0$ only the magnetic field remains and the system has the lowest energy when all spins point parallel to the magnetic field along the z-axis. This state is quantum-mechanically unordered since there is no spontaneously broken symmetry. One often speaks of a polarized or paramagnetic state which is denoted by

$$\left|\psi_0^h\right\rangle = |\uparrow\uparrow\cdots\uparrow\rangle\,. \tag{2.8}$$

The ground-state energy is given as

$$E_0^{\mathrm{h}} = \left\langle \psi_0^h \middle| \lim_{J\to 0} \hat{H}_{\mathrm{TFIM}} \middle| \psi_0^h \right\rangle = -Nh\,, \quad \text{for} \quad h>0\,. \tag{2.9}$$

The state is illustrated on a square lattice in Figure 2.2e.

For non-bipartite lattices the phases remain the same as long as the interaction strength $J>0$. If J is negative, competing interactions between nearest-neighbor spins can lead to geometric frustration. This can be easily illustrated on the triangular lattice and will become important in Sections 4.3.3 and 4.4.

Consider a single triangle with a spin on each corner such as the one illustrated in Figure 2.3. If the direction of one of the spins is fixed, the neighboring spins would minimize the energy of the interaction with the first spin by an antiparallel alignment

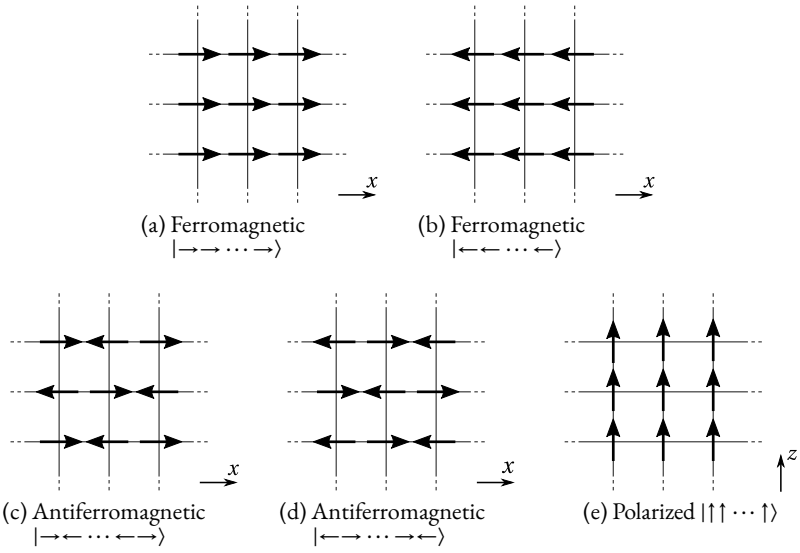

(a) Ferromagnetic $|{\rightarrow}{\rightarrow}\cdots{\rightarrow}\rangle$ (b) Ferromagnetic $|{\leftarrow}{\leftarrow}\cdots{\leftarrow}\rangle$

(c) Antiferromagnetic $|{\rightarrow}{\leftarrow}\cdots{\leftarrow}{\rightarrow}\rangle$ (d) Antiferromagnetic $|{\leftarrow}{\rightarrow}\cdots{\rightarrow}{\leftarrow}\rangle$ (e) Polarized $|{\uparrow}{\uparrow}\cdots{\uparrow}\rangle$

Figure 2.2: The different ground states of the quantum-mechanical TFIM are shown here for a two-dimensional square lattice. Without a field there are two spin configurations for each, the ferromagnetic (a, b) and the antiferromagnetic interaction (c, d). The ground state of the polarized phase (also called paramagnet) without any interaction is unique (e).

such as discussed for the Néel order. However, this alignment would maximize the interaction energy between the second two spins. No configuration can be found where the interaction between all spins is minimized. The optimum state for the whole triangular lattice would consist of triangles where two spins are aligned parallel and the third one points in the opposite direction. There are many possible configurations fulfilling this property consequently resulting in an extensively degenerate ground-state manifold.

When applying a magnetic field this leads to a different behavior than in the previously discussed cases. Starting from the field-free degenerate ground state, spin fluctuations introduced by the magnetic field are able to lower the energy of the system. Flipping the left highlighted spin in Figure 2.3 (right) results again in a (different) ground state of the manifold and therefore already contributes perturbatively in first order. This is only possible if the number of adjacent ferromagnetic and antiferromagnetic bonds is the same.

For a simpler illustration a dimer representation can be introduced. Ferromagnetic bonds are shown by putting a dimer (illustrated as a solid black line) on the bond of the dual honeycomb lattice while antiferromagnetic bonds are illustrated as dashed black lines. Flipping the spins inside an even loop of dimer sites, maps all dimers to non-dimers

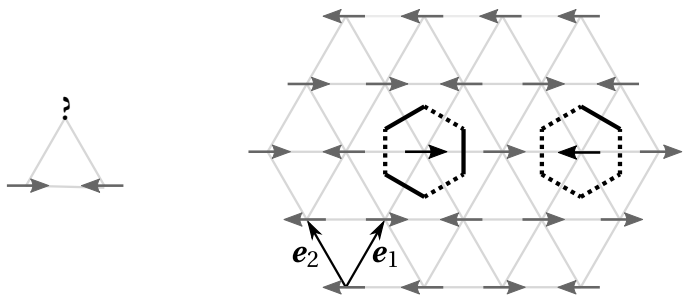

Figure 2.3: On non-bipartite lattices such as, e. g., a triangular lattice the Néel state cannot minimize the energy of the antiferromagnetic TFIM on all lattice bonds locally. (Left) This can already be seen in a single triangle where the energy of the bottom bond is minimized. Any choice of the top spin would violate the antiparallel alignment with one of the two other spins. (Right) This results in a highly degenerate ground-state manifold on the triangular lattice with lattice vectors $\boldsymbol{e}_1$ and $\boldsymbol{e}_2$, where each state with two parallel and one antiparallel spin per triangle has minimum energy. In the corresponding dimer model, dimers (solid black lines) are put on ferromagnetic bonds. A spin flip maps a hexagonal plaquette with three dimers again to a plaquette with three dimers switching between dimers and non-dimers (left plaquette). These flippable plaquettes stand in contrast to nonflippable plaquettes (right plaquette) which are also present in the ground state.

and vice versa. The shortest loop that can be found on the triangular lattice is a hexagon consisting of six sites. Each hexagon in the model is called a *plaquette* and can be sorted into *flippable* and *nonflippable* plaquettes. Flippable plaquettes consist of three dimers and flipping the central spin maps one ground state of the system to another ground state, therefore already contributing in first order of transverse-field perturbation.

As shown in previous work [Moe01] each ground state for $h = 0$ can be represented by a dimer covering $|c\rangle$ and the (perturbative) action of the perturbation by a magnetic field $\hat{H}_{\mathrm{TF}}$ can be captured by an effective quantum dimer model (QDM) of the form

$$\hat{H}_{\mathrm{QDM}} = E_0 + \sum_c E_c(h)\,|c\rangle\langle c| - h\sum_{\boldsymbol{\nu}} \left(\left|\mathrm{I}\right\rangle\!\right\rangle_{\boldsymbol{\nu}} \left\langle\!\left\langle \mathrm{I}\right|_{\boldsymbol{\nu}} + \mathrm{H.\,c.}\right), \tag{2.10}$$

where the first sum runs over all dimer coverings $|c\rangle$ so that $E_c(h)$ is the covering-dependent diagonal energy and the second sum runs over all plaquettes $\boldsymbol{\nu}$.

Flipping a plaquette lowers the energy of the state, which leads to an energetic preference of states with a larger number of flippable plaquettes if an infinitesimal field is applied. The *maximally flippable* state with the highest number of flippable plaquettes has the largest weight in the ground state for an infinitesimal field but is itself no eigenstate of the Hamiltonian anymore. The emergence of this *clock-order* state lifts

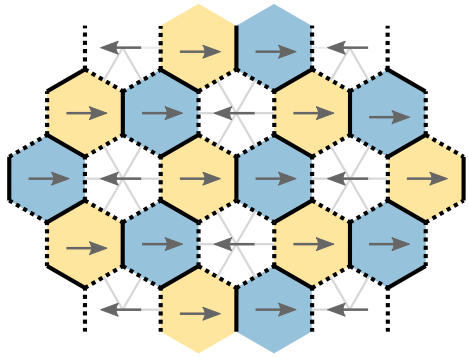

Figure 2.4: The maximally flippable state in the dimer model (2.10) on the triangular lattice has a flippable-plaquette density of 2/3 and a three-sublattice structure. Flippable plaquettes are indicated by blue and yellow hexagons. This eigenstate of the field-free Hamiltonian lowers the energy the most if an infinitesimal transverse-field perturbation is applied. Note, that the clock order (also known as $\sqrt{3}\times\sqrt{3}$-order) resulting from the field has the same periodicity with wave vector $\boldsymbol{k} = (\pm 2/3\pi, \mp 2/3\pi)^T$ with respect to the unit vectors shown in Figure 2.3.

the high degeneracy of the ground-state manifold present at $h = 0$ and the resulting introduction of a three-sublattice structure breaks the translational symmetry of the lattice. This phenomenon is known as *order by disorder*. For zero field the maximally flippable state is illustrated in Figure 2.4 where dimers are put on each ferromagnetic nearest-neighbor bond.

2.2.2 *Elementary excitations in the Ising model*

In the previous section we found that the ground state of the Ising model ($h = 0$) depends on the sign of the exchange interaction. This is also reflected in the elementary lowest-lying energetically excited states above the ground state. Additionally, the lattice geometry plays an important role in the determination of excited states.

As discussed above, for $J < 0$ the ferromagnetic coupling of nearest neighbors results in two ground states with a parallel spin orientation. For the sake of simplicity let me illustrate the elementary excitations above only one of these ground states which I denote as

$$\left|\psi_0^{\mathrm{F}}\right\rangle = |\leftarrow\leftarrow\cdots\leftarrow\rangle \tag{2.11}$$

in the following. The second state consists of inverted spins $|\rightarrow\rightarrow\cdots\rightarrow\rangle$ and has the same properties.

The first naïve idea to excite the system would be to flip a single spin on an arbitrary site of the lattice[2]. This is obviously still an eigenstate of the Hamiltonian with the energy

$$\left\langle \psi_0^{\mathrm{F}} \right| \sigma_{\boldsymbol{i}}^x \hat{H}_{\mathrm{IM}} \sigma_{\boldsymbol{i}}^x \left| \psi_0^{\mathrm{F}} \right\rangle = -\langle \leftarrow \cdots \leftarrow \rightarrow \leftarrow \cdots \leftarrow | \; J \sum_{\langle \boldsymbol{i},\boldsymbol{j} \rangle} \sigma_{\boldsymbol{i}}^z \sigma_{\boldsymbol{j}}^z \, | \leftarrow \cdots \leftarrow \rightarrow \leftarrow \cdots \leftarrow \rangle \tag{2.12}$$

$$= -(N - 2z_{\mathrm{c}})J \,, \tag{2.13}$$

with the coordination number z_{c}. The total energy difference results from *each bond* between spins that is not minimized contributing a difference of $2J$. While the energy is obviously (and as expected) higher than the ground-state energy one can ask if there is an eigenstate of $\hat{H}_{\mathrm{IM}}$ that has an even lower energy than that of a single spin flip.

For a one-dimensional Ising chain we can, indeed, find such a state by dividing our system into two parts. On the one-hand side the spins point into the opposite direction of the spins in the second part. Between both *domains* of parallel-pointing spins a domain wall (DW) is introduced. The energy of these kind of states is given as

$$\left\langle \psi^{\mathrm{1DW}} \right| \hat{H}_{\mathrm{IM}} \left| \psi^{\mathrm{1DW}} \right\rangle = -\left\langle \leftarrow \cdots \leftarrow \leftarrow \right| \rightarrow \rightarrow \cdots \rightarrow \Big| \; J \sum_{\langle \boldsymbol{i},\boldsymbol{j} \rangle} \sigma_{\boldsymbol{i}}^z \sigma_{\boldsymbol{j}}^z \left| \leftarrow \cdots \leftarrow \leftarrow \right| \rightarrow \rightarrow \cdots \rightarrow \right\rangle \tag{2.14}$$

$$= -(N - 2)J \,, \tag{2.15}$$

with the single domain-wall state $\left| \psi^{\mathrm{1DW}} \right\rangle = \left| \leftarrow \cdots \leftarrow \leftarrow \right| \rightarrow \rightarrow \cdots \rightarrow \right\rangle$ where the domain wall is indicated for clarity by a vertical line. In an Ising chain, these domain walls are the elementary excitations of the ferromagnetic Ising model with nearest-neighbor interactions. The state with a single spin flip we discussed before in Equation (2.12) can be constructed by putting two neighboring DWs into the system

$$\left| \leftarrow \cdots \leftarrow \right| \rightarrow \left| \leftarrow \cdots \leftarrow \right\rangle \,. \tag{2.16}$$

Adding two non-neighboring spin flips behaves like two isolated particles with twice the energy of a single particle relative to the ground state. Such a state contains four domain walls as in the state

$$\left| \leftarrow \cdots \leftarrow \right| \rightarrow \left| \leftarrow \cdots \leftarrow \right| \rightarrow \left| \leftarrow \cdots \leftarrow \right\rangle \,. \tag{2.17}$$

Bringing them close together results in a bound state with the lower energy of a single particle since two of the four domain walls vanish resulting in

$$\left| \leftarrow \cdots \leftarrow \right| \rightarrow \rightarrow \left| \leftarrow \cdots \leftarrow \right\rangle \,. \tag{2.18}$$

2 Remember that we are looking at an infinitely large system without a boundary. The flipped spin is supposed to be located between two non-flipped spins.

This concept can easily be extended to a larger number of spin flips which may also result in larger bound states.

For 2D lattices such as, e. g., the square lattice creating a DW would cost an infinite amount of energy since the spins on bonds along an infinitely extended line would be antiparallel aligned with each of them costing an energy of $2J$. Here, and also for higher dimensions, the single spin flips are the energetically most beneficial excited states. Bound states also exist on the square lattice and were studied using perturbative and exact-diagonalization methods in [Dus+10].

For an antiferromagnetic interaction the same arguments hold for the one-dimensional chain where a single DW separating two antiparallel-aligned domains is the lowest-lying excitation. A difference can be found in higher-dimensional systems with non-bipartite lattices. While for a bipartite lattice such as the square lattice, a single spin flip introducing four DWs with the energy difference

$$\Delta E^{\mathrm{4DW}}_{\mathrm{IM,\,square}} = 8J \tag{2.19}$$

relative to the ground state remains the lowest excitation above the ground state, for non-bipartite lattices frustration effects come into play which we already have observed in the ground state in Section 2.2.1.

The ground-state of the antiferromagnetic IM on a triangular lattice is highly degenerate and given by all states with two parallel and one antiparallel spin per lattice triangle. Due to this complex ground state the excitations need a little more consideration. In contrast to the square lattice the effect of a single spin flip is not uniquely defined. Here, it might lead to the transition to a different ground state. The easiest way to define an excitation is by looking at the triangles: The lowest-energy excitation is given by a single triangle that does not satisfy the ground-state condition and has three parallel spins while all other spin triangles are in the ground state.

2.2.3 *Elementary excitations in the polarized phase*

Consider the limit $J = 0$ of the TFIM in Equation (2.3) which reduces simply to the magnetic field Hamiltonian of Equation (2.2). The ground state of a system of non-interacting spins in the magnetic field is completely unaware of any underlying lattice structure of the system as each spin simply points parallel to the field. Excitations above this unique ground state are determined locally by a single spin flip

$$\sigma^x_{\boldsymbol{i}} |\uparrow \cdots \uparrow\rangle = |\uparrow \cdots \uparrow\downarrow\uparrow \cdots \uparrow\rangle \tag{2.20}$$

with the energy

$$\langle\uparrow \cdots \uparrow\downarrow\uparrow \cdots \uparrow|\hat{H}_{\mathrm{TF}}|\uparrow \cdots \uparrow\downarrow\uparrow \cdots \uparrow\rangle = -(N-2)h \quad \text{with} \quad h > 0. \tag{2.21}$$

Flipping more spins creates higher excitations which form an equidistant energy spectrum above the ground state with distance $2h$ between two neighboring energies.

This structure allows the interpretation of the single spin flips as quasiparticles (QPs) above a QP-free vacuum ground state. Technically they are introduced by the Matsubara-Matsuda transformation [MM56]

$$\sigma_{\boldsymbol{i}}^{x} = \hat{b}_{\boldsymbol{i}}^{\dagger} + \hat{b}_{\boldsymbol{i}} \quad \text{and} \quad \sigma_{\boldsymbol{i}}^{z} = 1 - 2\hat{n}_{\boldsymbol{i}} \,, \quad \text{with} \quad \hat{n}_{\boldsymbol{i}} = \hat{b}_{\boldsymbol{i}}^{\dagger}\hat{b}_{\boldsymbol{i}} \,. \tag{2.22}$$

The hard-core-bosonic creation and annihilation operators $\hat{b}_{\boldsymbol{i}}^{\dagger}$ and $\hat{b}_{\boldsymbol{i}}$ replace the quantum-number-raising and -lowering Pauli matrices $\sigma_{\boldsymbol{i}}^{+}$ and $\sigma_{\boldsymbol{i}}^{-}$ (see Appendix B.1)

$$\hat{b}_{\boldsymbol{i}}^{\dagger}|0\rangle_{\boldsymbol{i}} = |1\rangle_{\boldsymbol{i}} \qquad \hat{b}_{\boldsymbol{i}}^{\dagger}|1\rangle_{\boldsymbol{i}} = 0 \qquad \hat{b}_{\boldsymbol{i}}|1\rangle_{\boldsymbol{i}} = |0\rangle_{\boldsymbol{i}} \qquad \hat{b}_{\boldsymbol{i}}|0\rangle_{\boldsymbol{i}} = 0 \,, \tag{2.23}$$

where the original states are substituted as $|\uparrow\rangle \to |0\rangle$ (vacuum) and $|\downarrow\rangle \to |1\rangle$ (QP). The diagonal magnetic field term leads to a QP density $\hat{n}_{\boldsymbol{i}}$. The TFIM Hamiltonian in the QP image then reads

$$\hat{H}_{\mathrm{TFIM}} = -N + 2h\sum_{\boldsymbol{i}} \hat{n}_{\boldsymbol{i}} - J\sum_{\langle \boldsymbol{i},\boldsymbol{j}\rangle} \left(\hat{b}_{\boldsymbol{i}}^{\dagger}\hat{b}_{\boldsymbol{j}}^{\dagger} + \hat{b}_{\boldsymbol{i}}\hat{b}_{\boldsymbol{j}} + \hat{b}_{\boldsymbol{i}}^{\dagger}\hat{b}_{\boldsymbol{j}} + \hat{b}_{\boldsymbol{i}}\hat{b}_{\boldsymbol{j}}^{\dagger}\right) . \tag{2.24}$$

Note that, the magnetic field term remains diagonal while the Ising interaction is separated into two parts. First, two QPs can be created or destroyed on neighboring lattice sites. Second, a hopping of particles to an unoccupied neighbor site is allowed while the total number of QPs is preserved.

The simplicity and independence of the geometric setup of the this limit of the TFIM makes it a suitable starting point for perturbative approaches to the properties of the full Hamiltonian. For this reason, it will be used later in this thesis for the long-range Ising model introduced in Section 2.3.

2.2.4 *Exact solution of the nearest-neighbor transverse-field Ising chain*

In 1970 Pierre Pfeuty found a solution to the one-dimensional TFIM on a simple chain [Pfe70] which I will discuss here. Starting from Equation (2.3), we can introduce the ladder operators σ^{+} and σ^{-} (cf. Appendix B.1) and obtain

$$\hat{H}_{\mathrm{TFIM}}^{\mathrm{1D}} = -J\sum_{i}\left(\sigma_i^{+}\sigma_{i+1}^{-} + \sigma_i^{+}\sigma_{i+1}^{+} + \mathrm{H.\,c.}\right) - h\sum_{i}\left(2\sigma_i^{+}\sigma_i^{-} - 1\right) \tag{2.25}$$

where the position vectors were replaced by an integer due to the reduced dimensionality of the lattice. The Hamiltonian can be mapped to free fermions by using a Jordan-Wigner transformation [WJ28; Col15]

$$\sigma_i^{+} = \exp\left(\mathrm{i}\pi\sum_{k<i} c_k^{\dagger}c_k\right)c_i^{\dagger} \quad \text{and} \quad \sigma_i^{-} = \exp\left(-\mathrm{i}\pi\sum_{k<i} c_k^{\dagger}c_k\right)c_i \,, \tag{2.26}$$

where $c_i^\dagger$ and c_i are fermionic creation and annihilation operators. The Hamiltonian after the Jordan-Wigner transformation

$$\hat{H}_{\mathrm{TFIM}}^{\mathrm{1D}} = -J\sum_i \left(c_i^+ c_{i+1}^- + c_i^+ c_{i+1}^+ + \mathrm{H.\,c.}\right) - h\sum_i \left(2c_i^+ c_i^- - 1\right) \tag{2.27}$$

can be diagonalized by first applying a Fourier and then Bogoliubov transformation [Bog58] resulting in

$$\hat{H}_{\mathrm{TFIM}}^{\mathrm{1D}} = h\sum_k \Lambda_k \eta_k^\dagger \eta_k - \frac{h}{2}\sum_k \Lambda_k \,, \tag{2.28}$$

with the dispersion

$$\Lambda_k = 2\sqrt{1+\lambda^2 - 2\lambda\cos(k)}\,, \quad \lambda = \frac{J}{h}\,. \tag{2.29}$$

The ground state energy per site is given by

$$e_0 = -\frac{h}{\pi}\sum_k \Lambda_k \tag{2.30}$$

which becomes an elliptic integral in the bulk limit

$$\lim_{N\to\infty} e_0 = -\frac{h}{\pi}\int_0^\pi \mathrm{d}k\,\Lambda_k\,. \tag{2.31}$$

The energy gap between the ground state and the first excited state is given by the minimum of the dispersion, which is $k = 0$ for a ferromagnetic interaction ($J > 0$)

$$\Delta(\lambda) = \min_k \Lambda_k = 2h|1-\lambda|\,. \tag{2.32}$$

For $J = h$ the gap vanishes and the systems undergoes a phase transition between the disordered polarized state and the ferromagnetically ordered state with critical exponent $z\nu = 1$.

This could also have been seen by mapping the Hamiltonian to the dual lattice [SIC12]. To this end, new spins need to be introduced which are associated with the bonds of the 1D chain,

$$\tau_\nu^z = \sigma_i^x \sigma_{i+1}^x \quad \text{and} \quad \tau_\nu^x = \prod_{k<i}\sigma_k^z\,, \tag{2.33}$$

where ν labels the bond between spins on site i and $i+1$. Note, that the new spin operators τ_ν^α also respect the Pauli algebra defined in Appendix B.1. Rewriting the

Hamiltonian (2.3) in terms of the new operators we can see that the magnetic field and the Ising interaction terms change roles

$$\hat{H}_{\text{TFIM}}^{\text{1D, dual}} = -J\sum_{v}\tau_i^z - h\sum_i \tau_i^x\tau_{i+1}^x \,. \tag{2.34}$$

This self-duality between $\hat{H}_{\text{TFIM}}^{\text{1D, dual}}$ and the original Hamiltonian in Equation (2.3) implies that the critical value for the phase transition is $\lambda_c = (J/h)_c = 1$ and the gap closes linearly with $z\nu = 1$.

2.2.5 *Quantum-classical analogy*

The correspondence of a quantum spin model in d dimensions to a certain classical Ising model in $d+1$ dimensions with many-spin interactions was found numerically [EPW70] and later shown analytically by the application of what is known today as the *Suzuki-Trotter formalism* [Suz71; Suz76].

I illustrate the formalism on an example, here, which is mainly inspired by References [SIC12] and [Dut+15]. Starting from the quantum model, the principal idea is to introduce a new dimension (the Trotter dimension or imaginary-time direction) by writing down the partition function of the quantum spin system, e. g., for the TFIM chain

$$\mathcal{Z}_{\text{TFIM}} = \text{Tr}\,\exp\left(-\beta\hat{H}_{\text{TFIM}}\right) = \text{Tr}\,\exp\left[\sum_{j=1}^{N}\left(K\sigma_j^x\sigma_{j+1}^x + \beta h\sigma_j^z\right)\right] \tag{2.35}$$

with $K = \beta J$, $\beta = 1/(k_B T)$, and Boltzmann's constant k_B. Now, the Trotter formula [Tro59]

$$\exp\left(\hat{A}+\hat{B}\right) = \lim_{M\to\infty}\left[\exp\left(\hat{A}/M\right)\exp\left(\hat{B}/M\right)\right]^M \,, \tag{2.36}$$

where $\hat{A}$ and $\hat{B}$ are non-commuting quantum-mechanical operators, can be used to transform the partition function to

$$\mathcal{Z}_{\text{TFIM}} = \lim_{M\to\infty}\text{Tr}\left[\exp\left(\sum_{j=1}^{N}K\sigma_j^x\sigma_{j+1}^x\right)\exp\left(\sum_{j=1}^{N}\beta h\sigma_j^z\right)\right]^M \,. \tag{2.37}$$

Inserting a complete set of eigenvectors $|\sigma\rangle$ for Pauli operator σ^z, such that $\sigma^z|\sigma\rangle = \sigma|\sigma\rangle$, with eigenvalue $\sigma \in \{-1, 1\}$ gives

$$\mathcal{Z}_{\text{TFIM}} = \lim_{M\to\infty}\text{Tr}\prod_{k=1}^{M}\langle\sigma_{1,k},\sigma_{2,k},\ldots,\sigma_{N,k}| \tag{2.38}$$

$$\left[\exp\left(\sum_{j=1}^{N}K\sigma_j^x\sigma_{j+1}^x\right)\exp\left(\sum_{j=1}^{N}\beta h\sigma_j^z\right)\right]|\sigma_{1,k+1},\sigma_{2,k+1},\ldots,\sigma_{N,k+1}\rangle \tag{2.39}$$

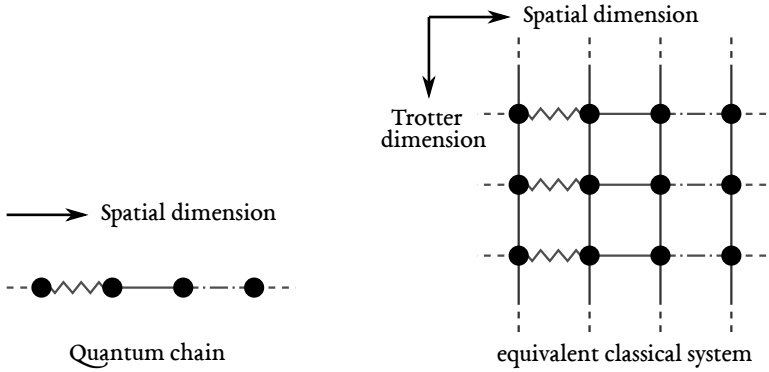

Figure 2.5: On the left an Ising chain with random interactions indicated by different line styles is shown. In the Suzuki-Trotter transformation this chain is repeated in Trotter direction in which the spins are coupled with ferromagnetic nearest-neighbor interactions. In this example the quantum chain is mapped to the equivalent two-dimensional classical model on a square lattice illustrated on the right. Adapted from [Dut+15].

Using the relation

$$\langle\sigma|\exp\left(\beta h\sigma^x\right)\left|\sigma'\right\rangle = [1/2\sinh(2\beta h)]^{1/2}\exp\left[1/2\ln\coth(\beta h)\sigma\sigma'\right] \tag{2.40}$$

the partition function can be transformed to

$$\mathcal{Z}_{\text{TFIM}} = \lim_{M\to\infty} A^{MN}\,\text{Tr}\,\exp\left[\sum_{j=1}^{N}\sum_{k=1}^{M}\left(\frac{K}{M}\sigma_{j,k}\sigma_{j+1,k} + K_M\sigma_{j,k}\sigma_{j,k+1}\right)\right], \tag{2.41}$$

with $A = [1/2\sinh(2\beta h/M)]^{1/2}$ and $K_M = 1/2\ln\left[\coth(\beta h/M)\right]$. For more details on the calculation see [Dut+15; SIC12] and references therein.

The introduction of the complete set of eigenstates in combination with the Trotter identity introduced a new dimension into the system while the transverse field disappears. This is most easily seen by comparing Equations (2.41) and (2.35). Equation (2.41) represents the partition function of a classical IM on an $M \times N$ square lattice with an anisotropic interaction in space and Trotter direction. Note, that when taking the limit $M \to \infty$ the first term would vanish while the second diverges logarithmically. Only in the limit $\beta \to \infty$ (which means $T \to 0$) the expression β/M remains finite and the equality of the quantum system to the classical system holds.

Randomness, anisotropy, and frustration in the quantum model translate to random, anisotropic, and frustrated interactions in d dimensions of the classical model. The interactions in the remaining Trotter dimension of the classical $d+1$-dimensional model, however, are always nearest-neighbor and ferromagnetic [Dut+15]. This is also visualized in Figure 2.5.

2.3 LONG-RANGE ISING MODEL

Up to now the TFIM has been introduced with interactions between nearest-neighbor spins. Historically it has played an important role and after several decades of studies, today, a lot is known about the short-range model with nearest-neighbor interactions. Since additional further-neighbor interactions also triggered the interest of researchers there have been studies on extended models, too. For example, in the axial next-nearest-neighbor Ising model additional frustrating antiferromagnetic interactions between next-nearest-neighbors are introduced (for a discussion see, e. g., [SIC12] and references therein).

However, replacing those nearest-neighbor interactions with algebraically decaying ones, such that all spins interact mutually, the model becomes much more involved and there is very little data on quantum-critical properties available. I choose the Ising model not only for it's simplicity (compared to other models) but because it stands as a paradigmatic representative of other models. The notion of universality classes permits the application of the obtained results to other models that fall within the same class.

In theoretical physics there are many examples for models being (or having been) studied mainly out of an academic interest[3]. Often, models introduced for purely theoretical purposes, however, turned out to have realistic applications[4]. While long-range interactions are per se present in realistic systems and a cut-off after nearest-neighbor exchanges is just an approximation, the explicit modeling of the form, as an algebraically decaying function with a variable parameter in the Ising interactions is a plausible choice since, e. g., Coulomb, dipolar, and van der Waals interactions display an algebraic form. In comparison to aforementioned examples there is yet an essential difference: The model studied here already has an experimental realization in form of an artificial system of cold ions trapped in an optical lattice [Bri+12].

In this thesis we focus on the long-range transverse-field Ising model (LRTFIM) with algebraically decaying interactions

$$\hat{H}_\alpha = -h\sum_{\boldsymbol{i}} \sigma_{\boldsymbol{i}}^z - J\sum_{\boldsymbol{i}\neq\boldsymbol{j}} \frac{1}{|\boldsymbol{i}-\boldsymbol{j}|^\alpha}\sigma_{\boldsymbol{i}}^x\sigma_{\boldsymbol{j}}^x\,, \quad J,\alpha\in\mathbb{R}\,, \quad h\in\mathbb{R}_0^+\,, \tag{2.42}$$

in d dimensions where each pair of spins appears only once in the sum. Additionally, the condition $\alpha > d$ is imposed to retain an extensive and additive system.

Several results for this model for various lattices and choices of α have been presented in Chapter 1 and are discussed in Chapter 4 along with the results of this thesis. Tuning

3 Examples are the Kasteleyn model [Kas63], the toric code [Kit03], Kitaev's honeycomb model [Kit06], and systems featuring fracton excitations [VHF15].

4 E. g., the Kasteleyn model "has practical applications to the main melting transition in biomembranes, to amphiphilic monolayers, and to physisorbed systems involving striped incommensurate phases" [DL89].

the parameter α, we immediately find notable limits for $\alpha \to 0$ and $\alpha \to \infty$ that are discussed below.

2.3.1 *Nearest-neighbor limit*

The LRTFIM in Equation (2.42) contains the nearest-neighbor Ising model in Equation (2.3) as a limiting case when setting $\alpha \to \infty$. This limit has been extensively discussed above and more details can be found in, e. g., Reference [SIC12].

2.3.2 *Uniform-interaction limit*

We already figured out that the parameter α tunes the model from the nearest-neighbor limit at $\alpha = \infty$ to long-ranging interactions that become stronger when α is decreased. The other obvious limit which has not been discussed so far is the limit $\alpha = 0$. Although this falls in the class of non-additive systems discussed in Section 1.2, I still want to quickly discuss some implications of the field-free long-range Ising model (LRIM) here.

If we think of a typical lattice geometry, this limit may seem strange at the first glance. Here, each spin interacts with every other spin with equal strength *independent of the distance*. But, indeed, it is possible to experimentally realize an antiferromagnetic interaction with $0 \leq \alpha \leq 3$ for finite systems in cold ion traps by tuning a spin-dependent optical dipole force [Bri+12]. The corresponding Hamiltonian can be written as

$$\hat{H}_{\alpha=0}\Big|_{h=0} = -J \sum_{i \neq j} \sigma_i^x \sigma_j^x \,, \tag{2.43}$$

where each spin-spin interaction is counted only once.

Surprisingly enough, this ultra-long-range interaction makes a theoretical description of the energy spectrum relatively easy. This is a result of the fact that the interaction is independent of the actual spins included in the interaction. We can introduce the total σ^x-component as a sum over all spins

$$\sigma_{\text{tot}}^x = \sum_i \sigma_i^x \,. \tag{2.44}$$

The square of the total spin

$$\left(\sigma_{\text{tot}}^x\right)^2 = N + 2 \sum_{i \neq j} \sigma_i^x \sigma_j^x \tag{2.45}$$

can be used to express the Hamiltonian in terms of σ_{tot}^x as

$$\hat{H}_{\alpha=0}\Big|_{h=0} = \frac{NJ}{2} - \frac{J}{2}\left(\sigma_{\text{tot}}^x\right)^2 \,, \tag{2.46}$$

where N is the total number of spins.

For an antiferromagnetic interaction ($J < 0$) the ground-state energy is mainly determined by the constant $\frac{N}{2}$. In the antiferromagnetic ground state the σ^z_{tot} quantum number is zero leading to a high degeneracy: Each state with half of the spins pointing up and the remaining spins pointing down has the ground-state energy

$$E_0^{\text{af}} = \frac{NJ}{2} \,. \tag{2.47}$$

Excited states are given by states with higher quantum numbers, such, that the energy spectrum in Figure 2.6a arises.

For a ferromagnetic interaction ($J > 0$) the ground state is given by a non-degenerate paramagnetic state. The energy growing overextensively as

$$E_0^{\text{f}} = \frac{NJ}{2} - \frac{N^2 J}{2} \tag{2.48}$$

requires the renormalization $J \to J/N$ to retain extensivity of the system, resulting in a renormalized extensive ground-state energy

$$E_0^{\text{f}} \to E_0^{\text{f}} = \frac{J}{2} - \frac{NJ}{2} \,. \tag{2.49}$$

Excited states above the renormalized ferromagnetic ground-state are created by flipping single spins. The change in quantum number of σ^x_{tot} results in the low-energy spectrum shown in Figure 2.6b.

The ground-state degeneracy of the antiferromagnetic model at magnetic field $h = 0$ is broken for any finite h, immediately resulting in a z-polarized phase [Hum16]. To obtain the full LRTFIM from Equation (2.43) the interaction

$$\frac{J}{2} \sum_{\boldsymbol{i} \neq \boldsymbol{j}} \left(\frac{1}{|\boldsymbol{i} - \boldsymbol{j}|^{\alpha}} - 1 \right) \sigma^z_{\boldsymbol{i}} \, \sigma^z_{\boldsymbol{j}} \tag{2.50}$$

needs to be added. If we consider the Taylor expansion of Equation (2.50) in leading order in α

$$-\alpha \frac{J}{2} \sum_{\boldsymbol{i} \neq \boldsymbol{j}} \log\left(|\boldsymbol{i} - \boldsymbol{j}|\right) \sigma^z_{\boldsymbol{i}} \, \sigma^z_{\boldsymbol{j}} \tag{2.51}$$

as a perturbation it is possible to use the infinitely degenerate limit $h = 0$ and $\alpha = 0$ as perturbative starting point. This perturbation describes an extensive ferromagnetic LRIM with logarithmically increasing Ising interaction strength.

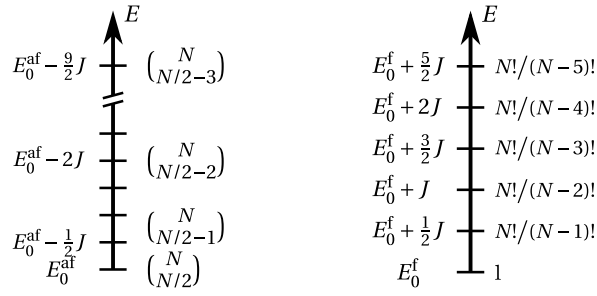

(a) $J < 0$ (b) $J > 0$

Figure 2.6: The lower part of the energy spectrum of the LRIM. On the left of the axis the energy is denoted while the right shows the number of degenerate states. (a) For an antiferromagnetic interaction the ground state is highly degenerate with a non-equidistant energy spectrum above. (b) For the LRIM with a ferromagnetic interaction renormalized as J/N the system has an equidistant spectrum above a non-degenerate ground state.

Studies of the model with uniform long-range interactions with an additional (transverse and longitudinal) magnetic field have also been done. The Husimi-Temperley-Curie-Weiss model

$$\hat{H}_{\mathrm{HTCW}} = -J \sum_{i \neq j} \sigma_i^x \sigma_j^x + \Gamma \sum_i \sigma_i^x + h \sum_i \sigma_i^z \tag{2.52}$$

with $J > 0$ is discussed in [SIC12] and its references. Here, a second-order phase transition line between a ferromagnetic and paramagnetic phase is found for all temperatures T including the quantum transition at $T = 0$.

An extension to the model in a transverse field has also been made by adding an anisotropic interaction

$$\hat{H}_{\mathrm{LMG}} = -\frac{J}{N} \sum_{i \neq j} \left(\sigma_i^x \sigma_j^x + \gamma \sigma_i^y \sigma_j^y \right) - h \sum_i \sigma_i^z \,, \tag{2.53}$$

with the anisotropy parameter γ and is known as the Lipkin-Meshkov-Glick model [LMG65; DV04].

2.3.3 *Excitations in the LRIM*

As we will see later, while the ground state in the antiferromagnetic case becomes much more complicated for long-range interactions due to their frustrating nature, the ferromagnetic ground state remains unchanged. Consequently, also the excitations above the

ground state are hard to quantify in the LRIM. The 1D spin chain, however, is still simple enough such that we are able to determine the energy of low-energy excitations leading to some interesting behavior depending on α. For the ferromagnetic LRIM Vanderstraeten *et al.* investigated this using variational matrix product state techniques and found that the lowest excitation above the ferromagnetic ground state switches from a trivial to a topological one [Van+18]. In this case "trivial" means a dressed single spin flip above the paramagnetic ground state, while "topological" means that the system is separated into two paramagnetic domains with antiparallel spin orientation.

This was also studied in the Bachelor's thesis of Magdalena Ritzau [Rit19] co-supervised by K. P. Schmidt and me. To this end, we introduced a new QP language where DWs as shown in Section 2.2.2 are interpreted as quasiparticles on the dual lattice of the 1D chain. This effectively reduces the Hilbert space since the $\mathbb{Z}_2$ symmetry introduced by flipping all spins is not present in the transformed system as both symmetric spin states are mapped onto the same state.

Here, we demonstrate for the ferromagnetic model that it is possible to determine the n-DW excited-state energies relative to the ground state energy

$$E_{0,\mathrm{f}}^{\mathrm{LRIM,ch}}(\alpha) = -NJ \sum_{\delta>0} \delta^{-\alpha} = -N\zeta(\alpha)J\,. \tag{2.54}$$

The single domain wall has the α-dependent energy

$$E_{1\mathrm{DW,f}}^{\mathrm{LRIM,ch}}(\alpha) = E_{0,\mathrm{f}}^{\mathrm{LRIM,ch}}(\alpha) + 2\zeta(\alpha-1)J\,, \tag{2.55}$$

while the two-domain-wall energy additionally depends on the distance d between the DWs

$$E_{2\mathrm{DW,f}}^{\mathrm{LRIM,ch}}(\alpha, d) = E_{0,\mathrm{f}}^{\mathrm{LRIM,ch}}(\alpha) + 4J\left[\zeta(\alpha)d - \sum_{i=1}^{d-1} \frac{d-1}{i^{\alpha}}\right]\,. \tag{2.56}$$

Higher energies can be derived iteratively for even and odd numbers of domain walls, respectively, based on the $(n-2)$-DW energies as discussed in [Rit19].

The respective expressions of the energies for antiferromagnetic interactions can be calculated in a similar fashion. In this case factors of $(-1)^{\delta}$ lead to alternating sums as shown in [Rit19]. The ground-state energy is given as

$$E_{0,\mathrm{af}}^{\mathrm{LRIM,ch}}(\alpha) = -NJ \sum_{\delta>0} (-1)^{\delta}\delta^{-\alpha} = -N(2^{1-\alpha}-1)\zeta(\alpha)J\,, \tag{2.57}$$

the 1-DW energy as

$$E_{1\mathrm{DW,af}}^{\mathrm{LRIM,ch}}(\alpha) = E_{0,\mathrm{af}}^{\mathrm{LRIM,ch}}(\alpha) + 2^{1-\alpha}(2^{\alpha}-4)\zeta(\alpha-1)J\,, \tag{2.58}$$

the two-domain wall energy again depends on the distance d between the two DWs

$$E^{\mathrm{LRIM,ch}}_{\mathrm{2DW,af}}(\alpha,d) = E^{\mathrm{LRIM,ch}}_{\mathrm{0,af}}(\alpha) + 4J\Big[(1-2^{1-\alpha})\zeta(\alpha)d - \sum_{i=1}^{d-1}(-1)^{i+1}\frac{d-1}{i^{\alpha}}\Big]\,, \tag{2.59}$$

the two-domain wall energy depends on the distances d_1 and d_2 between the three DWs

$$\begin{aligned} E^{\mathrm{LRIM,ch}}_{\mathrm{3DW,af}}(\alpha,d_1,d_2) &= E^{\mathrm{LRIM,ch}}_{\mathrm{1DW,af}}(\alpha,d_1,d_2) \\ &+ 2J\Big\{(1-2^{1-\alpha})\zeta(\alpha)d_1 - \sum_{i=1}^{d_1-1}(-1)^{i+1}\frac{d_1-i}{i^{\alpha}} + \sum_{i=1}^{d_2}\sum_{j=i}^{i+d_1-1}(-1)^{j+1}j^{-\alpha} \\ &- \sum_{i=d_2+d_1+1}^{d_2+d_1}\Big[(1-2^{1-\alpha})\zeta(\alpha) - \sum_{j=1}^{i-1}(-1)^{j+1}j^{-\alpha}\Big]\Big\}\,, \end{aligned} \tag{2.60}$$

and the 4-DW energy depends on three DW distances

$$\begin{aligned} &E^{\mathrm{LRIM,ch}}_{\mathrm{4DW,af}}(\alpha,d_1,d_2,d_3) = \\ &\quad E^{\mathrm{LRIM,ch}}_{\mathrm{2DW,af}}(\alpha,d_3) + 2J\Big\{(1-2^{1-\alpha})\zeta(\alpha)d_1 - \sum_{i=1}^{d_1-1}(-1)^{i+1}\frac{d_1-i}{i^{\alpha}} \\ &\qquad + \sum_{i=1}^{d_2}\sum_{j=i}^{i+d_1-1}(-1)^{j+1}j^{-\alpha} - \sum_{i=d_2+1}^{d_2+d_3}\sum_{j=i}^{i+d_1-1}(-1)^{j+1}j^{-\alpha} \\ &\qquad + \sum_{i=d_2+d_3+1}^{d_2+d_3+d_1}\Big[(1-2^{1-\alpha})\zeta(\alpha) - \sum_{j=1}^{i-1}(-1)^{j+1}j^{-\alpha}\Big]\Big\}\,. \end{aligned} \tag{2.61}$$

Returning to the ferromagnetic case, if we compare the two lowest excitations with the energies given in Equations (2.55) and (2.56) for different values of α an interesting property is found. In Figure 2.7 both energies relative to the ground-state energy are shown. For large values of α the single-DW state is the lowest-lying excitation and approaches the energy

$$\lim_{\alpha\to\infty} E^{\mathrm{LRIM,ch}}_{\mathrm{1DW,f}}(\alpha) = 2J \tag{2.62}$$

while the two-DW states become degenerate with energy

$$\lim_{\alpha\to\infty} E^{\mathrm{LRIM,ch}}_{\mathrm{2DW,f}}(\alpha,d) = 4J\,. \tag{2.63}$$

In the limit $\alpha \to 2$ the 1-DW energy diverges while the 2-DW energy remains finite for all $\alpha > 1$. This leads to a crossing of both energies at $\alpha \approx 2.478\,751$[5] where the excitation

5 The exact crossing point can be numerically evaluated to arbitrary precision by equating Equations (2.55) and (2.56).

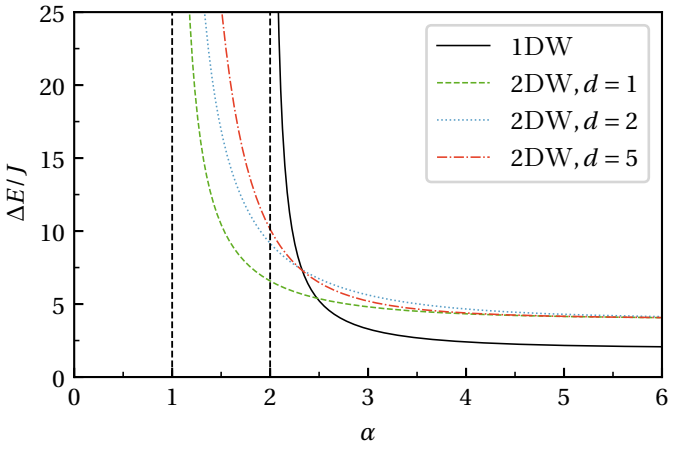

Figure 2.7: Low excitations of the ferromagnetic LRIM on a 1D chain relative to the ground-state energy. The 1-DW state is the lowest-lying excitation until $\alpha \approx 2.48$, while for smaller α the single spin flip with $E^{\mathrm{LRIM,ch}}_{\mathrm{2DW,f}}(\alpha, d = 1)$ becomes the lowest excitation. Vertical dashed black lines indicate the respective α-value where the single-DW and 2-DW energies diverge.

of the system switches from the topological at large α to the trivial at small α. Beware, that in the whole range of α the single spin flip, which represents a two-DW state with $d = 1$, always lies below all other two-DW states that have a larger distance between both DWs.

The energies for the antiferromagnetic LRIM are plotted relative to the ground-state energy in Figure 2.8. Here, the single-DW state also is the lowest-lying state which then gets replaced by a single-DW state at very small α. For $s \leq 1$ the analytical continuation of the Riemann zeta function $\zeta(s)$ is used such that the sums converge also for $\alpha \leq 1$. In contrast to the ferromagnetic case the distance between the two domain walls is $d = 2$, which is plausible considering that the antiferromagnetic Néel state has a magnetic unit cell that consists of two neighboring spins. In the low-α limit we find the spectrum of Figure 2.8 relative to the ground state energy $E^{\mathrm{LRIM,ch}}_{\mathrm{0,af}}(\alpha)$ as

$$\lim_{\alpha\to 0} \Delta E^{\mathrm{LRIM,ch}}_{\mathrm{1DW,af}}(\alpha) = \frac{J}{2} \tag{2.64}$$

$$\lim_{\alpha\to 0} \Delta E^{\mathrm{LRIM,ch}}_{\mathrm{2DW,af}}(\alpha, 1) = 2J \qquad \lim_{\alpha\to 0} \Delta E^{\mathrm{LRIM,ch}}_{\mathrm{2DW,af}}(\alpha, 2) = 0 \tag{2.65}$$

$$\lim_{\alpha\to 0} \Delta E^{\mathrm{LRIM,ch}}_{\mathrm{4DW,af}}(\alpha, 1, 2, 1) = 0 \qquad \lim_{\alpha\to 0} \Delta E^{\mathrm{LRIM,ch}}_{\mathrm{4DW,af}}(\alpha, 2, 2, 1) = 2J\,. \tag{2.66}$$

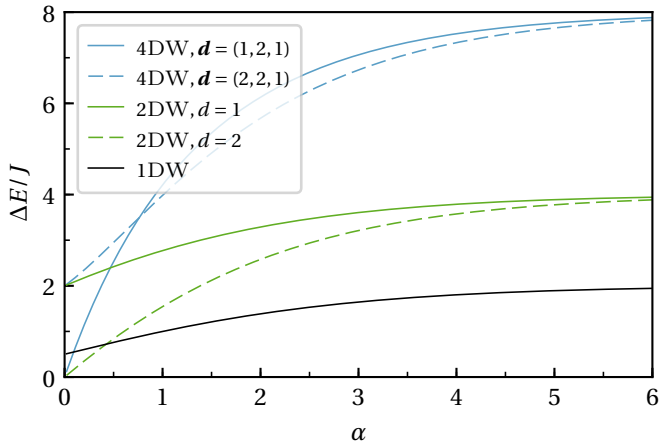

Figure 2.8: Low excitations of the antiferromagnetic LRIM on a 1D chain relative to the ground-state energy. The relative energies converge even for $\alpha < 1$ since the analytical continuation of the Riemann zeta function is used. The tuple $\boldsymbol{d} = (d_1, d_2, d_3)$ represents the distances between the domain walls.

The determination of the n-DW energies is necessary to set up a perturbative low-field approach in the thermodynamic limit. Such a perturbative expansion was performed up to second in order in h/J in Reference [Rit19] and is shortly discussed in Section 4.1.5.

In the present thesis the focus lies on the quantum phase transitions in the LRTFIM for various lattices. Although several studies have been performed on this topic there are still many open questions. In the next chapter I will discuss several steps and methods required to perform a series expansion on the long-range-interacting model and which I used to compute the results presented afterwards in Chapter 4.

3

METHODS

The methods chapter, while probably not the most interesting part of this thesis, is nevertheless an essential one, especially considering that part of this thesis consisted in developing the methods used to obtain the results presented in Chapter 4. Here, I try to give an overview of the several methods used for the calculation of the results presented within this thesis. The reader may be warned that this overview cannot (and does not have to) go into every detail of the methods as there is standard literature on most topics readily available.

When dealing with condensed matter systems one is usually interested in the properties of very large systems. "Very large" in this case means a number of particles of the magnitude of the Avogadro's constant $N_A \approx 10^{24}$ which, for all practical purposes, can be treated as infinity. The limit of an infinite system extension is often referred to as the *thermodynamic* or *bulk* limit.

As a result, the study of condensed-matter physics is therefore inherently difficult. This becomes even more clear when dealing with quantum-mechanical problems: Here, the Hilbert space grows exponentially with the system size. For a general system a diagonalization of the corresponding Hamilton matrix would yield the complete information necessary to understand its properties. Unfortunately, this is a prohibitively difficult task, even for todays most powerful computers. As an example, take a system of 18 spins-1/2 for which $2^{18} \cdot 2^{18} \approx 6.9 \cdot 10^{10}$ matrix elements need to be stored. Saving the elements of this – compared to the bulk limit – small system would already require 512 GB of memory and easily exceeds the available memory of most small computation clusters. The time necessary to run diagonalization algorithms on such a large amount of data does not even need to be considered here.

Unless there is a large number of conserved quantities, in most cases it becomes impossible to derive exact values for the quantities of interest, e. g., the complete energy spectrum of the system or observables like the magnetization or scattering amplitudes. There is only a small selection of quantum-mechanical condensed-matter problems which can be solved analytically – most of them specifically tailored to prove a certain property or analyze a certain aspect of quantum-mechanical solid-state systems (e. g., the Haldane model [Hal88] or Kitaev's honeycomb model [Kito6]). While they often have a certain beauty in their solution path and highlight a particular characteristic in a coherent way, it might be difficult to relate them to experimental setups.

At the same time, there are existing models that have proven to be good representatives of existing materials, able to reproduce the materials' distinctive features up to a high level of agreement, but are difficult to treat computationally. When there are no analytical solutions available, approximations need to be made to get certain information about the system. Obviously, every approximation taken has to compromise in one way or another. Therefore, many different directions have been explored in the past where each approximation truncates the problem in a unique way while trying to avoid problems of other methods. [Bet31; Lan50; Ogu60; Suz76; RH90; Whi92; Weg94; OR95; KF98; KU00; Fou+01; VMC08]

One way to approach this problem is to restrict the calculations to only a part of the total Hilbert space. When investigating quantum-mechanical models in the field of solid-state systems it is implied that the systems are at low temperatures. With increasing temperature the quantum effects become less and less important, since thermal compete with the quantum fluctuations, until we end up with a classical system. The quantum-critical point (QCP) is illustrated in Figure 3.1. Even though temperatures of absolute zero cannot be realized in a laboratory, quantum fluctuations are still relevant in a quantum critical region around the QCP. This gives us the justification for the simplification of ignoring the temperature axis and focusing on the parameter axes of our models and still obtaining meaningful results for experimental setups were $T = 0$ cannot be reached. Therefore, when talking about quantum phase transitions we assume a temperature of $T = 0$ for all calculations shown in this thesis.

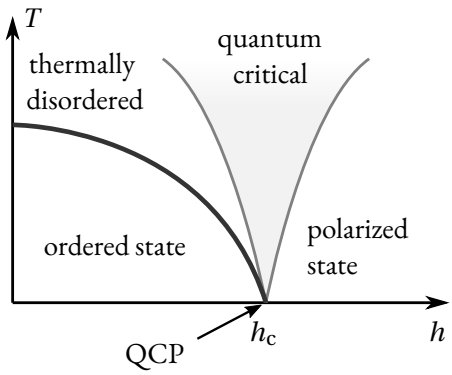

Figure 3.1: A phase diagram illustrating the parameter range for temperature T and magnetic field h where quantum effects become relevant.

In the world of low temperatures the ground state and lowest excited states play the most important role. Consequently, it is a logical approach to focus on the low-energy sectors of the Hamiltonian and try to reduce the Hilbert space by getting rid of the parts that are most relevant for *higher* energies. All energies of a Hamiltonian can be calculated exactly by writing the Hamiltonian as a matrix in a chosen basis and calculating its eigenvalues and eigenvectors numerically. Once the eigenvectors are known, any observable can be derived.

As this exact diagonalization (ED) is severely limited by the computational resources and the focus lies on the lower energies a widely used approximation is found in the Lanczos algorithm [Lan50] which is most of the time still just called ED. In this iterative

method a Krylov space is built by repeatedly acting with the Hamiltonian on a state from the Hilbert space. If the algorithm converges well, it is possible to obtain the lowest-energy eigenvalues of the Hamiltonian as a result. During computation only slightly more data than required by two Hilbert-space vectors must be kept in memory although numerical errors might require a reorthogonalizion to obtain an orthogonal basis and consequently require keeping more vectors in memory. While the treatment of larger systems is therefore possible, the difficulties with the exponentially growing Hilbert space remain limiting. Exploiting model- and lattice-dependent symmetries allows for further pushing the boundaries, but even the most sophisticated applications are limited to about 32 to 64 spins-1/2, depending on the model details [LL09]. For the LRTFIM a phase diagram of the one-dimensional Ising chain has been calculated for 22 spins [Kna+13].

Density-matrix renormalization group (DMRG) calculations have originally been developed for one-dimensional systems [Whi92] and proven very successful in this realm [Sch11]. They have also been successfully applied to one-dimensional long-range models, e. g., for dipolar interactions [Gor+11] and in the generalized formulation of matrix product states (MPS) for arbitrary algebraically decaying interactions of the ferromagnetic Ising model [Van+18]. However, in the 2018 paper the long-range interactions are approximated by exponentials which works well in the nearest-neighbor limit but becomes increasingly worse for more slowly-decaying long-range interactions [Van+18]. An attempt to apply the methods to two-dimensional systems has been made by Saadatmand *et al.* who investigated the antiferromagnetic long-range Ising model on quasi-one-dimensional triangular six-leg cylinders of infinite length [SBM18]. In practice, this method is not able to capture the true 2D properties. This is especially plausible for long-range interactions which, on a cylinder, have a hard cut-off in one dimension. In [Koz+19] we present a phase-transition scenario for the LRTFIM on such cylinder geometries that is qualitatively different from the expected 2D behavior [FKS19].

Quantum Monte Carlo (QMC) simulations are well-established numerical methods for treating quantum many-body systems [Suz76; BSS81]. The original Monte-Carlo methods were designed for classical problems [Kra06] and only later extended to quantum-mechanical problems where the sampling of high-dimensional Hilbert spaces becomes necessary. The goal of the method is to spend only a polynomial time for obtaining results in the exponentially growing Hilbert space [LY19]. Although being very successful in many situations, the method is plagued by the infamous "sign problem", which makes it unsuitable for treating fermionic or frustrated systems, although there are attempts to circumvent the obstacle by a clever mapping to a different formulation of the problem or by algorithmic optimizations [LY19; HS00]. These QMC methods have also been applied to the LRTFIM on the triangular lattice by S. Humeniuk [Hum16]. Although QMC methods have not been used for the results presented in this thesis,

classical Monte-Carlo methods proved very useful as an extension to the semi-analytic methods applied to the problems studied here. These methods are discussed extensively later in this chapter.

There are many more methods on the market, but, generally speaking, the best solution would arguably be to simply *know* or maybe guess the unitary transformation $\hat{U}$ diagonalizing the Hamiltonian

$$\hat{H}_{\text{diag}} = \hat{U}\hat{H}\hat{U}^{\dagger} . \tag{3.1}$$

As mentioned above, most of the time such an analytical solution is not available or at least unknown. But in the spirit of such a transformation it is possible to think of iteratively applying unitary transformations

$$\hat{H}' = \hat{U}_1\hat{U}_2\hat{U}_3\cdots\hat{H}\cdots\hat{U}_3^{\dagger}\hat{U}_2^{\dagger}\hat{U}_1^{\dagger} \tag{3.2}$$

to rotate the basis in a way that simplifies the Hamiltonian – e. g., transforms matrix elements to zero that are not close to the diagonal or divides it into smaller decoupled blocks. This idea is used in this thesis and will be elaborated in more detail in the next section.

The rest of this chapter is structured as follows. First, I continue on the notion of unitary transformations and introduce continuous unitary transformations before I discuss a perturbative ansatz in detail in Section 3.1.1. Afterwards, I point out the importance of graphs in this scheme and explain white-graph expansions for general models as an extension to the perturbative method. In Section 3.1.6, I connect the method to the long-range model studied in this thesis, show the appearance of complex nested infinite sums that need to be evaluated to obtain numerical results. Two methods are discussed in Section 3.2 to overcome this hurdle: First, Wynn's ε method is discussed as a convergence acceleration method and compared to fitting a scaling function to a finite series of partial sums. Afterwards I introduce Monte-Carlo summation and discuss it in detail as an improved tool to numerically evaluate the complex sums. Padé and DLog Padé extrapolations are then presented as a method to extend the radius of convergence for perturbative series. I illustrate the relationship and utilization of the introduced steps in a flow diagram in Section 3.4. At the end of this chapter mean-field calculations are presented for different lattices.

3.1 CONTINUOUS UNITARY TRANSFORMATIONS

A unitary transformation maps a matrix or an operator to its representation in a different basis. Take for example an arbitrary operator $\hat{A}$ of which we want to know the eigenvalues,

but which cannot easily be seen by looking at it. The operator can be transformed to a different basis by mapping it to operator $\hat{B}$

$$\hat{A} \to \hat{B} := \hat{U}\hat{A}\hat{U}^\dagger \tag{3.3}$$

with the unitary operator $\hat{U}$. One property of unitary transformations which is especially important for the calculation of energies is that the eigenvalues remain unchanged. Applying a unitary transformation created from $\hat{A}$'s eigenvectors to $\hat{A}$ itself would give a diagonal representation where the eigenvalues appear as diagonal operator elements. Unfortunately, the eigenvectors of a general Hamiltonian are usually unknown. But, still, it is possible to make use of unitary transformations for calculating eigenvalues by transforming the Hamiltonian into a basis in which it has a simpler representation, e. g., it is block-diagonal. The challenge is to find a suitable transformation for a given operator.

To this end, it will prove useful to split the single transformation into a succession of multiple smaller transformations where, with each transformation, the operator becomes more and more diagonal.

$$\hat{A} \to \hat{C} := \hat{U}_N \cdots \hat{U}_2 \hat{U}_1 \hat{A} \hat{U}_1^\dagger \hat{U}_2^\dagger \cdots \hat{U}_N^\dagger \,. \tag{3.4}$$

Beware that the single transformations $\hat{U}_n$ do not necessarily commute. Now, if we make these single transformations infinitesimally small and let $N \to \infty$, we obtain continuous unitary transformations (CUTs) which have first been proposed by Wegner in 1994 [Weg94] and reviewed in 2001 [Weg01]. The idea is that the flow of infinitesimal transformations can be created by using a generator $\hat{\eta}(l)$ of the unitary transformation which implicitly depends on the flow parameter $l \in \mathbb{R}$. The transformed matrix or operator can be controlled by this parameter and reproduces the initial operator for $l = 0$ and the (block-)diagonal operator for $l = \infty$ [Ste97].

Let us consider the flow of Hamiltonian $\hat{H}$

$$\hat{H}(l) = \hat{U}(l)\hat{H}\hat{U}^\dagger(l) \,, \tag{3.5}$$

where $\hat{H}(0)$ is the untransformed Hamiltonian and for any finite l the operator is rotated into a new basis. Taking the derivative of Equation (3.5) with respect to the flow parameter l gives the so-called *flow equation*

$$\frac{\mathrm{d}\hat{H}(l)}{\mathrm{d}l} = \left(\frac{\partial \hat{U}(l)}{\partial l}\right)\hat{U}^\dagger(l)\hat{H} + \hat{H}U(l)\left(\frac{\partial \hat{U}^\dagger(l)}{\partial l}\right) = \left[\hat{\eta}(l), \hat{H}(l)\right] \,. \tag{3.6}$$

This defines the generator $\hat{\eta}(l)$ which is anti-Hermitian, i. e.

$$\hat{\eta}(l) = \frac{\mathrm{d}\hat{U}(l)}{\mathrm{d}l}\hat{U}^\dagger(l) = -\hat{\eta}^\dagger(l) \tag{3.7}$$

and implicitly depends on the flow parameter. In practice it is chosen such that it ensures a good convergence of the Hamiltonian $\hat{H}(l)$ to the desired basis and therefore depends on the flowing Hamiltonian. With the introduction of the generator the difficulty of finding a suitable unitary-transformation operator $\hat{U}$ is shifted to finding an $\hat{\eta}$ generating the unitary transformation that simplifies the Hamiltonian the most. The generator proposed by Wegner [Weg94]

$$\hat{\eta} = [\hat{H}_\mathrm{d}, \hat{H}] \tag{3.8}$$

aims to rotate the Hamiltonian such that non-diagonal elements vanish. Here, $\hat{H}_\mathrm{d}$ is the diagonal part of the original Hamiltonian $\hat{H}$. However, there are some problems with this choice: Models with degeneracies are difficult to treat because matrix elements between degenerate or nearly degenerate states do not vanish or decay very slowly in these cases [Weg94]. Also, many-particle interactions are generated even if they were not present in the original Hamiltonian [Weg94]. These newly created operators lead to the effect that Hamiltonians loose any initial block-structure and therefore might become even more complicated. To overcome this problem Wegner also proposed to use only quasiparticle-conserving parts in $\hat{H}_\mathrm{d}$, where no complete but only a block-diagonalization is reached [Weg94]. The idea has also inspired others to search for and propose different generators [Mie98; KU00] to avoid some of the problems.

In 1998 Mielke introduced a generator conserving the initial band structure of band matrices by taking the matrix elements h_{nm} of a real, symmetric Hamilton matrix H and a sign function into account [Mie98]

$$\eta_{nm} = -\eta_{mn} = \mathrm{sgn}(n-m)\, h_{nm} \,. \tag{3.9}$$

This approach is not only valid for band-structured Hamiltonians nor is it limited to finite, real, or symmetric matrices or is it necessary to express the generator in quanta of the Hamiltonian basis. We can introduce a QP-counting operator $\hat{Q}$ with eigenbasis $\{|n\rangle\}$ which fulfills

$$\hat{Q}\,|n\rangle = n\,|n\rangle \,. \tag{3.10}$$

The scalar eigenvalue $n \in \mathbb{N}_0$ represents the number of quasiparticles in state $|n\rangle$. In CUTs the operator $\hat{Q}$ may, but must not necessarily be a part of the Hamiltonian $\hat{H}$ as discussed later. If the Hamiltonian is expressed in the eigenbasis of $\hat{Q}$ the generator may be written in the form

$$\hat{\eta} = \sum_m \mathrm{sgn}(m)\, \hat{T}_m \,, \tag{3.11}$$

where $\hat{T}_m$ represents the operators in the Hamiltonian changing the number of QPs by m.

The flow equation (3.6) can, e. g., be solved by choosing a suitable operator basis and writing the Hamiltonian in second quantization. By evaluating the commutator in Equation (3.6) differential equations for the coefficients of the operators are obtained. However, this generates new many-body-interaction processes which in turn have to be added to the initial Hamiltonian. Continuing the procedure leads to an infinite number of differential equations as has been outlined in, e. g., [DFU11]. In general it is impossible to solve the infinite set of differential equations so some truncation scheme has to be chosen to find a closed set.

From the initial idea of CUTs a plethora of methods has been developed, which still carry their origin in their names. The perturbative CUT (PCUT), which is elaborated on in the next section, was one of the first derivations that subsequently lead to the development of enhanced PCUTs (EPCUTs) [KDU12] and directly evaluated EPCUTs (DEEPCUTs) [KDU12]. Other directions which have been investigated include the graph-theory-based graph CUT (GCUT) [YS11] and the self-similar CUT (SCUT) [DFU11].

3.1.1 *Perturbative Continuous Unitary Transformations*

Each method dealing with complex enough condensed-matter problems today has to compromise in some way. Approximations can be made in the size of the system, the fraction of Hilbert space included in the calculations, or the perturbative order up to which the contribution of certain parts of a Hamiltonian are considered. PCUTs which are linked-cluster expansions (LCEs) require the Hamiltonian to be split into a diagonal unperturbed part and a perturbation containing the non-diagonal matrix elements. The flow equation (3.6) can then be expanded and used to apply high-order perturbation theory. It should be pointed out that the exact result of the perturbation theory is not independent of the method. Take, for example, an electron-phonon system in leading order. The Fröhlich transformation [Frö52] decouples phonon and electron degrees of freedom just as a unitary transformation using the generator $\hat{\eta} = [\hat{H}_\mathrm{d}, \hat{H}]$ [Weg94] would do. However, the matrix element of the attractive electron-electron interaction responsible for the formation of Cooper pairs [BCS57] looks slightly different. While both are attractive, the Fröhlich approach obtains a resonant energy denominator while it is absent in the CUT results. With an even different generator the outcome may vary again. Due to the different treatment of virtual processes the unitary transformations are different even in leading order [KDU12; Weg01]. As Wegner put it in his review of CUTs in 2001

> » The permanent adjustment of the infinitesimal unitary transformation to the Hamiltonian yields a smoother effective interaction than conventional perturbation theory. « (Wegner [Weg01])

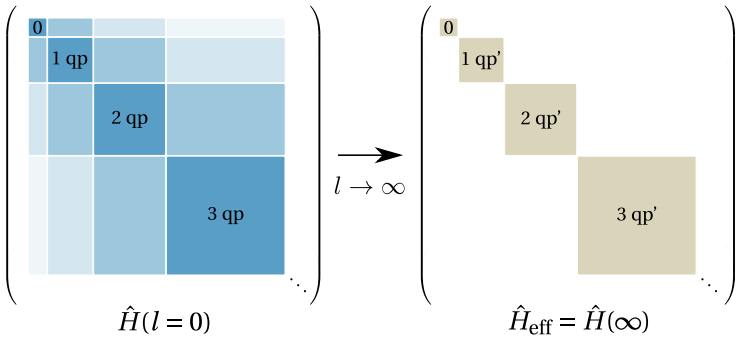

Figure 3.2: An illustration of the PCUT method that maps the original Hamiltonian (left) to a block-diagonal QP-conserving (right) Hamiltonian. Due to the rotation the new quasiparticles (indicated with a prime) are a superposition of previous states and therefore are sometimes called *dressed*.

The starting point for the PCUT method is a Hamiltonian that can be written as

$$\hat{H} = \hat{H}_0 + \lambda \hat{V} \,, \quad \hat{V} = \sum_{n=-N}^{N} \hat{T}_n \,. \tag{3.12}$$

It is essential that (a) the unperturbed part $\hat{H}_0$ has a known equidistant non-degenerate spectrum and (b) it must be possible to write the perturbation $\hat{V}$ in above form with $\hat{T}_n$ creating (annihilating) $|n|$ energy quanta for $n > 0$ ($n < 0$) where a finite upper bound N must exist. In practice, most of the time the Hamiltonian is scaled such that the distance between two neighboring energy levels is 1 such that

$$[\hat{H}_0, \hat{T}_n] = n\hat{T}_n \,. \tag{3.13}$$

Although, in principle, this is not necessary it proves helpful for purely practical purposes as outlined later in this section. For the Hamiltonian to be Hermitian the condition $\hat{T}_n = \hat{T}_{-n}^\dagger$ has to be fulfilled. $\hat{H}_0$ can therefore be written as a sum of the QP-counting operator $\hat{Q}$ for excitations and a constant offset.

The expansion parameter $\lambda \in \mathbb{R}$ should be small compared to $\hat{H}_0$ since it is handled perturbatively, even though it can be pushed to some extend by extrapolating the perturbation series as discussed later. Building on these prerequisites, the PCUT maps the original to an effective quasiparticle-conserving (i. e., block-diagonal) Hamiltonian as illustrated in Figure 3.2. The blocks correspond to different i-particle Hilbert subspaces. In general, quantities such as the ground-state energy and the dispersion can be derived from the 0- and 1-QP blocks.

For the flowing Hamiltonian $\hat{H}(l)$ described by Equation (3.6) the ansatz

$$\hat{H}(l) = \hat{H}_0 + \sum_{k=1}^{\infty} \lambda^k \sum_{\dim(\boldsymbol{m})=k} F(l;\boldsymbol{m})\,\hat{T}_{\boldsymbol{m}} \tag{3.14}$$

is chosen [KU00]. $F(l;\boldsymbol{m})$ are real-valued functions which are determined by nonlinear recursive differential equations derived from the flow equation. The vector $\boldsymbol{m}$, with $m_i \in 0, \pm 1, \ldots, \pm N$ is of dimension k in order k. The operator $\hat{T}_{\boldsymbol{m}}$ represents a product of annihilation and creation operators encoding all possible combinations of QP-number-changing operators.

$$\boldsymbol{m} = (m_1, m_2, \ldots m_k) \tag{3.15}$$

$$\hat{T}_{\boldsymbol{m}} = \hat{T}_{m_1}\hat{T}_{m_2}\cdots\hat{T}_{m_k} \tag{3.16}$$

$$M(\boldsymbol{m}) = \sum_i m_i\,. \tag{3.17}$$

The QP- conserving operator introduced in Equation (3.11) is used as the PCUT generator as proposed in [KU00] and is then given by

$$\hat{\eta}(l) = \sum_{k=1}^{\infty} \lambda^k \sum_{\dim(\boldsymbol{m})=k} \operatorname{sgn}(M(\boldsymbol{m}))\,F(l;\boldsymbol{m})\,\hat{T}_{\boldsymbol{m}}\,, \tag{3.18}$$

and consequently leads to a block-diagonal structure [KU00]. Inserting ansatz (3.14) and generator (3.18) in the flow equation (3.6) yields an infinite hierarchy of differential equations for the coefficients $F(l;\boldsymbol{m})$ which can be solved iteratively order by order. In the end, we are not interested in the coefficients of the flowing Hamiltonian $\hat{H}(l)$ but rather in the effective Hamiltonian for $l \to \infty$

$$\hat{H}_{\text{eff}} = \hat{H}_0 + \sum_{k=1}^{\infty} \lambda^k \sum_{\substack{\dim(\boldsymbol{m})=k \\ M(\boldsymbol{m})=0}} C(\boldsymbol{m})\,\hat{T}_{\boldsymbol{m}}, \quad \text{with } C(\boldsymbol{m}) = \lim_{l\to\infty} F(l;\boldsymbol{m})\,. \tag{3.19}$$

The important observation is here that only operators conserving the number of quasiparticles remain because contributions with $M(\boldsymbol{m}) \neq 0$ decay for $l \to \infty$.

The coefficients $C(\boldsymbol{m})$ can be calculated for any finite set of operators $\hat{T}_n$ in the original Hamiltonian. However, apart from that, they are model-independent and need only be calculated once. If the Hamiltonian is brought into the shape of Equation (3.12) the coefficients can simply be looked up if they have already been calculated. It is important to consider that the coefficients are rescaled if the energy gap of the unperturbed spectrum changes, which is the reason why it is usually scaled to 1.

To illustrate where the specific model becomes relevant for the method, we write out the first terms of Equation (3.19) for $n \in \{-2, 0, 2\}$

$$\hat{H}_{\text{eff}} = \hat{H}_0 + \hat{T}_0 + \frac{1}{2}\hat{T}_2\hat{T}_{-2} - \frac{1}{2}\hat{T}_{-2}\hat{T}_2 + \ldots\,. \tag{3.20}$$

The terms are not normal-ordered yet. A normal ordering of the expression yields different processes, such as constants and hopping terms. The normal ordering, however, is model-dependent so this must be done for every specific model individually.

Since PCUT is a perturbative method, the resulting matrix elements of the block-diagonal Hamiltonian will be a series in the perturbation parameter λ. The non-degenerate ground state energy per site is always given as a polynomial

$$e_0 = p_0^{0\mathrm{qp}} + p_1^{0\mathrm{qp}}\lambda + p_2^{0\mathrm{qp}}\lambda^2 + \dots \,. \tag{3.21}$$

The 1-QP block of the effective Hamiltonian has the form

$$\hat{H}^{1\mathrm{qp}} = E_0 + \sum_{\boldsymbol{i},\boldsymbol{j}} \sum_{\nu,\nu'=0}^{N_{\mathrm{suc}}-1} a_{\boldsymbol{\delta}}^{\nu,\nu'} \left(b_{\boldsymbol{i},\nu}^\dagger b_{\boldsymbol{j},\nu'} + \mathrm{H.\,c.} \right) \tag{3.22}$$

for a lattice with N_{suc} sites per unit cell, where $\boldsymbol{i}$ and $\boldsymbol{j}$ are the positions of two unit cells with distance $\boldsymbol{\delta} = \boldsymbol{j} - \boldsymbol{i}$ and $\nu, \nu' \in [0, N_{\mathrm{suc}} - 1]$ label the respective site positions within the unit cells. The hopping elements $a_{\boldsymbol{\delta}}^{\nu,\nu'}$ between the two lattice sites at $(\boldsymbol{i}, \nu)$ and $(\boldsymbol{j}, \nu')$ are in general complex numbers.

To exploit the translational invariance of the lattice, we can introduce the Fourier transformation

$$\hat{b}_{\boldsymbol{j},\nu}^\dagger = \frac{1}{\sqrt{N_{\mathrm{s}}}} \sum_{\boldsymbol{k}} \mathrm{e}^{\mathrm{i}\boldsymbol{k}\boldsymbol{j}} \hat{b}_{\boldsymbol{k},\nu}^\dagger \,, \qquad \hat{b}_{\boldsymbol{j},\nu} = \frac{1}{\sqrt{N_{\mathrm{s}}}} \sum_{\boldsymbol{k}} \mathrm{e}^{-\mathrm{i}\boldsymbol{k}\boldsymbol{j}} \hat{b}_{\boldsymbol{k},\nu} \tag{3.23}$$

with $N_{\mathrm{s}} \in \mathbb{N}$ lattice sites and the quasimomentum $\boldsymbol{k} \in \mathbb{R}^d$ in dimension d. Taking the bulk limit $N_{\mathrm{s}} \to \infty$ the momentum $\boldsymbol{k}$ becomes continuous. The effective 1-QP Hamiltonian in the new basis can be written as

$$\hat{H}_{\mathrm{eff}}^{1\mathrm{qp}} = E_0 + \sum_{\boldsymbol{k}} \hat{\boldsymbol{b}}_{\boldsymbol{k}}^\dagger \Omega_{\boldsymbol{k}} \hat{\boldsymbol{b}}_{\boldsymbol{k}} = E_0 + \sum_{\boldsymbol{k}} \sum_{\nu,\nu'} \omega_{\boldsymbol{k}}^{\nu',\nu} \hat{b}_{\boldsymbol{k},\nu'}^\dagger \hat{b}_{\boldsymbol{k},\nu} \tag{3.24}$$

with $\Omega_{\boldsymbol{k}}$ being a self-adjoint $N_{\mathrm{suc}} \times N_{\mathrm{suc}}$ matrix with matrix elements $\omega_{\boldsymbol{k}}^{\nu,\nu'} \in \mathbb{C}$. The individual matrix elements describe a hopping with wave vector $\boldsymbol{k}$ from site ν to ν' between unit cells.

To obtain the energy eigenvalues of the one-QP Hamiltonian $\Omega_{\boldsymbol{k}}$ needs to be diagonalized first, which is analytically possible for small unit cells or by using additional symmetries of the system.

The minimum of the eigenvalues $\omega_{\boldsymbol{k}}^\nu$ of $\Omega_{\boldsymbol{k}}$ defines the 1-QP energy gap

$$\Delta := \min_{\nu,\boldsymbol{k}} \omega_{\boldsymbol{k}}^\nu \,. \tag{3.25}$$

For lattices with a single site per unit cell $\Omega_{\boldsymbol{k}}$ is a 1×1 matrix where the eigenvalue $\omega_{\boldsymbol{k}} \in \mathbb{R}$ is a scalar function of $\boldsymbol{k}$. Taking the 1D chain as the easiest example one would simply get

$$\omega_k = a_0 + 2 \sum_{\delta>0} a_\delta \cos(k\delta) \,. \tag{3.26}$$

In this thesis we have calculated the energy gap for several lattice structures as a series

$$\Delta(\lambda) = 1 + \sum_{r=1}^{r_{\max}} p_r \lambda^r = 1 + p_1\lambda + p_2\lambda^2 + \cdots + p_{r_{\max}} \lambda^{r_{\max}} \tag{3.27}$$

in the perturbation parameter $\lambda \in \mathbb{R}$ up to order $r_{\max} \in \mathbb{N}$.

3.1.2 *High-field limit*

To study the Ising Hamiltonian introduced in Chapter 2 with PCUT calculations in the limit of high magnetic fields we need to write the Hamiltonian in the form of Equation (3.12). Therefore, we apply the same transformation to a quasiparticle picture introduced in Equation (2.22) to obtain the Hamiltonian analogously to the nearest-neighbor case (cf. Equation (2.24))

$$\hat{H}_{\text{LRTFIM}} = \hat{H}_0^{\text{LRTFIM}} + \lambda \hat{V}^{\text{LRTFIM}} \,, \quad \text{with} \quad \lambda = \frac{J}{2h} \tag{3.28}$$

and

$$\hat{H}_0^{\text{LRTFIM}} = -\frac{N}{2h} + \sum_{\boldsymbol{i}} \hat{n}_{\boldsymbol{i}} \tag{3.29}$$

$$\lambda \hat{V}^{\text{LRTFIM}} = \lambda \sum_{\boldsymbol{i}\neq\boldsymbol{j}} \frac{1}{|\boldsymbol{i}-\boldsymbol{j}|^{-\alpha}} \left(\hat{b}_{\boldsymbol{i}}^\dagger \hat{b}_{\boldsymbol{j}}^\dagger + \hat{b}_{\boldsymbol{i}} \hat{b}_{\boldsymbol{j}} + \hat{b}_{\boldsymbol{i}}^\dagger \hat{b}_{\boldsymbol{j}} + \hat{b}_{\boldsymbol{i}} \hat{b}_{\boldsymbol{j}}^\dagger \right) , \tag{3.30}$$

where each pair of spins $(\boldsymbol{i}, \boldsymbol{j})$ is only counted once in the sum. The unperturbed part is given by the field term while the long-range Ising interactions are added perturbatively with the perturbation parameter $\lambda = J/2h$. The Hamiltonian was divided by $2h$ such that all energies are measured relative to the strength of the magnetic field and, as already discussed, the unperturbed Hamiltonian has an equidistant spectrum with difference 1 between two neighboring energy levels.

3.1.3 *Linked-cluster expansion*

The PCUT matrix elements for a specific model are calculated on finite graphs. However, they are valid in the bulk limit because of the linked-cluster theorem [Bru55; Dus+10].

This is a direct consequence of the fact that the method is based on unitary transformations, which keep the linked-cluster property valid.

Inserting the generator and the Hamiltonian in the flow equation one obtains differential equations containing commutator relations of operators $\hat{T}_n$. While the flowing $\hat{T}_n(l)$ contain an infinite number of operators, they can still be solved by a perturbative expansion as discussed above. If the $\hat{T}_n$ are defined as a sum over local operators, acting on a finite number of neighboring sites, the commutators vanish if the contained operators act on far-apart sites not connected by the operators [Dus+10]. Below, when discussing the white-graph expansion, we will see that it is possible to apply the PCUT approach even if the perturbation acts on sites with any distance. As a result, the advantage of the linked-cluster property that allows the calculation of quantities in the bulk limit (a limit especially interesting for long-range interactions) can still be maintained.

3.1.4 *Graphs*

PCUT calculations are most efficiently done on small clusters of spins to make the best use of the available computing resources. This is possible due to the linked-cluster property discussed above. Here, a very brief overview of the meaning of graphs within this context is given to find a common language which then can be used in the thesis.

Graphs consist of vertices which can be connected to other vertices via edges. The vertices can be identified with a spin-1/2 located on a site. An edge represents an interaction of two spins, or rather an operator acting on two spins. Remembering the linked-cluster property discussed in the section before, it becomes clear that only connected graphs[1] contribute to the calculations.

The undirected graphs we use here can be uniquely identified by the *adjacency number* which we use as a canonical labeling for a graph. To this end, the single vertices are labeled with numbers starting from 0 to $N_{\text{vert}} - 1$, where $N_{\text{vert}} \in \mathbb{N}$ is the total number of vertices of a graph. The graph can then be represented by an *adjacency matrix* $A_{\mathcal{G}}$ with matrix elements

$$a^{\mathcal{G}}_{m,n} = \begin{cases} 1, & \text{if vertex labeled } m \text{ is connected to vertex } n \\ 0, & \text{otherwise.} \end{cases} \tag{3.31}$$

As the matrix of the undirected graph is symmetric and the diagonal elements are irrelevant – because vertices connected to themselves are not considered here – the upper triangular matrix contains all relevant information. We use this to derive a number by interpreting the 0s and 1s row-by-row as a binary number. This number is by no means unique for a single graph, because a permutation of the vertices' labels also changes the

1 A graph is called *connected* if a path between any two vertices can be found.

adjacency matrix and consequently the derived number. Both graphs are isomorphic and therefore have, e. g., the same characteristic polynomial, eigenvalues, and determinant. Nevertheless, there is one number that stands out from the others, which we I to represent the graph: I call the maximum of the permutations adjacency number $a_{\mathcal{G}}$ and use it to identify the graph $\mathcal{G}$.

The reason to select a single representative number is mainly given due to another property which becomes apparent when reshuffling the labels: There may be different permutations of labels which yield the same adjacency number. This is a direct consequence of the graph's symmetry and can be used in the embedding process of the PCUT results as discussed later.

The degree (number of connected edges) of any vertex can be easily calculated by summing over the respective row or column of the adjacency matrix.

To get a more illustrative picture let us simply look at an exemplary graph $\mathcal{G}_{60}$. In Figure 3.3 the graph with 4 vertices is shown. A random labeling would most probably not result in the maximum adjacency number. A permutation of the vertices' labels shows that the maximum number used for identifying the graph can be reached in two different ways, representing the graph's mirror symmetry about the horizontal.

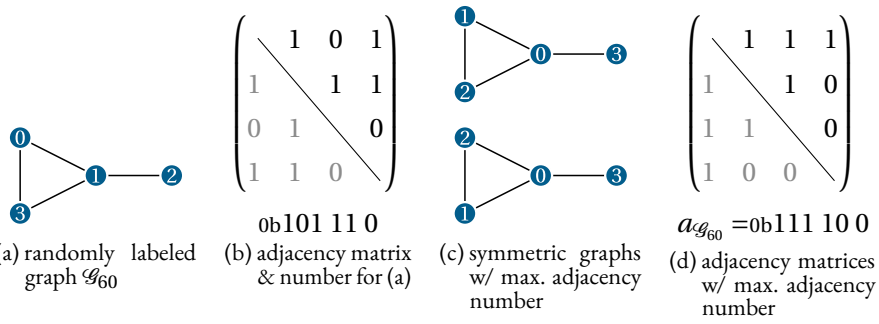

(a) randomly labeled graph $\mathcal{G}_{60}$

(b) adjacency matrix & number for (a)

(c) symmetric graphs w/ max. adjacency number

(d) adjacency matrices w/ max. adjacency number

Figure 3.3: Illustration of the adjacency-matrix and adjacency-number construction for a four-vertex graph. The randomly labeled graph (a) can be represented by the adjacency matrix in (b). Matrix elements $a^{\mathcal{G}}_{m,n}$ are set to 1 if there is an edge in between the sites labeled m and n. The adjacency number is derived by interpreting the rows of the matrix as a binary number. (c) For a labeling maximizing the adjacency number of the graph there are two possibilities that result in the same adjacency matrix (d). This is a consequence of the graph's mirror symmetry about the horizontal.

3.1.4.1 *Generating graphs*

Depending on the investigated model only a subset of all possible graphs is relevant and needs to be constructed.

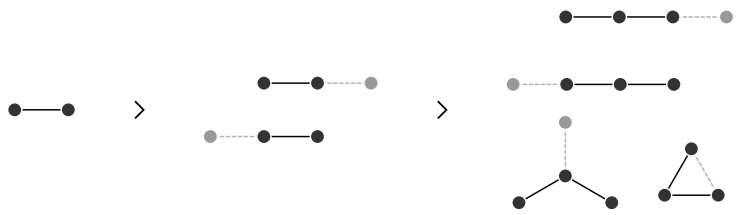

Figure 3.4: Iterative scheme for generating graphs. Starting from the simplest two-vertex graph shown on the left, in each step a new edge is added to any vertex or between vertices without a connecting edge. Already created isomorphic graphs are discarded, such as the second graph created in the first step.

E. g., for nearest-neighbor interactions the lattice geometry plays an important role: On a square lattice it is not possible to fit a graph containing loops with an odd number of vertices like a triangle. For different lattice structures different criteria result. Furthermore, in order k only graphs with up to k edges can contribute for a two-vertex interaction because each edge represents one or multiple applications of the perturbation operator.

For long-range interactions the lattice geometry does not matter in this context. Any graph can be embedded into the lattice because each spin interacts with any other spin, therefore realizing all possible clusters. In order 10 there are 3390 graphs while in order 11 this already leads to 11 461 graphs.

The practical generation is done in the following way: Starting from the smallest graph[2] with two vertices connected via an edge, a vertex is attached to each existing site, resulting in two new graphs. For the new graphs the adjacency number is computed and compared to a list of existing graphs. If the graph is not already in the list it is added, otherwise it is discarded. In the next step, again, new vertices are added with an edge connecting them to an already existing vertex. A second possibility is to add a new edge between previously unconnected vertices. This iterative scheme: adding new edges or vertices, calculating the graph numbers, and building a list of topologically distinct graphs is used to generate all relevant graphs order by order up to a given maximum order (cf. Figure 3.4). An overview of all graphs up to order 4 can be found in Figure C.1 in Section C.1.

The details of calculation of the adjacency number are given in Section C.1. During the calculation the number of symmetric labelings yielding the same adjacency number is counted. The number of labelings becomes important in the embedding of the graph results into the lattice to prevent an overcounting of contributions (see Section 3.2.2).

2 The two-vertex graph with a single edge is the only graph in order 1.

3.1.5 *White-graph expansion*

The idea of white-graph expansions was first presented by K. Coester and K. P. Schmidt in 2015 [CS15]. It can be seen as an extension of the original PCUT method: In the original implementation, for models with multiple different link types ("colors"), calculations on graphs where at least one link type differs from previous calculations need to be repeated. This becomes more and more inefficient if the number of link types in the model increases because the number of graphs that need to be considered grows exponentially.

To circumvent this problem, the interaction strength can be kept variable by using a distinct perturbation parameter for each bond. Ignoring the link colors for the topological classification of graphs significantly reduced the complexity, although a bit more bookkeeping during the calculation is necessary [CS15]. The result is a power series of multiple parameters in the PCUT matrix elements. These results are general for a given Hamiltonian structure and completely independent of the underlying lattice structure. Only after the PCUT calculation is done, the results need to be embedded in the respective lattice by adding up all contributions for all possible embeddings of a given graph to obtain the series for the original model and lattice. The procedure is explained in more detail in the following sections using the LRTFIM as an example.

One limitation of the idea is that the scheme is only applicable if the *value* of the different interaction types differs. The important point is that the *operators* must be identical. For different interactions with different operators, the calculations still need to be done on multiple graphs. Coester and Schmidt present the idea for a model with three different couplings $J_\perp$, $J_\parallel$, and J_{int} on a lattice of coupled spin ladders [CS15]. The idea can also be applied to disordered systems where interaction strengths are randomly distributed [HWS18] and long-range systems [FS16; FKS19; Koz+19] as is shown in this thesis.

3.1.6 *Embedding the PCUT results: Application to a long-range model*

Embedding the PCUT results can be best understood with an example. Here, I show the embedding of a selected matrix element of the LRTFIM on a one-dimensional chain. To this end, let us consider graph $\mathcal{G}_{60}$ shown in Figure 3.3 again. The matrix element of the 0-QP element is given by

$$\langle 0000|_{\mathcal{G}_{60}}\, \hat{V}\, |0000\rangle_{\mathcal{G}_{60}} = \frac{5}{8}\lambda_0^3\lambda_1\lambda_3 + \frac{5}{8}\lambda_0\lambda_1^3\lambda_3 - \frac{9}{8}\lambda_0\lambda_1\lambda_2^2\lambda_3 + \frac{5}{8}\lambda_0\lambda_1\lambda_3^3 \quad (3.32)$$

in order 5. The result also contains contributions from subgraphs, which can be easily identified by looking at the perturbation parameters of each summand. If not all edges are touched such as, e. g., in $\frac{5}{8}\lambda_0^3\lambda_1\lambda_3$ which misses λ_2, this contribution is al-

ready contained in a different graph. Removing all subgraph contributions the relevant contribution becomes

$$h_{\mathscr{G}_{60}}^{O(5),0\mathrm{qp}} = -\frac{9}{8}\lambda_0\lambda_1\lambda_2^2\lambda_3 \,. \tag{3.33}$$

By looking at the multiplicity of the perturbation parameters λ_n we can see that each edge of the graph is touched exactly once, except for the edge with parameter λ_2, connecting vertices 0 and 3 in canonical labeling. The perturbation parameters contain the algebraic decay of the interaction and depend on the distance of the connected lattice sites. It is possible to fit the graph onto the one-dimensional lattice in infinitely many ways by varying the positions of the graph's vertices. Naïvely, we simply need to sum over all these possibilities to obtain the total contribution of the graph to the final result.

$$-\frac{9}{8}\lambda^5 \sum_{i_0=-\infty}^{\infty}\sum_{i_1=-\infty}^{\infty}\sum_{i_2=-\infty}^{\infty}\sum_{i_3=-\infty}^{\infty} |i_1-i_0|^{-\alpha}|i_2-i_0|^{-\alpha}|i_3-i_0|^{-2\alpha}|i_2-i_1|^{-\alpha} \,. \tag{3.34}$$

However, doing this summation, we would double-count each configuration because swapping sites i_1 and i_2 the embedding on the lattice looks exactly the same (see again Figure 3.3). To account for this two-fold symmetry of graph $\mathscr{G}_{60}$ it is necessary to add a factor $\frac{1}{2}$

$$-\frac{1}{2}\frac{9}{8}\lambda^5 \sum_{i_0=-\infty}^{\infty}\sum_{i_1=-\infty}^{\infty}\sum_{i_2=-\infty}^{\infty}\sum_{i_3=-\infty}^{\infty} |i_1-i_0|^{-\alpha}|i_2-i_0|^{-\alpha}|i_3-i_0|^{-2\alpha}|i_2-i_1|^{-\alpha} \tag{3.35}$$

$$= -\lim_{N\to\infty}\frac{9}{16}N\lambda^5 \sum_{i_1=-\infty}^{\infty}\sum_{i_2=-\infty}^{\infty}\sum_{i_3=-\infty}^{\infty} |i_1|^{-\alpha}|i_2|^{-\alpha}|i_3|^{-2\alpha}|i_2-i_1|^{-\alpha} \,. \tag{3.36}$$

We used the translational invariance of the expression to get rid of one sum by setting $i_0 = 0$. Effectively, it is summed over all distances between vertices connected via an edge with the starting vertex fixed in the origin. Dividing the expression by N, we obtain the contribution of graph $\mathscr{G}_{60}$ to the ground-state energy *per site*

$$e_{0,\mathscr{G}_{60}} = -\frac{9}{16}\lambda^5 \sum_{i_1=-\infty}^{\infty}\sum_{i_2=-\infty}^{\infty}\sum_{i_3=-\infty}^{\infty} |i_1|^{-\alpha}|i_2|^{-\alpha}|i_3|^{-2\alpha}|i_2-i_1|^{-\alpha} \,. \tag{3.37}$$

The same concept can then be applied to different QP sectors, always yielding nested sums as the one above. The sums become more and more complex in higher orders. The larger amount of vertices in the maximally sized graphs immediately leads to a higher dimension of the nested sum. Additionally, one needs to consider the lattice dimension: For a two-dimensional, e. g., square lattice, the dimension of each expression is doubled, because for each vertex a summation in two directions needs to be done.

For long-range models the translational invariance can be exploited to diagonalize the 1-QP block of the Hamiltonian by Fourier-transforming the expression. This results in a cosine expressions within the nested sum for a lattice with a single site per unit cell and exponential expressions for lattices with multiple sites per unit cell.

For non-translational-invariant models, e. g., if disorder is present, the complete 1-QP block of the matrix needs to be diagonalized. For these systems only finite lattices can be studied [HWS18].

3.2 COMPUTATION OF NESTED INFINITE SUMS

The embedding scheme introduced with the White-Graph Expansion [CS15] and applied to long-range interactions gives rise to matrix elements in the form of nested infinite sums as discussed before. From these matrix elements an analytically exact expression for the 1-QP gap can be derived up to a given order. However, the infinite sums, now present in the coefficients of the energy gap's series, while exact, still remain to be evaluated. This is not an easy task and there is no obvious way to tackle the problem.

I implemented and compared several schemes for a calculation of these sums. In this section I give an overview of these methods and motivate which one turned out to be best suited for my specific needs.

3.2.1 *Exact solutions*

For low-dimensional nested sums there are some analytic expressions for their numerical values known (cf. [Bor13]). This allows expressing the ground-state energy and 1-QP gap of the ferro- and antiferromagnetic 1D Ising chain up to second order exactly. For the 2D Ising model on a square lattice the first order of these expressions can be expressed analytically. The results are shown in a later chapter. The calculation of higher-order terms and terms on higher-dimensional lattices need to be done by numerical algorithms.

3.2.2 *The structure of the nested sums*

Let us have a look at the general structure of the nested sums. In Section 3.1.6 an example for the contribution to the 0-QP coefficient of Graph $\mathcal{G}_{60}$ was derived. The sums become even more involved when non-local hopping terms in the 1-QP sector are studied. In general the sums for a hopping from $\boldsymbol{i}$ to $\boldsymbol{j}$ on graph $\mathcal{G}$ can be written in the form

$$h_{\mathcal{G}}^{\boldsymbol{i}\to\boldsymbol{j}} := \sum_{a} f_{\mathcal{G}}^{\boldsymbol{i}\to\boldsymbol{j}}(c)\,, \tag{3.38}$$

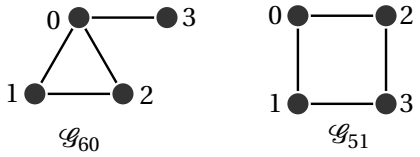

Figure 3.5: Illustration of graph $\mathcal{G}_{51}$ and $\mathcal{G}_{60}$ with a canonical labeling.

where the sum runs over all configurations $c = \{\boldsymbol{i}_0, \ldots, \boldsymbol{i}_{N_\mathcal{G}-1}\}$ with non-overlapping vertices obtained by placing the $N_\mathcal{G}$ vertices of graph $\mathcal{G}$ on a given lattice. The function over which the summation takes place is given as

$$f_\mathcal{G}^{\boldsymbol{i}\to\boldsymbol{j}}(c) := s_\mathcal{G}^{-1} \sum_p C_{\boldsymbol{i},\boldsymbol{j}}^{\mathcal{G},p} \left(\prod_{\boldsymbol{\ell}} g^{n_{p,\boldsymbol{\ell}}}(\boldsymbol{\ell}) \right) \exp\left[-\mathrm{i}\boldsymbol{k}\cdot(\boldsymbol{j}-\boldsymbol{i})\right], \tag{3.39}$$

where the product over $\prod_{\boldsymbol{\ell}}$ is taken over all links $\boldsymbol{\ell} = \boldsymbol{\xi} - \boldsymbol{\tau}$ with $\boldsymbol{\xi}$ and $\boldsymbol{\tau}$ being vertices belonging to an edge in graph $\mathcal{G}$. The function $g^{n_p,\boldsymbol{\ell}} \equiv |\boldsymbol{\xi} - \boldsymbol{\tau}|^{-n_{\boldsymbol{\ell},p}\alpha}$ with exponent $n_{p,\boldsymbol{\ell}} \in \mathbb{N}$ being the number of times the operator represented by the edge has been used in the PCUT calculation. $C_{\boldsymbol{i},\boldsymbol{j}}^{\mathcal{G},p} \in \mathbb{C}$ is the pth-order contribution to the matrix element from the PCUT calculation for a hopping from the vertex labeled $\boldsymbol{i}$ to vertex $\boldsymbol{j}$ and $s_\mathcal{G}$ is the graph's symmetry number used to prevent overcounting due to a symmetrical graph embedding. For each graph and hopping element multiple contributions with different sets of exponents $n_{\boldsymbol{\ell},p}$ can contribute which makes the sum over p necessary.

As an example, consider the hopping from vertex 0 to vertex 1 in canonical labeling of graph $\mathcal{G}_{51}$ (see Figure 3.5) in order 5 in the embedded form

$$h_{\mathcal{G}_{51}}^{O(5),0\to1} = -\frac{9}{128}\lambda^5 \sum_{\boldsymbol{i}_1}{}' \sum_{\boldsymbol{i}_2}{}' \sum_{\boldsymbol{i}_3}{}' |\boldsymbol{i}_1|^{-2\alpha} |\boldsymbol{i}_2|^{-\alpha} |\boldsymbol{i}_3 - \boldsymbol{i}_1|^{-\alpha} |\boldsymbol{i}_3 - \boldsymbol{i}_2|^{-\alpha} \exp(-\mathrm{i}\boldsymbol{k}\boldsymbol{i}_1) \tag{3.40}$$

where the prime at the sums indicates that $\mathbf{0}$ and all other configurations with overlapping vertices are excluded. Comparing the sum to the general form of Equation (3.38), we see that the sum over p gives only a single contribution with the element $C_{\boldsymbol{i}_0,\boldsymbol{i}_1}^{\mathcal{G}_{51},0} = -9/16$ while the graph supports $s_{\mathcal{G}_{51}} = 8$ symmetric labellings. The structure of the lattice is undetermined in the expression, so the sums run over all lattice sites, while $\boldsymbol{k}$ is the quasimomentum after Fourier transformation. For a lattice with a single spin per unit cell the hopping term could be combined with the inverse hopping element $h_{\mathcal{G}_{51}}^{O(5),1\to0}$ such that in the sum of both the exponentials can be reduced to a cosine. For lattices with larger unit cells where the Fourier transformation does not diagonalize the 1-QP block, both are separate matrix elements and therefore need to be computed separately.

Both matrix elements which have been presented up to now are representative of the nested sums (cf. Equations (3.33) and (3.40)). The sums run over lattice sites in a way that

no two vertices overlap. Each of the perturbation parameters, which are equivalent to the graph's edges, transforms into a long-range term with algebraic decay. The non-local hopping matrix elements show an exponential dependency on the quasi momentum and the hopping distance.

For terms with no $\boldsymbol{k}$ dependence the sums are geometric series which diverge for $\alpha \leq d$ in dimension d. This is always the case for the ground-state energy and local hopping terms in the 1-QP sector. Non-local 1-QP matrix elements with an exponential dependency do not have this limitation on α. For $\boldsymbol{k} = (\pi, \ldots, \pi)^T$ the sum gets an alternating sign and should converge for $\alpha > 0$.

There is (to my knowledge) no generic analytical solution to such a sum[3]. However, we know that the single terms of the sum get smaller with the distance between the vertices. Therefore, as a first step, we can have a look at the convergence behavior of the partial sums.

3.2.3 *Convergence analysis of partial nested multi sums*

As we presented in [FS16], as a first approximation to the correct value of the nested sums, we start summing from the smallest vertex distances because the summand are largest there. Since it is impossible to add up all infinite terms we stop the summation at a finite value $\mathcal{N}$. In 1D the sum over all configurations a as defined in Equation (3.38) becomes

$$h^{\boldsymbol{i}\to\boldsymbol{j}}_{\mathcal{G},\mathcal{N}} := \sum_{i_1=-\mathcal{N}}^{\mathcal{N}\prime} \sum_{i_2=-\mathcal{N}}^{\mathcal{N}\prime} \cdots \sum_{i_{N_\mathcal{G}-1}=-\mathcal{N}}^{\mathcal{N}\prime} f^{\boldsymbol{i}\to\boldsymbol{j}}_{\mathcal{G}}(c)\,, \tag{3.41}$$

where the primed sum excludes overlapping vertices. I omit the index for the PCUT order here to keep the notation more readable but the reader should be aware that the coefficients need to be calculated for each order separately. For higher dimensions the same principle holds but additional coordinates would need to be added. In practice, it is inconvenient to compute the sum for every matrix element on every possible graph. Therefore, I cluster the calculations of all matrix elements for all graphs with the same number of vertices. This directly implies that the number of nested sums is the same and the expression can be written as

$$S^{\mathcal{N}}_{N_\mathcal{G}} := \sum_{\mathcal{G}} \sum_{\boldsymbol{i}=\boldsymbol{i}_0}^{\boldsymbol{i}_{N_\mathcal{G}-1}} \sum_{\boldsymbol{j}=\boldsymbol{i}_0}^{\boldsymbol{i}_{N_\mathcal{G}-1}} h^{\boldsymbol{i}\to\boldsymbol{j}}_{\mathcal{G},\mathcal{N}}\,, \tag{3.42}$$

3 For orders 1 and 2 the sums are less involved and can be calculated analytically for the TFIM with long-range interactions in one dimension. This is shown in a later chapter.

where the sum $\sum_{\mathcal{G}}$ runs over the contributions of all graphs with $N_{\mathcal{G}}$ vertices. Taking the sum of all partial sums for the contributing graph sizes

$$p_r^{\mathcal{N}} := \sum_{N_{\mathcal{G}}} S_{N_{\mathcal{G}}}^{\mathcal{N}} \tag{3.43}$$

allows to extrapolate the value of the series coefficients p_r in the $\mathcal{N} \to \infty$ limit as discussed in the next sections.

For the study of second-order phase transitions, the 1-QP gap is an important quantity which allows the extraction of the critical point and the critical exponent $z\nu$. To compute the quantity directly, the ground-state energy can be subtracted from the diagonal (local) 1-QP matrix elements.

$$f_{\mathcal{G}}^{\boldsymbol{i}\to\boldsymbol{j}}(c) := \begin{cases} s_{\mathcal{G}}^{-1} \sum_p C_{\boldsymbol{i},\boldsymbol{j}}^{\mathcal{G},p} \left(\prod_{\boldsymbol{\ell}} g^{n_{p,\boldsymbol{\ell}}(\boldsymbol{\ell})}\right) \exp\left[-\mathrm{i}\boldsymbol{k}\cdot(\boldsymbol{j}-\boldsymbol{i})\right], & \text{for } \boldsymbol{i} \neq \boldsymbol{j} \\ s_{\mathcal{G}}^{-1} \sum_p C_{\boldsymbol{i},\boldsymbol{j}}^{\mathcal{G},p} \left(\prod_{\boldsymbol{\ell}} g^{n_{p,\boldsymbol{\ell}}(\boldsymbol{\ell})}\right) - s_{\mathcal{G}}^{-1} \sum_p C_{0\mathrm{qp}}^{\mathcal{G},p} \left(\prod_{\boldsymbol{\ell}} g^{n_{p,\boldsymbol{\ell}}(\boldsymbol{\ell})}\right), & \text{for } \boldsymbol{i} = \boldsymbol{j}\,. \end{cases} \tag{3.44}$$

In the following, first, I show the possibility of extrapolating the finite sums using the Wynn algorithm [Wyn56]. Second, the finite sums are analyzed with a proper scaling function to obtain the approximate sum value in the $\mathcal{N} \to \infty$ limit. Both is presented for the 1D Ising chain for both, a ferro- and an antiferromagnetic interaction, while it has proven to provide an insufficient accuracy for higher-dimensional systems. Also for small values of α the Markov-chain Monte Carlo method discussed later in this chapter proved to be a superior approach.

We found that the finite sums of the gap for a ferromagnetic interaction located at momentum $k = 0$ converges monotonously against the final value, while the sums for an antiferromagnetic interaction which is located at $k = \pi$ fluctuate around the final value after a threshold value of $\mathcal{N}$. Consequently, the convergence of the series coefficients p_r for the antiferromagnetic interaction converges much better than those of the ferromagnetic interaction.

3.2.3.1 *Wynn's ε method*

The ε method first introduced 1956 by Peter Wynn [Wyn56] is a method for convergence acceleration of slowly converging sums. With partial sums S_n the iterative algorithm is given as

$$\varepsilon_{k+1}(S_n) = \varepsilon_{k-1}(S_{n+1}) + \frac{1}{\varepsilon_k(S_{n+1}) - \varepsilon_k(S_n)}\,, \tag{3.45}$$

with $\varepsilon_0(S_n) = S_n$ and $\varepsilon_{-1}(S_n) = 0$.

For an extrapolation of the series coefficients, we consider a monotonically converging series of data points which is realized by using only every second point of the antiferromagnetic series of partial sums $p_r^{\mathcal{N}}$, with $\mathcal{N} \in [1, \mathcal{N}_{\max}]$ [FS16]. The extrapolations are done by starting from a small subset of partial sums $(p_r^1, \ldots, p_r^{\mathcal{N}})$, increasing $\mathcal{N}$ up to the maximum available boundary $\mathcal{N}_{\max}$, to obtain a set of extrapolations with an increasing data base. This allows us to check the convergence of the extrapolation in the following way: Initially the extrapolation of subsets show a wildly fluctuating behavior. This is most probable due to the complexity of the extrapolated sum which consists of a large amount of contributions from many hopping elements of various graphs. With increasing $\mathcal{N}$ the contributions of certain graphs become dominant as discussed in the next section and the fluctuations get smaller. To obtain a prediction for the series coefficient we average over the extrapolated values where the fluctuations settle and estimate the remaining error by calculating their standard deviation.

3.2.3.2 *Deriving scaling functions for the extrapolation of partial sums*

In the previous section we already introduced an extrapolation scheme for the truncated infinite sums to approximate the correct value for $\mathcal{N} \to \infty$. Now we discuss a systematic scaling behavior with $\mathcal{N}$ for the coefficients p_r which are a sum of all contributions from many differently behaving nested infinite sums, like we presented in [FS16]. Indeed, we find a scaling which is similar to a product of Riemann zeta functions, but different for a ferromagnetic and an antiferromagnetic interaction. This scaling can be applied to the numerical data of truncated sum values $p_r^{\mathcal{N}}$ to extract a comparison value to the Wynn extrapolation. We even find this scheme to give better results than the Wynn extrapolation although we will see later on that the introduction of Markov-chain Monte Carlo techniques does improve the result.

We divide the section into a part discussing the derivation of the scaling function for a ferromagnetic and an antiferromagnetic interaction.

Ferromagnetic case. The 1-QP gap for a ferromagnetic interaction is located at momentum $k = 0$. Inserting this value in the exponential in Equation (3.39) we find that the summands for single matrix elements have no alternating signs anymore. As a result, the total sum of all contributions for the partial sums of each p_r shows a monotonic convergence.

First, let us consider a single partial harmonic sum

$$\sum_{\delta=1}^{\mathcal{N}} \frac{1}{\delta^{\alpha}} \,. \tag{3.46}$$

By definition, for $\mathcal{N} \to \infty$ the sum converges to the Riemann zeta function. To study the asymptotics of the partial sum, we study the difference to the exact result

$$\sum_{\delta=\mathcal{N}+1}^{\infty} \frac{1}{\delta^\alpha} = \zeta(\alpha) - \sum_{\delta=1}^{\mathcal{N}} \frac{1}{\delta^\alpha} \,. \tag{3.47}$$

Approximating the remainder sum by an integral, for large $\mathcal{N}$ the equation becomes

$$\int_{\mathcal{N}+1}^{\infty} \mathrm{d}\delta \, \frac{1}{\delta^\alpha} = \frac{(\mathcal{N}+1)^{-\alpha+1}}{-\alpha+1} \approx \frac{\mathcal{N}^{-\alpha+1}}{-\alpha+1} \,. \tag{3.48}$$

For the moment, let us assume a nested sum with summands of independent summation indices such that they factorize into a product of harmonic sums

$$\left(\sum_{\delta_1=1}^{\mathcal{N}} \frac{1}{{\delta_1}^\alpha}\right)\left(\sum_{\delta_2=1}^{\mathcal{N}} \frac{1}{{\delta_2}^\alpha}\right)\cdots\left(\sum_{\delta_m=1}^{\mathcal{N}} \frac{1}{{\delta_m}^\alpha}\right) , \tag{3.49}$$

for a product over m edges. Using the scaling $\zeta(\alpha) + \frac{\mathcal{N}^{-\alpha+1}}{-\alpha+1}$ derived in Equation (3.48), the product's leading term reads

$$\zeta(\alpha)^m + m\zeta(\alpha)\frac{\mathcal{N}^{-\alpha+1}}{-\alpha+1} + \dots \,. \tag{3.50}$$

The important thing to notice is that the scaling exponent $(1-\alpha)$ is *independent* of the number of sums m. A sum of differently sized nested sums is therefore expected to show the same scaling behavior. In practice, the series coefficients p_r do not consist purely of sums that can be factorized in this way. However, several contributions can indeed be rewritten in the form of Equation (3.49). Additionally, the chain graph which has the largest number of sums for a given order can always be decomposed in such a way. Numerically, we find a good agreement of the function with our data confirming the approach's validity as shown below.

Antiferromagnetic case. Setting the momentum k to the gap location $k = \pi$, the nested sums become alternating[4] and consequently show a different scaling behavior than in the ferromagnetic case. Again, we start from a single, although in this case alternating, partial sum

$$\sum_{\delta=1}^{\mathcal{N}} (-1)^\delta \, \frac{1}{\delta^\alpha} \,. \tag{3.51}$$

4 Compare, e. g., to the matrix element in Equation (3.40) which, in combination with its inverse hopping, yields a cosine in the summand.

In the limit $\mathcal{N} \to \infty$ the value is known to be $\xi(\alpha) := -2^{-\alpha}\,(2^\alpha - 2)\,\zeta(a)$ which we use to determine the leading asymptotics for large $\mathcal{N}$ by considering the remainder as the difference

$$\sum_{\delta=\mathcal{N}+1}^{\infty} (-1)^\delta \frac{1}{\delta^\alpha} = \xi(\alpha) - \sum_{\delta=1}^{\mathcal{N}} (-1)^\delta \frac{1}{\delta^\alpha}\,. \tag{3.52}$$

The alternating sum can be transformed into a monotonically converging sum by combining the even positive and the odd negative elements

$$\sum_{\delta=\mathcal{N}+1}^{\infty} (-1)^\delta \frac{1}{\delta^\alpha} = \sum_{\delta=\frac{\mathcal{N}}{2}+1}^{\infty} \left(\frac{1}{(2\delta)^\alpha} - \frac{1}{(2\delta-1)^\alpha} \right), \tag{3.53}$$

where $\mathcal{N}$ is assumed to be even. For large enough $\mathcal{N}$ it is reasonable to approximate the second term of the summand by the Taylor series expansion

$$(2\delta-1)^{-\alpha} \approx (2\delta)^{-\alpha} \left(1 + \frac{\alpha}{2\delta} + \dots\right) \tag{3.54}$$

so we can take the sum over $\alpha/(2\delta)$. After replacing the sum by an integral the scaling behavior

$$\int_{\frac{\mathcal{N}}{2}+1}^{\infty} \mathrm{d}\delta\, \frac{\alpha}{(2\delta)^{\alpha+1}} = -\alpha \frac{\left(\frac{\mathcal{N}}{2}+1\right)^{-\alpha}}{2^{\alpha+1}} \approx -\frac{\alpha}{2} \mathcal{N}^{-\alpha} \tag{3.55}$$

is obtained. For a product of m independent sums the leading scaling behavior is given by

$$\xi(\alpha)^m - m\frac{\alpha}{2}\xi(\alpha)\,\mathcal{N}^{-\alpha} + \dots\,, \tag{3.56}$$

as was already discussed for a ferromagnetic interaction. The scaling exponent is again independent of the number of graph edges m of all contributions to the coefficient p_r if they have independent summations. We also checked numerically that for large $\mathcal{N}$ the scaling is valid for the series coefficients p_r. Exemplary results of the scaling is shown together with Wynn extrapolations in the next section.

3.2.3.3 *Demonstration of Wynn extrapolation and scaling*

Here, we compare the extrapolation and scaling schemes for the series coefficients p_r discussed above for several exemplary series coefficients for $\alpha = 1.5$. For a fixed order r the contributions of all matrix elements for the graphs with all possible number of vertices are summed up to an upper boundary $\mathcal{N}$. These partial sums $p_r^{\mathcal{N}}$, shown as green circles in Figure 3.6 are grouped to subsets and Wynn-extrapolated as discussed above. The

Wynn extrapolations are shown as yellow crosses while an average of the extrapolations is illustrated by a dashed black line together with its standard deviation in gray. For large $\mathcal{N}$ the bare partial sums are expected to show a linear behavior when plotted against $\mathcal{N}^{-\alpha}$ ($\mathcal{N}^{-(\alpha-1)}$) for an antiferromagnetic (ferromagnetic) interaction. Figure 3.6 clearly shows the expected behavior. The scaling is used to estimate the value of p_r in the $\mathcal{N} \to \infty$ limit by fitting a line through the two partial sums with the highest maximum boundary $p_r^{\mathcal{N}_{\max}}$ and $p_r^{\mathcal{N}_{\max}-1}$. For most of the coefficients both approaches are in good agreement. Due to the fluctuations in the Wynn extrapolation and considering the curvature of the partial sums the scaling seems to work slightly better.

3.2.4 *Monte-Carlo sampling*

The sums we want to evaluate are high-dimensional since with increasing perturbation order the maximum number of vertices in a graph increases as well. For each vertex a sum over all lattice positions must be introduced into the expression. For example, in order eight there are contributions of a graph with nine sites which, for a two-dimensional lattice, corresponds to a summation in 18 dimensions! Solving these high-dimensional sums numerically is not trivial. The algorithms which have been described previously failed to converge well-enough for such cases, so we decided to apply the method of Monte Carlo (MC) summations. With doing so we coincidentally follow the opinion of A. Sokal:

> » Monte Carlo is an extremely bad method; it should be used only when all alternative methods are worse. « (Sokal [Sok97])

The term *Monte-Carlo summation* is used analogously to "Monte-Carlo integration", which describes the numerical integration using random numbers. Since we are concerned with sums over discrete numbers instead of continuous variables, I emphasize this fact by explicitly speaking of summations although the main idea is the same:

Instead of evaluating the integrand on a regular grid during the numerical integration [Pre+07], Monte-Carlo techniques use a randomly sampled grid. The idea is that more important parts of an integral are sampled in higher detail than other parts in a statistical, non-deterministic fashion. We know that Monte-Carlo methods scale well with dimension since the standard error of the mean, which convergences to the exact integral value, decreases as $1/\sqrt{N}$ with the number of samples N independent of the dimension [Pre+07]. Therefore, they are especially well suited for the evaluation of our high-dimensional nested sums.

Let me shortly summarize the idea of Monte-Carlo summation before providing more details on the specific problem at hand including the resulting difficulties and our solutions. A nice introduction to and overview over Monte-Carlo methods can be found

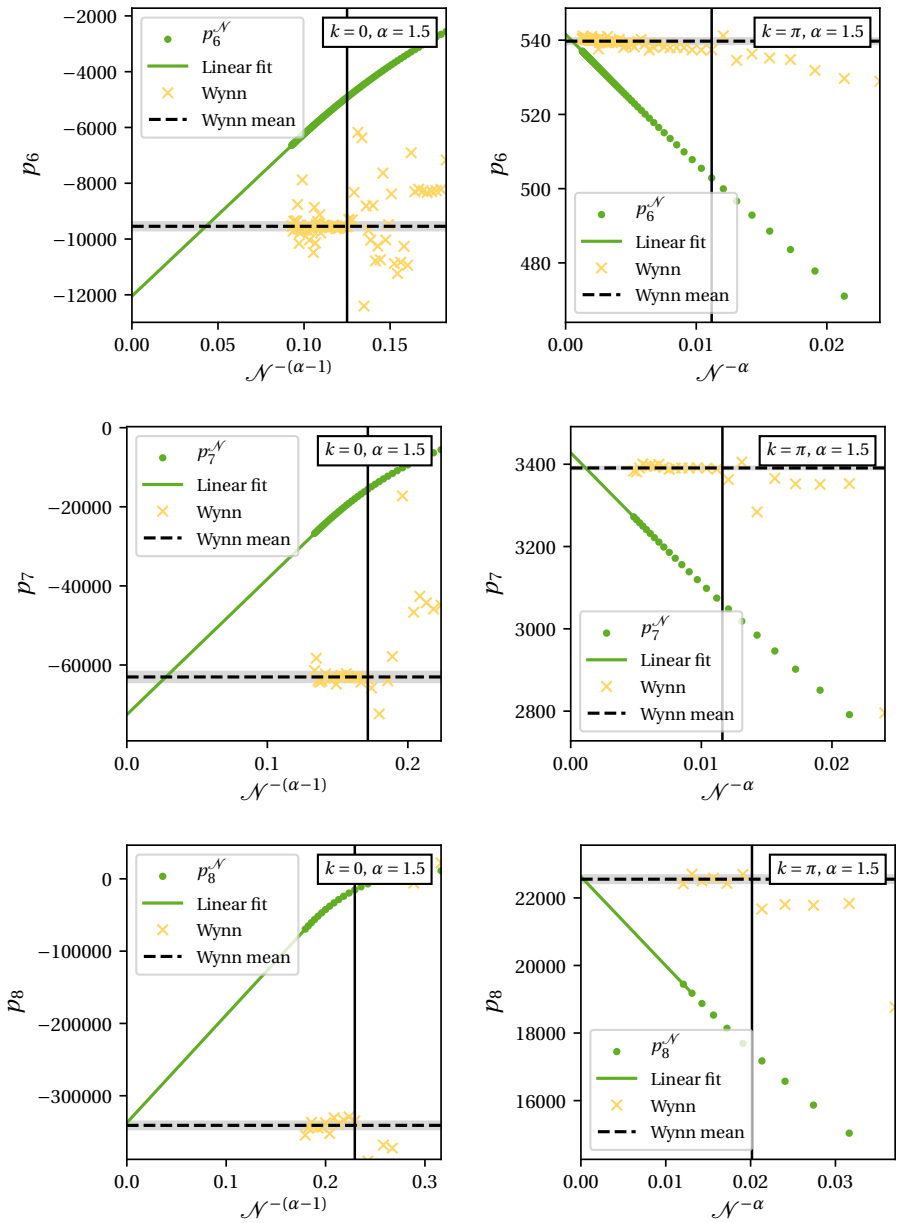

Figure 3.6: A comparison of the Wynn extrapolation values (yellow crosses) and the scaling (green line) of partial sums (green circles) for the series coefficient $p_r^{\mathcal{N}}$ for the ferro- ($k = 0$) and antiferromagnetic ($k = \pi$) interaction . The Wynn extrapolation average over values starting from minimal boundary $\mathcal{N}_{\text{av,min}}$ (indicated by a vertical black line up to $\mathcal{N}_{\text{max}}$) is shown as a black dashed line with the standard deviation in gray. For higher orders it becomes computationally challenging to push the maximum boundary of the partial sums.

in Werner Krauth's book titled *"Statistical Mechanics: Algorithms and Computations"* [Krao6]. An illustrative example for a Monte-Carlo integration, taken from above book, is the task of finding the value of π. Imagine a circle within a square (Figure 3.7). The square has such a size that pebbles can be randomly thrown inside the square. Afterwards the number of pebbles that end up within the circle are counted and compared to the total number of thrown pebbles. You find that that the ratio approaches $\pi/4$ for an increasing number of thrown pebbles.

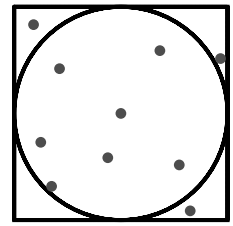

Figure 3.7: Randomly sampled circle.

In general, there are two basic concepts of obtaining samples (i. e., a set of random positions): *Direct sampling* and *Markov-chain sampling*. Both can be understood by the pebble-throwing example: The method described above is called *direct sampling* because each new pebble position is chosen independently of the previous positions. In our example this works as long as the square's area is small enough to reach all possible positions with a single throw of a pebble. However, if you can't cover the complete area you may switch to a different approach that is called Markov-chain sampling.

Imagine you throw a pebble into the square. Now, from that position you pick up the pebble, rotate about a random angle and throw the pebble again. This way you are also able to sample the complete area of the square. One immediately visible difference to direct sampling is in the correlation time. While for the direct approach each throw is independent of the previous throws and the correlation time is therefore zero, performing a Markov-chain sampling means taking a new sample based on the current state of the system. This dependence of newly created samples on the previous ones obviously increases the correlation time! Note, that a new configuration in a Markov chain only depends on the information of the previous step. Earlier configurations do not factor in the probability of generating a new configuration.

In the following I will introduce some nomenclature for the MC summation as well as the final design choices used for the algorithm in this thesis. In the Appendix I will elaborate more on approaches which *did not* work, one, for the sake of completeness and two, to prevent others from taking the same route and failing again.

3.2.4.1 *General setup of the Metropolis-Hastings Markov-Chain Monte Carlo summation*

The nested infinite sums run over all positions on a given lattice for each vertex of a given graph. A single configuration, meaning a single set of lattice positions of all $N_{\mathcal{G}}$ vertices $\boldsymbol{s}_v$, $v \in [0, N_{\mathcal{G}} - 1]$ of a graph $\mathcal{G}$ is denoted by

$$c = \{\boldsymbol{s}_v\} \tag{3.57}$$

in the following. For this general introduction, the summand which in our case results from the PCUT calculation is called $h_{N_\mathcal{G}}(c)$ and contains contributions of all graphs with the same number of vertices in a given order. For clarity, an index for the order is omitted in the notation in this section. Using this nomenclature, the total sum is thus written as

$$S_{N_\mathcal{G}} = \sum_c h_{N_\mathcal{G}}(c) \,. \tag{3.58}$$

We can rewrite the sum as an average

$$S_{N_\mathcal{G}} = \sum_c \frac{Z}{\pi(c)} \frac{\pi(c)}{Z} h_{N_\mathcal{G}}(c) = Z \left\langle \frac{h_{N_\mathcal{G}}(c)}{\pi(c)} \right\rangle_\pi \tag{3.59}$$

by introducing a convenient probability distribution $\pi(c)$ and the associated partition function

$$Z = \sum_c \pi(c) \,. \tag{3.60}$$

The fraction $\pi(c)/Z$ expresses the probability for configuration c in the expected value. To get rid of the unknown value of the partition function Z it is possible to introduce a reference sum

$$S^{\text{ref}}_{N_\mathcal{G}} = \sum_c h^0_{N_\mathcal{G}}(c) = Z \left\langle \frac{h^0_{N_\mathcal{G}}(c)}{\pi(c)} \right\rangle_\pi \,, \tag{3.61}$$

with a reference function $h^0_{N_\mathcal{G}}(c)$ and the same $\pi(c)$. The reference function and therefore the reference sum can, in principle, be chosen arbitrarily but it should have a considerable contribution[5] and a similar asymptotic form as $h_{N_\mathcal{G}}(c)$. Also, the value $S^{\text{ref}}_{N_\mathcal{G}}$ of the reference sum should be known analytically to prevent the introduction of unnecessary additional errors in the calculation. Using the reference sum (3.61), the partition function can be eliminated from Equation (3.59)

$$S_{N_\mathcal{G}} = Z \left\langle \frac{h_{N_\mathcal{G}}(c)}{\pi(c)} \right\rangle_\pi = \frac{\left\langle \frac{h_{N_\mathcal{G}}(c)}{\pi(c)} \right\rangle_\pi}{\left\langle \frac{h^0_{N_\mathcal{G}}(c)}{\pi(c)} \right\rangle_\pi} S^{\text{ref}}_{N_\mathcal{G}} \,. \tag{3.62}$$

Both expected values are calculated in the same loop in the MC sampling and converge to their respective exact result. The difficult problem of calculating the high-dimensional sums has been shifted to a sampling of configurations. What is still missing are two

5 This means that most configurations c of the configuration space should give a value in the reference function.

things: The exact form of the reference sum for the MC calculations of the LRTFIM is discussed in the next section. Afterwards the generation of samples, i. e., of vertex positions on the lattice, is discussed in Section 3.2.4.3. But before finishing this section, let us introduce the Metropolis-Hastings Markov Chain which will be important for the sampling and used in our calculations.

During the sampling new configurations are proposed in each step using the generalized Metropolis-Hastings Markov-chain Monte Carlo (MCMC) method [Met+53; Has70]. The vertices can be seen as random walkers moving randomly around the lattice while configurations with a higher contribution to the target sum are assigned higher probabilities. If the current configuration of the system is called a and configuration b is a newly proposed state, the acceptance probability of the new configuration is given as

$$p_{\text{acc}} = \min\left(1, \frac{\pi(b)}{\mathscr{A}(a \to b)} \frac{\mathscr{A}(b \to a)}{\pi(a)}\right) . \tag{3.63}$$

The function $\mathscr{A}(a \to b)$ describes the *a-priori*probability to propose a move from configuration a to b ($\mathscr{A}(b \to a)$ is the probability of the inverse move) while $\pi(c)$ is the weight of state c. The chosen acceptance probability fulfills the *detailed balance* condition which requires each transition $a \to b$ to be reversible for each pair of states a and b [Has70].

This setup describes the general summation scheme. For the practical application to a concrete problem we need to define two things: We need to choose an appropriate, analytically solvable reference sum and we need to define the Markov-chain moves for the graph vertices.

3.2.4.2 *Reference sum*

For the Monte-Carlo summation it is necessary to know the value of the reference sum as exactly as possible. The value of the target sum is then calculated with respect to the known reference sum. We can again use the very illustrative example of sampling π by throwing pebbles into a circle: Here the area of the square represents the value of the reference integral. The ratio of the number of pebbles that land within the circle to those that land within the square is calculated during the sampling. Knowing the ratio and the reference size of the square then allows the extraction of the value of π.

The analytic knowledge of the reference sum is not the only important property. When sampling the state space the number of hits should be as high as possible. If only every billionth random configuration has a nonzero value in the reference sum the total number of samples must be extremely high to give a meaningful result. We choose a reference summand which has a similar asymptotics as the summand of the target sum

$$h^0_{N_g,\text{1D}}(c) = \prod_{v=0}^{N_g-2} |s_{v+1} - s_v|^{-\rho} , \tag{3.64}$$

for the 1D chain, where s_v are the positions of the *ordered* vertices, such that $s_v < s_{v+1}$. In 1D this sum can be evaluated analytically

$$S^{\text{ref,1D}}_{N_\mathcal{G}} = \sum_c h^0_{N_\mathcal{G},\text{1D}}(c) \tag{3.65}$$

$$= N_\mathcal{G}! \cdot \sum_{s_0<s_1} \sum_{s_1<s_2} \cdots \sum_{s_{N_\mathcal{G}-1}<s_{N_\mathcal{G}-2}} |s_0 - s_1|^{-\rho} \cdot |s_1 - s_2|^{-\rho} \cdots \left|s_{N_\mathcal{G}-1} - s_{N_\mathcal{G}-2}\right|^{-\rho} \tag{3.66}$$

$$= N_\mathcal{G}! \cdot \sum_{\delta_1=1}^{\infty} \sum_{\delta_2=1}^{\infty} \cdots \sum_{\delta_{N_\mathcal{G}}=1}^{\infty} |\delta_1|^{-\rho} |\delta_2|^{-\rho} \cdots \left|\delta_{N_\mathcal{G}}\right|^{-\rho} \tag{3.67}$$

$$= N_\mathcal{G}! \cdot [\zeta(\alpha)]^{N_\mathcal{G}-1} . \tag{3.68}$$

For the other lattices we use as a reference sum

$$h^0_{N_\mathcal{G}}(c) = \prod_{v=0}^{N_\mathcal{G}-2} \prod_{i=1}^{d} \left(1 + \left|\boldsymbol{s}_{v+1,i} - \boldsymbol{s}_{v,i}\right|\right)^{-\rho} . \tag{3.69}$$

The products run over all d components of the ordered distances of all vertex positions $\boldsymbol{s}_v$ in configuration c. By taking only edges $(\boldsymbol{s}_v, \boldsymbol{s}_{v+1})$, $v \in [0, N_\mathcal{G} - 2]$ of a given vertex order into account, the reference summand differs from the summand of the target integral where contributions of a large amount of different graphs and hopping elements factor in. This approximation is a compromise which is fast in the computational evaluation time and where the decoupling of the dimensions allows an analytical evaluation of the sum

$$S^{\text{ref}}_{N_\mathcal{G}} = \sum_c h^0_{N_\mathcal{G}}(c) = \left[(2\zeta(\rho) - 1\right]^{(N_\mathcal{G}-1)d} \tag{3.70}$$

while still providing the algebraically decaying asymptotics.

Another difference to the target sum is that configurations with overlapping vertices are explicitly allowed in the sum, such that every configuration contributes to the target integral. This gives the required high count in this sum state during sampling. The reference integral can be used in any dimension d and the parameter $\rho \in \mathbb{R}$ is a free parameter which can be tuned to improve the convergence of the MCMC summation.

3.2.4.3 *The sampling scheme*

For a sampling of the configuration space we use a Markov chain where the vertices are moved from their current position to new positions in a new configuration if the move is accepted according to the Metropolis-Hastings acceptance probability introduced in Equation (3.63). Sampling the configuration space should provide two things: On the one hand, each state must be reachable and a large part of the configuration space should

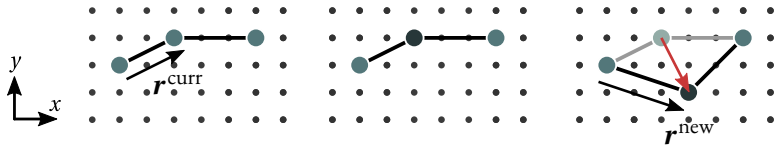

Figure 3.8: Illustration of a rift move. First, a vertex is randomly selected and the original difference to its neighbor vertex $\boldsymbol{r}^{\text{curr}}$ calculated. Second a new difference vector is calculated by drawing the elements of vector $\boldsymbol{r}^{\text{new}}$ from a ζ-distribution and the move is accepted with probability $p_{\text{acc}}^{\text{rift}}(c^{\text{curr}} \to c^{\text{new}})$. Edges between the vertices in this figure are randomly chosen just to visualize the graph.

be touched by the Markov chain. Therefore, it should be possible to have steps in the chain which allow for large movements of vertices on the infinite lattice. On the other hand, a fast convergence of the result requires spending more time in configurations that contribute stronger to the final integral (i. e., configurations where vertices are close to each other due to the summand being algebraically decaying with vertex distances). Here, a weighting of the proposed steps by their size proved helpful. At the same time, it is necessary to ensure a high acceptance rate: If a lot of proposed moves are rejected the system remains in the same configuration for a long time which obviously leads to a bad coverage of the configuration space. These considerations directly factor into the choice of two different kinds of moves that are discussed below.

The general structure of moves discussed here consists of a random selection of one or more vertices, calculating moves of one or more vertices by or to a randomly selected distance or position. For the generation of random numbers the *Mersenne-Twister* [MN98] was used.

The simplest imaginable random move is selecting a site randomly and moving it to some random position. This move fulfills the detailed balance condition and is in principle already sufficient for covering the complete configuration space. However, on the one hand a uniform distribution of positions is not possible since we are sampling the complete axis from $-\infty$ to $+\infty$ in each dimension. On the other hand, due to the nature of the summand, most of the sum's weight comes from those configurations where the vertices are separated by short distances. Proposed configurations with far-apart vertices would be declined mist if the time and the system would be stuck in a given configuration, leading to a slow convergence. The part of the configuration space with closely packed vertices should be sampled with a higher priority to ensure a faster convergence of the running mean of the MCMC summation to the target summand.

SINGLE-SITE RIFT MOVES For lattice unit cells containing a single spin site we implement three moves: We call the first move *(single-site) rift move* because it is able to

propose very large distances between vertices on the one hand and also close existing rifts between arbitrarily distant vertices. On the other hand, its asymptotics are based on the asymptotics of the target summand by drawing random numbers from a double-sided zeta distribution[6]. In the first step of this move a vertex $\boldsymbol{s}_{v_{\text{sel}}}$ is randomly selected from the set of vertices with a uniform distribution. Then the distance to a second randomly selected vertex $\boldsymbol{s}_{v'_{\text{sel}}}$ is calculated as

$$\boldsymbol{r}^{\text{curr}} = \boldsymbol{s}_{v'_{\text{sel}}} - \boldsymbol{s}_{v_{\text{sel}}} \tag{3.71}$$

Afterwards, each coordinate of the new distance $\boldsymbol{r}^{\text{new}}$ between the two selected vertices is drawn from a double-sided ζ-distribution which is given by the probability to get the value of the ith component r_i^{new}

$$p(r_i^{\text{new}}) = \frac{(1+|r_i^{\text{new}}|)^{-\gamma}}{2\zeta(\gamma)-1} \,. \tag{3.72}$$

For the proposed new configuration, the first selected vertex is moved by the difference of the old and new distance

$$\boldsymbol{s}_{v_{\text{sel}}} \to \boldsymbol{s}_{v_{\text{sel}}} + (r^{\text{new}} - r^{\text{curr}}) \,. \tag{3.73}$$

The adjustment of the exponent $\gamma \in \mathbb{R}$ of the ζ-distribution modifies the convergence behavior of the MCMC mean to the target-sum value. The rift moves respect the fact that configurations with vertices close to each other are sampled with a larger weight than those far away. The *a-priori* probability distribution from which the rift moves are sampled is given as

$$\mathscr{A}(c^{\text{curr}} \to c^{\text{new}}) = \mathscr{N}_\zeta \prod_{i=1}^{d} \left(1+|r_i^{\text{new}}|\right)^{-\gamma} \tag{3.74}$$

$$\mathscr{A}(c^{\text{new}} \to c^{\text{curr}}) = \mathscr{N}_\zeta \prod_{i=1}^{d} \left(1+|r_i^{\text{curr}}|\right)^{-\gamma} \tag{3.75}$$

with the normalization factor $\mathscr{N}_\zeta = [2\zeta(\gamma)-1]^{-d}$. Inserting them in Equation (3.63), the probability to accept the move from the current configuration c^{curr} to the configuration c^{new} with the newly drawn rift distance is calculated as

$$p_{\text{acc}}^{\text{rift}}(c^{\text{curr}} \to c^{\text{new}}) = \min\left(1, \frac{\pi(c^{\text{new}})}{\pi(c^{\text{curr}})} \cdot \frac{\left[\prod_{i=1}^{d}(1+r_i^{\text{new}})\right]^{\gamma}}{\left[\prod_{i=1}^{d}(1+r_i^{\text{curr}})\right]^{\gamma}}\right) . \tag{3.76}$$

An illustration of the rift move can be found in Figure 3.8.

6 The histogram and code for the double-sided zeta distribution can be found in Appendix C.2.

MULTI-SITE RIFT MOVES I found that to obtain a better convergence a second kind of rift moves proved helpful. The *multi-site rift move* is very similar to the previously discussed move but differs in the fact that not only one site is selected and moved to a random new position which is calculated using a zeta distribution. Instead, the position of the selected vertex $\boldsymbol{s}_{v_{\text{sel}}}$ is used as a reference position. Then the distance between the selected site and its neighbor is computed

$$\boldsymbol{r}^{\text{curr}} = \boldsymbol{s}_{v_{\text{sel}}+1} - \boldsymbol{s}_{v_{\text{sel}}} \tag{3.77}$$

As before, a new distance is drawn from a zeta distribution and in 1D every vertex v with $\boldsymbol{s}_v > \boldsymbol{s}_{v_{\text{sel}}}$ is shifted by the difference of the old and the new rift. In higher dimensions the vertices are labeled with increasing numbers and all vertices with a larger label than the randomly selected site $v > v_{\text{sel}}$ are shifted by the same distance to ensure the detailed balance condition. Different schemes of selecting vertices may be implemented and tested in future work.

This step is designed to overcome situations in which the graph is split in two clusters, where moving only a single site might have less of an effect than selecting multiple vertices and moving them towards the remaining vertices. The acceptance probability is the same as for a single-site rift move given in Equation (3.76). The move is illustrated for the 1D chain in Figure 3.9

(a) 1d decomposition. (b) Proposed multi-site rift move.

Figure 3.9: (a) Only moving single sites around leads to a decomposition of the graph. (b) To counter this, a new *multi-site rift move* is introduced which choses a random site, divides the graph into two subgraphs and moves one of the clusters by a random length.

SHIFT MOVES For very large exponents γ a clustering of vertices is preferred by the rift moves. However, the target summand has no contribution for states with overlapping vertices, i. e., edges of zero length. To ensure contributions to the target sum even for very large exponents γ, we introduce another move. The goal is to propose small fluctuations around the current configuration which have a proposal probability independent of the vertex distances. In this *shift move*, a vertex $\boldsymbol{s}_{v_{\text{sel}}}$ is randomly selected by drawing from a uniform distribution. For the selected vertex a translation by a distance $\boldsymbol{d}^{\text{shift}}$ where

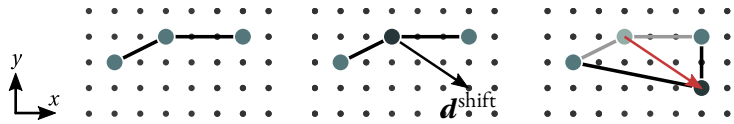

Figure 3.10: Illustration of a shift move. First, a vertex is randomly selected. Second the elements of vector $\boldsymbol{d}^{\text{shift}}$ are uniformly drawn from $[-N_{\mathcal{G}}, N_{\mathcal{G}}]$ and added to the position of the selected vertex. The move is accepted with probability $p_{\text{acc}}^{\text{shift}}(c^{\text{curr}} \to c^{\text{new}})$.

each component of the vector is uniformly drawn from $[-N_{\mathcal{G}}, N_{\mathcal{G}}]$ is proposed as a new configuration

$$\boldsymbol{s}_v^{\text{new}} = \begin{cases} \boldsymbol{s}_v + \boldsymbol{d}^{\text{shift}} & \text{if } v = v_{\text{sel}}, \\ \boldsymbol{s}_v & \text{otherwise.} \end{cases} \tag{3.78}$$

The acceptance probability for this move is simply given by

$$p_{\text{acc}}^{\text{shift}}(c^{\text{curr}} \to c^{\text{new}}) = \min\left(1, \frac{\pi(c^{\text{new}})}{\pi(c^{\text{curr}})}\right). \tag{3.79}$$

The proposed transition probabilities in Equation (3.63) cancel each other because $\mathscr{A}(c^{\text{curr}} \to c^{\text{new}}) = \mathscr{A}(c^{\text{new}} \to c^{\text{curr}})$ due to the fact that the translation is drawn from a uniform distribution.

To allow a considerable amount of rift moves in the simulation but dominantly keep the local shift moves which lead to new configurations with a high weight if such a configuration was realized before, we proposed rift moves with a probability of 0.3 in the implementation and shift moves with probability 0.7 for lattices with a single site per unit cell. For larger unit cells a third move needs to be introduced as discussed in Section 3.2.4.6.

During the development of the algorithm several different moves for single and multiple sites were tested. The problems that occurred with these moves and which lead to the final choice of MCMC moves are discussed in Appendix C.3.

3.2.4.4 *The probability distribution*

The choice of a probability distribution has a large impact on the final outcome of the summation. The probability distribution is chosen as

$$\pi(c) = \left\{[h^0_{N_{\mathcal{G}}}(c)]^2 + [w \cdot h_{N_{\mathcal{G}}}(c)]^2\right\}^{-1/2} \tag{3.80}$$

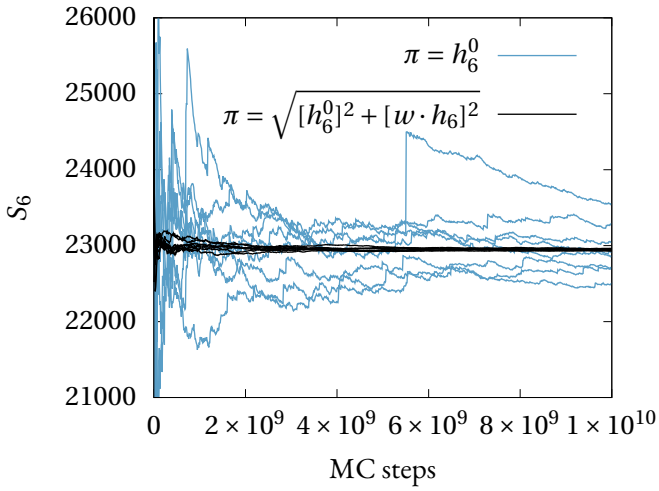

Figure 3.11: A comparison of different choices for $\pi(a)$ illustrates the effect of including the target summand into the weight. The running mean for eight different random-number generator (RNG) seeds is shown for using only the reference summand $\pi(a) = h_6^0(a)$ (blue) and a combination of reference and target summand $\pi(a) = \{[h_6^0(c)]^2 + [w \cdot h_6(c)]^2\}^{-1/2}$ (black). This is an example of sampling all contributions of graphs with six vertices to the LRTFIM on the square lattice for a ferromagnetic interaction and $\alpha = 4$.

for configuration c such that it incorporates both the reference summand $h_{N_g}^0(c)$ and the target summand $h_{N_g}^0(c)$ of the sum. The real-valued parameter w is determined by running the algorithm for several MC steps and determining an approximate ratio of the reference and target summand

$$w = \frac{\left\langle h_{N_g}^0(c) \right\rangle}{\left\langle h_{N_g}(c) \right\rangle} . \tag{3.81}$$

to ensure that reference and target summand contribute with a similar magnitude to the weight $\pi(c)$ of a proposed configuration c. The incorporation of both target and reference summand is necessary since we need to calculate the average of both to determine the target sum (see Equation (3.62)). With the above choice we are able to ensure a good convergence of the average of both the target and the reference sum to their respective value. At the same time, this choice allows to sample the important parts of the configuration space with higher priority. To illustrate the influence of the form of $\pi(a)$, a comparison to a different choice $\pi(a) = h_{N_g}^0(a)$ is given in Figure 3.11. In this

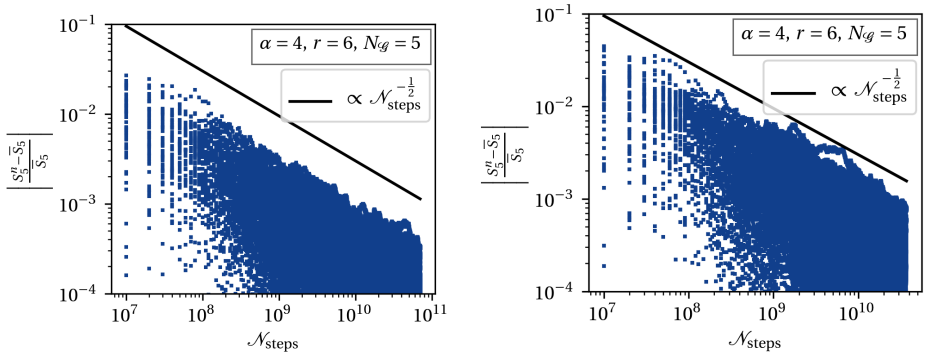

Figure 3.12: The relative error of the running average of the MCMC for $S_5[h]$ in order 6 is shown exemplarily for 50 seeds (blue dots) for (left) $k = 0$ and (right) $k = \pi$. The error is taken relative to the mean of over all runs. The solid black line illustrates the square-root dependency $(\mathcal{N}_{\text{steps}})^{-1/2}$ with the number of MC steps of the relative error.

figure the running mean of the Monte-Carlo summation for the $N_{\mathcal{G}} = 6$-vertex graph in order 8 for eight different RNG seeds is plotted against the number of MC steps. For the blue curves only the reference summand is considered in the MC weight. This choice results in strong fluctuations in the mean which in turn leads to a slow convergence to the exact result. Taking the value of the target summand $h_6(c)$ into account, the choice of the weight as $\pi(a) = \{[h_6^0(c)]^2 + [w \cdot h_6(c)]^2\}^{-1/2}$ leads to a much improved convergence with very little fluctuations. The running mean for the second choice of weight is shown as black lines.

3.2.4.5 *Monte-Carlo error*

The Monte-Carlo integration error is expected to decay as a square root with the number of steps

$$\left|\frac{S^n_{\mathcal{N}_{\mathcal{G}}}(\mathcal{N}_{\text{steps}}) - \overline{S}_{\mathcal{N}_{\mathcal{G}}}}{\overline{S}_{\mathcal{N}_{\mathcal{G}}}}\right| \propto {\mathcal{N}_{\text{steps}}}^{-1/2}, \tag{3.82}$$

where $S^n_{\mathcal{N}_{\mathcal{G}}}$ is the running average of the MCMC summation for seed n and $\overline{S}_{\mathcal{N}_{\mathcal{G}}}$ is the exact value. This expected behavior is exemplarily shown for different k in Figure 3.12 where the running average of MCMC summations for 50 different seeds is compared to a function decaying as ${\mathcal{N}_{\text{steps}}}^{-1/2}$. These curves are representative and show the typical behavior found in our calculations. One can see that the relative error shows the expected behavior with the number of MCMC calculation steps.

3.2.4.6 *Adapting the Monte-Carlo method to various lattice geometries*

The reference sum and sampling scheme described above can be used for any lattice in dimension $\boldsymbol{d}$ as long as single-site unit cells are considered. An extension of the approach to general regular lattices with larger unit cells is desirable. This can be done in the MC scheme by calculating single matrix elements of the Fourier-transformed effective Hamiltonian individually and diagonalizing the matrix afterwards. For lattices with more than a single site per unit cell such as, e. g., the Kagome or honeycomb lattice the algorithms needs to be slightly adapted. The good news is that rift and shift moves can still be used on a unit cell basis by moving a vertex between unit cells of the sampled distance while keeping the relative position within a unit cell. Also the reference integral can in principle be used by considering only the distance between the unit cells the vertices are located at. However, a movement of vertices within a unit cell needs to be allowed as well to sample all possible configurations on the lattice. To this end, we can rewrite the position of a vertex as

$$\begin{aligned} \boldsymbol{s}_\nu = \boldsymbol{r}_\nu + \boldsymbol{u}_\nu, \quad \text{with } \boldsymbol{r}_\nu = m_\nu \boldsymbol{e}_1 + n_\nu \boldsymbol{e}_2, \quad m_\nu, n_\nu \in \mathbb{Z}, \\ \boldsymbol{u}_\nu \in \{\boldsymbol{u}^0, \ldots, \boldsymbol{u}^{N_{\text{suc}}}\} \end{aligned} \tag{3.83}$$

for N_{suc} sites per unit cell. Vector $\boldsymbol{r}$ runs over all unit cells while $\boldsymbol{u}_\nu$ defines the offset within the unit cell. For the new move the proposal probabilities of the rift and shift move need to be adjusted. Since proposing a different sublattice for a vertex is also a local move, the shift probability is reduced to 0.4 while the rift probability is kept as 0.3. With the remaining probability of 30% we propose a move of a vertex within a unit cell. Modifying these probabilities might lead to a slightly changed dynamic in the moves but the impact on the convergence are hard to measure quantitatively. Therefore I chose proposal probabilities such that all moves are allowed with a considerable rate. The vectors $\boldsymbol{u}^i$ are a set of vectors that point to the lattice sites from the origin of the unit cell. For this move, first a vertex is randomly selected. The selection needs to be modified compared to single-site unit-cell systems: Since the effective Hamiltonian cannot be diagonalized directly by a Fourier transformation, which is executed with respect to the lattice vectors $\boldsymbol{r}_\nu$, we end up with an $N_{\text{suc}} \times N_{\text{suc}}$ matrix. The elements $h^{\text{eff}}_{i,j}$ of the Fourier-transformed effective Hamiltonian represent a hopping from sublattice i to sublattice j. To calculate a specific matrix element $h^{\text{eff}}_{i,j}$, the two vertices $\boldsymbol{s}_0$ and $\boldsymbol{s}_1$ are initialized on the sublattice with $\boldsymbol{u}_0 = \boldsymbol{u}^i$ and $\boldsymbol{u}_1 = \boldsymbol{u}^j$. These two vertices are excluded from the random vertex selection, such that both vertices remain fixed on their respective sublattice during the MCMC calculation. After selecting a vertex, a new unit-cell index u^{new} is proposed by drawing from a uniform distribution which contains all possible unit-cell indices $[\![0, N_{\text{suc}} - 1]\!]$.

We choose the reference summand nearly identical to Equation (3.69). The only difference is that the distances between two vertices here are only evaluated on the level of unit cell distances while the vertex position within a unit cell $\boldsymbol{u}_\nu$ is ignored. Using the syntax introduced for the position of vertices on a lattice with multi-site unit cells in Equation (3.83), we get the new reference summand

$$h_{N_\mathcal{G}}^{0,\text{multi}}(c) = \prod_{\nu=0}^{N_\mathcal{G}-2} \prod_{i=1}^{d} \left(1 + \left|\boldsymbol{r}_{\nu+1,i} - \boldsymbol{r}_{\nu,i}\right|\right)^{-\rho} . \tag{3.84}$$

While the shape of the reference integral can remain the same on the level of unit cells, it is necessary to account for an overcounting. The same contribution to the reference sum can now be obtained by multiple configurations where vertices are located on different sites within their respective unit cell. Consequently, the new reference sum is then given as

$$S_{N_\mathcal{G}}^{\text{ref,multi}} = \sum_c h_{N_\mathcal{G}}^{0,\text{multi}}(c) = (N_\text{suc})^{N_\mathcal{G}-1} \left[2\zeta(\rho) - 1\right]^{N_\mathcal{G}-1} . \tag{3.85}$$

The algorithm was tested for a simple spin chain, where the single-site unit cell was trivially extended to larger sizes and for the triangular-lattice cylinders discussed in the results chapter. Although the calculations were in agreement with the single-site unit cell results, I found that the convergence with this new algorithm was worse, so that only the single-site-unit-cell results are presented in Chapter 4. For the Kagome lattice the convergence was not sufficient to derive any meaningful results. For future calculations the MCMC calculation for this lattice needs to be further optimized, e. g., by the introduction of new MC moves or a different reference integral. However, let me illustrate the principal systematics with the simpler reference system. For the one-dimensional Ising chain series coefficients in the first two orders can be calculated analytically for arbitrary momenta k and are therefore an ideal demonstration system for testing the approach. Instead of using the obvious basis with one site per unit cell, now I group two neighboring sites to a unit cell as shown in Figure 3.13. In the 1-QP subspace, the result for the effective Hamiltonian will be a 2×2 matrix containing the hopping elements between the sites 0 and 1 of the unit cell after a Fourier transformation. In order zero we obtain a 2×2 identity matrix. The contribution in first order is calculated as

$$\hat{H}_\text{eff}^{(1)} = \lambda \begin{pmatrix} S_{0\to0}^{(1)} & S_{0\to1}^{(1)} \\ S_{1\to0}^{(1)} & S_{1\to1}^{(1)} \end{pmatrix} . \tag{3.86}$$

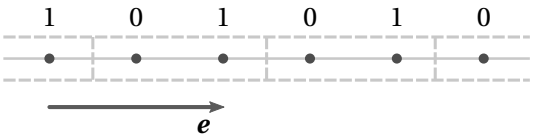

Figure 3.13: For an illustration of the MCMC method for systems with larger unit cells the 1D chain is divided into unit cells containing two sites. The lattice vector $\boldsymbol{e}$ has double the length of the original 1D-chain lattice vector and numbers indicate the two sublattices 0 and 1.

The matrix elements are the result of a summation of all embeddings of the first order results of the two-vertex graph

$$S^{(1)}_{0\to 0} = S^{(1)}_{1\to 1} = -\sum_{\substack{\Delta=-\infty \\ \Delta\neq 0}}^{\infty} \frac{\mathrm{e}^{\mathrm{i}k\Delta}}{|2\Delta|^{\alpha}} = -2^{-\alpha}\left[\mathrm{Li}_{\alpha}(\mathrm{e}^{-\mathrm{i}k}) + \mathrm{Li}_{\alpha}(\mathrm{e}^{\mathrm{i}k})\right] \tag{3.87}$$

$$\begin{aligned} S^{(1)}_{0\to 1} = \left(S^{(1)}_{1\to 0}\right)^{*} &= -\sum_{\Delta=-\infty}^{\infty} \frac{\mathrm{e}^{\mathrm{i}k\Delta}}{|1+2\Delta|^{\alpha}} \\ &= -2^{-\alpha}\left[\mathrm{e}^{-\mathrm{i}k}\Phi\left(\mathrm{e}^{-\mathrm{i}k}, \alpha, \frac{1}{2}\right) + \Phi\left(\mathrm{e}^{\mathrm{i}k}, \alpha, \frac{1}{2}\right)\right] \end{aligned} \tag{3.88}$$

with the Lerch transcendent $\Phi(z, s, a)$[7]. It becomes obvious that the target sums, which are the matrix elements of the effective Hamiltonian, are now complex-valued numbers. In cases where no analytical solution is available this property makes the computational effort, necessary for the evaluation of each single MC step, much more demanding.

For a ferromagnetic interaction the 1-QP gap is located at $k = 0$. Evaluating the results in the limit $k \to 0$ the analytic expressions of above sums become

$$S^{(1),k=0}_{0\to 0} = \lim_{k\to 0} S^{(1)}_{0\to 0} = -2^{1-\alpha}\zeta(\alpha) \tag{3.89}$$

$$S^{(1),k=0}_{0\to 1} = \lim_{k\to 0} S^{(1)}_{0\to 1} = -2^{1-\alpha}\Phi(1, \alpha, \frac{1}{2})\,, \tag{3.90}$$

leading to real-valued matrix elements. The corresponding results for the nearest-neighbor Hamiltonian and arbitrary k can be obtained by taking the limit $\alpha \to \infty$ in Equations (3.87) and (3.88). As expected, the diagonal elements vanish

$$S^{(1),\alpha=\infty}_{0\to 0} = \lim_{\alpha\to\infty} S^{(1)}_{0\to 0} = 0 \tag{3.91}$$

7 $\Phi(z, s, a) = \sum_{k=0}^{\infty} z^k/(a+k)^s,\ a \neq 0, -1, -2, \ldots$

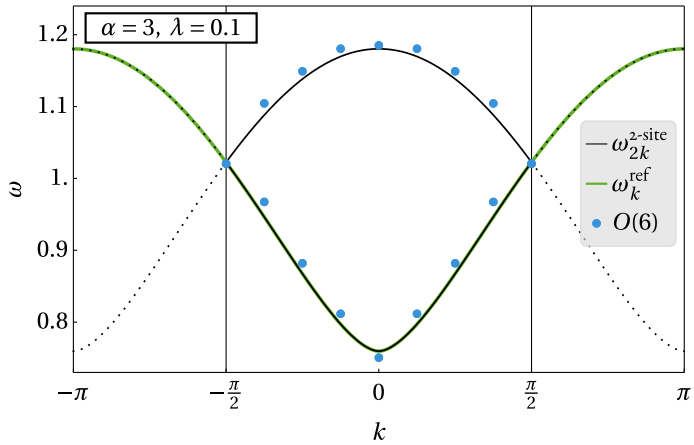

Figure 3.14: A comparison of the dispersion of the LRTFIM on a 1D chain with one and two sites per unit cell. First-order analytic results are shown as solid (dotted) lines, while red dots represent MCMC results for the two-site unit cell in sixth order. The plot for $\alpha = 3$ and $\lambda = 0.1$ shows that the dispersion of the single-site unit cell (green) is folded into the smaller Brillouin zone and results in the two dispersion branches of the 1D LRTFIM with two sites per unit cell (black). The doubling of the unit-cell size in real space leads to a halving in reciprocal space. Dotted lines indicate the periodic continuation of the two-site unit cell dispersion outside the Brillouin zone.

as there is no hopping to next-nearest neighbors possible in first order. The hopping between the two sites of the different sublattices is encoded in the off-diagonal elements

$$S_{0\to 1}^{(1),\alpha=\infty} = \lim_{\alpha\to\infty} S_{0\to 1}^{(1)} = -1 - \exp(-\mathrm{i}k)\,. \tag{3.92}$$

Using these analytic results, the eigenvalues of the system in first order can be calculated by a simple diagonalization of the small matrix. The two eigenvalues of the effective Hamiltonian represent two different energy levels. An illustration of the two dispersion branches in first order can be found in Figure 3.14 as solid and dotted lines. The doubling of the unit-cell size results in a folding of the original dispersion (solid green line) to the two branches (solid black line) in reciprocal space such that the Brillouin zone size is only half the size. The periodic continuation of the black curve is indicated by a dotted curve. For comparison the values of the bare series in order six, determined with the multi-site unit cell MCMC code, is shown as blue dots.

3.3 EXTRAPOLATION TECHNIQUES

The perturbative series in our calculations are always of the form

$$\tilde{F}(\lambda) = \sum_{m\geq 0}^{r} c_m \lambda^m = c_0 + c_1\lambda + c_2\lambda^2 + \cdots + c_r\lambda^r, \tag{3.93}$$

with the perturbation parameter $\lambda \in \mathbb{R}$ and the series coefficients $c_m \in \mathbb{R}$. Perturbative calculations can only offer exact results up to a given order r in the perturbation parameter. While this can give very good results for small values of λ, a direct evaluation of the perturbative series has several problems, especially in the investigation of critical phenomena. The obvious drawback lies in the magnitude of the perturbation. Not always, but often enough, the series needs to be evaluated for large perturbation strengths. This could be the case for the calculation of ground-state energies, e. g., if the crossing of different ground-state energies is used to determine the quantum-critical point λ_c, but also if energy gaps are used to estimate the critical points. Large means here, that already $\lambda/\lambda_c \lessapprox 1$, where the system approaches the QCP, needs extremely high orders to yield meaningful results, unless the series prefactors converge to zero with increasing order very quickly. Values of $\lambda > 1$ are difficult to handle because they mean that higher orders contribute more than lower orders which renders the bare results effectively useless if the polynom coefficients do not decay quickly.

Another problem arises when studying critical phenomena with, e. g., energies being described via polynomials. For second-order phase transitions the true physical function, which could be the gap between the ground-state energy and the first excited energy, has a power-law behavior close to $\lambda_c \in \mathbb{R}$

$$F(\lambda) \propto \left(1 - \frac{\lambda}{\lambda_c}\right)^{-\theta} A(\lambda)\,, \tag{3.94}$$

with a real-valued function $A(\lambda)$. The exponent θ is the critical exponent associated with the physical quantity and universal for a given class of phase transitions. The slope of the function with this critical exponent cannot be reproduced by a simple polynomial, except for very special cases such as, e. g., the 1D nearest-neighbor Ising model where the gap closes linearly and therefore the exponent $z\nu = 1$.

A technique which tries to mitigate both problems with bare series and has been applied very successfully in the past [Bre96] are Padé extrapolation methods. Padé extrapolations are convergence acceleration methods that increase the radius of convergence and make the evaluation of the series for much larger values of the perturbation parameter possible. We already discussed the setup in some detail in [FS16; FKS19] which I will recapitulate in this section.

3.3.1 *Padé extrapolations*

A detailed overview of Padé approximations, which have been known for a long time and date back to the 18th century [Bre96], is given in multiple books, e. g., [Gut89; BGM96]. The principal idea of Padé extrapolations is to interpret the perturbative series in Equation (3.93) as the Taylor series of a rational function

$$P^{L/M}[\tilde{F}(\lambda)] := \frac{R_L[\tilde{F}(\lambda)]}{Q_M[\tilde{F}(\lambda)]} = \frac{t_0 + t_1\lambda + t_2\lambda^2 + \cdots t_L\lambda^L}{1 + q_1\lambda + q_2\lambda^2 + \cdots q_M\lambda^M} \tag{3.95}$$

up to the perturbation order $r \geq L + M$ where higher-order terms are missing. Comparing the series expansion of Equation (3.95) to the perturbative series one obtains a linear set of equations which can be solved uniquely to obtain the coefficients t_i and $q_i \in \mathbb{R}$ for any given parameter set (L, M), with $L, M \in \mathbb{N}$.

In practice it turns out that diagonal extrapolations[8] typically yield better results in terms of convergence to the true function and hence to the critical value of a phase transition if the series, e. g., represents the 1-QP energy gap.

Note, that the rational function in Equation (3.95) allows for poles to occur if the denominator becomes zero for any value of λ. These poles can be divided into three categories: *physical*, *unphysical*, and *spurious*. Physical poles are real poles resulting from the underlying physical system. Looking again at the 1-QP gap for a second-order phase transition, we expect it to be a smooth function of λ for $\lambda \in [0, \lambda_c]$. If a pole appears before the gap closes this pole is unphysical and the extrapolation must be sorted out. Spurious poles can occur if, for an (L, M)-extrapolation without any zeros in the denominator for $\lambda \in [0, \lambda_c]$, the term $(\lambda - \tilde{\lambda}_{sp})/(\lambda - \lambda_{sp})$ is multiplied, where $\tilde{\lambda}_{sp} \approx \lambda_{sp}$, resulting in an $(L+1, M+1)$-extrapolation. Both terms should in principle cancel each other but due to numerical errors they might not be exactly the same. This higher-order extrapolation does not contain more information than the (L, M)-extrapolant and if a spurious pole appears at λ_{sp}, the evaluation for $\lambda > \lambda_{sp}$ is not sensible. Due to these problems this extrapolation which is called *defective* can be discarded from further evaluation.

From the valid high-order extrapolants the quantities of interest, which in my case are the energy and the position and exponent of the QCP, are extracted and compared for several sets of parameters (L, M). To obtain a single value for the quantity, the average over non-defective extrapolations is taken.

The different (L, M) extrapolations tend to show a convergence behavior when clustered as families $(n, n + m)$ with $n \in \mathbb{N}$ and $m \in \mathbb{Z}$. This is true for Padé as well as DLog Padé extrapolations, which I will introduce in the next section. This behavior is illustrated for DLog Padé extrapolations in Figure 3.15 where the critical value λ_c is shown

8 Extrapolations are called diagonal if the values of both parameters L and M are close to each other.

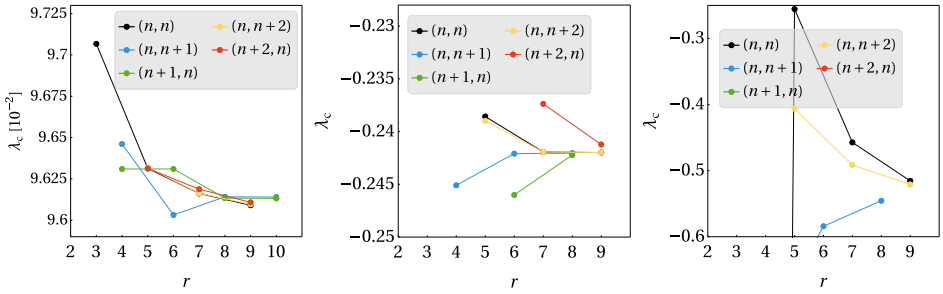

(a) Sq. lattice, $\boldsymbol{k} = \boldsymbol{0}$, $\alpha = 4$ (b) Sq. lattice, $\boldsymbol{k} = (\pi, \pi)^T$, $\alpha = 4$ (c) Tr. lattice, $\boldsymbol{k} = \boldsymbol{k}_{\text{clock}}$, $\alpha = 3$

Figure 3.15: The critical value λ_c for different families of (L, M) DLog Padé extrapolations for the square (sq.) and triangular (tr.) lattice where $L + M = r - 1$ in order r.

for different families. In case of a ferromagnetic QPT and for larger values of α a good convergence is found and it might be feasible to use a scaling approach for the families. However, for smaller values of α and different quasimomenta such as illustrated in Figure 3.15c for the transition to the clock order on the triangular lattice more and more extrapolations become defective and a scaling would become unfeasible. This approach would be especially interesting for a reduction of errors in the critical exponent but here the spread of the families is even worse since they are more sensitive to small deviations.

The extraction of a meaningful expression for the extrapolation error is generally difficult such that all error estimates for Padé extrapolations have to be taken with a grain of salt. This problem was already pointed out by A. C. Guttmann:

> » Nevertheless, it is difficult to quantify errors in any rigorous manner. As a consequence, error bounds are generally referred to as (subjective) confidence limits, and as such frequently measure the enthusiasm of the author rather than the quality of the data. « (Guttmann [Gut89])

Error bars for values extracted from Padé extrapolations which are shown in this thesis are derived by taking the standard deviation when averaging over non-defective extrapolants. Note, that if only a single extrapolant is available no error bar is displayed which should not be mistaken for an exact result. Rather than an error, these bars represent the scattering of extrapolants about the mean value.

3.3.2 *DLog Padé extrapolations*

For the extraction of critical points λ_c and exponents θ it is useful to look at Padé extrapolations of the logarithmic derivative of $F(\lambda)$, which can be written as

$$F(\lambda) \approx \left(1 - \frac{\lambda}{\lambda_c}\right)^{-\theta} A\Big|_{\lambda=\lambda_c} \left[1 + \mathcal{O}\left(1 - \frac{\lambda}{\lambda_c}\right)\right] . \tag{3.96}$$

If $A(\lambda)$ is analytic at $\lambda = \lambda_c$, the logarithmic derivative

$$D(\lambda) := \frac{\mathrm{d}}{\mathrm{d}\lambda} \ln F(\lambda) = \frac{F'(\lambda)}{F(\lambda)} \approx \frac{\theta}{\lambda_c - \lambda} \{1 + \mathcal{O}(\lambda - \lambda_c)\} . \tag{3.97}$$

should exhibit a single pole at $\lambda = \lambda_c$ for a power-law behavior of $F(\lambda)$ near the critical λ. In the following we call the extrapolation of the power series $\tilde{F}(\lambda)$

$$dP^{L/M}[\tilde{F}(\lambda)] := \exp\left(\int_0^\lambda \mathrm{d}\lambda' \, P^{L/M}[\tilde{D}(\lambda')]\right) , \tag{3.98}$$

which is based on the Padé extrapolant of the logarithmic derivative $\tilde{D}(\lambda)$ of $\tilde{F}(\lambda)$, *DLog Padé* extrapolation. The critical value λ_c is easily found by looking for poles, i. e., zeros in the denominator of $P^{L/M}[D(\lambda')]$. The algorithmically simple extraction of the critical exponent as

$$\theta \equiv \left.\frac{R_L[D(\lambda)]}{\frac{\mathrm{d}}{\mathrm{d}\lambda} Q_M[D(\lambda)]}\right|_{\lambda=\lambda_c} \tag{3.99}$$

is one reason to use DLog Padé extrapolations to investigate the series for critical phenomena. In practice, this may still be difficult and prone to error since the exponent varies strongly already for small deviations in λ_c.

Biased DLog Padé

However, in cases where the position of the critical point is known, e. g., analytically or from calculations using other methods with a higher numerical accuracy, it is possible to obtain the critical exponent with increased precision. If we define

$$\theta^*(\lambda) \equiv (\lambda_c - \lambda) D(\lambda) \approx \theta + \mathcal{O}(\lambda - \lambda_c), \tag{3.100}$$

the biased exponent can be calculated as

$$P^{L/M}_{\theta^*}[D(\lambda)]\Big|_{\lambda=\lambda_c} = \theta . \tag{3.101}$$

In Section 1.1 we already touched on the existence of multiplicative logarithmic corrections to the power-law dependency of $F(\lambda)$ defined in Equation (3.96). Extending the function with the logarithmic corrections such that we obtain the expected critical behavior close to λ_c, we get

$$\bar{F}(\lambda) \approx \left(1 - \frac{\lambda}{\lambda_c}\right)^{-\theta} \left[\ln\left(1 - \frac{\lambda}{\lambda_c}\right)\right]^{p} A(\lambda) \,. \tag{3.102}$$

Still assuming $A(\lambda)$ to be analytic close to λ_c, we write $\bar{F}(\lambda)$ as

$$\bar{F}(\lambda) \approx \left(1 - \frac{\lambda}{\lambda_c}\right)^{-\theta} \left[\ln\left(1 - \frac{\lambda}{\lambda_c}\right)\right]^{p} \bar{A}|_{\lambda=\lambda_c} \left[1 + \mathcal{O}\left(1 - \frac{\lambda}{\lambda_c}\right)\right] \,. \tag{3.103}$$

Due to the logarithmic factor a second summand enters the logarithmic derivative of $\bar{F}(\lambda)$

$$\bar{D}(\lambda) = \frac{\mathrm{d}}{\mathrm{d}\lambda} \ln \bar{F}(\lambda) \approx \frac{\theta}{\lambda_c - \lambda} + \frac{-p}{\ln(1 - \lambda/\lambda_c)\,(\lambda_c - \lambda)} + \mathcal{O}(\lambda - \lambda_c) \,. \tag{3.104}$$

The value of the logarithmic exponent p is even more sensitive to variations in λ_c than θ and additionally it also depends on θ itself. If we know the values of λ_c and θ exactly, we can dare trying to extract the logarithmic exponent. E. g., for the 1D LRTFIM chain we expect a logarithmic correction at $\alpha = 5/3$ and also know the exact mean-field value of $\theta = 1/2$ which has been calculated by Dutta *et al.* [DB01]. We can now bias the extrapolation just as for θ

$$p^*(\lambda) \equiv -\ln(1 - \lambda/\lambda_c)\,[(\lambda_c - \lambda)\,D(\lambda) - \theta] \approx p + \mathcal{O}(\lambda - \lambda_c), \tag{3.105}$$

only that we now fix two values – the position of the phase transition λ_c and the critical exponent θ. Analogously to the biased extrapolation for θ, we can calculate the logarithmic exponent as

$$P^{L/M}_{p*}[D(\lambda)]\Big|_{\lambda=\lambda_c} = p \,. \tag{3.106}$$

3.4 CALCULATION FLOW

In this thesis I present series expansions for QPTs in the LRTFIM. The method I used builds on established techniques such as perturbative continuous unitary transformations [Weg94; Mie98; KU00], Padé extrapolations[Gut89], and only recently developed schemes like white-graph expansions [CS15]. Nevertheless, new approaches needed to be developed and integrated in a multi-step evaluation and data processing. For the reader to obtain a better overview, a flow diagram is presented in Figure 3.16 where the single steps are illustrated. The diamond-shaped nodes represent the intermediate results while arrows indicate the steps between two results, which consist of:

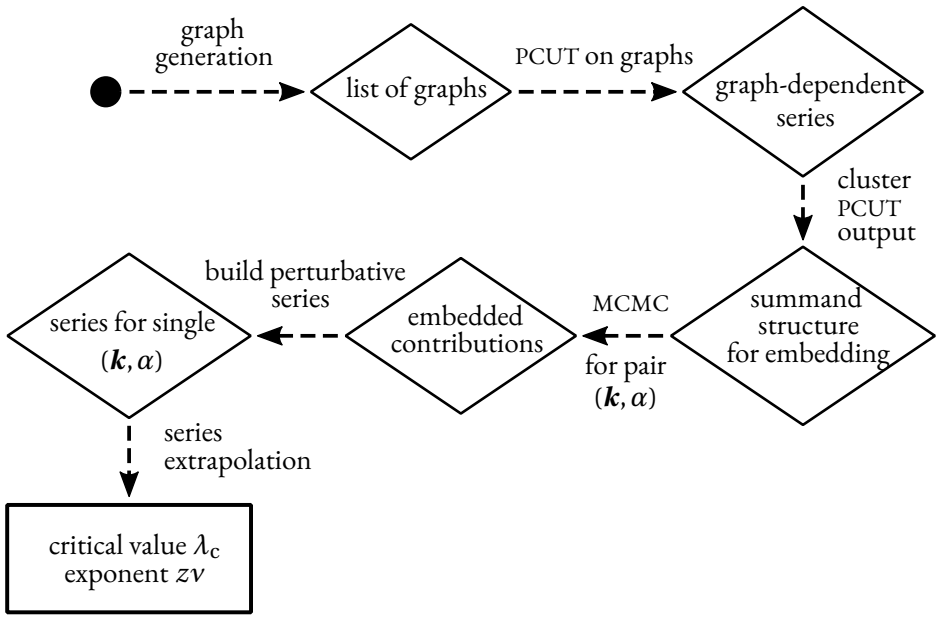

Figure 3.16: The flow diagram illustrates the methods necessary to compute series expansions for the long-range model and the required steps in data processing to obtain the critical value λ_c and exponent $z\nu$.

1. All connected graphs up to a given order are calculated.
2. On each white graph PCUT calculations for all hopping elements and the ground-state energy are done.
3. For each order the PCUT series with the same number of vertices on the associated graph are combined to a summand of a nested infinite sum.
4. The results are embedded into the chosen lattice which corresponds to an evaluation of the sum using MCMC. To this end the numeric values of the wave vector $\boldsymbol{k}$ and α must be fixed.
5. The contributions for different graph sizes in each respective order are summed up to obtain a bare perturbative series of the long-range model.
6. The series is extrapolated using DLog Padé expansions to extract the critical value λ_c and exponent $z\nu$ for the chosen parameter set $(\boldsymbol{k}, \alpha)$.

3.5 MEAN-FIELD CALCULATIONS

The ferromagnetic LRTFIM is expected to fall within the mean-field universality class, exhibiting mean-field critical exponents, in the limit of an interaction decaying very slowly with distance [DB01]. This can be easily understood in the limit $\alpha \to 0$, where each two spins interact with equal strength forming one large super-spin. Although, in this extreme limit, a renormalization of the exchange constant J would be necessary to avoid diverging energies, this picture can still serve as a means to physically understand the mean-field behavior for small values of α.

In this section I present the basic MF calculations of the LRTFIM for a ferromagnetic interaction as demonstrated in [Hum16] for the ferromagnet and the antiferromagnetic clock order. For an antiferromagnetic interaction the calculation is very similar if the structure of the magnetic order is taken into account. The results and calculations for the antiferromagnetic clock order and the ferromagnetic order on the triangular lattice as well as the square lattice are presented below. For the triangular lattice several possible orders are studied in the antiferromagnetic case: the clock, a straight-stripe, and a zigzag-stripe order (see Figure 3.17).

The calculation can be split into two parts: First, it is possible to derive a general lattice-independent expression for the energy and the phase boundary in the ferromagnetic case in terms of an interaction sum $\tilde{J}(0)$. Afterwards, the lattice sum needs to be evaluated and depends on the specific lattice geometry and the investigated magnetic order on the lattice. For an antiferromagnetic interaction a slight adaption must be made as discussed in the specific sections below.

We start from the TFIM with long-range interactions $J_{\boldsymbol{ij}}$ as already introduced in Equation (2.42)

$$\hat{H}_\alpha = -\sum_{\boldsymbol{i},\boldsymbol{j}} J_{\boldsymbol{ij}} \sigma_{\boldsymbol{i}}^x \sigma_{\boldsymbol{j}}^x - h \sum_{\boldsymbol{i}} \sigma_{\boldsymbol{i}}^z, \quad J_{\boldsymbol{ij}} = \frac{J}{|\boldsymbol{i}-\boldsymbol{j}|^\alpha} \,. \tag{3.107}$$

In the MF limit, the Pauli spin-operator can be written as its mean value $\langle \sigma_{\boldsymbol{i}}^x \rangle \equiv m$ with the addition of small fluctuations $\delta\sigma_{\boldsymbol{i}}^x$ about the average

$$\sigma_{\boldsymbol{i}}^x = \langle \sigma_{\boldsymbol{i}}^x \rangle + \delta\sigma_{\boldsymbol{i}}^x = m + \delta\sigma_{\boldsymbol{i}}^x \,. \tag{3.108}$$

If we insert this expression into Equation (3.107) and neglect quadratic fluctuations, we get an expression for the MF Hamiltonian

$$-\sum_{\boldsymbol{i},\boldsymbol{j}} J_{\boldsymbol{ij}} (m + \delta\sigma_{\boldsymbol{i}}^x)(m + \delta\sigma_{\boldsymbol{j}}^x) - h \sum_{\boldsymbol{i}} \sigma_{\boldsymbol{i}}^z \tag{3.109}$$

$$\approx -\sum_{\boldsymbol{i},\boldsymbol{j}} J_{\boldsymbol{ij}} \Big[m^2 + m\left(\delta\sigma_{\boldsymbol{i}}^x + \delta\sigma_{\boldsymbol{j}}^x\right) + \underbrace{\delta\sigma_{\boldsymbol{i}}^x \delta\sigma_{\boldsymbol{j}}^x}_{=0} \Big] - h \sum_{\boldsymbol{i}} \sigma_{\boldsymbol{i}}^z \equiv \hat{H}_{\mathrm{MF}} \,. \tag{3.110}$$

We can use the fact that the interaction parameter J_{ij} only depends on the distance between the spins $J_{ij} = J(\boldsymbol{\delta} \equiv \boldsymbol{i} - \boldsymbol{j})$

$$\hat{H}_{\mathrm{MF}} = -m^2 \sum_{\boldsymbol{i},\boldsymbol{\delta}} J(\boldsymbol{\delta}) - 2m \sum_{\boldsymbol{i},\boldsymbol{\delta}} J(\boldsymbol{\delta}) \delta\sigma_{\boldsymbol{i}}^x - h \sum_{\boldsymbol{i}} \sigma_{\boldsymbol{i}}^z \tag{3.111}$$

$$= -Nm^2 \sum_{\boldsymbol{\delta}} J(\boldsymbol{\delta}) - 2m \sum_{\boldsymbol{i}} \delta\sigma_{\boldsymbol{i}}^x \sum_{\boldsymbol{\delta}} J(\boldsymbol{\delta}) - h \sum_{\boldsymbol{i}} \sigma_{\boldsymbol{i}}^z \,. \tag{3.112}$$

A Fourier transformation of the interactions $\tilde{J}(\boldsymbol{q}) = \sum_{\boldsymbol{\delta}} J(\boldsymbol{\delta}) \mathrm{e}^{-\mathrm{i}\boldsymbol{q}\boldsymbol{\delta}}$ can be introduced to replace the sum over $\boldsymbol{\delta}$ by the constant $\tilde{J}(0)$

$$\hat{H}_{\mathrm{MF}} = -N\tilde{J}(0)m^2 - 2m\tilde{J}(0) \sum_{\boldsymbol{i}} \delta\sigma_{\boldsymbol{i}}^x - h \sum_{\boldsymbol{i}} \sigma_{\boldsymbol{i}}^z \,. \tag{3.113}$$

Reinserting the definition of the small fluctuations $\delta\sigma_{\boldsymbol{i}}^x = \sigma_{\boldsymbol{i}}^x - m$ we obtain

$$\hat{H}_{\mathrm{MF}} = \underbrace{N\tilde{J}(0)m^2}_{\text{constant}} \underbrace{-2m\tilde{J}(0) \sum_i \sigma_i^x - h \sum_i \sigma_i^z}_{\text{paramagnetic spins in transverse field}} \,. \tag{3.114}$$

This MF Hamiltonian represents N independent, noninteracting spins in a transverse field. Based on this, while neglecting the constant, we can now consider the single-spin Hamiltonian

$$\hat{H}_{1\mathrm{spin}} = -2\tilde{J}(0)m\sigma^x - h\sigma^z \tag{3.115}$$

to find its eigenvalues

$$E_{\pm} = \pm\sqrt{\left(2\tilde{J}(0)m\right)^2 + h^2} \tag{3.116}$$

with eigenvectors

$$|\phi_+\rangle = \begin{pmatrix} \cos\frac{\theta}{2} \\ \sin\frac{\theta}{2} \end{pmatrix} \quad \text{and} \quad |\phi_-\rangle = \begin{pmatrix} -\sin\frac{\theta}{2} \\ \cos\frac{\theta}{2} \end{pmatrix}, \quad \text{with } \tan\theta = \frac{h}{2\tilde{J}(0)m} \,. \tag{3.117}$$

To obtain the phase boundary we investigate the thermal average of σ^x at temperature T

$$m = \langle\sigma^x\rangle = \frac{\langle\phi_-|\sigma^x|\phi_-\rangle \mathrm{e}^{-\beta E_-} + \langle\phi_+|\sigma^x|\phi_+\rangle \mathrm{e}^{-\beta E_+}}{\mathrm{e}^{-\beta E_-} + \mathrm{e}^{-\beta E_+}} \tag{3.118}$$

$$= \frac{2\tilde{J}(0)m}{\sqrt{h^2 + \left(2m\tilde{J}(0)\right)^2}} \tanh\left(\beta\sqrt{h^2 + \left(2m\tilde{J}(0)\right)^2}\right), \tag{3.119}$$

where $\beta = 1/(k_B T)$ with the Boltzmann factor k_B. While the order parameter is finite in the current phase it vanishes at the phase-transition point. Therefore taking the limit $m \to 0$ yields

$$\frac{h}{2\tilde{J}(0)} = \tanh(\beta_c h) \,. \tag{3.120}$$

To compare the quantum-critical point to my results obtained with the PCUT method, it is necessary to look at the zero-temperature limit ($\beta_c \to \infty$) to obtain the value of the critical magnetic-field strength

$$h_c = 2\tilde{J}(0) \,. \tag{3.121}$$

Rearranging Equation (3.119) in this limit determines the magnetization

$$m = \pm\sqrt{\frac{1}{2} - \frac{h^2}{2\tilde{J}(0)^2}} \tag{3.122}$$

and, finally, inserting m in the single-spin Hamiltonian Equation (3.115) we get the energy eigenvalues

$$E_\pm = \pm\sqrt{\tilde{J}(0)^2\left(\frac{1}{2} - \frac{h^2}{2\tilde{J}(0)^2}\right) + h^2} = \pm\sqrt{2\tilde{J}(0)^2 - h^2} \,. \tag{3.123}$$

Most of the necessary work for calculating the critical magnetic field in the MF limit for a ferromagnetic interaction has been done now. The only unknown quantity that remains is the interaction sum $\tilde{J}(0) = \sum_{\mathbf{\Delta}} J(\mathbf{\Delta})$. The numeric value of the sum depends on the specific lattice structure and often results in a combination of Riemann-ζ functions and Dirichlet-L series.

3.5.1 *Square lattice*

Due to the added complexity in calculation of the MF results for an antiferromagnetic interaction this section is split into two parts. First, I present the ferromagnetic result for the square lattice and afterward I illustrate how the MF approach can be applied to the Néel order for an antiferromagnetic interaction.

3.5.1.1 *Ferromagnetic interaction*

The MF phase transition point for the LRTFIM on a square lattice can be calculated analytically by evaluating $\tilde{J}(0)$. On the square lattice, for the ferromagnetic LRTFIM one

obtains a Hardy-Lorenz sum the value of which can be found in Reference [Bor13]. The critical magnetic field is therefore given as

$$h_{\mathrm{c}}^{\mathrm{MF},\square,\mathrm{f}}(\alpha) = 2 \sum_{\nu,\mu=-\infty}^{\infty} \frac{1}{(\nu^2+\mu^2)^{\frac{\alpha}{2}}} = 8\zeta\left(\frac{\alpha}{2}\right) L_{-4}\left(\frac{\alpha}{2}\right) = 8\zeta\left(\frac{\alpha}{2}\right)\beta\left(\frac{\alpha}{2}\right), \quad (3.124)$$

with $\beta(s) = \sum_{s=0}^{\infty}(-1)^m(2m+1)^{-s}$ (cf. Section B.2).

3.5.1.2 *Antiferromagnetic interaction*

If an antiferromagnetic interaction is present the MF calculations become a bit more involved as the magnetic structure of the ordered phase needs to be taken into account. For the Néel-ordered ground state on the square lattice one finds that the magnetic unit cell consists of two lattice sites with an antiparallel spin orientation. Consequently, I introduce two sublattices A and B, where I assume the total magnetization $m_A + m_B = 0$. The variables m_A and m_B are the respective magnetizations of sublattice A and B. Let me now introduce the longitudinal mean field

$$H_l^x = \tilde{J}_{AA}(0)\, m_A + \tilde{J}_{AB}(0)\, m_B\,, \quad (3.125)$$

acting on the sites $l \in A$. This means we split the field into two parts: An interaction between the sites on A and an interaction between spins on sublattices A and B. Therefore, new interaction sums have been introduced that run over the lattice sites of sublattice A and B:

$$\tilde{J}_{AA}(0) = \sum_{\nu\in A} \frac{J}{r_\nu^\alpha} \quad \text{and} \quad \tilde{J}_{AB}(0) = \sum_{\nu\in B} \frac{J}{r_\nu^\alpha}\,. \quad (3.126)$$

The total interaction sum is given as $\tilde{J}(0) = \tilde{J}_{AA}(0) + \tilde{J}_{AB}(0)$. Using this definition (and comparing to Equation (3.119)) it is possible to write the magnetization m_A as the self-consistency equation of sublattice A

$$m_A \equiv \langle \sigma^x \rangle = \frac{H_l^x}{\sqrt{h^2 + (H_l^x)^2}} \tanh\left(\beta\sqrt{h^2 + (H_l^x)^2}\right), \quad (3.127)$$

while m_B can be obtained by exchanging the sublattice indices A and B. With the assumption that $m_A + m_B = 0$ the longitudinal mean field in Equation (3.125) becomes $H_l^x = m_A(\tilde{J}_{AA}(0) - \tilde{J}_{AB}(0))$ and the phase boundary in the limit of $m_A \to 0$ and $T \to 0$ is given by

$$h_{\mathrm{c}}^{\mathrm{MF},\square,\mathrm{af}} = 2[\tilde{J}_{AA}(0) - \tilde{J}_{AB}(0)]\,. \quad (3.128)$$

Again, this equation can be evaluated analytically (see [Bor13])

$$h_c^{\mathrm{MF},\square,\mathrm{af}}(\alpha) = 2\sum_{\nu,\mu=-\infty}^{\infty}(-1)^{\mu+\nu}\frac{1}{(\nu^2+\mu^2)^{\frac{\alpha}{2}}} = -8(1-2^{1-\frac{\alpha}{2}})\zeta(\frac{\alpha}{2})L_{-4}(\frac{\alpha}{2})$$
$$= -8(1-2^{1-\frac{\alpha}{2}})\zeta(\frac{\alpha}{2})\beta(\frac{\alpha}{2})\,. \tag{3.129}$$

3.5.2 *Triangular lattice*

Analogous to the square lattice section I split this part into two subsections. First, I show the results for the ferromagnetic model before I present the MF calculations for the clock and different stripe orders.

3.5.2.1 *Ferromagnetic interaction*

For a triangular lattice the critical value of the quantum phase transition in the MF limit can be calculated analytically as well. For a parametrization of the sum, the triangular-lattice unit vectors $\boldsymbol{e}_1$ and $\boldsymbol{e}_2$, defined as

$$\boldsymbol{e}_1 = \frac{1}{2}\begin{pmatrix}-1\\ \sqrt{3}\end{pmatrix} \quad \text{and} \quad \boldsymbol{e}_2 = \frac{1}{2}\begin{pmatrix}1\\ \sqrt{3}\end{pmatrix} \tag{3.130}$$

(cf. Figure 3.17) are used. Afterwards one has to sum over all multiples of the unit vectors $\boldsymbol{l}_{\mu,\nu} = \mu\boldsymbol{l}_1 + \nu\boldsymbol{l}_2$.

$$h_c^{\mathrm{MF},\triangle,\mathrm{f}}(\alpha) = 2\sum_{\nu,\mu=-\infty}^{\infty}\frac{1}{(\nu^2+\mu\nu+\nu^2)^{\frac{\alpha}{2}}} = 12\zeta\left(\frac{\alpha}{2}\right)L_{-3}\left(\frac{\alpha}{2}\right) = 12\zeta\left(\frac{\alpha}{2}\right)g\left(\frac{\alpha}{2}\right), \tag{3.131}$$

using the Riemann-ζ function and a Dirichlet L-series[9] [Bor13].

3.5.2.2 *Antiferromagnetic interaction*

We can do the mean-field calculation for different types of magnetic order. For the triangular lattice there are several possible orders that could be relevant. Here we look at two different variants of a stripe order[10] and the clock order that represents the ground state for low fields in the nearest-neighbor TFIM on the triangular lattice (see Figure 3.17 for an illustration).

9 $g(s) \equiv L_{-3}(s) = 1 - 2^{-s} + 4^{-s} - 5^{-s} + 7^{-s} - 8^{-s} \ldots$ (cf. Appendix B.2).

10 The straight-stripe order has been proposed as the ground-state of the LRTFIM for very small values of $\alpha \lesssim 2.4$ [SBM18]. Further investigations of the stripe orders are presented in Section 4.4.

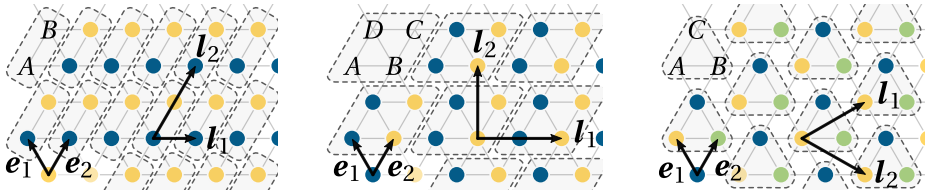

(a) Straight-stripe order (b) Zigzag-stripe order (c) Clock order

Figure 3.17: Three different types of magnetic order on the triangular lattice. The dashed lines illustrate the magnetic unit cells, capital letters represent different sublattices. The same color indicates the same spin orientation. Vectors $\boldsymbol{e}_{1/2}$ are the triangular lattice vectors, $\boldsymbol{l}_{1/2}$ are lattice vectors of the magnetic superlattice. Figure (a) shows a stripe order, (b) shows a different stripe order where the stripes form a zigzag pattern, and (c) illustrates the 120° order (aka clock order or $\sqrt{3}\times\sqrt{3}$-order) that is known to be the ground state of the nearest-neighbor antiferromagnetic TFIM [MS01; Pow+13].

CLOCK ORDER For the clock order on the triangular lattice we divide the lattice into three sublattices A, B, and C such that the magnetic unit cell consists of three lattice sites. The lattice vectors of the magnetic order are given as (compare Figure 3.17c)

$$\boldsymbol{l}_1 = 2\boldsymbol{e}_2 - \boldsymbol{e}_1 \quad \text{and} \quad \boldsymbol{l}_2 = \boldsymbol{e}_2 - 2\boldsymbol{e}_1 \,. \tag{3.132}$$

We assume the total magnetization $\sum_{\gamma\in\{A,B,C\}} m_\gamma$ to be zero, and introduce the longitudinal mean field

$$H_l^x = 2\tilde{J}_{AA}(0)\, m_A + 2\tilde{J}_{AB}(0)(m_B + m_C) \,, \tag{3.133}$$

acting at the sites $l \in A$. This means we split the field into three parts: An interaction between the sites on sublattice A and an interaction between spins on sublattice A and sublattices B and C, respectively. Therefore, new interaction sums are introduced as

$$\tilde{J}_{AA}(0) = \sum_{\nu\in A} \frac{J}{r_\nu^\alpha} \quad \text{and} \quad \tilde{J}_{AB}(0) = \tilde{J}_{AC}(0) = \sum_{\nu\in B} \frac{J}{r_\nu^\alpha} \,. \tag{3.134}$$

When calculating the quantities for sublattice A, the sites on B and C are equivalent due to the lattice symmetry. The total interaction sum is therefore given as

$$\tilde{J}(0) = \tilde{J}_{AA}(0) + \tilde{J}_{AB}(0) + \tilde{J}_{AC}(0) \,. \tag{3.135}$$

Using this definition (and comparing to (3.119)) it is possible to write the magnetization m_A as the self-consistency equation of sublattice A

$$m_A \equiv \langle S_l^x \rangle = \frac{H_l^x(m_A, m_B, m_C)}{\sqrt{h^2 + \left[H_l^x(m_A, m_B, m_C)\right]^2}} \tanh\left\{\beta\sqrt{h^2 + \left[H_l^x(m_A, m_B, m_C)\right]^2}\right\} .$$

(3.136)

The same can be done for the other magnetizations m_B and m_C by a cyclic permutation of the sublattice indices. With $\sum_{\gamma\in\{A,B,C\}} m_\gamma = 0$ the longitudinal mean field can be written in terms of the magnetization m_A as

$$H_l^x = 2m_A(\tilde{J}_{AA}(0) - \tilde{J}_{AB}(0)) \,. \tag{3.137}$$

We obtain the phase boundary for the antiferromagnetic interaction similar to the ferromagnetic case as

$$h_\mathrm{c}^{\mathrm{MF},\triangle,\mathrm{co,af}} = 2[\tilde{J}_{AA}(0) - \tilde{J}_{AB}(0)] \,. \tag{3.138}$$

The sum can be solved analytically as shown in [Bor13]. First, it is possible to parametrize the sum as

$$\begin{aligned} &h_\mathrm{c}^{\mathrm{MF},\triangle,\mathrm{co,af}}(\alpha) \\ &\quad = 2\frac{4}{3}\sum_{\nu,\mu=-\infty}^{\infty} \frac{\sin\left[\frac{2\pi}{3}(\mu+1)\right]\sin\left[\frac{2\pi}{3}(\nu+1)\right] - \sin\left[\frac{2\pi}{3}\mu\right]\sin\left[\frac{2\pi}{3}(\nu-1)\right]}{\left[(\mu+\frac{1}{2}\nu)^2 + 3(\frac{1}{2}\nu)^2)\right]^{\frac{\alpha}{2}}} \,. \end{aligned} \tag{3.139}$$

Then, the analytic solution to this sum is given as

$$h_\mathrm{c}^{\mathrm{MF},\triangle,\mathrm{af}}(\alpha) = 6\left(3^{1-\alpha/2} - 1\right)\zeta\left(\frac{\alpha}{2}\right)L_{-3}\left(\frac{\alpha}{2}\right) \,, \tag{3.140}$$

using the Riemann-ζ function and a Dirichlet L-series [Bor13].

STRAIGHT-STRIPE ORDER For a straight-stripe order the magnetic unit cell consists of two spins on sublattices A and B. The magnetic lattice vectors can be built from the lattice unit vectors as (compare Figure 3.17a)

$$\boldsymbol{l}_1 = \boldsymbol{e}_2 - \boldsymbol{e}_1 \quad \text{and} \quad \boldsymbol{l}_2 = 2\boldsymbol{e}_2 \,. \tag{3.141}$$

For the total magnetization I assume $m_A + m_B = 0$ and analogous to the previous calculation the field on site $l \in A$ is give as

$$\begin{aligned} H_l^x &= 2\tilde{J}_{AA}(0)m_A + 2\tilde{J}_{AB}(0)m_B = 2m_A[\tilde{J}_{AA}(0) - \tilde{J}_{AB}(0)] \,, \\ &\text{with } \tilde{J}_{AA}(0) = \sum_{\nu\in A}\frac{J}{r_\nu^\alpha} \quad \text{and} \quad \tilde{J}_{AB}(0) = \sum_{\nu\in B}\frac{J}{r_\nu^\alpha} \,. \end{aligned} \tag{3.142}$$

The critical magnetic field is

$$h_{\mathrm{c}}^{\mathrm{MF},\triangle,\mathrm{ss,af}} = 2[\tilde{J}_{AA}(0) - \tilde{J}_{AB}(0)]\,, \tag{3.143}$$

with the interaction sums

$$\tilde{J}_{AA}(0) = \sum_{\mu,\nu=-\infty}^{\infty} \left|\nu\boldsymbol{l}_1 + \mu\boldsymbol{l}_2\right|^{-\alpha} = \sum_{\mu,\nu} \left[4\mu^2 + 2\mu\nu + \nu^2\right]^{-\frac{\alpha}{2}} \tag{3.144}$$

$$\begin{aligned}\tilde{J}_{AB}(0) &= \sum_{\mu,\nu=-\infty}^{\infty} \left|\boldsymbol{e}_2 + \nu\boldsymbol{l}_1 + \mu\boldsymbol{l}_2\right|^{-\alpha} \\ &= \sum_{\mu,\nu} \left[4\mu^2 + 2\mu\nu + \nu^2 + 4\mu + \nu + 1\right]^{-\frac{\alpha}{2}}\,.\end{aligned} \tag{3.145}$$

ZIGZAG-STRIPE ORDER The magnetic unit cell of the zigzag-stripe order consists of four spins residing sublattices A, B, C, and D. The magnetic lattice vectors can be built from the lattice unit vectors as (compare Figure 3.17b)

$$\boldsymbol{l}_1 = 2\boldsymbol{e}_2 - 2\boldsymbol{e}_1 \quad \text{and} \quad \boldsymbol{l}_2 = \boldsymbol{e}_1 + \boldsymbol{e}_2\,. \tag{3.146}$$

Analogous to the previous calculations, and using the fact that $\tilde{J}_{AB}(0) = \tilde{J}_{AC}(0)$, the field on site $l \in A$ is given as

$$\begin{aligned}H_l^x &= 2\tilde{J}_{AA}(0)\,m_A + 2\tilde{J}_{AB}(0)\,m_B + 2\tilde{J}_{AC}(0)\,m_C + 2\tilde{J}_{AD}(0)\,m_D \\ &= 2m_A\tilde{J}_{AA}(0) + 2m_C\tilde{J}_{AC}(0) + 2\tilde{J}_{AB}(0)\,[m_B + m_D]\,, \\ &\qquad \text{with } \tilde{J}_{A\gamma}(0) = \sum_{\nu\in\gamma} \frac{J}{r_\nu^\alpha}, \quad \gamma \in \{A,B,C,D\}\,.\end{aligned} \tag{3.147}$$

With the total magnetization assumed to be zero $\sum_{\gamma\in\{A,B,C,D\}} m_\gamma = 0$ and $m_A = -m_C$ (to obtain the zigzag-stripe order, see Figure 3.17b), I get

$$H_l^x = 2[\tilde{J}_{AA}(0) - \tilde{J}_{AC}(0)]\,m_A \quad \Rightarrow \quad h_{\mathrm{c}}^{\mathrm{MF},\triangle,\mathrm{zzs,af}} = 2[\tilde{J}_{AA}(0) - \tilde{J}_{AC}(0)]\,. \tag{3.148}$$

The interaction sums can be calculated by summing over the lattice vectors

$$\tilde{J}_{AA}(0) = \sum_{\mu,\nu=-\infty}^{\infty} \left|\nu\boldsymbol{l}_1 + \mu\boldsymbol{l}_2\right|^{-\alpha} = \sum_{\mu,\nu} \left[3\mu^2 + 4\nu^2\right]^{-\frac{\alpha}{2}} \tag{3.149}$$

$$\tilde{J}_{AC}(0) = \sum_{\mu,\nu=-\infty}^{\infty} \left|2\boldsymbol{e}_2 - \boldsymbol{e}_1 + \nu\boldsymbol{l}_1 + \mu\boldsymbol{l}_2\right|^{-\alpha} = \sum_{\mu,\nu} \left[3\mu^2 + 4\nu^2 + 3\mu + 6\nu + 3\right]^{-\frac{\alpha}{2}}\,. \tag{3.150}$$

After a detailed introduction of the methods they are applied to the LRTFIM. In the next chapter results for several lattices in different dimensions are presented for both, a ferro- and an antiferromagnetic interaction. Along with the perturbative series expansions in the high-field limit, above MF results are presented for the square and triangular lattice.

4

CRITICAL PROPERTIES AND PHASE TRANSITIONS OF THE LONG-RANGE TRANSVERSE-FIELD ISING MODEL

Critical properties of the LRTFIM introduced in Section 2.3 have been calculated in recent years mainly for the one-dimensional chain. Using the methods presented in the previous chapter I calculate the phase diagrams and critical exponents $z\nu$ for the model an a variety of different lattice structures in order to obtain new insights on this exciting topic.

I begin with a discussion of the simplest model – the one-dimensional chain – and present my own results for the phase diagram of the ferro- and antiferromagnetic model. This serves two purposes: For one, I demonstrate the functionality of the algorithms discussed in the previous chapter. Otherwise, this serves as a benchmark of the method by comparing it to other results in the literature obtained with different methods. The one-dimensional Ising chain with ferromagnetic interactions already shows the generic property of continuously varying critical exponents; an interesting behavior, especially considering the notion of universality classes. However, it is not totally unexpected for models with long-range interactions as has been discussed in the literature before [Fis67; Sak73; Ent82]. These results are complemented with results for an antiferromagnetic interaction that are compared to recent MPS-calculation results.

Afterward, the study of hypercubic lattices is continued with results of the LRTFIM on the square and cubic lattice which are both, such as the chain, bipartite and consequently unfrustrated in the nearest-neighbor limit even for an antiferromagnetic interaction. Effects of frustration in the antiferromagnetic interactions already become visible in the one-dimensional Ising chain. In two dimensions this becomes more pronounced for the square lattice. The cubic-lattice results for the critical exponents, too, show no variation with the value of α.

For a triangular lattice and an antiferromagnetic interaction frustration effects, as briefly discussed for the ground states in Section 2.2.1, are already present in the nearest-neighbor limit. Since the effect of the extended interaction range on a frustrated model is *a priori* hard to estimate, this model is investigated in Section 4.3. To obtain a better understanding of the frustrated nature we also studied the model on cylindrical lattices with a triangular structure of different sizes to determine ground-state properties and boundaries of the phase diagram as shown in Section 4.4.

The sections of this chapter include parts from my publications [FS16; FKS19; Koz+19]. A breakdown of the contributions by the different respective authors can be found in Appendix A.

4.1 1D ISING CHAIN

First, I discuss the LCE results on the simplest lattice – a one-dimensional spin chain. This section is split into a section in which the exact low-order solution of the ground state is presented, a section in which the behavior of the one-QP dispersion is discussed, and phase diagrams and critical properties of the QPT are shown.

Parts of this section have been published in Reference [FS16] and the appendix of Reference [FKS19].

4.1.1 *Ground-state energy*

For the ground-state energy there is the rule that each bond between two sites has to be used twice in the PCUT operator sequence[1] unless there are loops in the graph. This results from the fact that (a) hopping terms in $\hat{T}_0$ cannot act on the ground state and do not change the number of particles and (b) every particle which is created by the $\hat{T}_2$ operators needs to be destroyed again by acting with a $\hat{T}_{-2}$ operator. Consequently, in first order no contribution to the ground-state energy can exist.

The contribution in second order results from graph $\mathcal{G}_1$ (cf. Figure C.1) where two particles are first created and then destroyed again and can be calculated analytically for an arbitrary value of α. For the energy per site we get

$$e_{0,\mathrm{ch}}^{(2)} = -\frac{1}{2}\lambda^2 \sum_{i_1=1}^{\infty} \frac{1}{|i_1|^{2\alpha}} = -\frac{1}{2}\lambda^2 \zeta(2\alpha) \tag{4.1}$$

where $\zeta(s)$ is the Riemann zeta function. In third order the sums are not easily separable since the (only) contributing graph $\mathcal{G}_7$ contains a loop. In third order each bond of the graph is touched once, resulting in the contribution

$$e_{0,\mathrm{ch}}^{(3)} = -\frac{1}{4}\lambda^3 \sum_{\substack{i_1=-\infty \\ i_1\neq 0}}^{\infty} \sum_{\substack{i_2=-\infty \\ i_2\neq 0 \\ i_2\neq i_1}}^{\infty} \frac{1}{|i_2|^{\alpha}} \frac{1}{|i_1|^{\alpha}} \frac{1}{|i_2 - i_1|^{\alpha}} , \tag{4.2}$$

where the excluded values prevent two vertices being embedded on the same lattice site. This nested sum and all higher-order contributions must be evaluated numerically as discussed in Chapter 3.

1 This property is often referred to as "double touch".

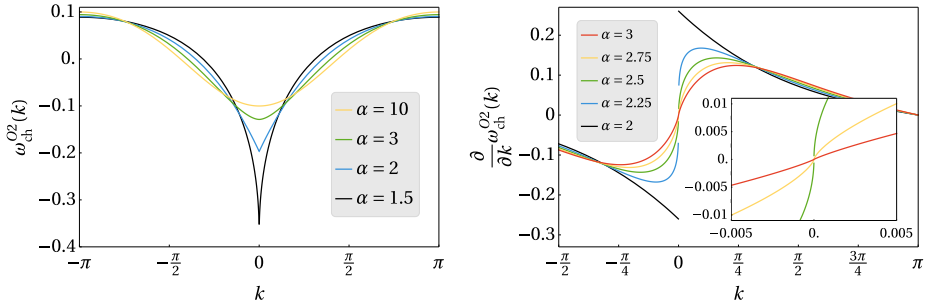

(a) $\omega_{\mathrm{ch}}^{O2}(k)$ (b) $\frac{\partial}{\partial k}\omega_{\mathrm{ch}}^{O2}(k)$

Figure 4.1: (a) Analytic dispersion of the 1D LRTFIM chain in order 2 for $\lambda = 0.1$. For decreasing α the dispersion becomes peaked at $k = 0$ and consequently (b) the derivative develops a discontinuity around $\alpha \approx 2.5$.

4.1.2 *Dispersion*

The two leading orders can be evaluated exactly since only the two chain graphs $\mathscr{G}_1$ and $\mathscr{G}_6$ (cf. Figure C.1), which both contain no loops, contribute to the dispersion. These contributions are given as

$$\omega_{\mathrm{ch}}^{(1)}(k) = \frac{1}{2}\lambda\left[\mathrm{Li}_\alpha(\mathrm{e}^{-\mathrm{i}k}) - \mathrm{Li}_\alpha(\mathrm{e}^{\mathrm{i}k})\right] \tag{4.3}$$

$$\begin{aligned}\omega_{\mathrm{ch}}^{(2)}(k) = &-\frac{1}{2}\cdot\frac{1}{2}\lambda^2 \sum_{\substack{i_1=-\infty\\ i_1\neq 0}}^{\infty}\sum_{\substack{i_2=-\infty\\ i_2\neq 0\\ i_2\neq i_1}}^{\infty} |i_1|^{-\alpha}|i_2|^{-\alpha}\cdot 2\cos[k(i_2-i_1)] \\ &-\lambda^2\Big(-\frac{1}{2}\sum_{\substack{i_1=-\infty\\ i_1\neq 0}} |i_1|^{-2\alpha}\Big) \\ &= 2\lambda^2\zeta(2\alpha) - \frac{1}{2}\lambda^2\left[\mathrm{Li}_\alpha(\mathrm{e}^{-\mathrm{i}k}) + \mathrm{Li}_\alpha(\mathrm{e}^{\mathrm{i}k})\right]^2\end{aligned} \tag{4.4}$$

resulting in the dispersion of the one-dimensional LRTFIM chain in second order

$$\begin{aligned}\omega_{\mathrm{ch}}(k) = 1 &+ \frac{\lambda}{2}\left[\mathrm{Li}_\alpha(\mathrm{e}^{-\mathrm{i}k}) - \mathrm{Li}_\alpha(\mathrm{e}^{\mathrm{i}k})\right] \\ &+ \lambda^2\left\{2\zeta(2\alpha) - \frac{1}{2}\left[\mathrm{Li}_\alpha(\mathrm{e}^{-\mathrm{i}k}) + \mathrm{Li}_\alpha(\mathrm{e}^{\mathrm{i}k})\right]^2\right\} + \mathscr{O}(\lambda^3)\end{aligned} \tag{4.5}$$

(see Section B.2 for a definition of the polylogarithm functions $\mathrm{Li}_s(z)$).

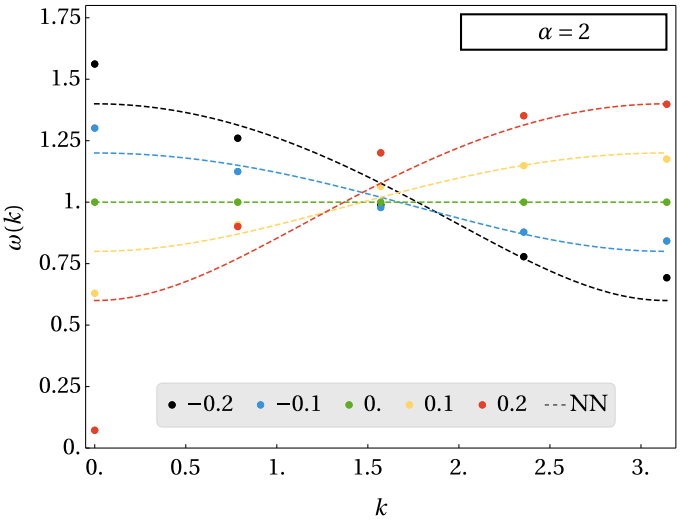

Figure 4.2: The dispersion for $\alpha = 2$ (dots) is evaluated at several k-points and multiple values of λ (see the legend). For comparison the nearest-neighbor dispersion for the same values of λ is plotted as dashed lines in the same color.

The dispersion curves for different values of α in second order are shown in Figure 4.1a for $\lambda = 0.1$. Here, we find an intriguing behavior: In the nearest-neighbor (NN) limit of $\alpha = \infty$, the dispersion is given by a smooth cosine curve. This property remains intact until a critical value of $\alpha \approx 2.5$ where a kink appears in the dispersion at quasimomentum $k = 0$. This can also be seen in Figure 4.1b where the first derivative of the dispersion is shown for several values of α.

To determine higher-order contributions the nested infinite sums need to be evaluated numerically. To this end, I need to fix the value of α and perform the necessary MCMC computations discussed in Chapter 3. For nearest-neighbor interactions the dispersion has a minimum at $k = 0$ for a ferromagnetic interaction ($\lambda > 0$) and at $k = \pi$ for an antiferromagnetic interaction ($\lambda < 0$) reflecting the respective parallel and alternating spin orientation of the ordered phase.

For the bipartite chain we expect these orders to keep existing also for $\alpha < \infty$. In Figure 4.2 the dispersion for $\alpha = 2$ is computed in order nine for several high-symmetry points of the lattice and compared to the nearest-neighbor dispersion. We find the same behavior which already became visible in the low-order dispersion: at $k = 0$ a peak forms in the curve for small α. As expected, we find that the minimum remains at the same value of k as in the nearest-neighbor limit.

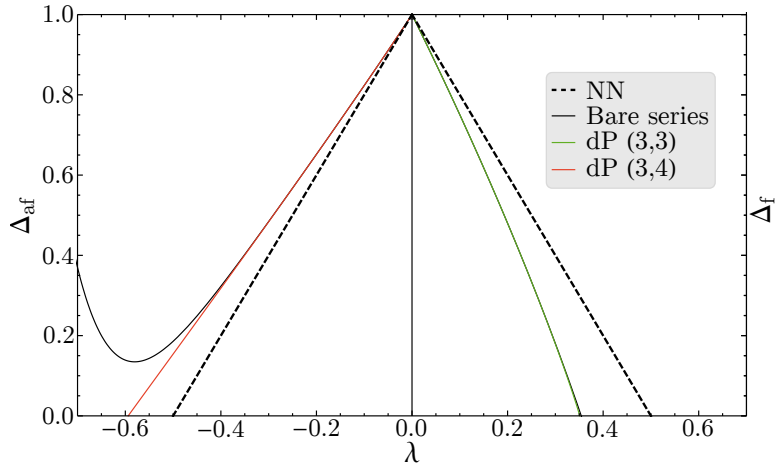

Figure 4.3: The one-QP gap $\Delta_{f/af}$ as a function of λ for ferromagnetic/antiferromagnetic Ising interactions with exponent $\alpha = 3$. Solid black lines correspond to the bare order-eight series, while colored solid lines refer to representative DLog Padé extrapolants. Dashed black lines are the exact one-QP gaps for the nearest-neighbor TFIM in the limit $\alpha \to \infty$ displaying a linear behavior with $z\nu = 1$ and λ_c. In the ferromagnetic case the bare series is nonalternating and already in very good agreement with the extrapolated curve up to the critical λ.

4.1.3 *Ferromagnetic interaction*

Let us focus on ferromagnetic interactions with the perturbation parameter $\lambda > 0$. Here, only exponents $\alpha > 1$ are well defined. In our LCE this becomes apparent due to divergences in the infinite sums for $\alpha \leq 1$. This is also reflected in the evaluation of the nested sums which become increasingly demanding with decreasing α since the weight of summands resulting from large distances is increased. In the opposite limit $\alpha \to \infty$ one recovers the exact solution of the nearest-neighbor TFIM

$$\Delta^{\mathrm{NN}}_{\mathrm{ch,\,f}} = 1 - 2\lambda \tag{4.6}$$

yielding a quantum phase transition between the polarized phase and the symmetry-broken phase at $\lambda_c^{\mathrm{ch,f,\,NN}} = 0.5$ with an exponent $z\nu = 1$. Any ferromagnetic long-range interaction with finite α stabilizes the symmetry-broken phase as the further-neighbor interactions also prefer parallel alignment of the spins and one expects $\lambda_c < 0.5$. This is illustrated in Fig. 4.3 for $\alpha = 3$.

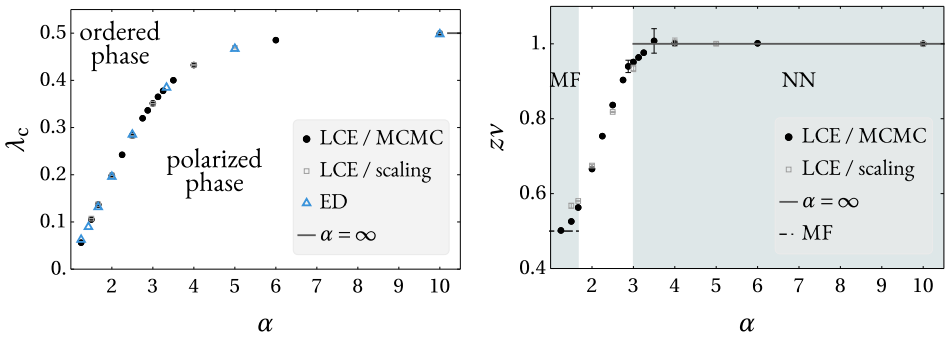

(a) Phase diagram (b) Critical exponent

Figure 4.4: Quantum-critical points λ_c (a) and critical exponents $z\nu$ (b) as a function of α for the ferromagnetic case. Black circles (gray squares) represent averaged DLog Padé extrapolants of $\Delta_{\mathrm{ch,\,f}}$ of the highest available order for MCMC-evaluated (scaling-evaluated) sums. Blue triangles correspond to scaled ED data from [Kna+13]. The mean field (MF) and nearest-neighbor (NN) TFIM universality classes are illustrated as shaded backgrounds and the associated critical exponents as horizontal lines.

The first two orders of the energy gap for a ferromagnetic interaction are given analytically as the minimum of the dispersion $\omega_{\mathrm{ch}}(k)$ which is located at $k = 0$, the first- and second-order contribution of which are given in Equations (4.3) and (4.4).

$$\Delta_{\mathrm{ch,\,f}} = 1 - 2\zeta(\alpha)\lambda + 2\left(\zeta(2\alpha) - \zeta(\alpha)^2\right)\lambda^2 + \mathcal{O}(\lambda^3)\,. \tag{4.7}$$

MCMC calculations are utilized to compute the higher orders individually for each α before the critical values are extracted from the DLog Padé extrapolations of the gap series. The constructed phase diagram is shown in Figure 4.4a where I compare the results obtained with the scaling method as discussed in Section 3.2.3.2 and those obtained with the MCMC summation introduced in Section 3.2.4. For the critical value λ_c the results of both approaches are in good agreement.

Next, we turn to the nature of the quantum phase transition as a function of α. From one-loop renormalization group calculations [Sak73; Kna+13; DB01], one expects three different domains: (i) the system is in the same universality class as the nearest-neighbor TFIM with $z\nu = 1$ for $\alpha \geq 3$, (ii) the system displays mean-field behavior $z\nu = 1/2$ for $\alpha \leq 5/3$, and (iii) the system has nontrivial continuously varying critical exponents for $5/3 < \alpha < 3$.

We extracted the critical exponent $z\nu$ as a function of α from the DLog Padé extrapolation of $\Delta_{\mathrm{ch,\,f}}$ which is shown in Figure 4.4b. As expected, the critical exponent is close to 1 for $\alpha \geq 3$ and then continuously decreases for smaller values of α. One should stress that any LCE is not able to resolve abrupt changes of critical exponents, since only finite

orders enter into the extrapolation of the series. Therefore, a smooth behavior of the curve is to be expected.

In the past there has been some discussion about the behavior of the critical exponents at the point between the domains of short-range and varying criticality. First, there is some disagreement on the location of this point in α for the 1D chain [Sak73; DB01] with some locating it at $\alpha = 3$, which we use to indicate the NN criticality range in Figure 4.4b, while others claim the value to be at $\alpha = 11/4$ [Mag+16; Hum19]. Second, up to now it is unclear if critical exponents display a continuous behavior at this point or if a finite jump exists [Sak73; Mag+16; Hum19]. Even for classical long-range systems where no discontinuity is expected [CC06], further studies are performed to verify the obtained result [LB02; Pic12; BPR13]. I tried to gain some insight on this property by densely sampling the exponent $z\nu$ in the relevant region. However, due to the resolution of the data and the inherently continuous behavior of the series expansion method no conclusive statement can be derived. Interestingly though, the curve of $z\nu$ looks nearly linear around $\alpha = 3$.

Although we have to expect a smooth behavior for the curve of $z\nu$, the visible deviation around $\alpha = 5/3$ is unexpected but can be traced back to the presence of multiplicative logarithmic corrections at the lower critical $\alpha = 5/3$ similar to the upper critical dimension $d = 3$ for the nearest-neighbor TFIM previously discussed in Section 1.1. For the latter one finds $p = -1/6$ for $d = 3$ from perturbative RG [LK69; BLGZJ73; WR73] and series expansions [ZOH94; Coe+16]. In our case, fixing $\lambda_c^{\mathrm{ch,f}} = 0.136405$ and $z\nu = 1/2$, we find $p_{\mathrm{ch}} \approx -0.16285(4)$ for $\alpha = 5/3$ when averaging over order-8 DLog Padé extrapolations. We stress that multiplicative logarithmic corrections are very sensitive to the exact value of $\lambda_c^{\mathrm{ch,f}}$. Larger error bars in the higher-order coefficients therefore strongly influence the numerical value of p. Order-nine and -ten contributions would have required a much higher effort to deliver a meaningful result. Still, the extracted value is therefore remarkably close to $-1/6$. This fully supports the idea that the quantum-critical behavior induced by the long-range Ising interaction can effectively be understood in terms of the nearest-neighbor TFIM in an effective spatial dimension d_{eff}. This property is confirmed in the literature where it has also been derived with RG methods for O(N) models with long-range interactions [DTC15].

Looking at the critical exponents for very small values of α, it becomes clear that the scaling approach for an evaluation of the sums is not able to provide meaningful results in this range.

4.1.4 *Antiferromagnetic interaction*

The antiferromagnetic LRTFIM with $\lambda < 0$ behaves fundamentally different to the ferromagnetic case, which is mainly due to the induced geometric frustration. As a conse-

quence, any finite value of α enlarges the polarized, or analogously reduces the symmetry-broken, phase compared to the nearest-neighbor TFIM for $\alpha \to \infty$. This is illustrated for $\alpha = 3$ in Figure 4.3.

As in the ferromagnetic case, the second-order gap can be calculated analytically as the minimum of the dispersion $\omega_{\mathrm{ch}}(k)$ in Section 4.1.2, which is located at $k = \pi$ for an antiferromagnetic $\lambda < 0$

$$\Delta_{\mathrm{ch,\,af}} = 1 + \left(2^{1-\alpha}\left(2^{\alpha}-2\right)\zeta(\alpha)\right)\lambda + \left(2\zeta(2\alpha) - 2^{1-2\alpha}\left(2^{\alpha}-2\right)^{2}\zeta(\alpha)^{2}\right)\lambda^{2} + \mathcal{O}(\lambda^{3})\,. \tag{4.8}$$

In Reference [KLT12] this phase diagram has been calculated by variational MPS. They found that, when varying α from ∞ to 0, the critical point monotonously increases from $\lambda_{\mathrm{c}}^{\mathrm{ch,af}} = -0.5$ to $\lambda_{\mathrm{c}}^{\mathrm{ch,af}} \to -\infty$.

We used DLog Padé extrapolation of $\Delta_{\mathrm{ch,\,af}}$ to extract the critical point $\lambda_{\mathrm{c}}^{\mathrm{ch,af}}$ and the critical exponent $z\nu$ for various values of α (see Figure 4.5). From RG calculations one expects the system to be in the same universality class as the nearest-neighbor TFIM for $\alpha \geq 9/4$ [KLT12]. Our LCE for the critical line are in quantitative agreement with MPS calculations in this α-regime and we find indeed a critical exponent $z\nu$ close to one, e. g., $z\nu = 1.012(3)$ for $\alpha = 9/4$. The situation is more peculiar for $\alpha < 9/4$. Here the MPS calculations suggests continuously varying critical exponents and, furthermore, a breakdown of the area law due to the long-range nature of the interaction even inside the gapped polarized phase [KLT12; Pet+12]. However, DMRG calculation find second-order QPTs with $\nu = 1$ for an arbitrary $\alpha > 0$ [Sun17], which is in agreement with our results where, although the calculations become more error sensitive, we cannot identify any consistent trend for $z\nu$ drifting away from $z\nu = 1$.

In Figure 4.5a we show that a good agreement with the MPS calculations (shown as red triangles) is reached with the linked-cluster expansion using MCMC. To put an emphasis on the superiority of the MCMC method for evaluating the nested infinite sums the critical values obtained with the scaling method discussed in Section 3.2.3.2 are also shown for comparison. With the scaling method series coefficients up to order eight could be computed. One finds that for the scaling approach the deviations between LCE and MPS are already large for $\alpha = 2$ and critical exponents which are sensitive on the position of λ_{c} cannot be extracted in a reliable fashion. For a wide range of α-values the critical exponent computed using MCMC has the same value as for the nearest-neighbor model at $\alpha = \infty$. For smaller α the critical exponents of the different extrapolants are spreading further but remain in the vicinity of the nearest-neighbor exponent $z\nu = 1$ shown as a solid gray line to guide the eye.

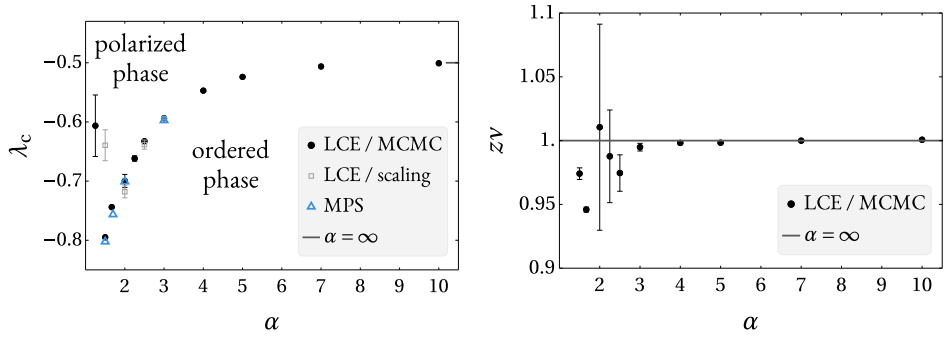

(a) Phase diagram (b) Critical exponent

Figure 4.5: Quantum-critical points λ_c (a) and corresponding critical exponents $z\nu$ (b) as a function of α for the antiferromagnetic case. Black circles represent averaged DLog Padé extrapolants of $\Delta_{ch,\,af}$. Gray squares represent the same values computed with the scaling approach. Blue triangles correspond to MPS data from [KLT12].

4.1.5 *General remarks*

For the 1D LRTFIM spin chain we expect second-order phase transitions from the paramagnet at high fields to a $\mathbb{Z}_2$-symmetry-broken ground state at small h. While the paramagnetic state is the same for an unfrustrated ferro- as well as a frustration-inducing antiferromagnetic interaction, the symmetry-broken state consists either of parallel spins pointing in x-direction or antiparallel neighbor spins (Néel state), respectively.

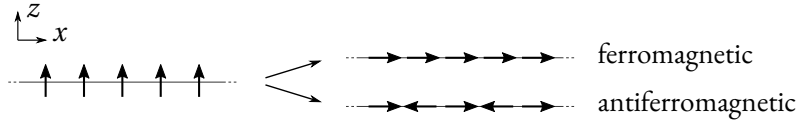

Starting from the high-field limit excitations are well defined as single spin flips above the polarized ground-state. Using LCE methods we were able to determine the phase diagram as well as the critical exponent $z\nu$ for several values of α. The main limiting factor here is the necessary computation time since for each chosen parameter set (k, α) multiple MCMC summations must be done as previously discussed in Section 3.2.4.

It is also possible to determine the low-field excitations for the long-range model on the spin chain. As previously discussed in Section 2.3.3 using the analytic continuation of Riemann's zeta function a smooth curve can be determined for the domain wall (DW)-excitation energies relative to the ground-state energy for all $\alpha > 0$ in the antiferromagnetic case. This is different for a ferromagnetic interaction where a single-domain-wall state

possesses the lowest energy above the ground state for all $\alpha \gtrapprox 2.48$. However, the energy diverges at $\alpha = 2$ and the state driving the phase transition to the paramagnet for smaller α is given by a 2-DW state with distance $d = 1$ between the DWs, which represents a single spin flip. Analyzing the perturbed one- and two-DW states shows that the property that both energies exchange their position in the energy spectrum persists even for finite magnetic fields h although the critical value α_c is slightly shifted to smaller values of α for an increasing perturbation strength. Based on these results, a low-field expansion in second order was used to compare and verify the phase boundary shown in Figure 4.4a [Rit19].

Due to the low perturbation order no critical exponents could be calculated in [Rit19], but a surprisingly good agreement was found between the critical values of both computations, especially considering the large value of the perturbation[2] necessary to drive the QPT from the low-field limit. Although we would presume that the nature of the phase transition changes with the new excitation closing the gap we did not find any signs in the LCE from the high-field limit as varying critical exponents are present, anyway.

4.2 HYPERCUBIC LATTICES

The lowest-dimensional instance of hypercubic lattices – the one-dimensional chain – has been discussed in the previous section. In this section I present results for the square lattice in two dimensions and the simple cubic lattice in three dimensions. For $d \geq 3$ and a ferromagnetic interaction the quantum phase transition is expected to exhibit mean-field criticality for the complete α-axis since, first, this is already the case for the TFIM [SIC12] and, second, any $\alpha < \infty$ has the effect of an increased effective dimension as seen in the previous section.

Parts of the square-lattice results have been published in Reference [FKS19] while the cubic-lattice results have not been published so far.

4.2.1 *Square lattice*

The nearest-neighbor TFIM on a square lattice with a ferro- and antiferromagnetic interaction has been the subject of past studies. For the ferromagnetic interaction the QPT between a polarized and a $\mathbb{Z}_2$-symmetry-broken phase is within the $(2+1)$D Ising universality class with $z\nu = 0.629\,971(4)$ [Kos+16]. The critical value has been computed to high accuracy as $\lambda_c = 0.164\,21(1)$ [Ham00].

2 E. g., for $\alpha = 2.5$ the gap closes at $h/J \approx 1.84$.

Based on the symmetries of the nearest-neighbor TFIM (2.3) on the square lattice it can be shown that it is possible to map the ferromagnetic and antiferromagnetic model onto each other [Mon+16]. The transformation of the interaction Pauli matrices

$$\sigma_{\boldsymbol{i}}^x \to (-1)^{i_x+i_y}\sigma_{\boldsymbol{i}}^x \tag{4.9}$$

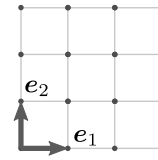

Figure 4.6: Square lattice vectors.

flips the sign of every second spin. The vector $\boldsymbol{i} = (i_x, i_y)$ runs over all lattice sites, where i_x and i_y are the coordinates relative to lattice vectors $\boldsymbol{e}_1$ and $\boldsymbol{e}_2$ defined in Figure 4.6. The order parameter in the ferromagnetic case

$$\hat{M} = \frac{1}{N}\sum_{\boldsymbol{i}} \sigma_{\boldsymbol{i}}^x \tag{4.10}$$

is mapped under the transformation to a staggered magetization

$$\hat{M}_{\text{stag}} = \frac{1}{N}\sum_{\boldsymbol{i}} (-1)^{i_x+i_y}\sigma_{\boldsymbol{i}}^x \,, \tag{4.11}$$

which is the antiferromagnetic order parameter. As a result of this mutual mapping between both nearest-neighbor models the phase transitions occur at the same critical value and can be assigned to the same universality class.

Parts of this section have been taken from our publication [FKS19].

4.2.1.1 *Dispersion*

For each selected value of quasi momentum $\boldsymbol{k}$, a separate MCMC calculation needs to be done for a fixed value of α. Analyzing the dispersion $\omega(\boldsymbol{k})$ allows localizing the minimum of the one-QP gap in momentum space and gives an indication of the magnetic order of the phase after a potential gap closing in case of second-order phase transitions. The dispersion of the LRTFIM on the square lattice is shown for an antiferromagnetic interaction $\lambda < 0$ for characteristic values $\alpha \in \{2.5, 3, 4\}$ in Figure 4.7.

The dispersion for the antiferromagnetic LRTFIM on the square lattice shows a clear minimum at $\boldsymbol{k}_{\text{Néel}} = (\pi, \pi)^T$ which corresponds to the Néel order. This is the correct phase for the nearest-neighbor TFIM in the low-field limit $\alpha \to \infty$ and we expect it to survive for all values of α. This expectation is reflected in the fact that with decreasing α none of the one-QP energies of the evaluated $\boldsymbol{k}$-points different to $\boldsymbol{k}_{\text{Néel}}$ shows a tendency to become the one-QP gap $\Delta_{\text{sq, af}}$.

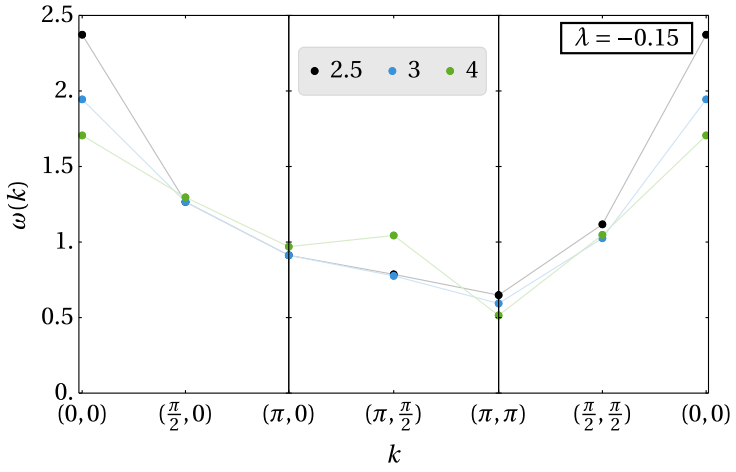

Figure 4.7: The dispersion of the antiferromagnetic LRTFIM on a square lattice has been evaluated at multiple high-symmetry points of the Brillouin zone to ensure the location of the one-QP gap. As expected the minimum is always located at $\boldsymbol{k} = (\pi, \pi)^T$, independent of α, suggesting a phase transition from the polarized to the Néel-ordered state. The shown data points are derived from the Padé extrapolations of the order-5 series.

4.2.1.2 *Ferromagnetic interaction*

While in the one-dimensional model an analytical result for the first two orders of the series expansion can be derived for quasimomentum $\boldsymbol{k} = \boldsymbol{0}$, on the square lattice this is only possible for the first-order contribution. Higher orders up to order 10 were evaluated using MCMC summation. The first order can be expressed via the Dirichlet L-series $\beta\left(\frac{\alpha}{2}\right)$

$$\Delta^{(1)}_{\text{sq, f}}(\lambda) = -4\zeta\left(\frac{\alpha}{2}\right)\beta\left(\frac{\alpha}{2}\right)\lambda\,. \tag{4.12}$$

As a function of α, for the square lattice a qualitatively similar behavior as for the 1D LRTFIM is expected [FS16; DB01] where the critical exponent $z\nu$ varies continuously in a certain range of α from the 2D-Ising to the MF value $z\nu = 1/2$ as discussed in the previous section. However, compared to the 1D chain the boundaries in α of continuously varying exponents are shifted to $\alpha = 10/3$ and $\alpha = 6$ [DB01]. In contrast to the Ising chain, for large α the system is expected to be in the 3D-Ising universality class.

In Figure 4.8 I show our results for the phase diagram and corresponding critical exponent $z\nu$. For a large $\alpha = 10$ the critical value λ_c is already very close to its nearest-neighbor correspondent. Strengthening the longer-range couplings by reducing α stabilizes the $\mathbb{Z}_2$-symmetry-broken phase and λ_c decreases. In the limit $\alpha \to 2$ the phase

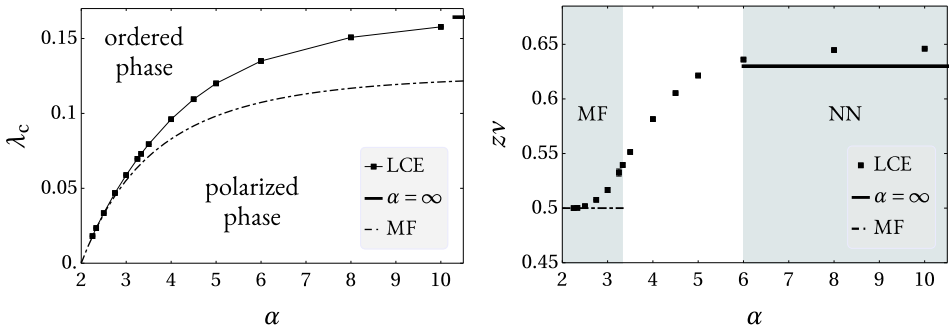

(a) Phase diagram (b) Critical exponent

Figure 4.8: Quantum-critical points λ_c (a) and critical exponents $z\nu$ (b) as a function of α for the ferromagnetic case of the LRTFIM on a square lattice. Black squares represent averaged DLog Padé extrapolants of $\Delta_{sq,\,f}$ of the highest available order. The mean field (MF) and NN TFIM universality classes are illustrated as shaded backgrounds and the associated critical exponents as horizontal lines. The phase diagram shows an extended ordered phase for decreasing α.

transition occurs at $\lambda_c \to 0$, while for exactly $\alpha = 2$ the sums diverge and the Hamiltonian (2.42) becomes ill-defined. However, let me stress that the results agree well with the MF calculations (dot-dashed lines in Figure 4.8) even in the regime $\alpha \leq 2.5$, where the MF ansatz is expected to be quantitatively correct.

For the critical exponent $z\nu$ it is known that the DLog Padé extrapolation slightly overestimates critical exponents since it ignores subleading corrections to the critical behavior. As a consequence, the estimate $z\nu \approx 0.65$ for large α is about 3% too large compared to the known value $z\nu \approx 0.63$ [Kos+16] of the nearest-neighbor TFIM [Kos+16; OHW91]. In the opposite limit of small α the critical exponent $z\nu$ approaches the value $z\nu = 1/2$ confirming the expected MF limit. In between we find an interesting continuous variation of $z\nu$ from the MF value to that of the 3D-Ising universality class. Note that we attribute the deviations from 0.5, which is exactly known to be correct for $\alpha \leq 10/3$ [DB01], to limitations of the extrapolation which neglects the subleading multiplicative logarithmic correction p at $\alpha = 10/3$ (for a definition of p see Section 1.1). Indeed, when extracting p for $\alpha = 10/3$ from the DlogPadé extrapolation by fixing $\lambda_c = 0.073\,037(25)$ and $z\nu = 1/2$ as for the one-dimensional LRTFIM [FS16], we find $p_{sq} \approx -0.17(4)$ for the square lattice. This value is remarkably close to $p = -1/6$ which is the prediction for the 3D TFIM from perturbative RG and series expansions [LK69; BLGZJ73; WR73; WOH94; Coe+16]. As already proposed in the study of the ferromagnetic 1D chain, the quantum-critical behavior induced by the long-range Ising interaction can therefore

effectively be understood in terms of the nearest-neighbor TFIM in an effective spatial dimension.

4.2.1.3 *Antiferromagnetic interaction*

As for the ferromagnetic interaction with $\boldsymbol{k} = \mathbf{0}$ it is possible to derive the first-order contribution for $\boldsymbol{k} = (\pi, \pi)^T$

$$\Delta^{(1)}_{\text{sq, af}}(\lambda) = 4\left(1 - 2^{1-\frac{\alpha}{2}}\right)\zeta\left(\frac{\alpha}{2}\right)\beta\left(\frac{\alpha}{2}\right)\lambda\,. \tag{4.13}$$

Higher orders up to order 10 were evaluated with MCMC calculations.

On the square lattice with an antiferromagnetic interaction we expect an inherently different behavior to the ferromagnetic case. The long-range Ising interaction again introduces frustration as in 1D which is, however, expected to be weaker than compared to the triangular lattice as discussed later in Section 4.3.3. No MF limit for small values of α can be expected and it is therefore not at all obvious how the quantum-critical behavior changes as a function of α in this frustrated system.

Our results for the critical value λ_c and exponent $z\nu$ are shown in Figure 4.9. As expected, stronger competing interactions introduced by decreasing α stabilize the quantum paramagnet. We observe that the MCMC becomes less reliable for α close to 2. Furthermore, small α values lead to alternating series in $|\lambda|$ with extremely large coefficients c_k which are hard to extrapolate (cf. Appendix F for a list of coefficients). This results in rather large error bars for $\alpha \leq 3$ as can be seen in Figure 4.9. Consequently, I only show results for $\alpha \geq 2.5$.

As outlined before, limitations in the extrapolation lead to a slightly overestimated $z\nu$ for large α [Pow+13; OHW91]. When decreasing α, $z\nu$ stays almost constant and close to the value of the nearest-neighbor TFIM for the investigated α-regime. We expect always the same quantum phase transition between the polarized and the Néel-ordered state in the full range of α in a similar fashion as deduced for the LRTFIM chain [Sun17] due to the following reasons: We do not find tendencies for a softening of other one-QP modes at different $\boldsymbol{k}$ (see dispersion in Figure 4.7) which points against a second-order quantum phase transition to a differently ordered state. The critical line of a variational calculation covering the polarized and the Néel phase is not in good agreement with the LCE results and therefore do not indicate a MF behavior of the system for any value of α. Finally, we expect the pure long-range Ising model to be Néel-ordered for all $\alpha > 0$. Our approach for the square lattice is therefore dominantly limited by the increasing relative error of the MCMC for $\alpha \lessapprox 2.5$ (cf. Appendix F).

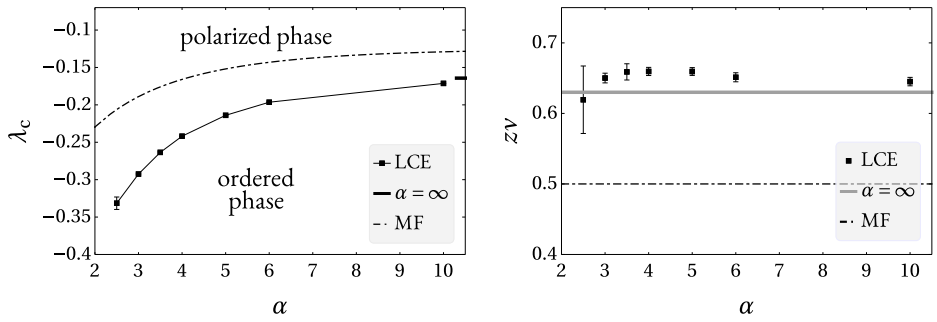

(a) Phase diagram (b) Critical exponent

Figure 4.9: Quantum-critical points λ_c (a) and corresponding critical exponents $z\nu$ as a function of α for the antiferromagnetic case of the LRTFIM on a square lattice. Black squares represent averaged DLog Padé extrapolants of $\Delta_{\text{sq, af}}$. The shown MF curves demonstrate that no MF limit is present for antiferromagnetic interactions.

4.2.2 *Cubic lattice*

As discussed before, the upper critical dimension for the TFIM is $d_u = 3$. Consequently, a MF behavior must be expected for the nearest-neighbor model on the 3D cubic lattice.

4.2.2.1 *Ferromagnetic interaction*

Since we can interpret α as a knob to tune a higher effective dimension d_{eff} than present in the NN limit, we expect MF criticality for lattices with $d \geq 3$ nearly for the complete range of α. Only exactly at $\alpha = \infty$, since d_u is the upper critical dimension, multiplicative logarithmic corrections are present. Higher-dimensional hypercubic lattices are expected to show a similar critical behavior as the 3D-cubic lattice except for the singular point $\alpha = \infty$.

The critical values of the QPT between the polarized and ordered phase in dependence of α are shown in the phase diagram in Figure 4.10a. Comparing the phase boundary to the phase diagram of the 1D chain (cf. Figure 4.4a) and the square lattice (cf. Figure 4.8a) we find a qualitatively identical behavior. The critical exponents $z\nu$ in Figure 4.10b display values which are very close to the expected MF exponent. As discussed above, for large α the LCE slightly overestimates the exponent as a consequence of the logarithmic corrections which cannot be captured in the LCE while for decreasing α it gets even closer to $z\nu = 0.5$. These results are consistent with previous LCE calculations where the exponent of the logarithmic corrections for the nearest-neighbor TFIM on a 3D

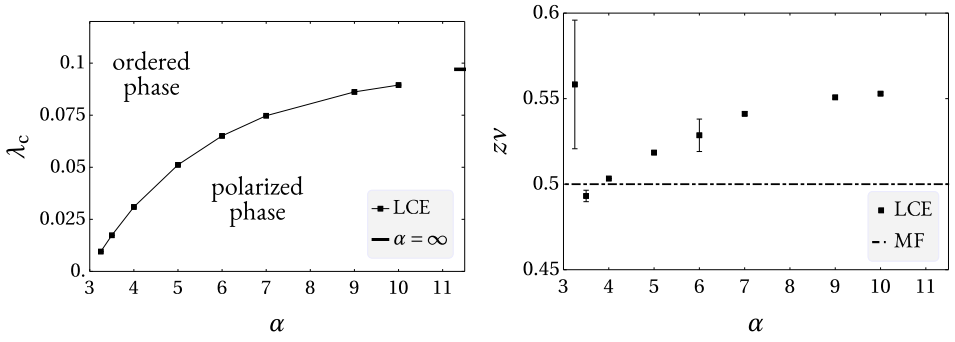

(a) Phase diagram (b) Critical exponent

Figure 4.10: Quantum-critical points λ_c (a) and critical exponents $z\nu$ (b) as a function of α for the ferromagnetic case of the LRTFIM on a cubic lattice. Black squares represent averaged DLog Padé extrapolants of $\Delta_{\text{cub, f}}$ of the highest available order. The mean field (MF) exponent is illustrated as a horizontal dashed line.

cubic lattice was determined as $p_{\text{cub}} = -0.143(5)$ and the exact MF value of the critical exponent was similarly overestimated as in Figure 4.10b.

While the critical value for $\alpha = 3.25$ leads to a smooth curve in the phase diagram, the corresponding exponent has a much larger deviation from the expected value with a large scattering of the DLog Padé extrapolants indicated by the error bar. For smaller values of α the MCMC calculations become more demanding. Small deviations in the critical value can result in a larger deviation in the critical exponent, which is therefore much more sensitive to numerical errors.

4.2.2.2 *Antiferromagnetic interaction*

The antiferromagnetic LRTFIM on the 3D cubic lattice exhibits a QPT between the paramagnetic and Néel-ordered phase just as seen on the square lattice. Here, also a mapping exists between the ferro- and antiferromagnetic model in the NN limit $\alpha \to \infty$. The phase diagram calculated with the LCE is shown in Figure 4.11 next to the critical exponents $z\nu$. As expected the critical exponents are close to the MF value of $(z\nu)_{\text{MF}} = 0.5$ in the complete investigated range of α. This behavior is similar to the antiferromagnetic LRTFIM on the square lattice and spin chain, where the critical exponents is close to the NN value for all studied α.

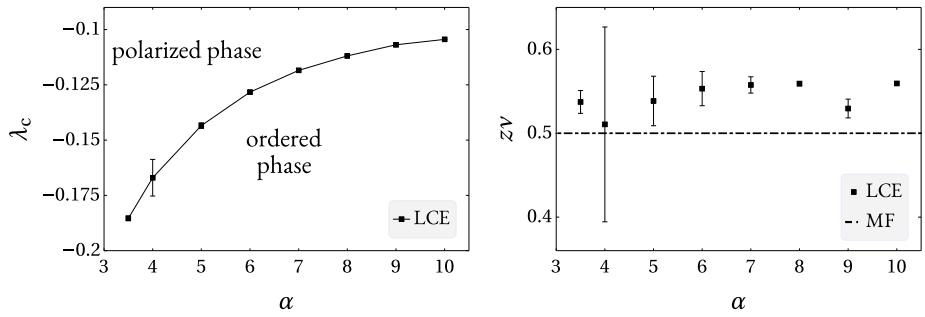

(a) Phase diagram (b) Critical exponent

Figure 4.11: Quantum-critical points λ_c (a) and critical exponents $z\nu$ (b) as a function of α for the antiferromagnetic case of the LRTFIM on a cubic lattice. Black squares represent averaged DLog Padé extrapolants of $\Delta_{\text{cub, f}}$ of the highest available order. The mean field (MF) exponent is illustrated as horizontal dashed line.

4.3 TRIANGULAR LATTICE

The TFIM on a triangular lattice is especially interesting due to its complex highly degenerate ground state present at low fields for nearest-neighbor antiferromagnetic Ising interactions. In this limit an order-by-disorder phenomenon drives a phase transition between a paramagnetic state and a clock-ordered state with a $\sqrt{3} \times \sqrt{3}$ structure that is located at $\lambda_c \approx -0.305$ [IM03; Pow+13] in the 3D-XY universality class with $z\nu \approx 0.67$ [GH94]. The clock order, visualized in Figure 4.12b, corresponds to the wave vector $\boldsymbol{k} = (2\pi/3, -2\pi/3)^T$ which is measured with respect to the lattice vectors defined in Figure 4.12a. In this section we study the effect of long-range interactions on this system which is already a demanding problem in the nearest-neighbor case [Pow+13].

For ferromagnetic interactions the question arises, if the same continuously varying exponents are present in the long-range-interacting model that were found in the LRTFIM on the hypercubic lattices (cf. Sections 4.1 and 4.2). The ferromagnetic NN model is unfrustrated and displays a 3D-Ising transition between a paramagnetic and a $\mathbb{Z}_2$-symmetry-broken ordered phase at $\lambda_c \approx 0.105$ [Yan77] with $z\nu \approx 0.63$ [Kos+16].

Parts of this section have been published in and are taken from Reference [FKS19].

4.3.1 *Dispersion*

As was also shown for the square lattice above, for different values of quasimomentum $\boldsymbol{k}$, the MCMC calculations are performed for different α-values. Analyzing the dispersion

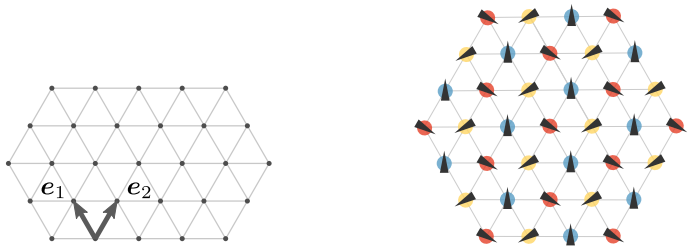

(a) Triangular lattice (b) Clock order

Figure 4.12: Definition of the unit vectors on the triangular lattice (a) and an illustration of the clock order with quasimomentum $\boldsymbol{k} = (2\pi/3, -2\pi/3)^T$ (b). Beware, that the arrows do not represent the spins in real space.

$\omega(\boldsymbol{k})$ allows again localizing the minimum of the one-QP gap in momentum space and gives an indication of the magnetic order of the phase after a potential gap closing in case of second-order phase transitions. The dispersion of the LRTFIM on the triangular lattice is shown for an antiferromagnetic interaction $\lambda = -0.3$ for characteristic values $\alpha \in \{2.5, 3, 4\}$ in Figure 4.13.

When investigating the dispersion for modes softening for small values of α we do not find any signs indicating a second-order phase transition to a different state than in the NN limit. The minimum of the dispersion remains fixed at $\boldsymbol{k}_{\text{clock}} = (\pm 2\pi/3, \mp 2\pi/3)^T$ for all computed high-symmetry $\boldsymbol{k}$-points and α therefore defining the location of the one-QP energy gap.

On the one hand, it is not possible to exclude a minimum at a $\boldsymbol{k}$ value which was not computed. Calculating more values is computationally very intensive such that I focused on the presented high-symmetry points in the Brillouin zone. Also, we expect an ordered phase to exist at a high-symmetry point which justifies the focus on these points.

On the other hand, with our calculations we are only able to detect second-order phase transitions. The possibility for a first-order QPT to a different phase than the clock order at small α cannot be excluded conclusively. For a more detailed discussion see Sections 4.3.3 and 4.4.

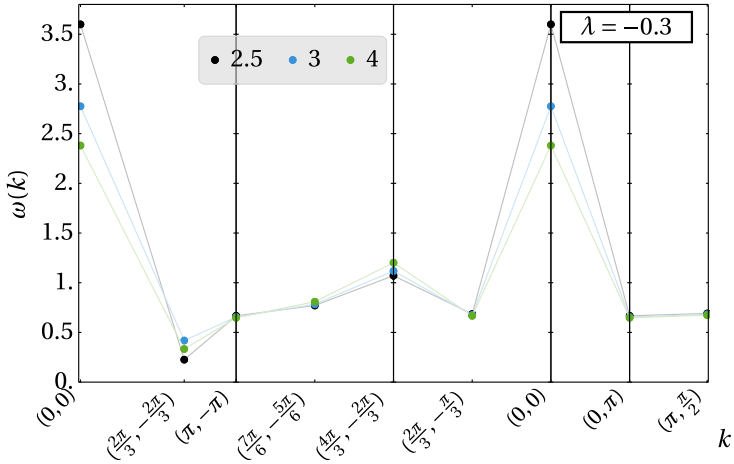

Figure 4.13: The one-QP dispersion of the antiferromagnetic LRTFIM on the triangular lattice for $\alpha = 2.5$ and $\lambda = -0.3$ shows a clear minimum at $\boldsymbol{k}_{\text{clock}} = (\frac{2}{3}\pi, -\frac{2}{3}\pi)^T$ which is the order momentum of the clock-order known from the nearest-neighbor limit. Within the calculated momenta at several high-symmetry points, we do not find any other momentum lowering the energy gap enough to replace the clock-order momentum.

4.3.2 *Ferromagnetic interaction*

Similar to the square lattice it is possible to express the first-order contribution analytically by introducing a Dirichlet L-series[3] for $\boldsymbol{k} = \boldsymbol{0}$, while higher orders up to order 10 were evaluated with MCMC calculations. The first-order contribution is given by

$$\Delta^{(1)}_{\text{tr, f}} = -6\zeta\left(\frac{\alpha}{2}\right) g\left(\frac{\alpha}{2}\right) . \tag{4.14}$$

Again, we start the discussion of the quantum-critical behavior with the ferromagnetic interaction. For $\alpha \to \infty$ the LRTFIM on the triangular lattice is in the 3D-Ising universality class with $z\nu \approx 0.63$ [Kos+16]. As a function of α, a similar behavior as for the LRTFIM on the hypercubic lattice is expected [FS16; DB01], with a critical exponent $z\nu$ that varies continuously in a certain range of α from the 3D-Ising to the MF value $(z\nu)_{\text{MF}} = 1/2$. The boundaries in α of continuously varying exponents are shifted to the same values $\alpha = 10/3$ and $\alpha = 6$ as for the square lattice [DB01] since only the dimension factors into the value. I show our results for λ_c and $z\nu$ in Figure 4.14 along with the MF results (dot-dashed lines) and the QMC data points for $\alpha = 3$ on the triangular lattice (blue triangles) [Hum16], which agrees well with our data. For a large $\alpha = 10$ the critical

3 In this case a different series $g\left(\frac{\alpha}{2}\right)$ is introduced (see Section B.2).

value λ_c is already very close to its nearest-neighbor correspondent. Strengthening the longer-range couplings by reducing α stabilizes the $\mathbb{Z}_2$-broken phase and λ_c decreases. In the limit $\alpha \to 2$ the phase transition happens at $\lambda_c \to 0$, while for exactly $\alpha = 2$ the sums diverge and Equation (2.42) becomes ill-defined. However, for very small $\alpha \leq 2.5$, where the MF ansatz is expected to be quantitatively correct, I find a very good agreement of the MF curve and the critical values calculated with the LCE.

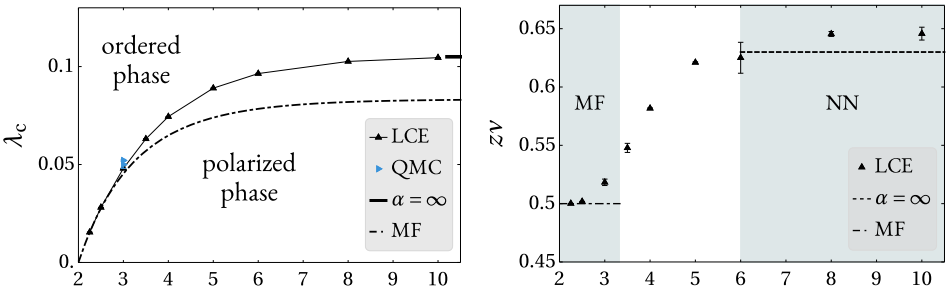

(a) Phase diagram (b) Critical exponent

Figure 4.14: Quantum-critical points λ_c (a) and critical exponents $z\nu$ (b) as a function of α for the ferromagnetic case of the LRTFIM on a triangular lattice. Black triangles represent averaged DLog Padé extrapolants of $\Delta_{\mathrm{tr,\,f}}$ of the highest available order. The mean field (MF) and NN TFIM universality classes are illustrated as shaded backgrounds and the associated critical exponents as horizontal lines.

The exponent $z\nu$ is again slightly overestimated by the DlogPadé extrapolation for large values of α since subleading corrections to the critical behavior are ignored. Compared to the known value $z\nu \approx 0.63$ [Kos+16] of the nearest-neighbor TFIM [Kos+16; OHW91] the presented results are about 3% too large. In the opposite limit of small α the critical exponent $z\nu$ approaches the MF value 0.5 also confirming the expected MF limit.

For the triangular lattice multiplicative logarithmic corrections at $\alpha = 10/3$ can be expected, too. While these are neglected in the evaluation, consequently leading to a deviation from the exact MF value $(z\nu)_{\mathrm{MF}} = 0.5$, we can extract the logarithmic exponent as for the square lattice and find $p_{\mathrm{tr}} \approx -0.143(7)$. This is remarkably close to the predicted value of $p = -1/6$ for the logarithmic correction of the 3D TFIM from perturbative RG and series expansions [LK69; BLGZJ73; WR73; WOH94; Coe+16] and further strengthens our interpretation of the long-range model as a TFIM in an effective dimension.

Another observation can be made when comparing the critical exponents for both, the square and triangular lattice. Not only are the boundaries for the MF and NN criticality

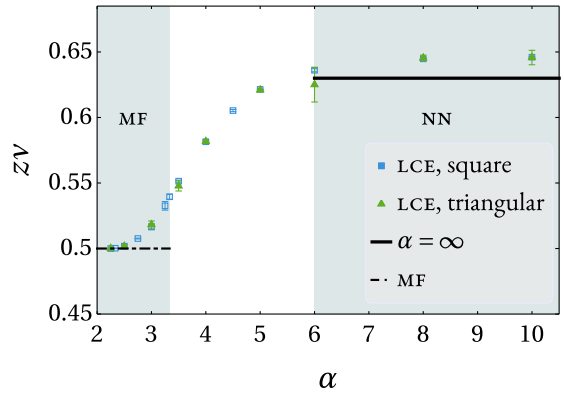

Figure 4.15: A comparison of the critical exponents $z\nu$ of the ferromagnetic LRTFIM on the square and triangular lattice shows a very good agreement between both curves. This independence of the criticality with respect to the underlying lattice structure and the dependence only on the dimension of the lattice can be seen as a meta-universality.

located at the same value of α and the same exponent p of the multiplicative logarithmic correction is expected. Also in the continuously varying regime the estimated critical exponents agree extremely well on both lattices. To illustrate this, the critical exponents $z\nu$ for both lattices are plotted on top of each other in Figure 4.15. This behavior can be described as a kind of meta-universality since the universality class of both models changes identically with the parameter α and independent of the microscopic lattice structure.

4.3.3 *Antiferromagnetic interaction*

Also for $\boldsymbol{k} = (2\pi/3, -2\pi/3)^T$ an analytic expression for the first order can be found as

$$\Delta^{(1)}_{\text{tr, af}} = -3\left(3^{1-\frac{\alpha}{2}} - 1\right)\zeta\left(\frac{\alpha}{2}\right)g\left(\frac{\alpha}{2}\right), \tag{4.15}$$

while again higher-order series coefficients up to order 10 were evaluated using MCMC calculations.

For an antiferromagnetic interaction an inherently different behavior can be expected not only with respect to the ferromagnetic case but also compared to the antiferromagnetic model on the square lattice. Already in the nearest-neighbor limit $\alpha \to \infty$ one finds a different universality class, since the TFIM on the triangular lattice displays 3D-XY universality due to the strong geometric frustration resulting in a $\sqrt{3} \times \sqrt{3}$ order at small fields [IM03; Pow+13]. There is no MF limit for small values of α and it is therefore not

at all obvious how the quantum-critical behavior changes as a function of α in these frustrated systems.

The results for λ_c and $z\nu$ are shown in Figure 4.16. As expected, stronger competing interactions introduced by decreasing α stabilize the quantum paramagnet. As for the square-lattice results, we observe that the MCMC becomes less reliable for α close to 2 and the resulting alternating series in $|\lambda|$ with extremely large coefficients c_k (cf. Appendix F) are hard to extrapolate. This results in rather large error bars for $\alpha \leq 3$ as can be seen in Figure 4.16a. Consequently, only results for $\alpha \geq 2.5$ are shown in the phase diagram.

The known overestimation of $z\nu$ for large α [Pow+13; OHW91] is found as before. For the investigated α-regime the exponent $z\nu$ stays almost constant and close to the value of the nearest-neighbor TFIM $z/nu \approx 0.67$[GH94]. The extrapolation becomes problematic for $\alpha \lessapprox 2.5$ but additionally we expect a different physical scenario than on the square lattice where a paramagnet to Néel-ordered QPT is found. As for the square lattice and already discussed in Section 4.3.1 no indication for a gap closing at different values of $\boldsymbol{k}$ is observed. Most likely, the phase transition becomes first order and a stripe-ordered state is realized at small fields for $\alpha \lessapprox 2.5$. Indeed, tensor network calculations of the LRTFIM on cylinders find a zigzag-stripe order for $\alpha \lessapprox 2.4$ [SBM18] and the bare 2D Ising model displays *straight*-stripe order [SKM16; Koz+19]. Most importantly, the phase transition between the straight-stripe order and the polarized phase is known to be first order because both $\mathbb{Z}_2 \times \mathbb{Z}_3$ symmetries are broken at the same time [SKM16; Koro5]. The only possibility to maintain a transition from one phase to the other without a first-order phase transition in this case can only be realized by two second-order phase transition where first one of the symmetries is broken and afterwards the second symmetry. Consequently, our approach for the triangular lattice is most probably primarily limited by the first-order nature of the phase transition for $\alpha \lessapprox 2.5$ which cannot be tracked by investigating gap closings. To further investigate the order phenomenon and perform a more direct comparison to the tensor network calculation cylindrical triangular lattices are studied in Section 4.4.

4.4 CYLINDRICAL TRIANGULAR LATTICE

In 2018 Saadatmand *et al.* set up a study of the quantum properties of the LRTFIM on a triangular lattice using infinite-size density matrix renormalization group (iDMRG) calculations. The applicability of the method is limited to one-dimensional lattice systems, so they chose to map the 2D lattice onto the surface of a cylinder [SBM18]. The cylinder, while infinite in one direction has a finite circumference and is therefore effectively a quasi-one-dimensional system. When investigating this system one has to be aware that effects that depend on the dimensionality of the system might thus be lost. However, for select values of the circumference, certain magnetic orders, which are also possible

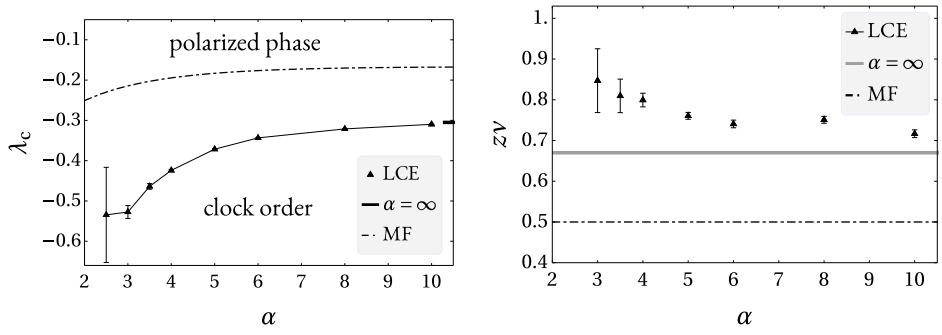

(a) Phase diagram (b) Critical exponent

Figure 4.16: Quantum-critical points λ_c (a) and corresponding critical exponents zv as a function of α for the antiferromagnetic case of the LRTFIM on a triangular lattice. Black triangles represent averaged DLog Padé extrapolants of $\Delta_{\text{tr, af}}$. The MF result for the clock-order is shown to emphasize the fact that a MF description is not suited in case of an antiferromagnetic interaction. Large scattering of λ_c for small α might indicate a different scenario than a second-order QPT to the clock order. The NN exponent $zv \approx 0.67$[GH94] and $\lambda_c \approx -0.305$[IM03; Pow+13].

candidates for the low-field phase of the LRTFIM with an antiferromagnetic interaction on the 2D system, are possible. For example, the cylinder with a circumference of six lattice sites is able to host several stripe-ordered quantum phases as well as the clock-ordered phase known from the NN model. In their publication, apart from such a type of clock order as well as a trivial polarized phase, a symmetry-broken columnar stripe phase is present in the ground-state phase diagram [SBM18].

The goal of this section is to gain a deeper understanding of the frustrated antiferromagnetic LRTFIM and complement the iDMRG results computed by Saadatmand *et al.* [SBM18]. To this end, LCEs in the high-field limit are combined with perturbative low-field expansions[4] about stripe-ordered phases and a perturbative evaluation of the clock-ordered ground state to map out the ground-state phase diagram. The focus is here on cylinders with circumference 4 and 6.

The phase diagrams are determined as follows: In the high-order linked-cluster expansion from the high-field limit we consider a second-order QPT from the polarized phase to the clock-ordered phase by investigating the closing of the one-QP gap similar to the previous sections. A continuous gap-closing of a certain mode signals a continuous quantum phase transition between the z-polarized phase and the associated ordered phase. The transition lines between the clock and stripe orders are located by determining the crossings of the respective ground-state energies for a selected α-value. The ground-

4 Details on the low-field expansion are given in Appendix Section E.

state energy for these orders is determined in a low-field expansion in order six. As a consequence of their symmetries we expect strong first-order phase transitions between those phases, although we are not able to extract the nature of the phase transition numerically.

Parts of this section have been published in Reference [Koz+19].

4.4.1 *Geometry*

The cylindrical lattice can be constructed by rings of spins-1/2 with circumference n. These rings are coupled along the x direction forming a triangular lattice with an infinite extension in this direction. The lattices, labeled XC(n) depending on their circumference, are exemplarily illustrated for the XC(6) cylinder in Figure 4.17. Next to the cylinder the planar geometry that is used for measuring the respective distances between the spins is shown with the corresponding unit vectors of the lattice.

The geometry leads to a discrete momentum in Fourier space for the direction $\boldsymbol{e}_2$ orthogonal to the infinite cylinder extension due to the finite circumference while it is continuous in the second direction $\boldsymbol{e}_1$ due to the infinite extension.

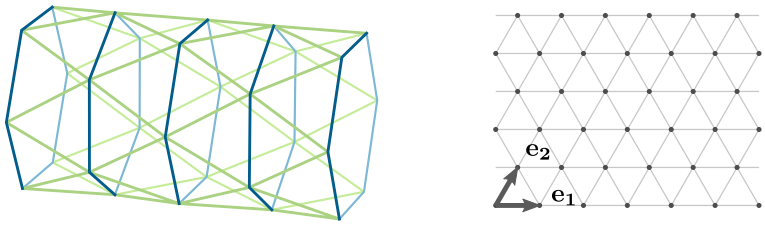

(a) 3D illustration (b) Lattice vectors

Figure 4.17: Illustration of the XC(n) cylinder geometry for $n = 6$. The left panel shows a 3D representation where the periodic rings are highlighted in blue while the right panel illustrates the planar geometry used to measure distances between the lattice sites and the lattice vectors. The lattice sites are periodically coupled in $\boldsymbol{e}_2$ direction and extend infinitely in $\boldsymbol{e}_1$ direction.

4.4.2 *Pure LRIM*

In the following, we consider the pure (classical) LRIM with vanishing transverse field $h = 0$. Here, it is *a priori* not clear as a function of α which classical state is the ground state. In the following we want to clarify the nature of the ground state for the XC(n) cylinders and their respective ground-state energy per site, which is then used to set up a

low-field expansion. The calculation in this limit has been done by J. Koziol [Koz+19] (cf. Appendix A).

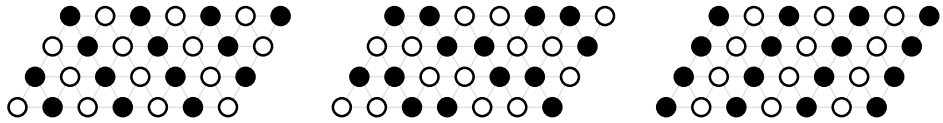

(a) Plain stripes (b) Zigzag stripes (c) Orthogonal stripes

Figure 4.18: Illustration of (left) plain-stripe state $[\boldsymbol{k} = (\pi, \pi)^T]$, (middle) zigzag-stripe state $[\boldsymbol{k} = (\pi/2, \pi)^T]$, and (right) orthogonal-stripe state $[\boldsymbol{k} = (\pi, 0)^T]$ on a triangular-cylinder lattice. Parallel (antiparallel) spins are shown as circles with same (different) colors. In the limit $n \to \infty$ plain and orthogonal stripes are symmetric.

By studying the energy of the NN ground states on finite cylinders with $N \approx 40$ spins for $\alpha < \infty$, we observe that the relevant states for the LRIM consist only of *non-flippable* plaquettes in the quantum dimer language on the dual lattice introduced in Section 2.2.1. These states are symmetry-broken and therefore gapped and stable against quantum fluctuations introduced by small transverse magnetic fields. We name the three relevant occurring order patterns *orthogonal* $[\boldsymbol{k} = (\pi, 0)^T]$, *plain* $[\boldsymbol{k} = (\pi, \pi)^T]$, and *zigzag* $[\boldsymbol{k} = (\pi/2, \pi)^T]$ *stripes* and illustrate them in Figure 4.18.

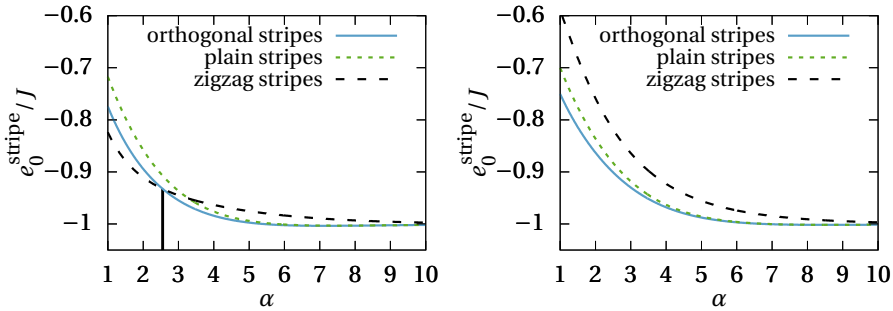

(a) XC(4) lattice (b) XC(6) lattice

Figure 4.19: Energy per site e_0^{stripe} for the considered stripe patterns evaluated on the XC(4) lattice for $N = 4 \times 10^3$ lattice sites (left panel) and on the XC(6) lattice for $N = 6 \times 10^3$ lattice sites (right panel) with periodic boundary conditions. The thick black vertical line in the left panel indicates the position α_c of the first-order phase transition between zigzag ($\alpha < \alpha_c$) and orthogonal ($\alpha > \alpha_c$) stripes for the XC(4) cylinder. For the XC(6) orthogonal stripes have the lowest energy for any finite α and consequently are realized for all α.

In the orthogonal-stripe configuration spins with the same orientation order along the second lattice vector $\boldsymbol{e}_2$, which does not point in the infinite direction of the cylinder, forming alternating rings of parallel spins. This leads to a two-fold degeneracy which results from the $\mathbb{Z}_2$ spin-flip symmetry of the state. Flipping every spin results in the same state on the infinite lattice only shifted by $\boldsymbol{e}_1$. In the plain-stripe state spins of the same orientation align in plain chains winding around the cylinder in direction of infinite extension. This pattern has a $\mathbb{Z}_2 \times \mathbb{Z}_2$ symmetry, which results from a spin-flip symmetry and a decoupling of the state into two sublattices. Additionally to flipping every spin it is possible to shift the pattern by $\boldsymbol{e}_2$ to obtain a symmetric state. In the 2D limit orthogonal and plain stripes are degenerate with a $\mathbb{Z}_2 \times \mathbb{Z}_3$ symmetry due to spin flips and the threefold rotational symmetry of the lattice. The absence of this rotational symmetry for the XC(n) cylinders leads to the energetic separation of orthogonal and plain stripes, where orthogonal stripes have lower energies for all decay exponents α on the XC(4) and XC(6) lattice. In fact, the preference of orthogonal stripes is seen for all studied XC(n) cylinders with even n.

The third identified ground-state pattern are the zigzag stripes where spins of the same orientation align in a zigzag shape in cylinder direction. This results in a four-fold degeneracy ($\mathbb{Z}_2 \times \mathbb{Z}_2$), again due to spin-flip symmetry and a decoupling into two sublattices. On the XC(n) cylinders with $n = 4s$ ($s \in \mathbb{N}$) it is actually possible to rotate the zigzag stripes by $2\pi/3$ and to remain in the subspace of states with only non-flippable plaquettes. These rotated zigzag stripes are always energetically less beneficial than the zigzag stripes with an alignment in infinite direction and we will not consider them any further.

At small α zigzag stripes are energetically lower compared to the orthogonal stripes for the XC(4), XC(8), and XC(12) cylinder (see Figure 4.19a). Consequently, there must be a first-order phase transition between these two stripe phases for these cylinders and we can determine the associated critical α_c which are listed in Table 4.1.

Table 4.1: Critical decay exponents α_c for a phase transition between orthogonal ($\alpha > \alpha_c$) and zigzag ($\alpha < \alpha_c$) stripes on the XC(n) lattices with $n \in \{4, 8, 12\}$. The denoted lattices are the ones where the transition occurs in the considered range of $\alpha > 1$ in the framework of our numerical real-space implementation.

n	4	8	12
α_c	2.55(1)	1.41(1)	1.13(1)

The favoring of these stripe patterns can be explained by looking at the dominant further-neighbor Ising interactions which are contributing differently to the energy, depending on the considered type of stripe order. For zigzag stripes the second-near-

est neighbors are contributing less beneficial than for the orthogonal stripes, but the third-nearest neighbors are lowering the energy more than they do for the orthogonal stripes. Together with the periodicity of the XC(n) cylinder this leads to a favoring of the zigzag stripes at low α for the lattices described above, since then the long-range Ising interactions come more and more into play. Such stripe patterns have also been found by Smerald *et al.* for a truncated long-range Ising interaction [SKM16]. For a classical Hamiltonian with arbitrary tunable antiferromagnetic nearest- and next-nearest-neighbor interaction it is a well established result that on the triangular 2D lattice $\mathbb{Z}_2 \times \mathbb{Z}_3$ plain stripes realize the ground state of the system [Met74; Koro5]. On any XC(n) lattice with finite n this degeneracy of plain and orthogonal stripes is lifted. Compared to the plain-stripe order, the $(n+1)$-nearest neighbors of the orthogonal stripes are missing two ferromagnetic interactions for each site along the cylinder ring due to the finite cylinder extension. Instead two additional antiferromagnetic interactions per site are present which leads in total to a lower energy of orthogonal stripes. A second consequence of the cylinder geometry is the relevance of a zigzag-striped order. Further, we note that these three stripe patterns are part of the $\alpha = 0$ and ∞ ground-state space. Using the $\alpha = 0$ limit of the LRIM with the logarithmically increasing perturbation described in Equation (2.51) confirms above findings. To this end, we considered all $\alpha = 0$ ground states on a finite cluster of $N \approx 40$ spins which leads to the same ground-state space of non-flippable plaquettes. Evaluating the energy for the three relevant stripe patterns on large clusters $N \approx 10\,000$, we find the same stripe-ordered ground states as calculated directly from the full LRIM.

We therefore conclude that the physical behavior of the LRIM is different for the two families of cylinders with $n = 4s$ ($s \in \mathbb{N}$) and $n = 4s+2$ ($s \in \mathbb{N}$). For $n = 4s+2$ orthogonal stripes are realized for all studied α, while in the other case orthogonal stripes become unstable towards a zigzag-stripe order for small α. This can be clearly seen in the energy evolution of the different stripe structures as a function of α, which is shown in Figure 4.19 for the smallest member of both families, XC(4) and XC(6), respectively, where we have studied finite cylinders with $N(\mathrm{XC}(n)) = n \times 10^3$ spins using periodic boundary conditions. In the limit of $n \to \infty$ we expect that both families display the same ground state. This is in accordance with our finding that α_c is reduced with increasing n.

Until now, only the classical LRIM was studied for several cylinder sizes n and values of α. In the following, we focus on these two cylinders and study the ground-state phase diagram of the full LRTFIM.

4.4.3 *XC(6)*

Let us first consider the XC(6) lattice which is built from rings with six sites. To find the ground-state symmetry for an infinitesimal field we can consider the dimer model introduced in Section 2.2.1. The clock-ordered state on the full 2D triangular lattice has a periodicity of 3 in each lattice direction which is compatible with the XC(6) lattice such that we expect the same order for small magnetic fields. We find that the maximally flippable state which is energetically selected indeed represents the clock order with a quasimomentum of $\boldsymbol{k} = (2\pi/3, -2\pi/3)^T$. The maximally flippable state on the XC(6) lattice is illustrated in Figure 4.20 along with an illustration of the clock order. Note, that the rotation of the clock-ordered spins is used to illustrate the phase factor between the spins on different sites and does not represent the orientation in real space.

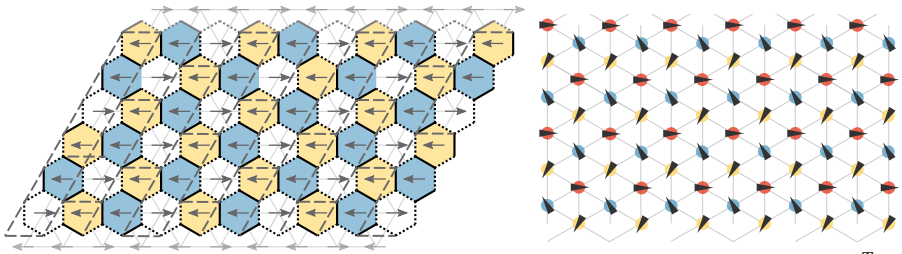

(a) Maximally flippable state

(b) Clock order $\boldsymbol{k} = (2\pi/3, -2\pi/3)^T$

Figure 4.20: (Left) The maximally flippable state of the XC(6) lattice and (right) the resulting clock order in the low-field limit of the NN model. Arrows represent phase factors and not the real-space orientation of the spins.

For the nearest-neighbor TFIM on the 2D triangular lattice, the quantum phase transition between the clock order and the high-field z-polarized phase is known to be second order in the 3D-XY universality class [MS01; IM03; Pow+13]. For finite $\alpha < \infty$, the nature of this quantum phase transition is unchanged for all $\alpha \gtrapprox 2.5$ [FKS19; Hum16].

Saadatmand *et al.* investigated the LRTFIM on the XC(6) cylinder for $\alpha \in (1, 5)$ as well as the TFIM using the iDMRG approach [SBM18]. For $\alpha > 2.40(5)$ they find the same quantum phases as for the 2D triangular lattice with a transition between the clock order and the z-polarized phase. The critical point for the TFIM is located at $h_c = 1.5(1)\,J$ as given in Reference [SBM18]. For $\alpha < 2.40(5)$, they observe a direct phase transition from the z-polarized phase into a different ordered phase, which we call zigzag-stripe phase (see Figure 4.18b for an illustration). Interestingly, our investigation of the pure LRIM for $h = 0$ confirms the appearance of stripe-ordered phases (for any finite α), although

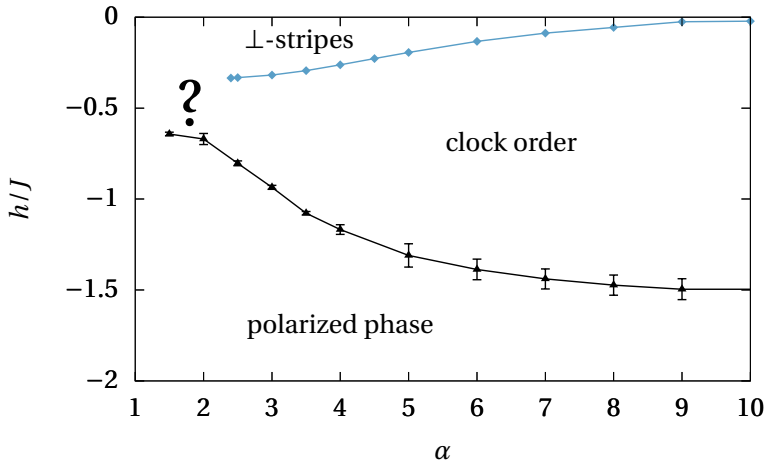

Figure 4.21: Ground-state phase diagram calculated for the XC(6) cylinder using series expansions. The black line is determined by the closing of the one-QP gap $\Delta_{(2/3\pi,-2/3\pi)}$ at momentum $\boldsymbol{k} = (2\pi/3, -2\pi/3)^T$ with the standard deviation of the Padé approximants up to tenth order. The blue line is determined by the energy intersection between the clock-order energy e_0^{clock} and the orthogonal(⊥)-stripe energy $e_0^{\perp}$ in sixth order. The question mark indicates the region of the phase diagram where the used methods break down.

we find a different stripe order to be realized which we attribute to a limitation due to the chosen unit cell in Reference [SBM18][5].

The obtained ground-state phase diagram for the LRTFIM on the XC(6) cylinder is shown in Figure 4.21. It displays the z-polarized phase, the clock order, and the orthogonal-stripe phase. The quantum phase transition between the z-polarized phase and the clock order is located by investigating the one-QP excitation energies of the z-polarized phase using the high-field expansion. For a non-first-order phase transition one expects that the one-QP gap of the z-polarized phase closes at the quantum-critical point with a momentum $\boldsymbol{k} = (2\pi/3, -2\pi/3)^T$, which is associated with the clock order. Here we locate such a gap-closing quantum-critical point by applying Padé extrapolations on the bare order 10 series (see Figure 4.22a) and we quantify the uncertainty of this extrapolation scheme by the standard deviation of different extrapolations shown as error bars in Figure 4.21. We can track this gap-closing up to decay exponents $\alpha = 1.5$. The calculated phase-transition points for $\alpha \gtrapprox 2.4$ are within error bars in good agreement with the numerical findings by Saadatmand *et al.* [SBM18]. Specifically, for the TFIM at $\alpha \to \infty$, the PCUT high-field calculation yields a gap closing at a transverse field $h = 1.54(7)\, J$,

5 This was confirmed in private communication with I. McCulloch.

which has to be compared to $h = 1.5(1)\,J$ determined numerically by investigating the order parameter for the clock order using iDMRG [SBM18].

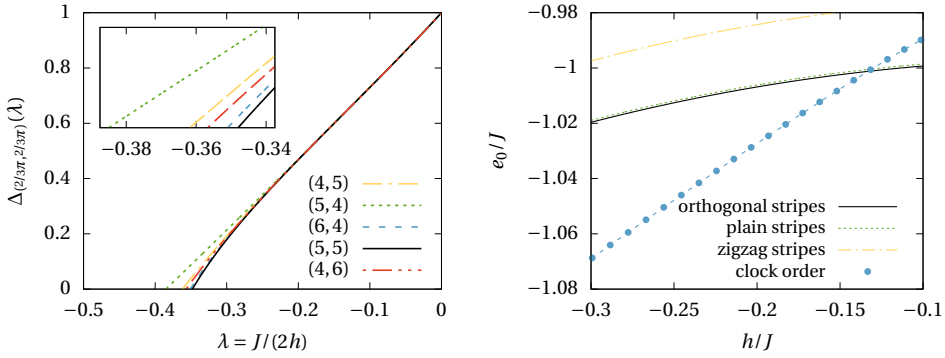

(a) Extrapolated one-QP gap (b) Ground-state energies

Figure 4.22: Determination of the phase boundaries of the XC(6) lattice, illustrated for $\alpha = 6$. (Left) The closing of the Padé-extrapolated one-QP gap determines the critical value between the high-field polarized and the clock-ordered state. (Right) The crossing between the ground-state energies is used to locate the expected first-order transitions.

The second type of phase transition present in the phase diagram is between the clock order and the orthogonal-stripe phase (see Figure 4.22b and top blue line in Figure 4.21). Since both phases break a different type of discrete translational lattice symmetry, this transition is first order. It can therefore be located by determining the level crossing $e_0^{\text{clock}} = e_0^{\perp}$ for a given value of α. As the ground-state energy e_0^{clock} of the clock-ordered state is evaluated on a finite cluster of six rings and the long-range interactions are included perturbatively, one has to be aware that the blue line in Figure 4.21 is certainly not quantitatively exact for small values of α. In fact, we expect the phase transition to occur at higher transverse fields h/J for small α, because a better treatment of the long-range interactions would result in an increased ground-state energy e_0^{clock} so that the orthogonal-stripe phase would be enlarged with respect to the clock order. In contrast, we (slightly) overestimate e_0^{clock} for large α due to the finite cluster extension and the approximate treatment of the field-induced quantum fluctuations. It is therefore plausible that for $\alpha \lesssim 2.4$ no clock order is present anymore in the phase diagram as suggested by Saadatmand *et al.* [SBM18] and there is a direct phase transition between the z-polarized and the orthogonal-stripe phase. Another possible scenario is the presence of an intermediate (gapless) phase as we discuss in Section 4.4.5. We stress again that orthogonal stripes are the true ground states of the zero-field LRIM and no zigzag stripes are realized in the LRTFIM as found by Reference [SBM18].

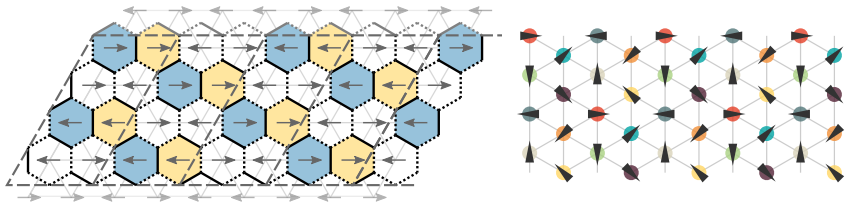

(a) Maximally flippable state (b) Clock order $\boldsymbol{k} = (5\pi/4, \pi/2)^T$

Figure 4.23: (Left) The maximally flippable state of the XC(4) lattice and the (right) the resulting clock order in the low-field limit of the NN model. Arrows represent phase factors and not the real-space orientation.

If there is a direct continuous phase transition between the orthogonal-stripe and the z-polarized phase, one expects that the high-field gap in the z-polarized phase closes at the critical point and is located at the associated momentum of the orthogonal-stripe phase $\boldsymbol{k} = (\pi, 0)^T$ for $\alpha \lessapprox 2.4$. To study the transition to the orthogonal-stripe phase, we therefore evaluated the one-QP energy at momentum $\boldsymbol{k} = (\pi, 0)^T$ in the high-field limit using Padé extrapolations. Interestingly, no closing of the gap could be observed so that we cannot confirm a direct phase transition between the z-polarized and the orthogonal-stripe phase using series expansion methods. There are two possible interpretations of this result: Either the situation is similar to the case of the 2D triangular lattice, where the direct phase transition is known to be generically first order due to the $\mathbb{Z}_2 \times \mathbb{Z}_3$ symmetry of the stripe order or the phase diagram contains an intermediate phase which we elaborate on further below.

4.4.4 *XC(4)*

Now, let us consider the XC(4) lattice which is built from rings with four sites. Again, we consider the dimer model to investigate the NN low-field ground-state. The clock-ordered state on the full 2D triangular lattice with a periodicity of 3 in each lattice direction is incompatible with the XC(4) lattice such that we expect a different order for small magnetic fields. We find that the maximally flippable state which is energetically selected also represents a clock order, but with a different quasimomentum of $\boldsymbol{k} = (5\pi/4, \pi/2)^T$. The maximally flippable state on the XC(4) lattice is illustrated in Figure 4.23 along with an illustration of the new clock order. Note, that the rotation of the clock-ordered spins is used to illustrate the phase factor between the spins on different sites and does not represent the orientation in real space.

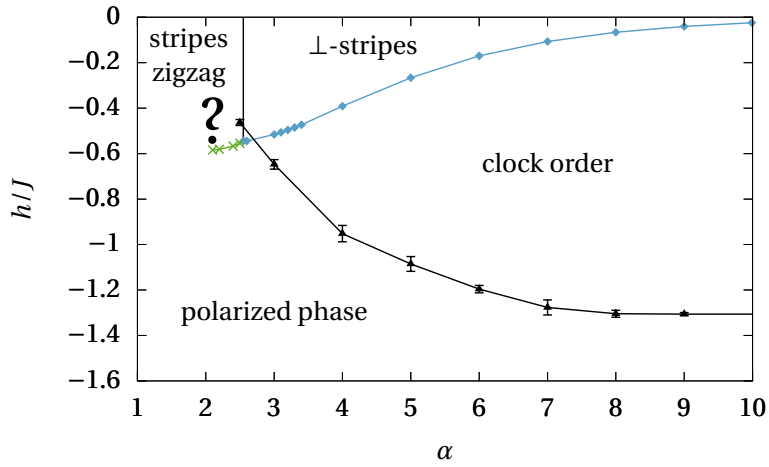

Figure 4.24: Ground-state phase diagram calculated for the XC(4) cylinder using series expansions. The black curve is determined by the closing of the one-QP gap with the standard deviation of the Padé approximants up to order ten. The blue line is determined by the energy intersection between the clock-order energy e_0^{clock} and the orthogonal(⊥)-stripe energy $e_0^{\perp}$ in sixth order. The green line denotes the intersection between the energy of the QDM in third order and the zigzag-stripe energy in sixth order. The almost vertical black line represents the first-order phase transition line between the zigzag and orthogonal stripes, which is determined by comparing the ground-state energies of both stripe phases. The question mark indicates the region of the phase diagram where the used methods break down.

The phase diagram of the XC(4) lattice, which has been calculated analogously to the phase diagram of the XC(6) lattice by employing high- and low-field series expansions, is shown in Figure 4.24.

Besides the z-polarized phase, a clock-ordered phase with a different momentum $\boldsymbol{k} = (5\pi/4, \pi/2)^T$ from the XC(6) (and, consequently, also from the 2D triangular) lattice arises. In addition to the orthogonal-stripe order with $\boldsymbol{k} = (\pi, 0)^T$ at finite large α already discussed for the XC(6) lattice, we find zigzag stripes with $\boldsymbol{k} = (\pi/2, \pi)^T$ for small fields. The first-order phase transition from the orthogonal to a zigzag order for small fields occurs at $\alpha \approx 2.55(1)$ (cf. Figure 4.19a). Interestingly, the phase transition between these two stripe orders is almost independent of h/J so that a nearly vertical phase transition line results (see black line in Figure 4.24). Further, for small α, one might predict a direct phase transition between the z-polarized phase realized at high field strength and the zigzag stripes at low field strength in similarity to the XC(6) cylinder. Padé extrapolations of the one-QP gap with $\boldsymbol{k} = (\pi/2, \pi)^T$ again do not point towards a continuous phase transition signaled by a gap closing in this α-regime. We therefore expect that the physical situation is similar to the XC(6) cylinder.

In the calculated phase diagram the intersection between the clock-order energy and the different stripe orders is calculated for all values of α for which the clock-order expansion is available. Even though the clock order is not expected to be the ground state for small α, the calculated line gives a reference point for the extension of the stripe-ordered phases. As for the XC(6) cylinder, we have to stress that the calculated energy for the clock order is underestimated because the long-range interactions are truncated due to the evaluation on finite clusters. This implies that the transition between stripes and clock order occurs at higher transverse fields for small decay exponents ($\alpha \lessapprox 3.5$).

4.4.5 *Physics of the LRTFIM on the XC(n) lattice*

In this section we investigated the ground-state phase diagram of the LRTFIM on triangular-lattice cylinders using various approaches. The goal was on the one hand to gain a deeper understanding of the physics of frustrated systems with long-range interactions and on the other hand to complement the iDMRG studies on such systems presented by Saadatmand *et al.* [SBM18]. We found that the physical behavior of the classical LRIM is different for the two families of cylinders with $n = 4s$ ($s \in \mathbb{N}$) and $n = 4s + 2$ ($s \in \mathbb{N}$). For $n = 4s + 2$ orthogonal stripes are realized for all studied α, while in the other case orthogonal stripes become unstable towards a zigzag-stripe order for small α. Our results are therefore distinct from the zigzag stripes obtained numerically for the XC(6) cylinder [SBM18], which is most likely due to the chosen unit cell in the iDMRG approach[6]. The full quantum phase diagram of the LRTFIM on the XC(4) and XC(6) cylinder contains at least three different types of gapped quantum phases. A z-polarized paramagnetic high-field phase, stripe phases triggered by the long-range Ising interaction, as well as clock-ordered phases being stabilized via an order-by-disorder mechanism about the highly-degenerate classical spin liquid of the nearest-neighbor Ising model [IM03]. The extension of these phases in the parameter space of the LRTFIM has been located approximately by a variety of different perturbative expansions. In contrast to the high- and low-field high-order expansion, the obtained ground-state energy of the clock-ordered phase is the least accurate due to the low order three of the effective Hamiltonian and due to the finite cluster size. The obtained ground-state phase diagrams are valid as long as one assumes that no other phase is present. However, this is not obvious, which leads to the following two points which deserve further investigations.

First, we turn our attention to the nearest-neighbor TFIM on the XC(6) cylinder, which realizes the same kind of clock order as the TFIM on the two-dimensional triangular lattice. For the 2D triangular lattice the QPT between the z-polarized and the clock-ordered phase is a continuous second-order transition which falls into the $(2+1)$D-XY universality class [MS01; IM03; Pow+13]. This follows from a mapping of the TFIM

6 Private communication with I. McCulloch.

onto a classical XY-model in three dimensions [Bla+84]. By applying the same kind of quantum-to-classical mapping to the quasi one-dimensional cylinders, one would expect that the transition falls into the $(1+1)$D-XY universality class, which is known to be the archetype of an infinite-order Kosterlitz-Thouless (KT) phase transition [KT73]. However, since the KT phase transition involves one phase with critical (algebraically-decaying) correlations and both the z-polarized and the clock-ordered phase are gapped, this implies the existence of a gapless intermediate phase in the ground-state phase diagram of the nearest-neighbor TFIM on the XC(6) cylinder so that there are two Kosterlitz-Thouless transitions out of this intermediate phase. For the corresponding classical phase transitions in the TFIM on the 2D triangular lattice as a function of temperature, such an intermediate phase as well as the associated KT transitions are well established theoretically [MSC00; IM03; Wan+17] and confirmed experimentally recently in the Ising-type triangular antiferromagnet $TmMgGaO_4$ [She+19; Li+20]. Clearly, this intermediate phase in the XC(6) cylinder will also extend in a finite α-window in the phase diagram of the LRTFIM and, by similarity, one would expect a similar phase also for the XC(4) cylinder. Let us note that the detection of a KT transition is not possible with our high-field expansion since the gap displays a non-analytic behavior close to such a phase transition. Further, we find it interesting that iDMRG calculations based on translational invariant states are in good agreement with our findings with respect to the phase transition line between the z-polarized and clock-ordered phase as a function of α [SBM18]. It is likely that both approaches are not sensitive enough to pinpoint the intermediate phase on the quasi one-dimensional XC(6) cylinder, but rather yield a good estimation for the transition line of the corresponding two-dimensional system on the triangular lattice. In any case, the existence and nature of the intermediate phase has to be clarified in the future.

Second, it is not clear how the ground-state phase diagram looks for smaller values of α when the clock order and potentially the just-discussed intermediate phase are not realized anymore. The numerical work of Reference [SBM18] on the XC(6) cylinder suggests a direct second-order phase transition between the z-polarized and a stripe-ordered phase. We stress again that our investigation clearly yields a different ordering pattern for the stripes, namely the orthogonal stripes shown in Figure 4.18. Extrapolations of the one-QP high-field gap with the corresponding stripe-momentum give no evidence for a gap-closing (second-order) phase transition. So this phase transition might be either (weakly) first order as for the LRTFIM on the triangular lattice [Kor05; SKM16; FKS19] or, again, an intermediate phase could be present between the z-polarized and the stripe phase which prevents a controlled extrapolation of the gap. An indication for the latter scenario might be the presence of an intermediate classical spin liquid as a function of temperature for a deformed classical Ising model with dipolar interactions on the triangular lattice [SM18].

5

FINAL REMARKS

In the final chapter of this thesis, let me shortly review the motivation for studying the topic, the algorithmic development and the presented results and give a short outlook on possible future projects.

The Ising model has been one of the most studied quantum spin models in the past as a result of its simplicity compared to other models while still providing meaningful results in the realm of quantum magnets and quantum phase transitions. With the focus shifting from the original model containing short-range, mostly nearest-neighbor, interactions to long-range-interacting systems [DB01; KLT12; Kna+13; Vod+15; SBM18] new approaches for treating such numerically-demanding systems with long-range interactions become necessary.

The increasing interest in these systems is a result of, on the one hand, the development and prospective availability of experimental setups [Bri+12; YJZ19] for directly verifying theoretical predictions. These artificial setups are pushing the development of quantum simulators further and require a thorough validation before predictions for systems can be determined that are unreachable with current theoretical methods. Also, in many naturally occurring systems long-range interactions are present and cannot be represented by a nearest-neighbor model [BRA96; BG01; Lah+09]. On the other hand, from a theoretical point of view, long-range interactions introduce effective dimensions and allow to study systems in non-integer dimensions [DTC15]. This results in continuously varying critical exponents of quantum phase transitions [Fis67; DB01; LB02], multiplicative logarithmic corrections [LK69; BLGZJ73; WR73; WOH94; Coe+16] even in dimensions below the upper critical dimension and classical phase transitions in one-dimensional systems, where previously no phase transition was possible [Isi25; Dys69; AY71; FS82]. Antiferromagnetic interactions can introduce frustration into the system and allow the occurrence of new phases [Koz+19].

Especially for long-range interactions finite-size effects are very pronounced [Jas+17] and increase when the value of parameter α is decreased. As a consequence, this demands methods that do not strongly limit the systems' size. Taking this into account, we developed a new perturbative ansatz in the high-field limit based on linked-cluster expansions with white graphs [CS15] to deal with such systems in the bulk limit. Using this new tool I was able to study the ground-state phase diagram and extract critical properties of quantum phase transitions (QPTs) for several lattice geometries. In this thesis I focused on the Ising model with long-range interactions decaying algebraically as $r^{-\alpha}$ with distance

r between two spins-1/2 at temperature $T = 0$. An additional transverse field introduces quantum fluctuations and allows tuning the system between different phases connected via a QPT.

For ferromagnetic long-range-interacting systems the continuous variation of critical exponents of the QPT within a certain range of α has been predicted in the past [Fis67; LB02] and analytical boundaries for the region have been determined [DB01]. I was able to confirm this property by deriving the critical exponents $z\nu$ from the perturbative series and found varying exponents for the ferromagnetic chain, the square, and the triangular lattice. For higher dimensions, i. e. dimensions three and upwards, mean field (MF) behavior is expected for the QPT with the exact MF exponent $z\nu = 0.5$. Since $d = 3$ is the upper critical dimension [Dut+15] of the classical Ising model, we expect multiplicative logarithmic corrections with exponent $p = -1/6$ in the nearest-neighbor limit $\alpha = \infty$ [LK69; BLGZJ73; WR73; WOH94; Coe+16]. This results in slightly overestimated exponents in our perturbative approach and a slight variation of the exponents with α appears also for the LRTFIM on the 3D cubic lattice which, however, has a different origin than that on the lower-dimensional lattices. We found that it is possible to interpret the parameter α as a modifier of the system's dimension such that we can consider an effective dimension of the system as also discussed in [DTC15] using RG methods. Therefore, for the two-dimensional lattices, we expect the same multiplicative logarithmic corrections as on the cubic lattice although at a finite value of $\alpha = 10/3$, while on a one-dimensional spin chain they are present at $\alpha = 5/3$ [DB01]. The critical exponent of those corrections is extremely sensitive on the exact numerical value of the QPT's location λ_c and the value of the critical exponent $z\nu$. However, we know that $z\nu = 1/2$ exactly at this point [DB01] so I was able to use this exponent as a bias for the extrapolations. The extracted values of $p_{ch} = -0.16285(4)$, $p_{sq} = -0.17(4)$, and $p_{tr} = -0.143(7)$[1] for the 1D chain, the square, and the triangular lattice are therefore remarkably close to the prediction of $p = -1/6$ for the cubic TFIM [WOH94], supporting our interpretation of α as introducing an effective dimension into the system.

A long-range antiferromagnetic interaction introduces frustration into the previously unfrustrated TFIM on bipartite lattices such as the chain and 2D square lattice. Here, no continuously varying exponents and no MF behavior were found. For the complete investigated range of α the computed critical exponents remained close to their nearest-neighbor pendant as was also predicted in [Sun17] for the 1D case.

We also performed an in-depth evaluation of the antiferromagnetic LRTFIM on the triangular lattice which is especially demanding because it is already highly frustrated in the nearest-neighbor limit and the effect of additional long-range interactions is unknown so far. A previous study indicated the occurrence of stripe-ordered ground

1 Values in brackets represent standard deviations of the different DLog Padé extrapolations.

states in the low-field limit for small values of α [SKM16; SBM18] while for the $\alpha \to \infty$ limit a clock order introduced by an order-by-disorder phenomenon is expected [IM03; Pow+13]. I was able to confirm the second-order phase transition to the clock-ordered state at quasimomentum $\boldsymbol{k} = (\pm 2\pi/3, \mp 2\pi/3)$ for large α while for small $\alpha \lessapprox 2.5$ the series expansions yielded unreliable results. The breakdown of the method for small values of α can be a sign for a different scenario than a second-order phase transition to the clock-ordered state.

These insights required further investigation which could also be compared to the results of Saadatmand *et al.* [SBM18] and was performed on triangular lattices, mapped to a finite cylinder geometry. We were able to confirm the existence of a stripe-ordered low-field ground state, though a different one from the state predicted by iDMRG calculations [SBM18]. For the cylindrical lattice the phase diagram becomes much more complex than in the 2D case. We expect cylinders with a circumference of 6 sites, which is compatible with the clock order present in the TFIM on the triangular lattice, to support a QPT from the polarized phase in the high-field limit to the clock-ordered state. A similar quantum-to-classical mapping as between the classical XY and the quantum Ising model that proves the existence of a second-order QPT in the $(2+1)$D-XY universality class for the 2D triangular lattice, implies an infinite-order $(1+1)$D-XY transition on the effectively one-dimensional cylinder lattices. Consequently, it can be assumed that a gapless intermediate phase between the z-polarized and clock-ordered phase should exist with two separate KT transitions which is a well established theoretical phenomenon [MSC00; IM03; Wan+17] and recently even confirmed experimentally [She+19; Li+20].

For even smaller magnetic fields a second phase transition of first-order from the clock order to a stripe order is expected. For small values of α the picture becomes less clear. However, we found indications for the absence of a clock-order phase and a direct first-order transition from the polarized to the stripe phase for values of $\alpha \lesssim 2.4$.

The phase diagram is slightly different when the cylinder circumference is decreased to 4 sites. For once, the clock order has a different order momentum of $\boldsymbol{k} = (5\pi/4, \pi/2)^T$ since the original clock order of the 2D Ising model on the triangular lattice is incompatible with this cylinder geometry. For large α we also find a second-order phase transition from the polarized high-field phase to this clock order, followed by a transition to the same stripe order as for the 6-site cylinder at $\alpha < \infty$. In contrast to the larger cylinder, a different stripe phase appears for small values of $\alpha \lessapprox 2.55(1)$ with an expected first-order transition between the polarized and the stripe state.

For a future investigation of this topic there are several pathways that I hope will be followed. First of all, the study of the LRTFIM on triangular cylinder lattices leaves several questions open. Since the gapless phase involved in the KT transition on the cylinder lattices cannot be detected by high-field LCEs, this demands a further investigation of this point using different methods.

The effects of frustration which become already visible on the spin chain and square lattice and led to the interesting properties on the triangular lattices can be studied further in the LRTFIM on different lattice geometries, including lattices with larger unit cells such as, e. g., the honeycomb or Kagome lattice. With ferromagnetic interactions the critical exponents should display the same variation of critical exponents as found for the investigated two-dimensional lattices. For antiferromagnetic interactions on the honeycomb lattice I expect a qualitatively similar behavior as found for the square lattice since both, honeycomb and square lattice, are unfrustrated in the nearest-neighbor limit. The LRTFIM on the Kagome lattice should display a behavior which is closer to the triangular lattice. In the nearest-neighbor limit the TFIM on the Kagome lattice is highly frustrated for zero magnetic field comparable to the TFIM on the triangular lattice. However, applying an infinitesimal magnetic field displays a disorder-by-disorder scenario with the system immediately realizing a polarized phase in contrast to the clock order induced for the triangular lattice [Pow+13]. With additional long-range interactions I would expect the degeneracy on the Kagome lattice at zero field to be lifted such that a QPT from this ordered to the disordered high-field phase can be expected for all $\alpha < \infty$.

Additional quantities such as magnetization or structure factors can in principle be determined with LCE methods and a computation might allow the comparison to different properties measured in future experiments. It should also be straightforward to determine two-QP energies and examine the possible presence of bound states, although only the study of finite systems would be feasible which is a strong limitation for the long-range-interacting system.

The basic approach further offers the possibility to study different models. Here, the original Ising model can be extended by randomizing the interactions or using random magnetic fields. The former has already been proven feasible for perturbative LCEs for the short-range Heisenberg model [HWS18]. It would be interesting to see if disorder effects that break the translational invariance of the system such as, e. g., many-body localization survive in long-range-interacting systems. Light-matter interactions often induce long-range interactions [JSM16; Vai+18; OPR16; Dou+15] and can be studied in effective models. An appealing different path would be the inclusion of these interactions directly in the Hamiltonian. Additionally, the application of the methodological setup developed in this thesis to Heisenberg, XY, and other models and also to systems displaying topological order should be straightforward if the general conditions of the PCUT method are fulfilled.

Most perturbative calculations presented in this thesis were done in the high-field limit, where Ising interactions acted as a perturbation. As a first step of an investigation from the opposite limit, we evaluated the model from the ordered phase with a perturbative transverse magnetic field for the one-dimensional spin chain for a low perturbation

order [Rit19]. An evaluation to higher orders and a possible transfer of the approach to other lattices would be a promising ansatz for further numerical computations.

The presented results in this thesis are a first glimpse into the exciting possibilities of the application of perturbative linked-cluster methods to systems with long-range interactions. This opens a new window into prospective studies of properties induced into familiar models by considering true long-range physics. With current developments in the experimental realizations of tunable spin systems I expect more research into this field being presented in the future.

APPENDICES

A OWN PUBLICATIONS AND CONTRIBUTIONS OF THE AUTHORS

In this appendix I list my work that was published in scientific journals during the research of this thesis and the contributions by the respective authors to the results presented therein. Some ideas, paragraphs, and figures presented in this thesis have previously appeared in following publications:

[FKS19] S. Fey, S. C. Kapfer, and K. P. Schmidt. "Quantum Criticality of Two-Dimensional Quantum Magnets with Long-Range Interactions." In: *Phys. Rev. Lett.* 122 (1 Jan. 2019), p. 017203. DOI: 10.1103/PhysRevLett.122.017203.

[FS16] S. Fey and K. P. Schmidt. "Critical behavior of quantum magnets with long-range interactions in the thermodynamic limit." In: *Phys. Rev. B* 94 (7 Aug. 2016), p. 075156. DOI: 10.1103/PhysRevB.94.075156.

[Koz+19] J. Koziol et al. "Quantum criticality of the transverse-field Ising model with long-range interactions on triangular-lattice cylinders." In: *Phys. Rev. B* 100 (14 Oct. 2019), p. 144411. DOI: 10.1103/PhysRevB.100.144411.

A.1 *Critical behavior of quantum magnets with long-range interactions in the thermodynamic limit*

The publication titled "Critical behavior of quantum magnets with long-range interactions in the thermodynamic limit" [FS16] was published by S. Fey and K. P. Schmidt. All calculations and results presented within this publication were done by myself while the main idea and concept was incentivized by my supervisor Prof. K. P. Schmidt. The text was written in cooperation of both authors.

The contents of the publication have a Copyright (2016) by The American Physical Society. Parts of the article are reproduced in 4.1 with kind permission of the journal and contains slight changes in order to fit the style of the thesis.

A.2 *Quantum Criticality of Two-Dimensional Quantum Magnets with Long-Range Interactions*

The publication titled "Quantum Criticality of Two-Dimensional Quantum Magnets with Long-Range Interactions" [FKS19] was published by S. Fey, S. C. Kapfer, and K. P. Schmidt. The work was a natural continuation of the previous publication [FS16] to new lattice geometries. Technically, improvements were made by replacing the old evaluation schemes for the nested infinite sums by an MCMC algorithm. The suggestion to use this method came from S. C. Kapfer and the corresponding algorithm was developed in cooperation of me and S. C. Kapfer and supervised by K. P. Schmidt. I performed all consequent calculations presented in the publication. The text was written mainly in cooperation of me and K. P. Schmidt and then revised by all three authors.

The contents of the publication have a Copyright (2019) by The American Physical Society. Parts of the article are reproduced in 4.1, 4.2, and 4.3 with kind permission of the journal and contains slight changes in order to fit the style of the thesis.

A.3 *Quantum criticality of the transverse-field Ising model with long-range interactions on triangular-lattice cylinders*

The third publication titled "Quantum criticality of the transverse-field Ising model with long-range interactions on triangular-lattice cylinders" [Koz+19] was published by J. Koziol, S. Fey, S. C. Kapfer, and K. P. Schmidt. It contains results for the LRTFIM on triangular-lattice cylinders computed with different methods. The classical states in the field-free LRIM with results presented in Figure 6 and Table I of the publication were investigated by J. Koziol. With some guidance by K. P. Schmidt, J. Koziol and I developed the low-field expansion of the clock-ordered states and computed results with J. Koziol computing the highest order and determining the crossing with stripe-state energies. The maximally-flippable states in the dimer representation and high-field expansions and extrapolations of the ground-state energy and the one-QP gap for single-site unit cells were done by myself. The extension of the MCMC algorithm to larger unit cells was done by me with some support of S. C. Kapfer. The text was written mainly in cooperation of K. P. Schmidt, J. Koziol and me and then revised by all four authors.

The contents of the publication have a Copyright (2019) by The American Physical Society. Parts of the article are reproduced in 4.4 and E with kind permission of the journal and contains slight changes in order to fit the style of the thesis.

B DEFINITIONS

B.1 *Pauli matrices*

The Pauli matrices are defined as follows

$$\sigma^x = \begin{pmatrix} 0 & 1 \\ 1 & 0 \end{pmatrix}, \quad \sigma^y = \begin{pmatrix} 0 & -\mathrm{i} \\ \mathrm{i} & 0 \end{pmatrix}, \text{ and } \quad \sigma^z = \begin{pmatrix} 1 & 0 \\ 0 & -1 \end{pmatrix} \tag{B.1}$$

and together with the two-dimensional identity matrix $\mathbb{1}_{2\times 2}$ form a complete basis of the 2×2 $\mathbb{C}$ vector space. We can also derive ladder operators from the Pauli matrices as

$$\sigma^+ = \frac{1}{2}\left(\sigma^x + \mathrm{i}\sigma^y\right) = \begin{pmatrix} 0 & 1 \\ 0 & 0 \end{pmatrix} \quad \text{and} \quad \sigma^- = \frac{1}{2}\left(\sigma^x - \mathrm{i}\sigma^y\right) = \begin{pmatrix} 0 & 0 \\ 1 & 0 \end{pmatrix}, \tag{B.2}$$

that lower or raise the quantum number of the eigenvectors $|\uparrow\rangle = (1,0)^T$ and $|\downarrow\rangle = (0,1)^T$ of σ^z with eigenvalues $+1$ and -1 resulting in

$$\sigma^+ |\downarrow\rangle = |\uparrow\rangle\,, \quad \sigma^+ |\uparrow\rangle = 0\,, \quad \sigma^- |\uparrow\rangle = |\downarrow\rangle\,, \text{ and } \quad \sigma^- |\downarrow\rangle = 0\,. \tag{B.3}$$

The Pauli matrices have the following commutation and anticommutation relations:

$$[\sigma^\alpha, \sigma^\beta] = 2\mathrm{i}\varepsilon_{\alpha\beta\gamma}\sigma^\gamma \quad \text{and} \quad \{\sigma^\alpha, \sigma^\beta\} = 2\delta_{\alpha\beta}\mathbb{1}_{2\times 2}\,. \tag{B.4}$$

on the same site, while they commute on different sites

$$[\sigma_i^\alpha, \sigma_j^\beta] = 0 \quad \text{for} \quad i \neq j\,. \tag{B.5}$$

B.2 *Mathematical functions and series*

A *Dirichlet L-series* has the form

$$L_n(s,\chi) \equiv \sum_{k=1}^{\infty} \frac{\chi_n(k)}{k^s}\,, \tag{B.6}$$

where $\chi_n(k)$ is an integer function with period n. The number-theoretic character (or Dirichlet character) $\chi_n(k)$ fulfills

$$\chi_n(1) = 1\,, \quad \chi_n(k) = \chi_n(k+n)\,, \quad \text{and} \quad \chi_n(k)\chi_n(l) = \chi_n(kl) \tag{B.7}$$

for all k and l. If k and n are not coprime, i. e., if they have a common divisor $\neq 1$, then $\chi_n(k) = 0$.

Some specially named L-series are, e. g., the *Riemann zeta function*

$$\zeta(s) = \sum_{k=1}^{\infty} \frac{1}{k^s} = 1 + 2^{-s} + 3^{-s} + 4^{-s} + \cdots , \tag{B.8}$$

the *Dirichlet eta function*, also known as the alternating zeta function,

$$\eta(s) = L_{-1}(s) = \sum_{k=1}^{\infty} \frac{(-1)^{k-1}}{k^s} = 1 - 2^{-s} + 3^{-s} - 4^{-s} + \cdots , \tag{B.9}$$

$$g(s) \equiv L_{-3}(s) = 1 - 2^{-s} + 4^{-s} - 5^{-s} + 7^{-s} - 8^{-s} \ldots , \tag{B.10}$$

and the *Dirichlet beta function*

$$\beta(s) = L_{-4}(s) = \sum_{k=0}^{\infty} (-1)^k (2k+1)^{-s} = 1 - 3^{-s} + 5^{-s} - 7^{-s} + \ldots . \tag{B.11}$$

An extension of the zeta function, the *generalized Hurwitz ζ function*, is defined as

$$\zeta(s, a) = \sum_{k=1}^{\infty} \frac{1}{(a+k)^s} = (a+1)^{-s} + (a+2)^{-s} + (a+3)^{-s} + \cdots . \tag{B.12}$$

The *Polylogarithm* is defined as

$$\mathrm{Li}_s(z) = \sum_{k=1}^{\infty} \frac{z^k}{k^s} = z + \frac{z^2}{2^s} + \frac{z^3}{3^s} + \cdots . \tag{B.13}$$

The *Lerch transcendent* is defined as

$$\Phi(z, s, a) = \sum_{k=0}^{\infty} \frac{z^k}{(a+k)^s} = \frac{z}{a+1} + \frac{z^2}{(a+2)^s} + \frac{z^3}{(a+3)^s} + \cdots . \tag{B.14}$$

C ALGORITHMS

C.1 *Adjacency-number-calculation algorithm*

The adjacency number as defined in Section 3.1.4 is calculated as the maximum number of all vertex-label permutations, where the number is derived from representing all graph edges as a 1 and non-edges as a 0 in a corresponding adjacency matrix and then interpreting the upper triangular matrix as a binary number in a row-major fashion. Therefore, given a graph with a random vertex labeling, the goal is to find the permutation

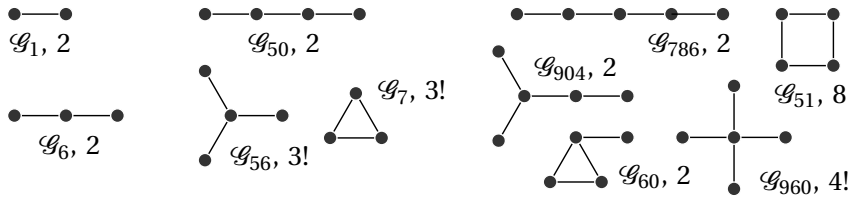

Figure C.1: An overview of all graphs with their corresponding adjacency number as a subscript and the number of labellings $i_{\mathcal{G}}$ which yield the same adjacency number up to order 4. The order in which they can become relevant equals the number of graph edges.

maximizing the number in an efficient way since the complexity grows exponentially with the number of vertices. In order 10 there are already 3390 graphs to consider.

The general idea is to take the randomly labeled graph and look for the most the vertex that should be labeled with 0 – depending on certain rules. After setting the label, repeat the procedure for label 1 and continue until all vertices are labeled. If there are multiple vertices that fulfill the rule, both are labeled in parallel and the resulting adjacency number is compared in the end to find the correct labeling. If there are multiple different labelings yielding the same adjacency number, they represent a symmetry of the graph.

The rules I applied are:

1. For the first label take all vertices with the maximum number of neighbors and calculate an adjacency number for each case in a separate calculation with the respective vertex label set to 0.

2. The next labels are assigned recursively. For all unlabeled vertices connected to vertex 0 a separate calculation with the new label is started. If no unlabeled vertex is connected to 0 (i. e., if all neighbor vertices of 0 are already labeled), vertices that are neighbors of 1 are chosen, etc. This second step is repeated until all vertices have been assigned a label.

3. From the list of possible graph-label permutations the one with the maximum graph number is chosen.

Optimizations to the rules of this approach are certainly possible. If more details of the graph are exploited, loops need to be considered which makes the coding more prone to errors. However, the performance was sufficient to compute the graph properties for this thesis in a reasonable time.

An overview of all graphs that must be considered in a perturbative calculation in order 4 is given in Figure C.1 with their corresponding adjacency number.

Listing 1: Rejection sampling for double-sided ζ-distribution. `rng` is a random-number generator; `random_uniform(rng)` returns a uniform random number in the interval $[0, 1)$; `random_sign(rng)` returns a -1 with probability of 50% and $+1$ otherwise.

```
double prob_zero = 1/(2*zeta(exponent)-1);
long int random_zeta_double_sided( double exponent, rng_t &
    rng )
{
  // see if we want to return 0
  if( random_uniform(rng) < prob_zero )
    return 0;

  // simple rejection-sampling scheme
  while( true )
  {
    double x = pow( random_uniform(rng), -1/(exponent-1) );
    if( x >= LONG_MAX/2 )
    {
      // accounting for poss. overflow of long int
      throw OverflowError();
    }
    long int ret = x + 1;
    if ( x * pow( random_uniform(rng), -1/exponent ) > ret
        )
    {
      return random_sign(rng) * ( ret - 1 );
    }
  }
}
```

C.2 *Double-sided zeta distribution*

The normalized double-sided zeta distribution with exponent γ is given by the probability to obtain the value x

$$p(x) = \frac{(1+|x|)^{-\gamma}}{2\zeta(\gamma) - 1}. \tag{C.1}$$

The term double-sided refers to the fact that the absolute value of x follows the ζ-distribution such that both positive and negative values can be obtained by drawing random values from the distribution. Those values are calculated using the rejection-sampling algorithm presented in Listing 1.

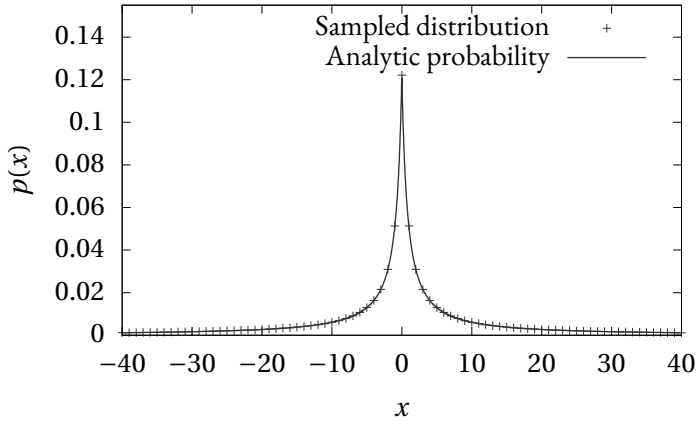

Figure C.2: Normalized histogram of the double-sided zeta distribution using 10^8 samples (black crosses) with the exact function from Equation (C.1) (solid black line). Values with $|x| > 40$ are not shown.

For illustration purposes the distribution has been sampled with 10^8 steps. The resulting normalized histogram is shown in Figure C.2 together with the analytic distribution.

C.3 *Deprecated Markov-Chain Monte-Carlo moves*

Before settling on the MCMC setup discussed in Section 3.2.4.3 several different approaches were tested. To help the reader get an overview of these possibilities some of them are discussed with their respective drawbacks in this section.

When analyzing the movement of the sites, it becomes clear that quite often a situation appears where the graph splits into two (or more) parts which tend to drift apart. Once the two subgraphs are far away from each other a proposed configuration of moving a single particle closer to the other subgraph is in the about as likely as increasing the distance. The two subsystems are nearly freely floating about the configuration space. To prevent this behavior the rift moves were introduced for one-dimensional lattice. Before implementing the 2D rift moves presented in the methods chapter, a different move was tested that also used one-dimensional rifts. To this end, a random direction was uniformly drawn from a set of directions (horizontal, vertical, diagonal) and the vertex positions were projected onto it. This allowed to sort the vertices along this direction. Afterwards, as in the one-dimensional move, a new rift was proposed between two clusters of spins that were selected by splitting the ordered vertices at a random position. The idea is illustrated in Figure C.3.

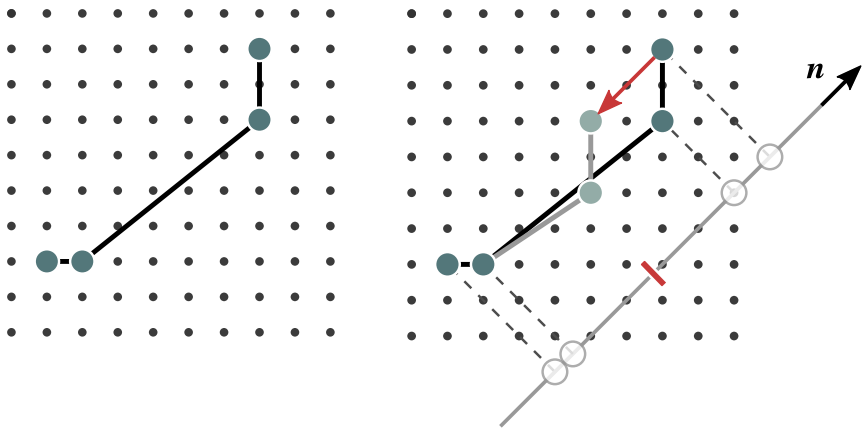

(a) 2d decomposition. (b) Proposed rift move.

Figure C.3: (a) In two dimensions the graph can be decomposed along random directions. (b) To counter this, a new "rift" move is introduced which (i) projects the sites on a direction $\boldsymbol{n}$, randomly selected from a set of directions, (ii) sorts the sites by their projected position, (iii) divides the graph into two subgraphs at a random position and (iv) moves one of the clusters by a random length.

C.3.1 *Optimized sampling of the antiferromagnetic interaction*

In Monte-Carlo calculations for problems with alternating signs of the energy the *sign-problem* is very common [TW05]. While we do not have this exact situation when sampling the sums of the series coefficients, we do still have alternating summands if the quasi momentum is not zero. This becomes obvious when studying the following example: Let us take a look on the contribution of the three-vertex graph $\mathcal{G}_6$ (see Figure C.1) in second order to the hopping from the left site to the rightmost site. Embedding the PCUT result on a 1D spin chain requires the evaluation of

$$-\frac{1}{2}\sum_{i_2\neq i_1}\sum_{i_1}|i_1|^{-\alpha}|i_2-i_1|^{-\alpha}\cos(k\cdot i_2) \tag{C.2}$$

Now, we immediately see that choosing $k=0$ leads to the same sign for every summand as the cosine reduces to a factor 1. However, for an antiferromagnetic interaction, we know that the dispersion minimum is located at $k=\pi$. This is the extreme opposite choice of k in the sense that now the summand's signs become alternating[1]. For an antiferromagnetic interaction on different lattices (like the two-dimensional triangular lattice) the 1-QP gap minimum is not necessarily located at momentum $\boldsymbol{k}=(\pi,\pi)^T$. The

1 In higher dimensions the same argument holds for vectors $\boldsymbol{k}=(\pi,\ldots,\pi)^T$.

signs change over a wider range of lattice sites and are therefore not exactly alternating. But even the existence of these slower fluctuations hinders the fast convergence and asks for a new ansatz to be remedied.

To overcome this problem the idea was the evaluation of the sum during the Monte-Carlo summation is slightly modified to ensure a smoother convergence to the correct result. In each evaluation step not only the randomly drawn configuration of lattice sites for a graph contributes to the target sum. Additionally, all possible $2^{N_{\text{vert}}}$ configurations where the positions of the graph on the lattice are shifted by one or stay the same are taken into account. The procedure is illustrated in Figure C.4 and Listing 2. Effectively, the contributions of odd and even lattice sites are merged into one. Unfortunately, I did not found much of an improvement using this idea.

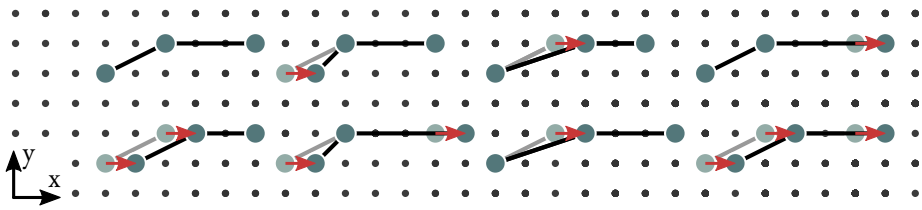

Figure C.4: To lower the influence of the cosine terms on the summand sign for quasi momenta $\boldsymbol{k} \neq \mathbf{0}$, in each MCMC summation step, several vertex configurations are combined. To this end, all possible shifts of the graph vertices by one lattice site along the positive x-axis are considered. To illustrate this, the eight contributing configurations of a three-vertex graph are shown here exemplarily on the square lattice.

In my ansatz to determine the coefficients of the perturbation series I performed single embeddings of all graphs with a fixed number of vertices in a given order. The sum of all graph contributions then yields the series coefficient. A different possibility to perform the MCMC calculations is to create a random walk over all possible graphs and add the contribution of each graph in every step. This would eliminate the need to perform multiple single computations, although much longer run times for each calculations would be necessary evening out the advantage. A second argument in favor of this idea is that graphs with a larger contribution in a given configuration on the lattice might be sampled more often than other graphs. However, to identify the contribution of a graph, first, the adjacency number needs to be calculated, which requires to find the canonical labeling of the graph. Doing this in each MCMC step requires a lot of computational overhead, especially in higher orders. The ansatz was not implemented in this thesis but might be worth testing in a future implementation.

Listing 2: Exemplary implementation of the optimized antiferromagnetic sampling for a 2D lattice. Contributions of shifts along the x-coordinates of different graph sites are combined into one to reduce the effect of fluctuating summand signs. `State` is a `std::array` containing the coordinates of the different graph vertices. `ret.target` is a `double` variable counting the contributions to the target sum. The function `isOverlapping` ensures that only configurations contribute where no two vertex sites are on the same lattice site.

```
ret.target = 0.;
const unsigned num_subconf = 1u<<N; // 2^N
for (unsigned subconf = 0; subconf != num_subconf; ++
    subconf)
{
    State shifted_state = state;
    for (unsigned i = 0; i != N; ++i)
        shifted_state[i][0] += !!(subconf & (1<<i));
    if (! isOverlapping (shifted_state))
        ret.target += f (shifted_state);
}
ret.target /= num_subconf;
```

C.3.2 *Old reference sums*

For the one-dimensional chain an appropriate reference sum for graphs of size N are sorted linear graphs. The value of the sum can be calculated analytically

$$I^{\mathrm{ch}}_{\mathrm{ref},N} = \sum_{s_{N-1}<s_N} \cdots \sum_{s_2<s_3} \sum_{s_1<s_2} \frac{1}{|s_1-s_2|^\alpha} \frac{1}{|s_2-s_3|^\alpha} \cdots \frac{1}{|s_{N-1}-s_N|^\alpha} \tag{C.3}$$

$$= \sum_{\delta_{N-1}=1}^{\infty} \cdots \sum_{\delta_2=1}^{\infty} \sum_{\delta_1=1}^{\infty} \frac{1}{\delta_1^\alpha} \frac{1}{\delta_2^\alpha} \cdots \frac{1}{\delta_{N-1}^\alpha} \tag{C.4}$$

$$= \zeta(\alpha)^{N-1} \tag{C.5}$$

For the two-dimensional square lattice I do not know of a sum that can be calculated analytically. Even for the simplest graph (two connected vertices) the calculation is demanding. The corresponding formula is

$$I^{\mathrm{sq}}_{\mathrm{ref},2} = \sum_{\boldsymbol{\delta}\neq\mathbf{0}} \frac{1}{|\boldsymbol{\delta}|^\alpha} = \sum_{\delta_x=-\infty}^{\infty} \sum_{\substack{\delta_y=-\infty \\ (\delta_x,\delta_y)\neq(0,0)}}^{\infty} \frac{1}{\sqrt{\delta_x^2+\delta_y^2}^{\,\alpha}}\,, \tag{C.6}$$

where the α-dependent value could obtained by a brute-force summation of partial sums and a subsequent extrapolation to the upper sum limit of ∞. However, using this

value the same idea as for the one-dimensional lattice can be applied for an N-vertex sum. To this end, we order the positions $\boldsymbol{i}_1, \ldots, \boldsymbol{i}_N$ by their x-coordinate and get

$$\begin{aligned} I^{\mathrm{sq}}_{\mathrm{ref},N} = \sum_{\substack{i_{N-1,x} < i_{N,x} \\ i_{N-1,y}}} \cdots \sum_{\substack{i_{2,x} < i_{3,x} \\ i_{2,y}}} \sum_{\substack{i_{1,x} < i_{2,x} \\ i_{1,y}}} & \sqrt{(i_{1,x} - i_{2,x})^2 + (i_{1,y} - i_{2,y})^2}^{-\alpha} \\ & \cdot \sqrt{(i_{2,x} - i_{3,x})^2 + (i_{2,y} - i_{3,y})^2}^{-\alpha} \\ & \cdots \sqrt{(i_{N-1,x} - i_{N,x})^2 + (i_{N-1,y} - i_{N,y})^2}^{-\alpha} \end{aligned} \tag{C.7}$$

$$\begin{aligned} = \sum_{\boldsymbol{\delta}_1 \neq \mathbf{0}} \sum_{\boldsymbol{\delta}_2 \neq \mathbf{0}} \cdots \sum_{\boldsymbol{\delta}_{N-1} \neq \mathbf{0}} & \sqrt{\delta^2_{1,x} + \delta^2_{1,y}}^{-\alpha} \sqrt{\delta^2_{2,x} + \delta^2_{2,y}}^{-\alpha} \\ & \cdots \sqrt{\delta^2_{N-1,x} + \delta^2_{N-1,y}}^{-\alpha} \end{aligned} \tag{C.8}$$

$$= \sum_{\boldsymbol{\delta}_1 \neq \mathbf{0}} \sum_{\boldsymbol{\delta}_2 \neq \mathbf{0}} \cdots \sum_{\boldsymbol{\delta}_{N-1} \neq \mathbf{0}} \frac{1}{|\boldsymbol{\delta}_1|^\alpha} \frac{1}{|\boldsymbol{\delta}_2|^\alpha} \frac{1}{|\boldsymbol{\delta}_{N-1}|^\alpha} \tag{C.9}$$

$$= \left(\sum_{\boldsymbol{\delta} \neq \mathbf{0}} \frac{1}{|\boldsymbol{\delta}|^\alpha} \right)^{N-1} . \tag{C.10}$$

Again, we reduced the sum for N vertices to the calculation for the two-vertex graph. However, since in the two-dimensional case the result for this simple graph is not exactly known, the relative error in the calculation for this graph propagates to the larger reference graphs linearly in N

$$\frac{\Delta I^{\mathrm{sq}}_{\mathrm{ref},N}}{I^{\mathrm{sq}}_{\mathrm{ref},N}} = (N-1) \frac{\Delta I^{\mathrm{sq}}_{\mathrm{ref},2}}{I^{\mathrm{sq}}_{\mathrm{ref},2}} . \tag{C.11}$$

The problem is then that any error introduced in the reference sum is an additional error to the MCMC-inherent statistical errors. As a consequence, this error should be avoided if possible and it is worth aspiring to use a reference sum that is known analytically or can easily be evaluated to an arbitrary precision. Therefore, I finally settled on the reference sum presented in Section 3.2.4.2.

D WAVE VECTORS OF MAGNETIC ORDERS

The magnetic order of a phase can be studied by looking at the static structure factor

$$S(\boldsymbol{k}) = \frac{1}{N} \sum_{\boldsymbol{j}} \sum_{\boldsymbol{\Delta}} \mathrm{e}^{\mathrm{i}\boldsymbol{k}\boldsymbol{\delta}(\boldsymbol{\Delta})} \left\langle \sigma^z_{\boldsymbol{j}} \sigma^z_{\boldsymbol{j}+\boldsymbol{\Delta}} \right\rangle , \tag{D.1}$$

where $\boldsymbol{j}$ and $\boldsymbol{\Delta}$ run over all pairs of lattice sites and vector $\boldsymbol{\delta}(\boldsymbol{\Delta})$ is the difference vector between the unit cells of both lattice sites.

In scenarios where a second-order QPT connects two phases, the minimum of the one-QP gap is often located at the wave vector corresponding to the order after the gap closure. If certain magnetic orders are expected it is helpful to determine the corresponding wave vectors.

In this section I exemplarily derive the wave vector for the columnar phase on the triangular lattice.

D.1 *Columnar (zigzag-striped) phase on the triangular lattice*

The columnar order as shown in Figure D.1a has a four-site unit cell with two spins pointing antiparallel to the other two. Consequently, the total number of unit cells can be calculated from the total number of spins N as $N_{\mathrm{uc}} = N/4$. As defined in the figure the lattice vectors of the magnetic super lattice are composed of the triangular-lattice unit vectors

$$\boldsymbol{l}_1 = 2\,(\boldsymbol{e}_1 - \boldsymbol{e}_2) \qquad \text{and} \qquad \boldsymbol{l}_2 = \boldsymbol{e}_1 + \boldsymbol{e}_2\,. \tag{D.2}$$

The positions of spins within a unit cell as illustrated in Figure D.1b are defined by $\boldsymbol{u}_0$ to $\boldsymbol{u}_3$, where $\boldsymbol{u}_0 = \mathbf{0}$, $\boldsymbol{u}_1 = \boldsymbol{e}_2$, $\boldsymbol{u}_2 = \boldsymbol{e}_1$, and $\boldsymbol{u}_3 = \boldsymbol{e}_1 - \boldsymbol{e}_2$.

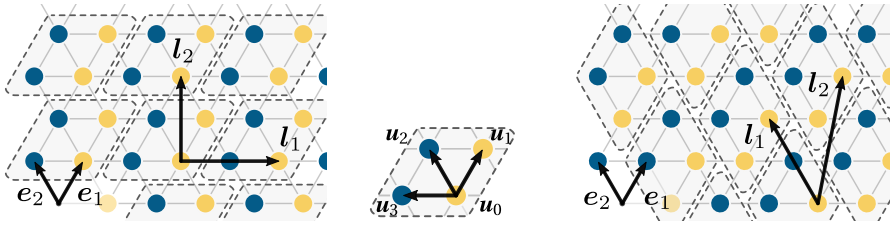

(a) Columnar order (b) Positions within a unit cell (c) Symmetric columnar order

Figure D.1: Symmetric columnar (zigzag-stripe) orders on the triangular lattice with different momenta. The associated momentum is $\boldsymbol{k}_{\mathrm{col,tr}} = (3\pi/2, \pi/2)^T$ for (a) [FKS19] and $\boldsymbol{k}_{\mathrm{col,tr}} = (\pi, \pi/2)^T$ for (c). Figure (b) shows the definition of position vectors within a single unit cell for the order in (a). Parallel spins are shown with the same color.

The goal is now to obtain a relation between the magnetic structure and the quasi-momentum $\boldsymbol{k}$. To this end, we look at the structure factor as defined in Equation (D.1). The sum of expectation values between all possible spin pairs within different unit cells

can be explicitly written out. The expectation value of a pair with parallel pointing spins is +1 while the expectation value of a pair with antiparallel pointing spins is −1.

$$
\begin{aligned}
S(\boldsymbol{k}) = \frac{N_{\mathrm{uc}}}{N} \sum_{\boldsymbol{\delta}} \mathrm{e}^{\mathrm{i}\boldsymbol{k}\boldsymbol{\delta}} \Bigg(& \underbrace{\left\langle \sigma^z_{\boldsymbol{u}_0} \sigma^z_{\boldsymbol{u}_0+\boldsymbol{\delta}} \right\rangle + \left\langle \sigma^z_{\boldsymbol{u}_1} \sigma^z_{\boldsymbol{u}_1+\boldsymbol{\delta}} \right\rangle + \left\langle \sigma^z_{\boldsymbol{u}_2} \sigma^z_{\boldsymbol{u}_2+\boldsymbol{\delta}} \right\rangle + \left\langle \sigma^z_{\boldsymbol{u}_3} \sigma^z_{\boldsymbol{u}_3+\boldsymbol{\delta}} \right\rangle}_{4} \\
& + \left\langle \sigma^z_{\boldsymbol{u}_0} \sigma^z_{\boldsymbol{u}_1+\boldsymbol{\delta}} \right\rangle \mathrm{e}^{\mathrm{i}\boldsymbol{k}\boldsymbol{e}_2} + \left\langle \sigma^z_{\boldsymbol{u}_1} \sigma^z_{\boldsymbol{u}_0+\boldsymbol{\delta}} \right\rangle \mathrm{e}^{-\mathrm{i}\boldsymbol{k}\boldsymbol{e}_2} \\
& + \left\langle \sigma^z_{\boldsymbol{u}_2} \sigma^z_{\boldsymbol{u}_3+\boldsymbol{\delta}} \right\rangle \mathrm{e}^{-\mathrm{i}\boldsymbol{k}\boldsymbol{e}_2} + \left\langle \sigma^z_{\boldsymbol{u}_3} \sigma^z_{\boldsymbol{u}_2+\boldsymbol{\delta}} \right\rangle \mathrm{e}^{\mathrm{i}\boldsymbol{k}\boldsymbol{e}_2} \Bigg\} 4\cos(\boldsymbol{k}\boldsymbol{e}_2) \\
& + \left\langle \sigma^z_{\boldsymbol{u}_0} \sigma^z_{\boldsymbol{u}_3+\boldsymbol{\delta}} \right\rangle \mathrm{e}^{\mathrm{i}\boldsymbol{k}(\boldsymbol{e}_1-\boldsymbol{e}_2)} + \left\langle \sigma^z_{\boldsymbol{u}_3} \sigma^z_{\boldsymbol{u}_0+\boldsymbol{\delta}} \right\rangle \mathrm{e}^{-\mathrm{i}\boldsymbol{k}(\boldsymbol{e}_1-\boldsymbol{e}_2)} \\
& + \left\langle \sigma^z_{\boldsymbol{u}_1} \sigma^z_{\boldsymbol{u}_2+\boldsymbol{\delta}} \right\rangle \mathrm{e}^{\mathrm{i}\boldsymbol{k}(\boldsymbol{e}_1-\boldsymbol{e}_2)} + \left\langle \sigma^z_{\boldsymbol{u}_2} \sigma^z_{\boldsymbol{u}_1+\boldsymbol{\delta}} \right\rangle \mathrm{e}^{-\mathrm{i}\boldsymbol{k}(\boldsymbol{e}_1-\boldsymbol{e}_2)} \Bigg\} - 4\cos[\boldsymbol{k}(\boldsymbol{e}_2-\boldsymbol{e}_1)] \\
& + \underbrace{\left\langle \sigma^z_{\boldsymbol{u}_0} \sigma^z_{\boldsymbol{u}_2+\boldsymbol{\delta}} \right\rangle \mathrm{e}^{\mathrm{i}\boldsymbol{k}\boldsymbol{e}_1} + \left\langle \sigma^z_{\boldsymbol{u}_2} \sigma^z_{\boldsymbol{u}_0+\boldsymbol{\delta}} \right\rangle \mathrm{e}^{-\mathrm{i}\boldsymbol{k}\boldsymbol{e}_1}}_{-2\cos(\boldsymbol{k}\boldsymbol{e}_1)} \\
& + \underbrace{\left\langle \sigma^z_{\boldsymbol{u}_1} \sigma^z_{\boldsymbol{u}_3+\boldsymbol{\delta}} \right\rangle \mathrm{e}^{-\mathrm{i}\boldsymbol{k}(2\boldsymbol{e}_2-\boldsymbol{e}_1)} + \left\langle \sigma^z_{\boldsymbol{u}_3} \sigma^z_{\boldsymbol{u}_1+\boldsymbol{\delta}} \right\rangle \mathrm{e}^{\mathrm{i}\boldsymbol{k}(2\boldsymbol{e}_2-\boldsymbol{e}_1)}}_{-2\cos[\boldsymbol{k}(2\boldsymbol{e}_2-\boldsymbol{e}_1)]} \Bigg)
\end{aligned}
\tag{D.3}
$$

Using the magnetic super-lattice vectors defined in Equation (D.2), the difference between the two unit cell positions can be expressed as $\boldsymbol{\delta} = m\boldsymbol{l}_1 + n\boldsymbol{l}_2$, with $m, n \in \mathbb{Z}$. Rewriting the sum over all unit cells in terms of m and n yields

$$
\begin{aligned}
S(\boldsymbol{k}) = \frac{1}{4} \sum_{m,n} \mathrm{e}^{\mathrm{i}\boldsymbol{k}(m\boldsymbol{l}_1+n\boldsymbol{l}_2)} \Big\{ & 4 + 4\cos(\boldsymbol{k}\boldsymbol{e}_2) - 4\cos[\boldsymbol{k}(\boldsymbol{e}_2-\boldsymbol{e}_1)] \\
& - 2\cos(\boldsymbol{k}\boldsymbol{e}_1) - 2\cos[\boldsymbol{k}(2\boldsymbol{e}_2-\boldsymbol{e}_1)] \Big\} .
\end{aligned}
\tag{D.4}
$$

Using $\boldsymbol{k} = k_1\boldsymbol{e}_{k_1} + k_2\boldsymbol{e}_{k_2}$ and $\boldsymbol{e}_{k_i} \cdot \boldsymbol{e}_j = \delta_{ij}$ this can be brought into the form

$$
\begin{aligned}
S(\boldsymbol{k}) = & \sum_m \mathrm{e}^{\mathrm{i}\left(k_1\boldsymbol{e}_{k_1}+k_2\boldsymbol{e}_{k_2}\right)\cdot 2(\boldsymbol{e}_2-\boldsymbol{e}_1)m} \sum_n \mathrm{e}^{\mathrm{i}\left(k_1\boldsymbol{e}_{k_1}+k_2\boldsymbol{e}_{k_2}\right)\cdot(\boldsymbol{e}_1+\boldsymbol{e}_2)n} \\
& \cdot \underbrace{\left\{ 1 + \cos(k_2) - \cos(k_2-k_1) - \frac{1}{2}\cos(k_1) - \frac{1}{2}\cos(2k_2-k_1) \right\}}_{f(k_1,k_2)}
\end{aligned}
\tag{D.5}
$$

$$
= \sum_m \mathrm{e}^{\mathrm{i}(2k_2-2k_1)m} \sum_n \mathrm{e}^{\mathrm{i}(k_1+k_2)n} f(k_1,k_2)
\tag{D.6}
$$

Now, we can look for the maximum of the structure factor representing the magnetic order. The values for k_1 and k_2 are determined by the prefactor of $f(k_1, k_2)$. From the equation system

$$
2k_2 - 2k_1 = 2\pi
\tag{D.7}
$$

$$
k_1 + k_2 = 2\pi
\tag{D.8}
$$

we get the momentum $\boldsymbol{k}_{\text{col,tr}} = (3\pi/2, \pi/2)^T$ for the columnar phase with $f(\boldsymbol{k}_{\text{col,tr}}) = 2$. Now, there are several symmetric columnar magnetic orders such as the one shown in Figure D.1c. Repeating the calculation for this structure results in the structure factor

$$S(\boldsymbol{k}) = \sum_m \mathrm{e}^{2\mathrm{i}k_1 m} \sum_n \mathrm{e}^{\mathrm{i}(k_1+2k_2)n} f(k_1, k_2) \tag{D.9}$$

with $f(k_1, k_2) = 1 - \cos(k_1) + \cos(k_2) - \frac{1}{2}\cos(k_1 + k_2) - \frac{1}{2}\cos(k_1 - k_2)$. Solving the corresponding equation system results in the momentum $\boldsymbol{k}_{\text{col,tr}} = (\pi, \pi/2)^T$.

D.2 *Further magnetic structures*

The scheme shown above can be repeated for different magnetic structures. For the clock order we find a wave vector of $\boldsymbol{k}_{\text{cl}} = (\pm 2\pi/3, \mp 2\pi/3)^T$. The wave vector $\boldsymbol{k}_{\text{ss}} = (0, \pi)^T$ is associated with straight stripes on the triangular lattice.

The Néel order on the 1D chain, the 2D square lattice, and the 3D cubic lattice has a wave vector of $\boldsymbol{k}_{\text{Néel}} = \pi$, $(\pi, \pi)^T$, and $(\pi, \pi, \pi)^T$, respectively. The columnar order on the square lattice is given by $\boldsymbol{k}_{\text{col,sq}} = (\pi, 0)^T$.

As discussed for the zigzag-striped order on the triangular lattice, for the listed orders there are additional wave vectors representing symmetric instances of the same order.

E LOW-FIELD EXPANSION OF THE TRIANGULAR-LATTICE CYLINDER

In order to obtain the ground-state phase diagram of the LRTFIM on different triangular-cylinder lattices as presented in Section 4.4 several perturbative series expansions were performed. Here, I discuss the low-field approaches we used to determine the ground-state energy of the stripe- and clock-ordered phases. These sections are taken from our publication [Koz+19].

E.1 *Stripe-ordered phases*

Most of the perturbative results presented in this thesis were determined from the high-field limit, where the Ising interaction was perturbatively added to the field Hamiltonian (see Section 3.1.2). The opposite limit of small transverse fields $h/J \ll 1$ can also be treated by high-order series expansions for $\alpha < \infty$, since the extensive ground-state degeneracy for the NN case $\alpha = \infty$ is lifted by the long-range Ising interaction. Therefore, we have determined the ground state of the LRIM as a function of α by considering large but finite triangular cylinders XC(n), with periodic boundary conditions, for general even n. These findings are outlined and discussed in Section 4.4.2. As a result of these calculations we find that the pure LRIM realizes different types of ordered stripe structures depending

on n and α and we can determine the associated ground-state energy per site e_0^{stripe} in units of J by considering finite cylinders of the order of $N = 10^5$ spins.

These ordered stripe structures represent gapped phases which allows us to set up a high-order (non-degenerate) series expansion about the zero-field ground state. To this end, we apply Takahashi's perturbation theory [Tak77] in real space and we obtain the ground-state energy per site e_0^{stripe} for various stripe structures up to order six in the parameter h/J. To do this, we calculate the even-order contributions directly by evaluating the expectation value of the perturbation-operator sequences with respect to the considered classical stripe state. We stress that only even orders are present in the low-field expansion of e_0^{stripe} while odd orders vanish exactly. This originates from a double-touch property, because each excitation created locally by the perturbing magnetic field in virtual states has to be destroyed by acting again with the magnetic field on the same site. As a consequence, every site has to be touched an even number of times by the magnetic field to get a non-vanishing result. The perturbation-operator sequences in rth order read as follows [Tak77]

$$\hat{P}\hat{V}\hat{S}^{k_1}\hat{V}\hat{S}^{k_2}\hat{V}\ldots\hat{V}\hat{S}^{k_{r-1}}\hat{V}\hat{P}\,, \tag{E.1}$$

where $\hat{V} \equiv \hat{H}_{\text{TF}}$ is the perturbation, $\hat{P}$ the projection operator on the ground-state space,

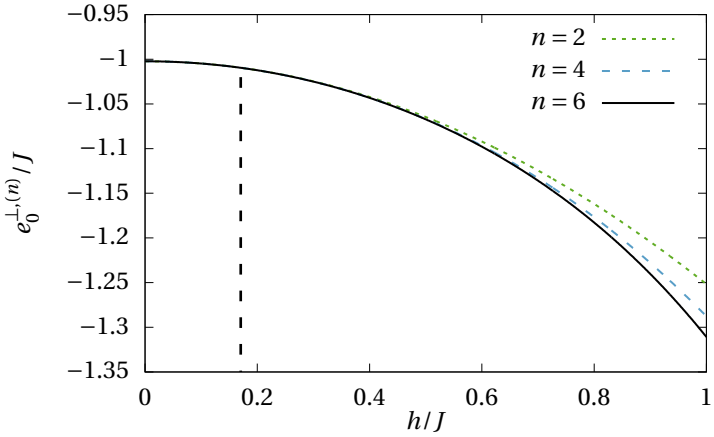

Figure E.1: Bare series of the ground-state energy per site $e_0^{\perp,(n)}$ for orthogonal stripes in order n as a function of h/J for $\alpha = 6$ for the XC(4) cylinder. The bare series is converged up to $h/J \approx 0.6$. The behavior of other stripe configurations as well as other α-values is similar. The calculated phase transition into the clock order, visualized by the dashed black vertical line, takes place at approximately $h/J = 0.17$.

the resolvent $\hat{S}$ is given as

$$\hat{S} = \frac{(1-\hat{P})}{E_0^{\text{stripe}} - \hat{H}_{\text{LRIM}}} \quad \text{with} \quad \hat{S}^k = \begin{cases} \hat{P} & \text{for} \quad k = 0 \\ \hat{S}^k & \text{for} \quad k > 0 \end{cases}, \tag{E.2}$$

and the constraint $\sum_{i=1}^{n-1} k_i = r - 1$. We evaluate all contributions up to order six in h/J by calculating the expectation values

$$\langle \text{stripe} | \hat{P}\hat{V}\hat{S}^{k_1}\hat{V}\hat{S}^{k_2}\hat{V} \ldots \hat{V}\hat{S}^{k_{r-1}}\hat{P} | \text{stripe} \rangle \tag{E.3}$$

for the classical stripe state $|\text{stripe}\rangle$ on finite clusters with $n \times 10^3$ spins for the XC(n) cylinder and by treating the perturbing magnetic field in real space. We have further reduced the summation effort by identifying the non-vanishing processes in advance and exploiting the translational invariance for the first excitation that is created by the perturbation $\hat{V}$. Finally, for a fixed α we obtain the following order-six series of the ground-state energy per site for $J = 1$

$$e_0^{\text{stripe}}(\alpha, h) = e_0^{\text{stripe}}(\alpha, h = 0) + \rho_2^{\text{stripe}}(\alpha)\, h^2 + \rho_4^{\text{stripe}}(\alpha)\, h^4 + \rho_6^{\text{stripe}}(\alpha)\, h^6 \,. \tag{E.4}$$

As a representative example, the bare series in order two, four, and six of the ground-state energy per site of orthogonal stripes for $\alpha = 6$ are displayed in Figure E.1. In general, we observe that the first-order phase transition out of the stripe-ordered phase is well located in the regime where the bare series is still converged. Consequently, an extrapolation of the series of the low-field expansions is not necessary.

F DATA

F.1 *Series coefficients*

In this section I list the series coefficients used for the extrapolations and the extraction of critical values and exponents. The number in brackets states the standard deviation of the distribution of the coefficient and is determined by taking the standard deviation over all seeds for an MCMC run for a fixed parameter set $(\alpha, \boldsymbol{k}, r, N_{\text{vert}})$, where $\boldsymbol{k}$ is the momentum, r the perturbation order, and N_{vert} the number of vertices. For the coefficient in order r the uncertainties of the averages for all N_{vert} contributing in order r is propagated.

F.1.1 *1D chain*

Table F.1: Coefficients c_r of the ground-state energy per site e_0 for each order r in the LRTFIM on the one-dimensional chain. The first order is exactly zero.

r \ α	1.5	5/3	2	2.25	3
2	$-6.013(25) \times 10^{-1}$	$-5.738(6) \times 10^{-1}$	$-5.4113(17) \times 10^{-1}$	$-5.27358(27) \times 10^{-1}$	$-5.08672(5) \times 10^{-1}$
3	$-9.97(8) \times 10^{-1}$	$-7.713(9) \times 10^{-1}$	$-5.086(4) \times 10^{-1}$	$-3.9228(5) \times 10^{-1}$	$-2.04226(4) \times 10^{-1}$
4	$-3.24(4)$	$-2.079(6)$	$-1.0456(18)$	$-7.009(4) \times 10^{-1}$	$-3.03628(18) \times 10^{-1}$
5	$-1.341(21) \times 10^{1}$	$-6.95(4)$	$-2.501(8)$	$-1.3635(5)$	$-3.4662(5) \times 10^{-1}$
6	$-6.56(11) \times 10^{1}$	$-2.738(13) \times 10^{1}$	$-7.114(14)$	$-3.2356(22)$	$-6.0954(15) \times 10^{-1}$
7	$-3.56(10) \times 10^{2}$	$-1.191(8) \times 10^{2}$	$-2.210(5) \times 10^{1}$	$-8.266(8)$	$-9.969(5) \times 10^{-1}$
8	$-2.09(7) \times 10^{3}$	$-5.57(5) \times 10^{2}$	$-7.370(15) \times 10^{1}$	$-2.2734(15) \times 10^{1}$	$-1.9183(17)$
9	$-1.30(4) \times 10^{4}$	$-2.76(4) \times 10^{3}$	$-2.584(15) \times 10^{2}$	$-6.558(10) \times 10^{1}$	$-3.680(5)$
10	$-8.1(7) \times 10^{4}$	$-1.335(21) \times 10^{4}$	$-8.23(9) \times 10^{2}$	$-1.5876(18) \times 10^{2}$	$-4.217(19)$

r \ α	4	6	8
2	$-5.020394(25) \times 10^{-1}$	$-5.001239(13) \times 10^{-1}$	$-5.000077(5) \times 10^{-1}$
3	$-9.62611(10) \times 10^{-2}$	$-2.350291(7) \times 10^{-2}$	$-5.861168(8) \times 10^{-3}$
4	$-1.72627(11) \times 10^{-1}$	$-1.29324(9) \times 10^{-1}$	$-1.25439(12) \times 10^{-1}$
5	$-9.8383(17) \times 10^{-2}$	$-1.7106(6) \times 10^{-2}$	$-3.9839(17) \times 10^{-3}$
6	$-2.0334(14) \times 10^{-1}$	$-1.2961(11) \times 10^{-1}$	$-1.2542(28) \times 10^{-1}$
7	$-1.8942(16) \times 10^{-1}$	$-3.029(7) \times 10^{-2}$	$-7.16(4) \times 10^{-3}$
8	$-3.866(10) \times 10^{-1}$	$-2.048(16) \times 10^{-1}$	$-1.95(4) \times 10^{-1}$
9	$-4.736(19) \times 10^{-1}$	$-6.90(8) \times 10^{-2}$	$-1.61(6) \times 10^{-2}$
10	$-5.42(13) \times 10^{-1}$	$-3.90(22) \times 10^{-1}$	$-3.8(5) \times 10^{-1}$

Table F.2: Coefficients c_r of $\Delta_{\mathrm{ch,\,f}}$ for each order r in the ferromagnetic LRTFIM on the one-dimensional chain ($k = 0$).

r \ α	1.25	1.5	5/3	2	2.25	2.5
3	$-3.44(19) \times 10^{2}$	$-4.853(27) \times 10^{1}$	$-2.111(30) \times 10^{1}$	$-6.1040(8)$	$-2.8798(14)$	$-1.4584(9)$
4	$-3.8(4) \times 10^{3}$	$-2.844(25) \times 10^{2}$	$-9.46(16) \times 10^{1}$	$-1.8659(4) \times 10^{1}$	$-7.236(4)$	$-3.2108(24)$
5	$-4.7(5) \times 10^{4}$	$-1.870(26) \times 10^{3}$	$-4.71(11) \times 10^{2}$	$-6.1260(20) \times 10^{1}$	$-1.8236(13) \times 10^{1}$	$-6.233(11)$
6	$-6.4(7) \times 10^{5}$	$-1.330(24) \times 10^{4}$	$-2.55(8) \times 10^{3}$	$-2.2497(9) \times 10^{2}$	$-5.417(10) \times 10^{1}$	$-1.587(4) \times 10^{1}$
7	$-8.7(12) \times 10^{6}$	$-9.92(25) \times 10^{4}$	$-1.45(7) \times 10^{4}$	$-8.624(6) \times 10^{2}$	$-1.647(5) \times 10^{2}$	$-3.912(14) \times 10^{1}$
8	$-1.3(4) \times 10^{8}$	$-7.63(18) \times 10^{5}$	$-8.6(6) \times 10^{4}$	$-3.4520(29) \times 10^{3}$	$-5.304(12) \times 10^{2}$	$-1.059(11) \times 10^{2}$
9	$-1.9(5) \times 10^{9}$	$-6.03(28) \times 10^{6}$	$-5.2(10) \times 10^{5}$	$-1.4203(20) \times 10^{4}$	$-1.752(6) \times 10^{3}$	$-2.91(4) \times 10^{2}$
10			$-3.2(4) \times 10^{6}$			

r \ α	2.75	2.875	3	3.125	3.25	3.5
3	$-7.5808(11) \times 10^{-1}$	$-5.4538(26) \times 10^{-1}$	$-3.8881(6) \times 10^{-1}$	$-2.7267(22) \times 10^{-1}$	$-1.8599(12) \times 10^{-1}$	$-7.230(14) \times 10^{-2}$
4	$-1.5687(4)$	$-1.1291(8)$	$-8.2745(19) \times 10^{-1}$	$-6.168(7) \times 10^{-1}$	$-4.675(6) \times 10^{-1}$	$-2.821(6) \times 10^{-1}$
5	$-2.2729(15)$	$-1.374(4)$	$-8.178(7) \times 10^{-1}$	$-4.696(23) \times 10^{-1}$	$-2.494(18) \times 10^{-1}$	$-2.22(20) \times 10^{-2}$
6	$-5.324(6)$	$-3.218(10)$	$-1.9948(24)$	$-1.270(9)$	$-8.35(8) \times 10^{-1}$	$-3.99(6) \times 10^{-1}$
7	$-1.0534(17) \times 10^{1}$	$-5.59(4)$	$-2.961(9)$	$-1.530(30)$	$-7.51(26) \times 10^{-1}$	$-7.4(18) \times 10^{-2}$
8	$-2.519(9) \times 10^{1}$	$-1.291(16) \times 10^{1}$	$-6.79(4)$	$-3.68(12)$	$-2.05(11)$	$-7.2(8) \times 10^{-1}$
9	$-5.83(4) \times 10^{1}$	$-2.72(9) \times 10^{1}$	$-1.300(15) \times 10^{1}$	$-6.2(6)$	$-2.9(6)$	$-4(4) \times 10^{-1}$

r \ α	4	6	10
3	$2.606(13) \times 10^{-2}$	$3.483(21) \times 10^{-2}$	$2.7(5) \times 10^{-3}$
4	$-1.247(4) \times 10^{-1}$	$-2.28(7) \times 10^{-2}$	$-2.5(29) \times 10^{-3}$
5	$9.33(15) \times 10^{-2}$	$3.64(17) \times 10^{-2}$	$0(5) \times 10^{-3}$
6	$-1.46(6) \times 10^{-1}$	$-3.7(7) \times 10^{-2}$	$2(19) \times 10^{-3}$
7	$1.71(17) \times 10^{-1}$	$5.6(23) \times 10^{-2}$	$0(1) \times 10^{-1}$
8	$-2.1(7) \times 10^{-1}$	$-6(11) \times 10^{-2}$	$-3(25) \times 10^{-2}$
9	$3.1(28) \times 10^{-1}$	$2(6) \times 10^{-1}$	$0(23) \times 10^{-1}$

Table F.3: Coefficients c_r of $\Delta_{\text{ch, af}}$ for each order r in the antiferromagnetic LRTFIM on the one-dimensional chain ($k = \pi$).

r \ α	1.5	5/3	2	2.25	2.5
3	4.17(8)	3.101(5)	1.9069(26)	1.40505(27)	1.06670(17)
4	1.78(4) $\times 10^{1}$	1.0843(26) $\times 10^{1}$	4.952(6)	3.0833(15)	2.0411(6)
5	9.2(4) $\times 10^{1}$	4.562(13) $\times 10^{1}$	1.511(6) $\times 10^{1}$	7.828(4)	4.4549(16)
6	5.43(13) $\times 10^{2}$	2.149(10) $\times 10^{2}$	5.137(19) $\times 10^{1}$	2.2141(19) $\times 10^{1}$	1.0844(7) $\times 10^{1}$
7	3.44(13) $\times 10^{3}$	1.088(7) $\times 10^{3}$	1.865(5) $\times 10^{2}$	6.681(7) $\times 10^{1}$	2.8246(19) $\times 10^{1}$
8	2.30(14) $\times 10^{4}$	5.78(7) $\times 10^{3}$	7.08(4) $\times 10^{2}$	2.100(4) $\times 10^{2}$	7.647(12) $\times 10^{1}$
9	1.61(10) $\times 10^{5}$	3.21(7) $\times 10^{4}$	2.78(4) $\times 10^{3}$	6.808(21) $\times 10^{2}$	2.128(7) $\times 10^{2}$

	3	4	5	7
3	6.4949(15) $\times 10^{-1}$	2.6925(21) $\times 10^{-1}$	1.1978(26) $\times 10^{-1}$	2.62(4) $\times 10^{-2}$
4	1.0051(4)	3.128(6) $\times 10^{-1}$	1.155(8) $\times 10^{-1}$	2.09(12) $\times 10^{-2}$
5	1.7421(10)	4.135(7) $\times 10^{-1}$	1.354(19) $\times 10^{-1}$	2.1(4) $\times 10^{-2}$
6	3.369(4)	6.060(30) $\times 10^{-1}$	1.76(5) $\times 10^{-1}$	2.7(9) $\times 10^{-2}$
7	7.078(8)	1.002(13)	2.65(20) $\times 10^{-1}$	4(4) $\times 10^{-2}$
8	1.548(5) $\times 10^{1}$	1.76(5)	4.0(9) $\times 10^{-1}$	6(15) $\times 10^{-2}$
9	3.471(22) $\times 10^{1}$	3.20(18)	7(4) $\times 10^{-1}$	2(9) $\times 10^{-1}$

F.1.2 *2D square lattice*

Table F.4: Coefficients c_r of the ground-state energy per site e_0 for each order r in the LRTFIM on the two-dimensional square lattice. The first order is exactly zero.

r \ α	2.5	3	10/3	3.5	4
2	−1.27256(9)	−1.16472(4)	−1.122015(28)	−1.105783(23)	−1.070357(20)
3	−5.2569(7)	−3.41320(22)	−2.73168(14)	−2.47333(11)	−1.89568(7)
4	−4.2606(17) $\times 10^{1}$	−2.0487(6) $\times 10^{1}$	−1.44929(28) $\times 10^{1}$	−1.25424(21) $\times 10^{1}$	−8.8525(10)
5	−4.534(4) $\times 10^{2}$	−1.5090(7) $\times 10^{2}$	−8.951(4) $\times 10^{1}$	−7.1765(21) $\times 10^{1}$	−4.1389(11) $\times 10^{1}$
6	−5.808(11) $\times 10^{3}$	−1.3242(12) $\times 10^{3}$	−6.654(7) $\times 10^{2}$	−4.9918(28) $\times 10^{2}$	−2.4817(12) $\times 10^{2}$
7	−8.43(4) $\times 10^{4}$	−1.2889(19) $\times 10^{4}$	−5.430(6) $\times 10^{3}$	−3.787(5) $\times 10^{3}$	−1.5767(11) $\times 10^{3}$
8	−1.339(10) $\times 10^{6}$	−1.357(5) $\times 10^{5}$	−4.776(9) $\times 10^{4}$	−3.099(5) $\times 10^{4}$	−1.0894(10) $\times 10^{4}$
9	−2.280(22) $\times 10^{7}$	−1.513(10) $\times 10^{6}$	−4.435(13) $\times 10^{5}$	−2.672(6) $\times 10^{5}$	−7.874(14) $\times 10^{4}$
10	−4.07(8) $\times 10^{8}$	−1.73(5) $\times 10^{7}$	−4.142(16) $\times 10^{6}$	−2.295(11) $\times 10^{6}$	−5.526(17) $\times 10^{5}$

	4.5	5	6	8	10
2	−1.047816(18)	−1.032941(17)	−1.016002(18)	−1.003924(22)	−1.000980(23)
3	−1.49976(7)	−1.20951(5)	−8.12489(24) $\times 10^{-1}$	−3.88100(18) $\times 10^{-1}$	−1.90562(13) $\times 10^{-1}$
4	−6.8838(9)	−5.7425(7)	−4.6067(6)	−3.9286(10)	−3.7901(12)
5	−2.6892(6) $\times 10^{1}$	−1.8894(4) $\times 10^{1}$	−1.07578(22) $\times 10^{1}$	−4.5274(20)	−2.1429(12)
6	−1.4788(7) $\times 10^{2}$	−1.0052(4) $\times 10^{2}$	−6.118(4) $\times 10^{1}$	−4.147(6) $\times 10^{1}$	−3.780(10) $\times 10^{1}$
7	−8.165(6) $\times 10^{2}$	−4.899(4) $\times 10^{2}$	−2.3215(22) $\times 10^{2}$	−8.629(18) $\times 10^{1}$	−3.976(17) $\times 10^{1}$
8	−5.039(7) $\times 10^{3}$	−2.824(4) $\times 10^{3}$	−1.3172(23) $\times 10^{3}$	−6.98(4) $\times 10^{2}$	−5.90(12) $\times 10^{2}$
9	−3.202(6) $\times 10^{4}$	−1.617(4) $\times 10^{4}$	−6.226(26) $\times 10^{3}$	−1.995(22) $\times 10^{3}$	−8.9(9) $\times 10^{2}$
10	−1.932(7) $\times 10^{5}$	−8.76(5) $\times 10^{4}$	−3.04(6) $\times 10^{4}$	−1.0(4) $\times 10^{4}$	

Table F.5: Coefficients c_r of $\Delta_{\mathrm{sq,\,f}}$ for each order r in the ferromagnetic LRTFIM on the two-dimensional square lattice ($\boldsymbol{k} = \boldsymbol{0}$).

r \ α	2.25	7/3	2.5	2.75	3
2	$-3.7995(4) \times 10^{2}$	$-2.25666(20) \times 10^{2}$	$-1.11013(7) \times 10^{2}$	$-5.66521(27) \times 10^{1}$	$-3.61442(18) \times 10^{1}$
3	$-1.04348(12) \times 10^{4}$	$-4.7596(4) \times 10^{3}$	$-1.62566(12) \times 10^{3}$	$-5.8076(4) \times 10^{2}$	$-2.89181(18) \times 10^{2}$
4	$-3.6061(7) \times 10^{5}$	$-1.26838(22) \times 10^{5}$	$-3.0358(4) \times 10^{4}$	$-7.7049(8) \times 10^{3}$	$-3.03941(28) \times 10^{3}$
5	$-1.3956(5) \times 10^{7}$	$-3.7863(10) \times 10^{6}$	$-6.3570(11) \times 10^{5}$	$-1.14801(14) \times 10^{5}$	$-3.5900(5) \times 10^{4}$
6	$-5.786(4) \times 10^{8}$	$-1.2109(5) \times 10^{8}$	$-1.4272(4) \times 10^{7}$	$-1.8363(5) \times 10^{6}$	$-4.5598(9) \times 10^{5}$
7	$-2.512(4) \times 10^{10}$	$-4.0559(26) \times 10^{9}$	$-3.3558(14) \times 10^{8}$	$-3.0791(10) \times 10^{7}$	$-6.0755(15) \times 10^{6}$
8	$-1.128(4) \times 10^{12}$	$-1.4049(19) \times 10^{11}$	$-8.161(5) \times 10^{9}$	$-5.3411(22) \times 10^{8}$	$-8.378(4) \times 10^{7}$
9	$-5.19(4) \times 10^{13}$	$-4.988(14) \times 10^{12}$	$-2.0349(20) \times 10^{11}$	$-9.503(7) \times 10^{9}$	$-1.1856(9) \times 10^{9}$
	3.25	10/3	3.5	4	4.5
2	$-2.59986(9) \times 10^{1}$	$-2.37180(12) \times 10^{1}$	$-2.01472(9) \times 10^{1}$	$-1.38799(6) \times 10^{1}$	$-1.06952(4) \times 10^{1}$
3	$-1.72329(13) \times 10^{2}$	$-1.49030(27) \times 10^{2}$	$-1.15001(7) \times 10^{2}$	$-6.3440(4) \times 10^{1}$	$-4.19616(30) \times 10^{1}$
4	$-1.52263(15) \times 10^{3}$	$-1.2542(5) \times 10^{3}$	$-8.8709(8) \times 10^{2}$	$-4.0104(4) \times 10^{2}$	$-2.31058(28) \times 10^{2}$
5	$-1.51153(17) \times 10^{4}$	$-1.1856(8) \times 10^{4}$	$-7.6827(12) \times 10^{3}$	$-2.8427(4) \times 10^{3}$	$-1.42888(26) \times 10^{3}$
6	$-1.6165(4) \times 10^{5}$	$-1.2080(13) \times 10^{5}$	$-7.1812(14) \times 10^{4}$	$-2.1819(4) \times 10^{4}$	$-9.5833(30) \times 10^{3}$
7	$-1.8143(5) \times 10^{6}$	$-1.2916(25) \times 10^{6}$	$-7.0459(20) \times 10^{5}$	$-1.7579(5) \times 10^{5}$	$-6.7474(29) \times 10^{4}$
8	$-2.1087(8) \times 10^{7}$	$-1.432(4) \times 10^{7}$	$-7.1632(26) \times 10^{6}$	$-1.4691(8) \times 10^{6}$	$-4.932(4) \times 10^{5}$
9	$-2.5158(17) \times 10^{8}$	$-1.628(8) \times 10^{8}$	$-7.477(5) \times 10^{7}$	$-1.2613(13) \times 10^{7}$	$-3.705(5) \times 10^{6}$
	5	6	8	10	
2	$-8.8236(4)$	$-6.7887(4)$	$-5.1497(5)$	$-4.5319(9)$	
3	$-3.11638(24) \times 10^{1}$	$-2.12938(21) \times 10^{1}$	$-1.51239(27) \times 10^{1}$	$-1.3308(5) \times 10^{1}$	
4	$-1.55106(23) \times 10^{2}$	$-9.2128(18) \times 10^{1}$	$-5.5384(24) \times 10^{1}$	$-4.441(4) \times 10^{1}$	
5	$-8.7312(20) \times 10^{2}$	$-4.6560(17) \times 10^{2}$	$-2.6300(21) \times 10^{2}$	$-2.114(4) \times 10^{2}$	
6	$-5.3181(17) \times 10^{3}$	$-2.4950(14) \times 10^{3}$	$-1.2107(22) \times 10^{3}$	$-8.86(5) \times 10^{2}$	
7	$-3.4081(20) \times 10^{4}$	$-1.4285(15) \times 10^{4}$	$-6.464(18) \times 10^{3}$	$-4.77(6) \times 10^{3}$	
8	$-2.2651(19) \times 10^{5}$	$-8.380(12) \times 10^{4}$	$-3.267(19) \times 10^{4}$	$-2.19(5) \times 10^{4}$	
9	$-1.550(4) \times 10^{6}$	$-5.115(19) \times 10^{5}$	$-1.86(8) \times 10^{5}$	$-1.24(9) \times 10^{5}$	

Table F.6: Coefficients c_r of $\Delta_{\text{sq, af}}$ for each order r in the antiferromagnetic LRTFIM on the two-dimensional square lattice ($\boldsymbol{k} = (\pi, \pi)^T$).

r \ α	2.5	3	3.5	4	5
2	2.1515(10)	1.1586(6)	$3.851(5) \times 10^{-1}$	$-2.589(4) \times 10^{-1}$	−1.2822(4)
3	$2.3853(16) \times 10^{1}$	$1.5072(5) \times 10^{1}$	$1.13546(22) \times 10^{1}$	9.6405(15)	8.6559(13)
4	$2.495(5) \times 10^{2}$	$1.0271(6) \times 10^{2}$	$5.1616(22) \times 10^{1}$	$2.7367(13) \times 10^{1}$	4.035(9)
5	$3.433(10) \times 10^{3}$	$1.0238(7) \times 10^{3}$	$4.5085(26) \times 10^{2}$	$2.5320(11) \times 10^{2}$	$1.3571(7) \times 10^{2}$
6	$5.338(27) \times 10^{4}$	$1.0776(13) \times 10^{4}$	$3.6259(27) \times 10^{3}$	$1.5870(13) \times 10^{3}$	$4.094(6) \times 10^{2}$
7	$9.14(10) \times 10^{5}$	$1.2364(20) \times 10^{5}$	$3.292(4) \times 10^{4}$	$1.2761(14) \times 10^{4}$	$3.979(6) \times 10^{3}$
8	$1.668(24) \times 10^{7}$	$1.492(4) \times 10^{6}$	$3.072(6) \times 10^{5}$	$9.846(18) \times 10^{4}$	$2.028(7) \times 10^{4}$
9	$3.24(13) \times 10^{8}$	$1.878(9) \times 10^{7}$	$2.993(11) \times 10^{6}$	$8.136(30) \times 10^{5}$	$1.552(10) \times 10^{5}$

r \ α	6	8	10
2	−2.0407(4)	−3.0015(6)	−3.4982(6)
3	8.8971(16)	$1.00499(27) \times 10^{1}$	$1.09394(27) \times 10^{1}$
4	−8.110(12)	$-2.1665(20) \times 10^{1}$	$-2.8654(24) \times 10^{1}$
5	$1.1595(6) \times 10^{2}$	$1.3041(14) \times 10^{2}$	$1.4982(20) \times 10^{2}$
6	$3.64(6) \times 10^{1}$	$-2.974(11) \times 10^{2}$	$-4.676(21) \times 10^{2}$
7	$2.509(5) \times 10^{3}$	$2.513(8) \times 10^{3}$	$2.973(17) \times 10^{3}$
8	$5.22(6) \times 10^{3}$	$-4.57(10) \times 10^{3}$	$-9.27(19) \times 10^{3}$
9	$6.97(7) \times 10^{4}$	$5.66(9) \times 10^{4}$	$7.0(13) \times 10^{4}$

F.1.3 2*D triangular lattice*

Table F.7: Coefficients c_r of the ground-state energy per site e_0 for each order r in the LRTFIM on the two-dimensional triangular lattice. The first order is exactly zero.

r \ α	2.25	2.5	3	3.5	4
2	−1.78031(14)	−1.69049(10)	−1.59397(5)	−1.54881(4)	−1.526121(23)
3	$-1.12890(30)\times10^{1}$	−8.8479(13)	−6.3957(4)	−5.19887(25)	−4.50738(24)
4	$-1.3453(12)\times10^{2}$	$-8.3828(29)\times10^{1}$	$-4.4874(10)\times10^{1}$	$-3.0124(6)\times10^{1}$	$-2.29006(24)\times10^{1}$
5	$-2.220(5)\times10^{3}$	$-1.0655(10)\times10^{3}$	$-4.1045(19)\times10^{2}$	$-2.2472(6)\times10^{2}$	$-1.4881(4)\times10^{2}$
6	$-4.509(22)\times10^{4}$	$-1.624(4)\times10^{4}$	$-4.403(4)\times10^{3}$	$-1.9504(12)\times10^{3}$	$-1.1218(6)\times10^{3}$
7	$-1.063(16)\times10^{6}$	$-2.801(10)\times10^{5}$	$-5.257(8)\times10^{4}$	$-1.8696(17)\times10^{4}$	$-9.307(9)\times10^{3}$
8	$-2.74(11)\times10^{7}$	$-5.30(9)\times10^{6}$	$-6.777(15)\times10^{5}$	$-1.9246(24)\times10^{5}$	$-8.272(10)\times10^{4}$
9	$-8.0(16)\times10^{8}$	$-1.075(18)\times10^{8}$	$-9.27(4)\times10^{6}$	$-2.091(5)\times10^{6}$	$-7.742(14)\times10^{5}$
10	$-4(4)\times10^{10}$	$-2.28(7)\times10^{9}$	$-1.3(4)\times10^{8}$	$-2.275(10)\times10^{7}$	$-7.11(4)\times10^{6}$

	5	6	8	10
2	−1.507855(24)	−1.502455(28)	−1.500253(28)	−1.500027(30)
3	−3.77200(15)	−3.41750(15)	−3.12970(15)	−3.04148(17)
4	$-1.63202(18)\times10^{1}$	$-1.35961(15)\times10^{1}$	$-1.16443(18)\times10^{1}$	$-1.11089(20)\times10^{1}$
5	$-8.9745(20)\times10^{1}$	$-6.8519(17)\times10^{1}$	$-5.4636(21)\times10^{1}$	$-5.1044(23)\times10^{1}$
6	$-5.7347(21)\times10^{2}$	$-4.0335(20)\times10^{2}$	$-3.0217(21)\times10^{2}$	$-2.7758(24)\times10^{2}$
7	$-4.0219(29)\times10^{3}$	$-2.6031(26)\times10^{3}$	$-1.8302(25)\times10^{3}$	$-1.652(4)\times10^{3}$
8	$-3.018(4)\times10^{4}$	$-1.799(4)\times10^{4}$	$-1.188(4)\times10^{4}$	$-1.055(5)\times10^{4}$
9	$-2.380(5)\times10^{5}$	$-1.306(5)\times10^{5}$	$-8.10(6)\times10^{4}$	$-7.08(12)\times10^{4}$
10	$-1.771(9)\times10^{6}$	$-8.73(10)\times10^{5}$	$-5.0(4)\times10^{5}$	$-3.00(16)\times10^{5}$

Table F.8: Coefficients c_r of $\Delta_{\mathrm{tr,\,f}}$ for each order r in the ferromagnetic LRTFIM on the two-dimensional triangular lattice ($\boldsymbol{k} = \boldsymbol{0}$).

r \ α	2.25	7/3	2.5	3	10/3
2	$-5.2241(4) \times 10^{2}$	$-3.13485(22) \times 10^{2}$	$-1.57409(12) \times 10^{2}$	$-5.4501(5) \times 10^{1}$	$-3.72541(19) \times 10^{1}$
3	$-1.68233(19) \times 10^{4}$	$-7.7922(9) \times 10^{3}$	$-2.74402(29) \times 10^{3}$	$-5.340(6) \times 10^{2}$	$-2.91260(20) \times 10^{2}$
4	$-6.8157(12) \times 10^{5}$	$-2.4464(5) \times 10^{5}$	$-6.0962(10) \times 10^{4}$	$-6.867(20) \times 10^{3}$	$-3.0556(4) \times 10^{3}$
5	$-3.0924(7) \times 10^{7}$	$-8.6051(21) \times 10^{6}$	$-1.5193(5) \times 10^{6}$	$-9.94(4) \times 10^{4}$	$-3.6053(6) \times 10^{4}$
6	$-1.5029(8) \times 10^{9}$	$-3.2427(16) \times 10^{8}$	$-4.0588(20) \times 10^{7}$	$-1.547(5) \times 10^{6}$	$-4.5835(9) \times 10^{5}$
7	$-7.650(6) \times 10^{10}$	$-1.2799(9) \times 10^{10}$	$-1.1360(7) \times 10^{9}$	$-2.525(9) \times 10^{7}$	$-6.1169(20) \times 10^{6}$
8	$-4.027(8) \times 10^{12}$	$-5.223(6) \times 10^{11}$	$-3.2872(27) \times 10^{10}$	$-4.269(20) \times 10^{8}$	$-8.455(4) \times 10^{7}$
9	$-2.174(12) \times 10^{14}$	$-2.185(6) \times 10^{13}$	$-9.753(18) \times 10^{11}$	$-7.40(8) \times 10^{9}$	$-1.1998(10) \times 10^{9}$

r \ α	3.5	4	5	6	8
2	$-3.22939(21) \times 10^{1}$	$-2.36263(14) \times 10^{1}$	$-1.6830(4) \times 10^{1}$	$-1.43161(8) \times 10^{1}$	$-1.26312(12) \times 10^{1}$
3	$-2.30987(23) \times 10^{2}$	$-1.37616(14) \times 10^{2}$	$-7.6763(21) \times 10^{1}$	$-5.7613(8) \times 10^{1}$	$-4.6010(11) \times 10^{1}$
4	$-2.2420(4) \times 10^{3}$	$-1.12591(22) \times 10^{3}$	$-5.2550(29) \times 10^{2}$	$-3.6656(9) \times 10^{2}$	$-2.7981(14) \times 10^{2}$
5	$-2.4454(6) \times 10^{4}$	$-1.03022(25) \times 10^{4}$	$-3.965(4) \times 10^{3}$	$-2.5227(10) \times 10^{3}$	$-1.7989(15) \times 10^{3}$
6	$-2.8767(11) \times 10^{5}$	$-1.0206(4) \times 10^{5}$	$-3.264(6) \times 10^{4}$	$-1.9154(16) \times 10^{4}$	$-1.2913(22) \times 10^{4}$
7	$-3.5538(17) \times 10^{6}$	$-1.0617(6) \times 10^{6}$	$-2.815(6) \times 10^{5}$	$-1.5170(16) \times 10^{5}$	$-9.592(26) \times 10^{4}$
8	$-4.5484(28) \times 10^{7}$	$-1.1458(10) \times 10^{7}$	$-2.529(12) \times 10^{6}$	$-1.2546(28) \times 10^{6}$	$-7.49(4) \times 10^{5}$
9	$-5.978(7) \times 10^{8}$	$-1.2697(21) \times 10^{8}$	$-2.336(19) \times 10^{7}$	$-1.066(11) \times 10^{7}$	$-6.0(4) \times 10^{6}$

r \ α	10
2	$-1.21853(27) \times 10^{1}$
3	$-4.318(5) \times 10^{1}$
4	$-2.6012(16) \times 10^{2}$
5	$-1.646(8) \times 10^{3}$
6	$-1.164(5) \times 10^{4}$
7	$-8.46(10) \times 10^{4}$
8	$-6.3(13) \times 10^{5}$
9	$-4.0(25) \times 10^{6}$

Table F.9: Coefficients c_r of $\Delta_{\mathrm{tr,\,af}}$ for each order r in the antiferromagnetic LRTFIM on the two-dimensional triangular lattice ($\boldsymbol{k} = (2\pi/3, -2\pi/3)^T$).

r \ α	2.25	2.5	3	3.5	4
2	4.942(5)	4.3943(16)	3.6574(9)	3.1636(4)	2.8010(4)
3	5.286(13) $\times 10^{1}$	3.9088(27) $\times 10^{1}$	2.5376(10) $\times 10^{1}$	1.8759(4) $\times 10^{1}$	1.499 14(26) $\times 10^{1}$
4	8.76(6) $\times 10^{2}$	5.148(7) $\times 10^{2}$	2.4772(15) $\times 10^{2}$	1.5071(5) $\times 10^{2}$	1.046 11(30) $\times 10^{2}$
5	1.85(4) $\times 10^{4}$	8.358(18) $\times 10^{3}$	2.9021(26) $\times 10^{3}$	1.4511(6) $\times 10^{3}$	8.870(4) $\times 10^{2}$
6	4.55(22) $\times 10^{5}$	1.547(6) $\times 10^{5}$	3.778(6) $\times 10^{4}$	1.5324(10) $\times 10^{4}$	8.172(5) $\times 10^{3}$
7	1.26(22) $\times 10^{7}$	3.143(19) $\times 10^{6}$	5.295(11) $\times 10^{5}$	1.7256(17) $\times 10^{5}$	7.990(7) $\times 10^{4}$
8	3.7(20) $\times 10^{8}$	6.83(6) $\times 10^{7}$	7.830(21) $\times 10^{6}$	2.036(4) $\times 10^{6}$	8.154(13) $\times 10^{5}$
9	1(7) $\times 10^{10}$	1.574(27) $\times 10^{9}$	1.207(7) $\times 10^{8}$	2.492(7) $\times 10^{7}$	8.606(28) $\times 10^{6}$

r \ α	5	6	8	10
2	2.3043(5)	1.9948(4)	1.6816(5)	1.5645(6)
3	1.11057(29) $\times 10^{1}$	9.3368(21)	8.0165(27)	7.654(4)
4	6.3726(25) $\times 10^{1}$	4.7125(16) $\times 10^{1}$	3.5224(20) $\times 10^{1}$	3.1888(23) $\times 10^{1}$
5	4.7002(29) $\times 10^{2}$	3.2851(20) $\times 10^{2}$	2.4022(22) $\times 10^{2}$	2.1819(27) $\times 10^{2}$
6	3.701(4) $\times 10^{3}$	2.3943(22) $\times 10^{3}$	1.646(4) $\times 10^{3}$	1.467(5) $\times 10^{3}$
7	3.092(5) $\times 10^{4}$	1.862(4) $\times 10^{4}$	1.219(4) $\times 10^{4}$	1.078(6) $\times 10^{4}$
8	2.680(9) $\times 10^{5}$	1.496(5) $\times 10^{5}$	9.27(7) $\times 10^{4}$	8.03(20) $\times 10^{4}$
9	2.393(17) $\times 10^{6}$	1.239(19) $\times 10^{6}$	7.2(4) $\times 10^{5}$	6.3(12) $\times 10^{5}$

F.1.4 3*D cubic lattice*

Table F.10: Coefficients c_r of $\Delta_{\text{cub, f}}$ for each order r in the ferromagnetic LRTFIM on the three-dimensional cubic lattice ($\boldsymbol{k} = \boldsymbol{0}$).

r \ α	3.25	3.5	4	5	6
1	$-5.31(11) \times 10^{1}$	$-2.899(8) \times 10^{1}$	$-1.653\,22(20) \times 10^{1}$	$-1.037\,754(16) \times 10^{1}$	$-8.401\,90(13)$
2	$-1.44(16) \times 10^{3}$	$-4.133(17) \times 10^{2}$	$-1.297\,05(28) \times 10^{2}$	$-4.742\,07(25) \times 10^{1}$	$-2.909\,41(16) \times 10^{1}$
3	$-7.6(13) \times 10^{4}$	$-1.180(9) \times 10^{4}$	$-2.0505(19) \times 10^{3}$	$-4.4051(7) \times 10^{2}$	$-2.089\,67(25) \times 10^{2}$
4	$-5.1(11) \times 10^{6}$	$-4.26(7) \times 10^{5}$	$-4.1384(27) \times 10^{4}$	$-5.3579(15) \times 10^{3}$	$-1.9967(6) \times 10^{3}$
5	$-3.6(8) \times 10^{8}$	$-1.73(6) \times 10^{7}$	$-9.360(11) \times 10^{5}$	$-7.281(5) \times 10^{4}$	$-2.1205(11) \times 10^{4}$
6	$-3.0(10) \times 10^{10}$	$-7.4(4) \times 10^{8}$	$-2.272(5) \times 10^{7}$	$-1.0644(10) \times 10^{6}$	$-2.4303(17) \times 10^{5}$
7	$-2.3(5) \times 10^{12}$	$-3.5(10) \times 10^{10}$	$-5.775(24) \times 10^{8}$	$-1.6315(23) \times 10^{7}$	$-2.920(4) \times 10^{6}$
8	$-2.0(8) \times 10^{14}$	$-1.55(8) \times 10^{12}$	$-1.518(9) \times 10^{10}$	$-2.588(5) \times 10^{8}$	$-3.633(6) \times 10^{7}$
9	$-1.7(8) \times 10^{16}$	$-7.7(21) \times 10^{13}$	$-4.091(28) \times 10^{11}$	$-4.211(16) \times 10^{9}$	$-4.637(16) \times 10^{8}$

r \ α	7	8	9	10
1	$-7.467\,04(13)$	$-6.945\,78(13)$	$-6.628\,86(14)$	$-6.426\,12(14)$
2	$-2.178\,02(14) \times 10^{1}$	$-1.807\,38(13) \times 10^{1}$	$-1.594\,69(15) \times 10^{1}$	$-1.463\,55(12) \times 10^{1}$
3	$-1.355\,58(20) \times 10^{2}$	$-1.034\,64(20) \times 10^{2}$	$-8.6839(19) \times 10^{1}$	$-7.7301(15) \times 10^{1}$
4	$-1.1280(4) \times 10^{3}$	$-7.8863(27) \times 10^{2}$	$-6.2366(24) \times 10^{2}$	$-5.3243(25) \times 10^{2}$
5	$-1.0414(7) \times 10^{4}$	$-6.696(5) \times 10^{3}$	$-5.033(4) \times 10^{3}$	$-4.165(4) \times 10^{3}$
6	$-1.0375(8) \times 10^{5}$	$-6.102(6) \times 10^{4}$	$-4.315(7) \times 10^{4}$	$-3.418(5) \times 10^{4}$
7	$-1.0853(14) \times 10^{6}$	$-5.868(10) \times 10^{5}$	$-3.942(9) \times 10^{5}$	$-3.027(11) \times 10^{5}$
8	$-1.1748(23) \times 10^{7}$	$-5.819(16) \times 10^{6}$	$-3.683(21) \times 10^{6}$	$-2.706(26) \times 10^{6}$
9	$-1.306(5) \times 10^{8}$	$-5.95(5) \times 10^{7}$	$-3.56(8) \times 10^{7}$	$-2.53(7) \times 10^{7}$

Table F.11: Coefficients c_r of $\Delta_{\text{cub, af}}$ for each order r in the antiferromagnetic LRTFIM on the three-dimensional cubic lattice ($\boldsymbol{k} = (\pi, \pi, \pi)^T$).

r \ α	3.5	4	5	6	7
1	3.5642(6)	3.8631(4)	4.37859(23)	4.78844(18)	5.10544(20)
2	1.117(10)	$-5.16(4) \times 10^{-1}$	−3.1601(24)	−5.2623(18)	−6.9346(18)
3	$5.14(4) \times 10^{1}$	$3.739(9) \times 10^{1}$	$3.003(4) \times 10^{1}$	$3.1770(27) \times 10^{1}$	$3.6150(27) \times 10^{1}$
4	$7.54(17) \times 10^{2}$	$3.358(24) \times 10^{2}$	$5.89(6) \times 10^{1}$	$-5.48(4) \times 10^{1}$	$-1.293(4) \times 10^{2}$
5	$1.71(10) \times 10^{4}$	$6.15(8) \times 10^{3}$	$1.871(10) \times 10^{3}$	$1.254(5) \times 10^{3}$	$1.296(4) \times 10^{3}$
6	$4.2(4) \times 10^{5}$	$1.087(20) \times 10^{5}$	$1.728(14) \times 10^{4}$	$2.59(5) \times 10^{3}$	$-3.15(5) \times 10^{3}$
7	$1.20(23) \times 10^{7}$	$2.17(7) \times 10^{6}$	$2.672(28) \times 10^{5}$	$9.18(8) \times 10^{4}$	$6.92(10) \times 10^{4}$
8	$3.8(12) \times 10^{8}$	$4.58(22) \times 10^{7}$	$3.59(7) \times 10^{6}$	$6.50(17) \times 10^{5}$	$1.5(14) \times 10^{4}$
9	$1.3(8) \times 10^{10}$	$1.03(10) \times 10^{9}$	$5.41(18) \times 10^{7}$	$1.031(29) \times 10^{7}$	$5.0(4) \times 10^{6}$
10	$6(7) \times 10^{11}$	$2.4(4) \times 10^{10}$	$8.0(5) \times 10^{8}$	$1.04(13) \times 10^{8}$	$1.7(13) \times 10^{7}$

r \ α	8	9	10
1	5.34557(19)	5.52470(22)	5.65670(23)
2	−8.2390(18)	−9.2374(25)	−9.9871(26)
3	$4.0944(29) \times 10^{1}$	$4.530(4) \times 10^{1}$	$4.893(4) \times 10^{1}$
4	$-1.865(4) \times 10^{2}$	$-2.319(6) \times 10^{2}$	$-2.677(5) \times 10^{2}$
5	$1.511(5) \times 10^{3}$	$1.755(9) \times 10^{3}$	$1.983(6) \times 10^{3}$
6	$-6.96(5) \times 10^{3}$	$-9.96(28) \times 10^{3}$	$-1.241(7) \times 10^{4}$
7	$7.66(6) \times 10^{4}$	$9.2(8) \times 10^{4}$	$1.08(4) \times 10^{5}$
8	$-2.94(6) \times 10^{5}$	$-5.3(15) \times 10^{5}$	$-7.0(6) \times 10^{5}$
9	$4.74(25) \times 10^{6}$	$6(4) \times 10^{6}$	$6.7(20) \times 10^{6}$
10	$-1.4(17) \times 10^{7}$	$-4(12) \times 10^{7}$	$-4(7) \times 10^{7}$

F.2 *Critical values and exponents*

Table F.12: The critical value λ_c and exponent $z\nu$ of the ferromagnetic LRTFIM on the 1D chain ($\boldsymbol{k} = 0$) for various α calculated as the mean of the shown DLog Padé extrapolants with the standard deviation of the extrapolants in round brackets.

α	λ_c	$z\nu$	DLog Padé
1.25	0.056061(28)	0.50164(26)	(3, 5), (4, 4)
1.5	0.105170(12)	0.5257(9)	(3, 5), (4, 4), (5, 3)
1.66667	0.13675(8)	0.560(4)	(3, 5), (4, 4), (4, 5), (5, 4)
2	0.19834(4)	0.6658(19)	(4, 3), (5, 3)
2.5	0.283129(20)	0.8365(8)	(3, 5), (4, 4), (5, 3)
2.75	0.31968(4)	0.9034(13)	(3, 5), (4, 4), (5, 3)
3	0.35134(16)	0.951(5)	(4, 3), (3, 5), (4, 4), (5, 3)
3.25	0.37782(5)	0.9763(14)	(3, 5), (4, 4), (5, 3)
3.5	0.4002(8)	1.01(4)	(4, 3), (3, 4), (3, 5), (4, 4), (5, 3)
4	0.43245(3)	1.0013(7)	(3, 4), (4, 3), (3, 5), (4, 4), (5, 3)
10	0.49912(7)	1.0001(8)	(3, 4), (4, 3), (3, 5), (4, 4), (5, 3)

Table F.13: The critical value λ_c and exponent $z\nu$ of the antiferromagnetic LRTFIM on the 1D chain ($\boldsymbol{k} = \pi$) for various α calculated as the mean of the shown DLog Padé extrapolants with the standard deviation of the extrapolants in round brackets.

α	λ_c	$z\nu$	DLog Padé
1.25	−0.61(6)	0.44(12)	(3, 4), (3, 5), (4, 4)
1.5	−0.7949(10)	0.974(5)	(3, 5), (4, 4)
1.666 66	−0.7439(4)	0.9459(20)	(3, 5), (4, 4)
2	−0.700(12)	1.01(9)	(3, 4), (4, 3), (4, 4), (5, 3), (3, 5)
2.25	−0.662(5)	0.99(4)	(5, 3), (3, 4), (4, 3)
2.5	−0.6326(14)	0.975(15)	(4, 3), (4, 4), (5, 3), (3, 5)
3	−0.593 76(30)	0.9949(30)	(4, 3), (4, 4), (5, 3), (3, 5)
4	−0.547 10(6)	0.9982(7)	(3, 4), (4, 3), (4, 4), (5, 3), (3, 5)
5	−0.523 94(5)	0.9983(5)	(4, 3), (3, 4), (5, 3)
7	−0.506 312 0(15)	0.999 932(17)	(4, 3), (3, 4)
10	−0.500 84(5)	1.0007(7)	(4, 3), (4, 4), (5, 3), (3, 4)

Table F.14: The critical value λ_c and exponent $z\nu$ of the ferromagnetic LRTFIM on the 2D square lattice ($\boldsymbol{k} = (0,0)^T$) for various α calculated as the mean of the shown DLog Padé extrapolants with the standard deviation of the extrapolants in round brackets.

α	λ_c	$z\nu$	DLog Padé
2.25	$1.810520(15) \times 10^{-2}$	0.499981(28)	(3, 4), (4, 3), (3, 5), (4, 4), (5, 3)
2.33333	$2.34762(8) \times 10^{-2}$	0.50023(13)	(3, 4), (4, 3), (3, 5), (4, 4), (5, 3)
2.5	$3.3447(13) \times 10^{-2}$	0.5018(16)	(3, 4), (4, 3), (3, 5), (4, 4), (5, 3)
2.75	$4.68721(28) \times 10^{-2}$	0.5076(4)	(4, 3), (3, 5), (4, 4), (5, 3)
3	$5.8843(19) \times 10^{-2}$	0.5166(23)	(4, 3), (3, 5), (4, 4), (5, 3)
3.25	$6.966(4) \times 10^{-2}$	0.533(4)	(4, 3), (3, 4), (3, 5), (4, 4), (5, 3)
3.33333	$7.3037(25) \times 10^{-2}$	0.5395(19)	(3, 4), (3, 5), (4, 4), (5, 3)
3.5	$7.9442(11) \times 10^{-2}$	0.5514(8)	(4, 3), (3, 4), (3, 5), (4, 4), (5, 3)
4	$9.6114(23) \times 10^{-2}$	0.5815(17)	(4, 3), (3, 4), (3, 5), (4, 4), (5, 3)
4.5	$1.09460(14) \times 10^{-1}$	0.6053(9)	(4, 3), (3, 4), (3, 5), (4, 4), (5, 3)
5	$1.20039(4) \times 10^{-1}$	0.62143(17)	(4, 3), (3, 4), (3, 5), (4, 4), (5, 3)
6	$1.34990(27) \times 10^{-1}$	0.6360(13)	(4, 3), (3, 4), (4, 4), (5, 3)
8	$1.50761(25) \times 10^{-1}$	0.6447(8)	(3, 4), (4, 3), (3, 5), (4, 4)
10	$1.57783(14) \times 10^{-1}$	0.6460(5)	(3, 4), (4, 3), (3, 5), (4, 4), (5, 3)

Table F.15: The critical value λ_c and exponent $z\nu$ of the antiferromagnetic LRTFIM on the 2D square lattice ($\boldsymbol{k} = (\pi,\pi)^T$) for various α calculated as the mean of the shown DLog Padé extrapolants with the standard deviation of the extrapolants in round brackets.

α	λ_c	$z\nu$	DLog Padé
2.5	−0.331(9)	0.62(5)	(3, 4), (3, 5), (4, 4)
3	−0.2925(9)	0.650(7)	(3, 4), (3, 5), (4, 4)
3.5	−0.2635(9)	0.659(12)	(3, 4), (4, 3), (3, 5), (4, 4), (5, 3)
4	−0.2419(4)	0.660(6)	(3, 4), (4, 3), (3, 5), (4, 4), (5, 3)
5	−0.2140(8)	0.659(6)	(3, 4), (4, 3), (3, 5), (4, 4), (5, 3)
6	−0.1965(4)	0.651(7)	(3, 4), (4, 3), (3, 5), (4, 4), (5, 3)
10	−0.17130(22)	0.645(6)	(4, 3), (3, 5), (4, 4), (5, 3)

Table F.16: The critical value λ_c and exponent $z\nu$ of the ferromagnetic LRTFIM on the 2D triangular lattice ($\boldsymbol{k} = (0,0)^T$) for various α calculated as the mean of the shown DLog Padé extrapolants with the standard deviation of the extrapolants in round brackets.

α	λ_c	$z\nu$	DLog Padé
2.25	$1.544\,325(8) \times 10^{-2}$	0.500 137(11)	(3, 4), (4, 3)
2.333 33	$1.992\,20(20) \times 10^{-2}$	0.4999(7)	(3, 4), (3, 5), (4, 4), (5, 3)
2.5	$2.810\,56(9) \times 10^{-2}$	0.501 80(17)	(3, 4), (3, 5), (4, 4), (5, 3)
3	$4.8040(24) \times 10^{-2}$	0.5183(28)	(4, 3), (3, 4), (3, 5), (4, 4), (5, 3)
3.333 33	$5.8518(27) \times 10^{-2}$	0.5376(30)	(3, 4), (3, 5), (4, 4), (5, 3)
3.5	$6.307(4) \times 10^{-2}$	0.548(4)	(4, 3), (3, 4), (3, 5), (4, 4), (5, 3)
4	$7.4444(7) \times 10^{-2}$	0.5817(6)	(4, 3), (3, 4), (3, 5), (4, 4), (5, 3)
5	$8.8989(23) \times 10^{-2}$	0.6210(6)	(4, 3), (3, 4), (3, 5), (4, 4), (5, 3)
6	$9.643(13) \times 10^{-2}$	0.625(14)	(4, 3), (3, 4)
8	$1.0262(7) \times 10^{-1}$	0.6455(22)	(3, 4), (3, 5), (4, 4), (5, 3)
10	$1.0454(12) \times 10^{-1}$	0.646(6)	(4, 3), (3, 5), (4, 4), (5, 3)

Table F.17: The critical value λ_c and exponent $z\nu$ of the antiferromagnetic LRTFIM on the 2D triangular lattice ($\boldsymbol{k} = (2\pi/3, -2\pi/3)^T$) for various α calculated as the mean of the shown DLog Padé extrapolants with the standard deviation of the extrapolants in round brackets.

α	λ_c	$z\nu$	DLog Padé
2.5	−0.53(12)	0.7(4)	(3, 4), (3, 5), (4, 4)
3	−0.527(17)	0.85(8)	(3, 4), (3, 5), (4, 4)
3.5	−0.464(7)	0.81(5)	(3, 4), (3, 5), (4, 4)
4	−0.4240(24)	0.799(17)	(3, 4), (3, 5), (4, 4)
5	−0.3714(10)	0.761(9)	(3, 4), (3, 5), (4, 4)
6	−0.3435(11)	0.741(10)	(3, 4), (3, 5), (4, 4)
8	−0.3211(6)	0.751(9)	(3, 4), (4, 3), (3, 5), (4, 4), (5, 3)
10	−0.3098(10)	0.717(10)	(3, 4), (3, 5), (4, 4)

Table F.18: The critical value λ_c and exponent $z\nu$ of the ferromagnetic LRTFIM on the 3D cubic lattice ($\boldsymbol{k} = (0,0,0)^T$) for various α calculated as the mean of the shown DLog Padé extrapolants with the standard deviation of the extrapolants in round brackets.

α	λ_c	$z\nu$	DLog Padé
3.25	0.009 53(8)	0.56(4)	(3, 4), (5, 3)
3.5	0.017 316(15)	0.493(4)	(3, 5), (4, 4), (5, 3)
4	0.030 938 4	0.503 294 15(13)	(4, 4), (3, 5)
5	0.051 168(8)	0.5185(10)	(3, 4), (3, 5), (4, 4), (5, 3)
6	0.065 08(8)	0.529(10)	(3, 4), (3, 5), (4, 4), (5, 3)
7	0.074 760(15)	0.5412(12)	(3, 4), (3, 5), (4, 4), (5, 3)
9	0.086 180(15)	0.5507(10)	(3, 5), (4, 4), (5, 3)
10	0.089 468(15)	0.5529(9)	(3, 5), (4, 4), (5, 3)

Table F.19: The critical value λ_c and exponent $z\nu$ of the antiferromagnetic LRTFIM on the 3D cubic lattice ($\boldsymbol{k} = (\pi,\pi,\pi)^T$) for various α calculated as the mean of the shown DLog Padé extrapolants with the standard deviation of the extrapolants in round brackets.

α	λ_c	$z\nu$	DLog Padé
3.5	−0.1854(11)	0.537(14)	(3, 4), (4, 3)
4	−0.167(9)	0.51(12)	(3, 4), (4, 4), (5, 3)
5	−0.1434(13)	0.538(30)	(4, 4), (3, 5), (5, 3), (6, 3)
6	−0.1283(7)	0.553(21)	(3, 5), (4, 4), (5, 3), (6, 3)
7	−0.118 47(24)	0.558(10)	(4, 4), (3, 5), (5, 3), (6, 3)
8	−0.111 92(8)	0.5592(27)	(4, 3), (3, 4), (6, 2)
9	−0.106 89(17)	0.529(12)	(4, 4), (3, 5), (5, 3)
10	−0.104 45(4)	0.5594(14)	(3, 5), (4, 5), (5, 3), (6, 3)

F.3 *Dispersion data points*

Table F.20: Data points of the antiferromagnetic 2D square lattice dispersion $\omega_{\mathrm{sq}}^{O5}(\boldsymbol{k})$. The data points were determined after a Padé extrapolation $P^{L/M}[\omega_{\mathrm{sq}}^{O5}(\boldsymbol{k})]$ in order 5.

$\boldsymbol{k}$	$\alpha = 2.5$	$\alpha = 3$	$\alpha = 4$
$(0,0)$	2.37(5)	1.944(7)	1.7057(8)
$(\pi/2,0)$	1.266(4)	1.266(4)	1.296 10(26)
$(\pi,0)$	0.912(4)	0.912(4)	0.969(7)
$(\pi,\pi/2)$	0.7861(15)	0.7760(8)	1.0436(13)
(π,π)	0.649(7)	0.594(13)	0.514(4)
$(\pi/2,\pi/2)$	1.12(20)	1.025(7)	1.0476(16)

Table F.21: Data points of the antiferromagnetic 2D triangular lattice dispersion $\omega_{\mathrm{tr}}^{O5}(\boldsymbol{k})$. The data points were determined after a Padé extrapolation $P^{L/M}[\omega_{\mathrm{tr}}^{O5}(\boldsymbol{k})]$ in order 5.

$\boldsymbol{k}$	$\alpha = 2.5$	$\alpha = 3$	$\alpha = 4$
$(0,0)$	3.6(5)	2.78(10)	2.38(10)
$(2\pi/3,-2\pi/3)$	0.2(5)	0.42(4)	0.333(16)
$(\pi,-\pi)$	0.667(11)	0.6548(20)	0.647(12)
$(7\pi/6,-5\pi/6)$	0.7712(23)	0.783(10)	0.81(4)
$(4\pi/3,-2\pi/3)$	1.071(11)	1.118(16)	1.201(28)
$(2\pi/3,-\pi/3)$	0.685(10)	0.6747(7)	0.667(14)
$(0,\pi)$	0.667(11)	0.6548(20)	0.647(12)
$(\pi,\pi/2)$	0.691(9)	0.681 65(12)	0.673(15)

BIBLIOGRAPHY

[AY71] P. W. Anderson and G. Yuval. "Some numerical results on the Kondo problem and the inverse square one-dimensional Ising model." In: *J. Phys. C: Solid State Physics* 4.5 (Apr. 1971), pp. 607–620. DOI: 10.1088/0022-3719/4/5/011.

[Aru+19] F. Arute et al. "Quantum supremacy using a programmable superconducting processor." In: *Nature* 574.7779 (Oct. 2019), pp. 505–510. DOI: 10.1038/s41586-019-1666-5.

[Asb+05] J. K. Asbóth et al. "Self-organization of atoms in a cavity field: Threshold, bistability, and scaling laws." In: *Phys. Rev. A* 72 (5 Nov. 2005), p. 053417. DOI: 10.1103/PhysRevA.72.053417.

[BGM96] G. A. Baker and P. R. Graves-Morris. *Padé Approximants.* 2nd ed. Vol. 59. Encyclopedia of Mathematics and Its Applications. Cambridge University Press, 1996. ISBN: 9780521450072.

[Bal10] L. Balents. "Spin liquids in frustrated magnets." In: *Nature* 464 (2010), pp. 199–208. DOI: 10.1038/nature08917.

[BCS57] J. Bardeen, L. N. Cooper, and J. R. Schrieffer. "Theory of Superconductivity." In: *Phys. Rev.* 108 (5 Dec. 1957), pp. 1175–1204. DOI: 10.1103/PhysRev.108.1175.

[BBW04] J. Berges, Sz. Borsányi, and C. Wetterich. "Prethermalization." In: *Phys. Rev. Lett.* 93 (14 Sept. 2004), p. 142002. DOI: 10.1103/PhysRevLett.93.142002.

[Bet31] H. Bethe. "Zur Theorie der Metalle." In: *Z. Phys* 71.3 (Mar. 1931), pp. 205–226. ISSN: 0044-3328. DOI: 10.1007/BF01341708.

[BRA96] D. Bitko, T. F. Rosenbaum, and G. Aeppli. "Quantum Critical Behavior for a Model Magnet." In: *Phys. Rev. Lett.* 77 (5 July 1996), pp. 940–943. DOI: 10.1103/PhysRevLett.77.940.

[BPR13] T. Blanchard, M. Picco, and M. A. Rajabpour. "Influence of long-range interactions on the critical behavior of the Ising model." In: *Europhys. Lett.* 101.5 (2013), p. 56003. DOI: 10.1209/0295-5075/101/56003.

[BSS81] R. Blankenbecler, D. J. Scalapino, and R. L. Sugar. "Monte Carlo calculations of coupled boson-fermion systems. I." In: *Phys. Rev. D* 24 (8 Oct. 1981), pp. 2278–2286. DOI: 10.1103/PhysRevD.24.2278.

[Bla+84] D. Blankschtein et al. "Orderings of a stacked frustrated triangular system in three dimensions." In: *Phys. Rev. B* 29 (9 May 1984), pp. 5250–5252. DOI: 10.1103/PhysRevB.29.5250.

[Bog58] N. N. Bogoljubov. "On a new method in the theory of superconductivity." In: *Il Nuovo Cimento (1955-1965)* 7.6 (Mar. 1958), pp. 794–805. ISSN: 1827-6121. DOI: 10.1007/BF02745585.

[Boh+16] G. Bohnet J et al. "Quantum spin dynamics and entanglement generation with hundreds of trapped ions." In: *Science* 352.6291 (2016), pp. 1297–1301. ISSN: 0036-8075. DOI: 10.1126/science.aad9958. eprint: http://science.sciencemag.org/content/352/6291/1297.full.pdf.

[Bor13] J. M. Borwein. *Lattice sums then and now*. 150. Cambridge University Press, 2013.

[BG01] S. T. Bramwell and M. J. P. Gingras. "Spin ice state in frustrated magnetic pyrochlore materials." In: *Science* 294 (2001), pp. 1495–1501. DOI: 10.1126/science.1064761.

[BLGZJ73] E. Brezin, J. C. Le Guillou, and J. Zinn-Justin. "Approach to Scaling in Renormalized Perturbation Theory." In: *Phys. Rev. D* 8 (8 Oct. 1973), pp. 2418–2430. DOI: 10.1103/PhysRevD.8.2418.

[Bre96] C. Brezinski. "Extrapolation algorithms and Padé approximations: a historical survey." In: *Appl. Numer. Math.* 20.3 (Mar. 1996), pp. 299 –318. ISSN: 0168-9274. DOI: 10.1016/0168-9274(95)00110-7.

[Bri+12] J. W. Britton et al. "Engineered two-dimensional Ising interactions in a trapped-ion quantum simulator with hundreds of spins." In: *Nature* 484.7395 (2012), pp. 489–492. DOI: 10.1038/nature10981.

[Bru55] K. A. Brueckner. "Many-Body Problem for Strongly Interacting Particles. II. Linked Cluster Expansion." In: *Phys. Rev.* 100 (1 Oct. 1955), pp. 36–45. DOI: 10.1103/PhysRev.100.36.

[Buy+16] A. S. Buyskikh et al. "Entanglement growth and correlation spreading with variable-range interactions in spin and fermionic tunneling models." In: *Phys. Rev. A* 93 (5 May 2016), p. 053620. DOI: 10.1103/PhysRevA.93.053620.

[CC06] P. Calabrese and J. Cardy. "Time Dependence of Correlation Functions Following a Quantum Quench." In: *Phys. Rev. Lett.* 96 (13 Apr. 2006), p. 136801. DOI: 10.1103/PhysRevLett.96.136801.

[Cal71] F. Calogero. "Solution of the One-Dimensional N-Body Problems with Quadratic and/or Inversely Quadratic Pair Potentials." In: *J. Math. Phys.* 12.3 (1971), pp. 419–436. DOI: 10.1063/1.1665604. eprint: https://doi.org/10.1063/1.1665604.

[Cam+14] A. Campa et al. *Physics of long-range interacting systems*. OUP Oxford, 2014.

[CDR09] Alessandro Campa, Thierry Dauxois, and Stefano Ruffo. "Statistical mechanics and dynamics of solvable models with long-range interactions." In: *Phys. Rep.* 480.3 (2009), pp. 57–159. ISSN: 0370-1573. DOI: https://doi.org/10.1016/j.physrep.2009.07.001.

[Cam+01] M. Campostrini et al. "Critical behavior of the three-dimensional XY universality class." In: *Phys. Rev. B* 63 (21 May 2001), p. 214503. DOI: 10.1103/PhysRevB.63.214503.

[CMS08] C. Castelnovo, R. Moessner, and S. L. Sondhi. "Magnetic monopoles in spin ice." In: *Nature* 451.7174 (2008), pp. 42–45. DOI: 10.1038/nature06433.

[Cha+04] P. B. Chakraborty et al. "Theory of the magnetic phase diagram of $LiHoF_4$." In: *Phys. Rev. B* 70 (14 Oct. 2004), p. 144411. DOI: 10.1103/PhysRevB.70.144411.

[CS15] K. Coester and K. P. Schmidt. "Optimizing linked-cluster expansions by white graphs." In: *Phys. Rev. E* 92 (2 Aug. 2015), p. 022118. DOI: 10.1103/PhysRevE.92.022118.

[Coe+16] K. Coester et al. "Linked-cluster expansions for quantum magnets on the hypercubic lattice." In: *Phys. Rev. B* 94 (12 Sept. 2016), p. 125109. DOI: 10.1103/PhysRevB.94.125109.

[Col15] Piers Coleman. *Introduction to Many-Body Physics*. Cambridge University Press, 2015. DOI: 10.1017/CBO9781139020916.

[CLP19] Federico Corberi, Eugenio Lippiello, and Paolo Politi. "Universality in the time correlations of the long-range 1d Ising model." In: *J. Stat. Mech.* 2019.7 (July 2019), p. 074002. DOI: 10.1088/1742-5468/ab270a.

[CS04] J. A. Cuesta and A. Sánchez. "General Non-Existence Theorem for Phase Transitions in One-Dimensional Systems with Short Range Interactions, and Physical Examples of Such Transitions." In: *J. Stat. Phys.* 115.3 (May 2004), pp. 869–893. ISSN: 1572-9613. DOI: 10.1023/B:JOSS.0000022373.63640.4e.

[Dau+02] T. Dauxois et al. "Dynamics and Thermodynamics of Systems with Long-Range Interactions: An Introduction." In: *Dynamics and Thermodynamics of Systems with Long-Range Interactions*. Ed. by T. Dauxois et al. Berlin, Heidelberg: Springer Berlin Heidelberg, 2002, pp. 1–19. ISBN: 978-3-540-45835-7. DOI: 10.1007/3-540-45835-2_1.

[DEH19] N. Defenu, T. Enss, and J. C. Halimeh. "Dynamical criticality and domain-wall coupling in long-range Hamiltonians." In: *Phys. Rev. B* 100 (1 July 2019), p. 014434. DOI: 10.1103/PhysRevB.100.014434.

[DTC15] N. Defenu, A. Trombettoni, and A. Codello. "Fixed-point structure and effective fractional dimensionality for O(N) models with long-range interactions." In: *Phys. Rev. E* 92 (5 Nov. 2015), p. 052113. DOI: 10.1103/PhysRevE.92.052113.

[DL89] C. Domb and J. Lebowitz. "Preface." In: *Phase Transitions and Critical Phenomena*. Ed. by C. Domb and J. Lebowitz. Vol. 13. New York: Academic Press, 1989, pp. ix–x.

[Dou+15] J. S. Douglas et al. "Quantum many-body models with cold atoms coupled to photonic crystals." In: *Nat. Photonics* 9.5 (May 2015), pp. 326–331. ISSN: 1749-4893. DOI: 10.1038/nphoton.2015.57.

[DFU11] N. Drescher, T. Fischer, and G. S. Uhrig. "Truncation errors in self-similar continuous unitary transformations." In: *Eur. Phys. J. B* 79.2 (Jan. 2011), pp. 225–240. ISSN: 1434-6036. DOI: 10.1140/epjb/e2010-10723-6.

[DV04] S. Dusuel and J. Vidal. "Finite-Size Scaling Exponents of the Lipkin-Meshkov-Glick Model." In: *Phys. Rev. Lett.* 93 (23 Dec. 2004), p. 237204. DOI: 10.1103/PhysRevLett.93.237204.

[Dus+10] S. Dusuel et al. "Bound states in two-dimensional spin systems near the Ising limit: A quantum finite-lattice study." In: *Phys. Rev. B* 81 (6 Feb. 2010), p. 064412. DOI: 10.1103/PhysRevB.81.064412.

[DB01] A. Dutta and J. K. Bhattacharjee. "Phase transitions in the quantum Ising and rotor models with a long-range interaction." In: *Phys. Rev. B* 64 (18 Oct. 2001), p. 184106. DOI: 10.1103/PhysRevB.64.184106.

[Dut+15] A. Dutta et al. *Quantum Phase Transitions in Transverse Field Spin Models: From Statistical Physics to Quantum Information*. Cambridge University Press, 2015. ISBN: 978-1-107-06879-7.

[Dys69] F. J. Dyson. "Existence of a phase-transition in a one-dimensional Ising ferromagnet." In: *Commun. Math. Phys.* 12.2 (1969), pp. 91–107. DOI: 10.1007/BF01645907.

[Edw+10] E. E. Edwards et al. "Quantum simulation and phase diagram of the transverse-field Ising model with three atomic spins." In: *Phys. Rev. B* 82 (6 Aug. 2010), p. 060412. DOI: 10.1103/PhysRevB.82.060412.

[ES+14] S. El-Showk et al. "Solving the 3d Ising Model with the Conformal Bootstrap II. c-Minimization and Precise Critical Exponents." In: *J. Stat. Phys.* 157.4 (Dec. 2014), pp. 869–914. ISSN: 1572-9613. DOI: 10.1007/s10955-014-1042-7.

[EPW70] R. J. Elliott, P. Pfeuty, and C. Wood. "Ising model with a transverse field." In: *Phys. Rev. Lett.* 25.7 (1970), p. 443. DOI: 10.1103/PhysRevLett.25.443.

[Ent82] A. C. D. van Enter. "Instability of phase diagrams for a class of "irrelevant" perturbations." In: *Phys. Rev. B* 26 (3 Aug. 1982), pp. 1336–1339. DOI: 10.1103/PhysRevB.26.1336.

[Fen19] P. Fendley. *Modern Statistical Mechanics*. Book in preparation. 2019. URL: http://users.ox.ac.uk/~phys1116/book.html (visited on 08/20/2019). Unpublished.

[FKS19] S. Fey, S. C. Kapfer, and K. P. Schmidt. "Quantum Criticality of Two-Dimensional Quantum Magnets with Long-Range Interactions." In: *Phys. Rev. Lett.* 122 (1 Jan. 2019), p. 017203. DOI: 10.1103/PhysRevLett.122.017203.

[FS16] S. Fey and K. P. Schmidt. "Critical behavior of quantum magnets with long-range interactions in the thermodynamic limit." In: *Phys. Rev. B* 94 (7 Aug. 2016), p. 075156. DOI: 10.1103/PhysRevB.94.075156.

[Fis67] M. E. Fisher. "The theory of equilibrium critical phenomena." In: *Rep. Prog. Phys.* 30.2 (1967), p. 615. DOI: 10.1103/RevModPhys.46.597.

[Fis74] M. E. Fisher. "The renormalization group in the theory of critical behavior." In: *Rev. Mod. Phys.* 46 (4 Oct. 1974), pp. 597–616. DOI: 10.1088/0034-4885/30/2/306.

[FMN72] M. E. Fisher, S.-k. Ma, and B. G. Nickel. "Critical Exponents for Long-Range Interactions." In: *Phys. Rev. Lett.* 29 (14 Oct. 1972), pp. 917–920. DOI: 10.1103/PhysRevLett.29.917.

[Fou+01] W. M. C. Foulkes et al. "Quantum Monte Carlo simulations of solids." In: *Rev. Mod. Phys.* 73 (1 Jan. 2001), pp. 33–83. DOI: 10.1103/RevModPhys.73.33.

[Fri+08] A. Friedenauer et al. "Simulating a quantum magnet with trapped ions." In: *Nat. Phys.* 4.10 (2008), p. 757. DOI: 10.1038/nphys1032.

[Frö52] H. Fröhlich. "Interaction of electrons with lattice vibrations." In: *Proc. R. Soc. London, Ser. A* 215.1122 (1952), pp. 291–298. DOI: 10.1098/rspa.1952.0212.

[FS82] J. Fröhlich and T. Spencer. "The phase transition in the one-dimensional Ising Model with 1/r2 interaction energy." In: *Commun. Math. Phys.* 84.1 (Mar. 1982), pp. 87–101. ISSN: 1432-0916. DOI: 10.1007/BF01208373.

[GLP19] M. Gabbrielli, L. Lepori, and L. Pezzè. "Multipartite-entanglement tomography of a quantum simulator." In: *New J. Phys.* 21.3 (Mar. 2019), p. 033039. DOI: 10.1088/1367-2630/aafb8c.

[GL50] V. L. Ginzburg and L. D. Landau. "Phenomenological theory." In: *Sov. Phys. JETP* 20 (1950), p. 1064.

[Gor+11] A. V. Gorshkov et al. "Tunable Superfluidity and Quantum Magnetism with Ultracold Polar Molecules." In: *Phys. Rev. Lett.* 107 (11 Sept. 2011), p. 115301. DOI: 10.1103/PhysRevLett.107.115301.

[GH94] A. P. Gottlob and M. Hasenbusch. "The XY model and the three-state antiferromagnetic Potts model in three dimensions: Critical properties from fluctuating boundary conditions." In: *J. Stat. Phys.* 77.3 (1994), pp. 919–930. DOI: 10.1007/BF02179470.

[Gre+02] M. Greiner et al. "Quantum phase transition from a superfluid to a Mott insulator in a gas of ultracold atoms." In: *Nature* 415.6867 (2002), p. 39.

[Gut89] A. C. Guttmann. "Asymptotic Analysis of Power-Series Expansions." In: *Phase Transitions and Critical Phenomena*. Ed. by C. Domb and J. Lebowitz. Vol. 13. New York: Academic Press, 1989. Chap. 1, pp. 3–229.

[GE94] A. J. Guttmann and I. G. Enting. "The high-temperature specific heat exponent of the 3D Ising model." In: *J. Phys. A* 27.24 (Dec. 1994), pp. 8007–8010. DOI: 10.1088/0305-4470/27/24/012.

[Hal88] F. D. M. Haldane. "Model for a Quantum Hall Effect without Landau Levels: Condensed-Matter Realization of the "Parity Anomaly"." In: *Phys. Rev. Lett.* 61 (18 Oct. 1988), pp. 2015–2018. DOI: 10.1103/PhysRevLett.61.2015.

[Ham00] C. J. Hamer. "Finite-size scaling in the transverse Ising model on a square lattice." In: *J. Phys. A* 33.38 (2000), p. 6683. DOI: 10.1088/0305-4470/33/38/303.

[Har+18] R. Harris et al. "Phase transitions in a programmable quantum spin glass simulator." In: *Science* 361.6398 (2018), pp. 162–165. DOI: 10.1126/science.aat2025.

[Has70] W. K. Hastings. "Monte Carlo sampling methods using Markov chains and their applications." In: *Biometrika* 57.1 (1970), pp. 97–109. DOI: 10.1093/biomet/57.1.97.

[HS00] P. Henelius and A. W. Sandvik. "Sign problem in Monte Carlo simulations of frustrated quantum spin systems." In: *Phys. Rev. B* 62 (2 July 2000), pp. 1102–1113. DOI: 10.1103/PhysRevB.62.1102.

[HFB04] M. Hermele, M. P. A. Fisher, and L. Balents. "Pyrochlore photons: The $U(1)$ spin liquid in a $S = \frac{1}{2}$ three-dimensional frustrated magnet." In: *Phys. Rev. B* 69 (6 Feb. 2004), p. 064404. DOI: 10.1103/PhysRevB.69.064404.

[HPK13] M. Heyl, A. Polkovnikov, and S. Kehrein. "Dynamical Quantum Phase Transitions in the Transverse-Field Ising Model." In: *Phys. Rev. Lett.* 110 (13 Mar. 2013), p. 135704. DOI: 10.1103/PhysRevLett.110.135704.

[HVUH71] L. M. Holmes, L. G. Van Uitert, and G. W. Hull. "Magnetoelectric effect and critical behavior in the Ising-like antiferromagnet, $DyAlO_3$." In: *Solid State Commun.* 9.16 (1971), pp. 1373–1376. ISSN: 0038-1098. DOI: https://doi.org/10.1016/0038-1098(71)90398-X.

[HWS18] M. Hörmann, P. Wunderlich, and K. P. Schmidt. "Dynamic Structure Factor of Disordered Quantum Spin Ladders." In: *Phys. Rev. Lett.* 121 (16 Oct. 2018), p. 167201. DOI: 10.1103/PhysRevLett.121.167201.

[Hum16] S. Humeniuk. "Quantum Monte Carlo study of long-range transverse-field Ising models on the triangular lattice." In: *Phys. Rev. B* 93 (10 Mar. 2016), p. 104412. DOI: 10.1103/PhysRevB.93.104412.

[Hum19] S. Humeniuk. "Quantum Monte Carlo studies of strongly correlated systems for quantum simulators." Ph.D. Thesis. Universität Stuttgart, 2019. DOI: 10.18419/opus-9938.

[IM03] S. V. Isakov and R. Moessner. "Interplay of quantum and thermal fluctuations in a frustrated magnet." In: *Phys. Rev. B* 68 (10 Sept. 2003), p. 104409. DOI: 10.1103/PhysRevB.68.104409.

[Isi25] E. Ising. "Beitrag zur Theorie des Ferromagnetismus." In: *Z. Phys* 31.1 (1925), pp. 253–258. ISSN: 0044-3328. DOI: 10.1007/BF02980577.

[Isl+11] R. Islam et al. "Onset of a quantum phase transition with a trapped ion quantum simulator." In: *Nat. Commun.* 2 (2011), p. 377. DOI: 10.1038/ncomms1374.

[Isl+13] R. Islam et al. "Emergence and frustration of magnetism with variable-range interactions in a quantum simulator." In: *Science* 340.6132 (2013), pp. 583–587. DOI: 10.1126/science.1232296.

[JSM16] S. B. Jäger, S. Schütz, and G. Morigi. "Mean-field theory of atomic self-organization in optical cavities." In: *Phys. Rev. A* 94 (2 Aug. 2016), p. 023807. DOI: 10.1103/PhysRevA.94.023807.

[Jas+17] D Jaschke et al. "Critical phenomena and Kibble--Zurek scaling in the long-range quantum Ising chain." In: *New J. Phys.* 19.3 (2017), p. 033032. DOI: 10.1088/1367-2630/aa65bc.

[Joy66] G. S. Joyce. "Spherical Model with Long-Range Ferromagnetic Interactions." In: *Phys. Rev.* 146 (1 June 1966), pp. 349–358. DOI: 10.1103/PhysRev.146.349.

[Jur+14] P. Jurcevic et al. "Quasiparticle engineering and entanglement propagation in a quantum many-body system." In: *Nature* 511.7508 (2014), pp. 202–205. DOI: 10.1038/nature13461.

[KUH63] M. Kac, G. E. Uhlenbeck, and P. C. Hemmer. "On the van der Waals Theory of the Vapor-Liquid Equilibrium. I. Discussion of a One-Dimensional Model." In: *J. Math. Phys.* 4.2 (1963), pp. 216–228. DOI: 10.1063/1.1703946. eprint: https://doi.org/10.1063/1.1703946.

[Kas63] P. W. Kasteleyn. "Dimer Statistics and Phase Transitions." In: *J. Math. Phys.* 4.2 (Feb. 1963), pp. 287–293. DOI: 10.1063/1.1703953. eprint: https://doi.org/10.1063/1.1703953.

[KSZ19] N. Kellermann, M. Schmidt, and F. M. Zimmer. "Quantum Ising model on the frustrated square lattice." In: *Phys. Rev. E* 99 (1 Jan. 2019), p. 012134. DOI: 10.1103/PhysRevE.99.012134.

[Kim+09] K. Kim et al. "Entanglement and Tunable Spin-Spin Couplings between Trapped Ions Using Multiple Transverse Modes." In: *Phys. Rev. Lett.* 103 (12 Sept. 2009), p. 120502. DOI: 10.1103/PhysRevLett.103.120502.

[Kim+10] K. Kim et al. "Quantum simulation of frustrated Ising spins with trapped ions." In: *Nature* 465.7298 (2010), p. 590. DOI: 10.1038/nature09071.

[Kit03] A. Y. Kitaev. "Fault-tolerant quantum computation by anyons." In: *Ann. Phys. (N. Y.)* 303.1 (Jan. 2003), pp. 2–30. ISSN: 0003-4916. DOI: 10.1016/S0003-4916(02)00018-0.

[Kit06] A. Y. Kitaev. "Anyons in an exactly solved model and beyond." In: *Ann. Phys. (N. Y.)* 321.1 (2006). January Special Issue, pp. 2–111. ISSN: 0003-4916. DOI: 10.1016/j.aop.2005.10.005.

[Kna+13] M. Knap et al. "Probing Real-Space and Time-Resolved Correlation Functions with Many-Body Ramsey Interferometry." In: *Phys. Rev. Lett.* 111 (14 Oct. 2013), p. 147205. DOI: 10.1103/PhysRevLett.111.147205.

[KU00] C. Knetter and G. S. Uhrig. "Perturbation theory by flow equations: dimerized and frustrated S= 1/2 chain." In: *Eur. Phys. J. B* 13.2 (2000), pp. 209–225. DOI: 10.1007/s100510050026.

[KLT12] T. Koffel, M. Lewenstein, and L. Tagliacozzo. "Entanglement entropy for the long-range Ising chain in a transverse field." In: *Phys. Rev. Lett.* 109.26 (2012), p. 267203. DOI: 10.1103/PhysRevLett.109.267203.

[KW17] C. Koop and S. Wessel. "Quantum phase transitions in effective spin-ladder models for graphene zigzag nanoribbons." In: *Phys. Rev. B* 96.16 (2017), p. 165114. DOI: 10.1103/PhysRevB.96.165114.

[Kor05] S. E. Korshunov. "Nature of phase transitions in the striped phase of a triangular-lattice Ising antiferromagnet." In: *Phys. Rev. B* 72 (14 Oct. 2005), p. 144417. DOI: 10.1103/PhysRevB.72.144417.

[Kos+16] F. Kos et al. "Precision islands in the Ising and O(N) models." In: *J. High Energy Phys.* 2016.8 (Aug. 2016), p. 36. ISSN: 1029-8479. DOI: 10.1007/JHEP08(2016)036.

[Kos74] J. M. Kosterlitz. "The critical properties of the two-dimensional xy model." In: *J. Phys. C: Solid State Physics* 7.6 (Mar. 1974), pp. 1046–1060. DOI: 10.1088/0022-3719/7/6/005.

[KT73] J. M. Kosterlitz and D. J. Thouless. "Ordering, metastability and phase transitions in two-dimensional systems." In: *J. Phys. C: Solid State Physics* 6.7 (Apr. 1973), pp. 1181–1203. DOI: 10.1088/0022-3719/6/7/010.

[Koz+19] J. Koziol et al. "Quantum criticality of the transverse-field Ising model with long-range interactions on triangular-lattice cylinders." In: *Phys. Rev. B* 100 (14 Oct. 2019), p. 144411. DOI: 10.1103/PhysRevB.100.144411.

[Kra06] W. Krauth. *Statistical Mechanics: Algorithms and Computations*. Vol. 13. OUP Oxford, 2006. ISBN: 9780198515364.

[KDU12] H. Krull, N. A. Drescher, and G. S. Uhrig. "Enhanced perturbative continuous unitary transformations." In: *Phys. Rev. B* 86 (12 Sept. 2012), p. 125113. DOI: 10.1103/PhysRevB.86.125113.

[KF98] Y. Kuramoto and N. Fukushima. "Dynamical Effective Medium Theory for Quantum Spins and Multipoles." In: *J. Phys. Soc. Jpn.* 67.2 (1998). arXiv:1907.08173, pp. 583–593. DOI: 10.1143/JPSJ.67.583. eprint: https://doi.org/10.1143/JPSJ.67.583.

[LAB05] N. Laflorencie, I. Affleck, and M. Berciu. "Critical phenomena and quantum phase transition in long range Heisenberg antiferromagnetic chains." In: *J. Stat. Mech.* 2005.12 (Dec. 2005), P12001–P12001. DOI: 10.1088/1742-5468/2005/12/p12001.

[Lah+09] T. Lahaye et al. "The physics of dipolar bosonic quantum gases." In: *Rep. Prog. Phys.* 72.12 (2009), p. 126401. DOI: 10.1088/0034-4885/72/12/126401.

[Lan50] C. Lanczos. *An iteration method for the solution of the eigenvalue problem of linear differential and integral operators*. United States Governm. Press Office Los Angeles, CA, 1950.

[Lan94] D. P. Landau. "Computer simulation studies of critical phenomena." In: *Physica A: Statistical Mechanics and its Applications* 205.1 (Apr. 1994), pp. 41–64. ISSN: 0378-4371. DOI: https://doi.org/10.1016/0378-4371(94)90490-1.

[Lan37] L. D. Landau. "On the theory of phase transitions." In: *Zh. Eksp. Teor. Fiz. [Sov. Phys. JETP]* 7 (1937). [Ukr. J. Phys.53,25(2008)], pp. 19–32.

[Lan+11] B. P. Lanyon et al. "Universal Digital Quantum Simulation with Trapped Ions." In: *Science* 334.6052 (2011), pp. 57–61. ISSN: 0036-8075. DOI: 10.1126/science.1208001. eprint: https://science.sciencemag.org/content/334/6052/57.full.pdf.

[LK69] A. I. Larkin and D. E. Khmel'Nitskii. "Phase transition in uniaxial ferroelectrics." In: *Sov. Phys. JETP* 29 (1969), pp. 1123–1128.

[LGZJ80] J. C. Le Guillou and J. Zinn-Justin. "Critical exponents from field theory." In: *Phys. Rev. B* 21 (9 May 1980), pp. 3976–3998. DOI: 10.1103/PhysRevB.21.3976.

[Len21] Wilhelm Lenz. "Beiträge zum Verständnis der magnetischen Eigenschaften in festen Körpern." In: *Phys. Z.* 21 (1921), pp. 613–615.

[Ler+19] A. Lerose et al. "Quasilocalized excitations induced by long-range interactions in translationally invariant quantum spin chains." In: *Phys. Rev. B* 99 (12 Mar. 2019), p. 121112. DOI: 10.1103/PhysRevB.99.121112.

[LKG77] M. Ley-Koo and M. S. Green. "Revised and extended scaling for coexisting densities of SF_6." In: *Phys. Rev. A* 16 (6 Dec. 1977), pp. 2483–2487. DOI: 10.1103/PhysRevA.16.2483.

[Li+20] H Li et al. "Kosterlitz-Thouless melting of magnetic order in the triangular quantum Ising material $TmMgGaO_4$." In: *Nat. Commun.* 11.1 (Feb. 2020), p. 1111. ISSN: 2041-1723. DOI: 10.1038/s41467-020-14907-8.

[LY19] Z.-X. Li and H. Yao. "Sign-Problem-Free Fermionic Quantum Monte Carlo: Developments and Applications." In: *Annu. Rev. Condens. Matter Phys.* 10.1 (2019). DOI: 10.1146/annurev-conmatphys-033117-054307.

[Lie86] R. Liebmann. "Statistical mechanics of periodic frustrated Ising systems." In: *Statistical Mechanics of Periodic Frustrated Ising Systems*. Vol. 251. 1986.

[LMG65] H. J. Lipkin, N. Meshkov, and A. J. Glic. "Validity of many-body approximation methods for a solvable model: (I). Exact solutions and perturbation theory." In: *Nucl. Phys.* 62.2 (1965), pp. 188–198. ISSN: 0029-5582. DOI: 10.1016/0029-5582(65)90862-X.

[Liu+19] F. Liu et al. "Confined Quasiparticle Dynamics in Long-Range Interacting Quantum Spin Chains." In: *Phys. Rev. Lett.* 122 (15 Apr. 2019), p. 150601. DOI: 10.1103/PhysRevLett.122.150601.

[LB02] E. Luijten and H. W. J. Blöte. "Boundary between Long-Range and Short-Range Critical Behavior in Systems with Algebraic Interactions." In: *Phys. Rev. Lett.* 89 (2 June 2002), p. 025703. DOI: 10.1103/PhysRevLett.89.025703.

[LM01] E. Luijten and H. Meßingfeld. "Criticality in One Dimension with Inverse Square-Law Potentials." In: *Phys. Rev. Lett.* 86 (23 June 2001), pp. 5305–5308. DOI: 10.1103/PhysRevLett.86.5305.

[LL09] A. Lüscher and A. M. Läuchli. "Exact diagonalization study of the antiferromagnetic spin-$\frac{1}{2}$ Heisenberg model on the square lattice in a magnetic field." In: *Phys. Rev. B* 79 (19 May 2009), p. 195102. DOI: 10.1103/PhysRevB.79.195102.

[Mag+16] M. F. Maghrebi et al. "Causality and quantum criticality in long-range lattice models." In: *Phys. Rev. B* 93 (12 Mar. 2016), p. 125128. DOI: 10.1103/PhysRevB.93.125128.

[Mah+15] S. Mahmoudian et al. "Glassy dynamics in geometrically frustrated Coulomb liquids without disorder." In: *Phys. Rev. Lett.* 115.2 (2015), p. 025701. DOI: 10.1103/PhysRevLett.115.025701.

[Mal18] A. G. Mal'shukov. "Nonexponential long-range interaction of magnetic impurities in spin-orbit coupled superconductors." In: *Phys. Rev. B* 98 (5 Aug. 2018), p. 054504. DOI: 10.1103/PhysRevB.98.054504.

[MM56] T. Matsubara and H. Matsuda. "A lattice model of liquid helium, I." In: *Prog. Theor. Phys* 16.6 (1956), pp. 569–582. DOI: 10.1143/PTP.16.569.

[MN98] M. Matsumoto and T. Nishimura. "Mersenne Twister: A 623-dimensionally Equidistributed Uniform Pseudo-random Number Generator." In: *ACM Trans. Model. Comput. Simul.* 8.1 (Jan. 1998), pp. 3–30. ISSN: 1049-3301. DOI: 10.1145/272991.272995.

[Men+09] E. Mengotti et al. "Dipolar energy states in clusters of perpendicular magnetic nanoislands." In: *J. Appl. Phys* 105.11 (2009), p. 113113. DOI: 10.1063/1.3133202.

[MW66] N. D. Mermin and H. Wagner. "Absence of Ferromagnetism or Antiferromagnetism in One- or Two-Dimensional Isotropic Heisenberg Models." In: *Phys. Rev. Lett.* 17 (22 Nov. 1966), pp. 1133–1136. DOI: 10.1103/PhysRevLett.17.1133.

[Met74] B. D. Metcalf. "Ground state spin orderings of the triangular Ising model with the nearest and next nearest neighbor interaction." In: *Phys. Lett. A* 46.5 (Jan. 1974), pp. 325–326. ISSN: 0375-9601. DOI: https://doi.org/10.1016/0375-9601(74)90247-3.

[Met+53] N. Metropolis et al. "Equation of state calculations by fast computing machines." In: *J. Chem. Phys.* 21.6 (1953), pp. 1087–1092. DOI: 10.1063/1.1699114.

[Mie98] A. Mielke. "Flow equations for band-matrices." In: *Eur. Phys. J. B* 5.3 (Oct. 1998), pp. 605–611. ISSN: 1434-6036. DOI: 10.1007/s100510050485.

[Mit+98] T. B. Mitchell et al. "Direct Observations of Structural Phase Transitions in Planar Crystallized Ion Plasmas." In: *Science* 282.5392 (1998), pp. 1290–1293. ISSN: 0036-8075. DOI: 10.1126/science.282.5392.1290. eprint: https://science.sciencemag.org/content/282/5392/1290.full.pdf.

[Moe01] R. Moessner. "Magnets with strong geometric frustration." In: *Can. J. Phys.* 79.11-12 (2001), pp. 1283–1294. DOI: 10.1139/p01-123. eprint: https://doi.org/10.1139/p01-123.

[MS01] R. Moessner and S. L. Sondhi. "Ising models of quantum frustration." In: *Phys. Rev. B* 63 (22 May 2001), p. 224401. DOI: 10.1103/PhysRevB.63.224401.

[MSC00] R. Moessner, S. L. Sondhi, and P. Chandra. "Two-Dimensional Periodic Frustrated Ising Models in a Transverse Field." In: *Phys. Rev. Lett.* 84 (19 May 2000), pp. 4457–4460. DOI: 10.1103/PhysRevLett.84.4457.

[Mon+16] R. Mondaini et al. "Eigenstate thermalization in the two-dimensional transverse field Ising model." In: *Phys. Rev. E* 93.3 (2016), p. 032104. DOI: 10.1103/PhysRevE.93.032104.

[Mor19] T. Mori. "Prethermalization in the transverse-field Ising chain with long-range interactions." In: *J. Phys. A* 52.5 (Jan. 2019), p. 054001. DOI: 10.1088/1751-8121/aaf9db.

[NB70] J. F. Nagle and J. C. Bonner. "Numerical studies of the Ising chain with long-range ferromagnetic interactions." In: *J. Phys. C: Solid State Physics* 3.2 (Feb. 1970), pp. 352–366. DOI: 10.1088/0022-3719/3/2/017.

[Nam+19] Y. Nam et al. "Ground-state energy estimation of the water molecule on a trapped ion quantum computer." In: *arXiv* (2019).

[Ogu60] T. Oguchi. "Theory of Spin-Wave Interactions in Ferro- and Antiferromagnetism." In: *Phys. Rev.* 117 (1 Jan. 1960), pp. 117–123. DOI: 10.1103/PhysRev.117.117.

[OHW91] J. Oitmaa, C. J. Hamer, and Z. Weihong. "Low-temperature series expansions for the (2+1)-dimensional Ising model." In: *J. Phys. A* 24.12 (1991), p. 2863. DOI: 10.1088/0305-4470/24/12/024.

[Ons44] L. Onsager. "Crystal Statistics. I. A Two-Dimensional Model with an Order-Disorder Transition." In: *Phys. Rev.* 65 (3-4 Feb. 1944), pp. 117–149. DOI: 10.1103/PhysRev.65.117.

[OPR16] S. Ostermann, F. Piazza, and H. Ritsch. "Spontaneous Crystallization of Light and Ultracold Atoms." In: *Phys. Rev. X* 6 (2 May 2016), p. 021026. DOI: 10.1103/PhysRevX.6.021026.

[OR95] Stellan Östlund and Stefan Rommer. "Thermodynamic Limit of Density Matrix Renormalization." In: *Phys. Rev. Lett.* 75 (19 Nov. 1995), pp. 3537–3540. DOI: 10.1103/PhysRevLett.75.3537.

[OI03] Y. Ozeki and N. Ito. "Nonequilibrium relaxation analysis of fully frustrated XY models in two dimensions." In: *Phys. Rev. B* 68 (5 Aug. 2003), p. 054414. DOI: 10.1103/PhysRevB.68.054414.

[Pap+18] S. Pappalardi et al. "Scrambling and entanglement spreading in long-range spin chains." In: *Phys. Rev. B* 98 (13 Oct. 2018), p. 134303. DOI: 10.1103/PhysRevB.98.134303.

[PT75] P. Pearce and C. J. Thompson. "The anisotropic Heisenberg model in the long-range interaction limit." In: *Commun. Math. Phys.* 41.2 (June 1975), pp. 191–201. ISSN: 1432-0916. DOI: 10.1007/BF01608757.

[Pei36] R. Peierls. "On Ising's model of ferromagnetism." In: *Math. Proc. Cambridge Philos. Soc.* 32.3 (1936), pp. 477–481. DOI: 10.1017/S0305004100019174.

[Pet+12] D. Peter et al. "Anomalous Behavior of Spin Systems with Dipolar Interactions." In: *Phys. Rev. Lett.* 109 (2 July 2012), p. 025303. DOI: 10.1103/PhysRevLett.109.025303.

[Pfe70] P. Pfeuty. "The one-dimensional Ising model with a transverse field." In: *Ann. Phys. (N. Y.)* 57.1 (1970), pp. 79–90. DOI: 10.1016/0003-4916(70)90270-8.

[Pic12] M. Picco. "Critical behavior of the Ising model with long range interactions." In: *arXiv* (2012).

[PDM79] C. Pittman, T. Doiron, and H. Meyer. "Equation of state and critical exponents of ^{3}He and a ^{3}He-^{4}He mixture near their liquid-vapor critical point." In: *Phys. Rev. B* 20 (9 Nov. 1979), pp. 3678–3689. DOI: 10.1103/PhysRevB.20.3678.

[Pow+13] M. Powalski et al. "Disorder by disorder and flat bands in the kagome transverse field Ising model." In: *Phys. Rev. B* 87 (5 Feb. 2013), p. 054404. DOI: 10.1103/PhysRevB.87.054404.

[Pre+07] W. H. Press et al. *Numerical recipes 3rd edition: The art of scientific computing*. Cambridge University Press, 2007. ISBN: 978-0521880688.

[PHA91] V. Privman, P. C. Hohenberg, and A. Aharony. *Phase Transitions and Critical Phenomena*. Ed. by C. Domb and J. Lebowitz. Vol. 14. New York: Academic Press, 1991. ISBN: 0-12-220314-3.

[RL19] M. Rader and A. M. Läuchli. "Floating Phases in One-Dimensional Rydberg Ising Chains." In: *arXiv* (2019).

[Ric+13] P. Richerme et al. "Quantum Catalysis of Magnetic Phase Transitions in a Quantum Simulator." In: *Phys. Rev. Lett.* 111 (10 Sept. 2013), p. 100506. DOI: 10.1103/PhysRevLett.111.100506.

[Ric+14] P. Richerme et al. "Non-local propagation of correlations in quantum systems with long-range interactions." In: *Nature* 511.7508 (2014), pp. 198–201. DOI: 10.1038/nature13450.

[Rit19] M. M. Ritzau. "Excitation energies of the ordered long-range transverse field Ising chain." Bachelor's Thesis. Friedrich-Alexander Universität Erlangen-Nürnberg, 2019.

[RBS16] J. Roechner, L. Balents, and K. P. Schmidt. "Spin liquid and quantum phase transition without symmetry breaking in a frustrated three-dimensional Ising model." In: *Phys. Rev. B* 94 (2016), p. 201111. DOI: 10.1103/PhysRevB.94.201111.

[RH90] M. Roger and J. H. Hetherington. "Coupled-cluster approximation for spin lattices: Application to solid ^{3}He." In: *Phys. Rev. B* 41 (1 Jan. 1990), pp. 200–219. DOI: 10.1103/PhysRevB.41.200.

[Ros+08] T. Rosenband et al. "Frequency Ratio of Al+ and Hg+ Single-Ion Optical Clocks; Metrology at the 17th Decimal Place." In: *Science* 319.5871 (2008), pp. 1808–1812. ISSN: 0036-8075. DOI: 10.1126/science.1154622. eprint: https://science.sciencemag.org/content/319/5871/1808.full.pdf.

[RD19] S. S. Roy and H. S. Dhar. "Effect of long-range interactions on multipartite entanglement in Heisenberg chains." In: *Phys. Rev. A* 99 (6 June 2019), p. 062318. DOI: 10.1103/PhysRevA.99.062318.

[SBM18] S. N. Saadatmand, S. D. Bartlett, and I. P. McCulloch. "Phase diagram of the quantum Ising model with long-range interactions on an infinite-cylinder triangular lattice." In: *Phys. Rev. B* 97 (15 Apr. 2018), p. 155116. DOI: 10.1103/PhysRevB.97.155116.

[Sac11] S. Sachdev. *Quantum Phase Transitions*. 2nd ed. Cambridge University Press, 2011. DOI: 10.1017/CBO9780511973765.

[Sak73] J. Sak. "Recursion Relations and Fixed Points for Ferromagnets with Long-Range Interactions." In: *Phys. Rev. B* 8 (1 July 1973), pp. 281–285. DOI: 10.1103/PhysRevB.8.281.

[San03] A. W. Sandvik. "Stochastic series expansion method for quantum Ising models with arbitrary interactions." In: *Phys. Rev. E* 68 (5 Nov. 2003), p. 056701. DOI: 10.1103/PhysRevE.68.056701.

[San10] Anders W. Sandvik. "Ground States of a Frustrated Quantum Spin Chain with Long-Range Interactions." In: *Phys. Rev. Lett.* 104 (13 Mar. 2010), p. 137204. DOI: 10.1103/PhysRevLett.104.137204.

[SPR15] J. Schachenmayer, A. Pikovski, and A. M. Rey. "Dynamics of correlations in two-dimensional quantum spin models with long-range interactions: a phase-space Monte-Carlo study." In: *New J. Phys.* 17.6 (2015), p. 065009. DOI: 10.1088/1367-2630/17/6/065009.

[SPS12] C. Schneider, D. Porras, and T. Schaetz. "Experimental quantum simulations of many-body physics with trapped ions." In: *Rep. Prog. Phys.* 75.2 (2012), p. 024401. DOI: 10.1088/0034-4885/75/2/024401.

[Sch11] Ulrich Schollwöck. "The density-matrix renormalization group in the age of matrix product states." In: *Ann. Phys. (N. Y.)* 326.1 (Jan. 2011). January 2011 Special Issue, arXiv:1008.3477, pp. 96 –192. ISSN: 0003-4916. DOI: https://doi.org/10.1016/j.aop.2010.09.012.

[SHM13] S. Schütz, H. Habibian, and G. Morigi. "Cooling of atomic ensembles in optical cavities: Semiclassical limit." In: *Phys. Rev. A* 88 (3 Sept. 2013), p. 033427. DOI: 10.1103/PhysRevA.88.033427.

[SM14] S. Schütz and G. Morigi. "Prethermalization of Atoms Due to Photon-Mediated Long-Range Interactions." In: *Phys. Rev. Lett.* 113 (20 Nov. 2014), p. 203002. DOI: 10.1103/PhysRevLett.113.203002.

[Sha+12] N. Shannon et al. "Quantum Ice: A Quantum Monte Carlo Study." In: *Phys. Rev. Lett.* 108 (6 Feb. 2012), p. 067204. DOI: 10.1103/PhysRevLett.108.067204.

[She+19] Y. Shen et al. "Intertwined dipolar and multipolar order in the triangular-lattice magnet $TmMgGaO_4$." In: *Nat. Commun.* 10.1 (Oct. 2019), p. 4530. ISSN: 2041-1723. DOI: 10.1038/s41467-019-12410-3.

[Sim97] B. Simons. *Phase Transitions and Collective Phenomena*. Lecture notes. https://www.tcm.phy.cam.ac.uk/~bds10/phase.html. University of Cambridge, 1997.

[SKM16] A. Smerald, S. Korshunov, and F. Mila. "Topological Aspects of Symmetry Breaking in Triangular-Lattice Ising Antiferromagnets." In: *Phys. Rev. Lett.* 116 (19 May 2016), p. 197201. DOI: 10.1103/PhysRevLett.116.197201.

[SM18] A. Smerald and F. Mila. "Spin-liquid behaviour and the interplay between Pokrovsky-Talapov and Ising criticality in the distorted, triangular-lattice, dipolar Ising antiferromagnet." In: *SciPost Phys.* 5 (3 2018), p. 30. DOI: 10.21468/SciPostPhys.5.3.030.

[Sok97] A. Sokal. "Monte Carlo Methods in Statistical Mechanics: Foundations and New Algorithms." In: *Functional Integration: Basics and Applications*. Ed. by Cecile DeWitt-Morette, Pierre Cartier, and Antoine Folacci. Boston, MA: Springer US, 1997, pp. 131–192. ISBN: 978-1-4899-0319-8. DOI: 10.1007/978-1-4899-0319-8_6.

[SH76] R. Sokel and W. A. Harrison. "Long-Range Interactions in Semiconductors." In: *Phys. Rev. Lett.* 36 (1 Jan. 1976), pp. 61–64. DOI: 10.1103/PhysRevLett.36.61.

[Sta87] H. E. Stanley. *Introduction to Phase Transitions and Critical Phenomena*. Oxford University Press, 1987. ISBN: 0-19-505316-8.

[Ste97] Jürgen Stein. "Flow equations and the strong-coupling expansion for the Hubbard model." In: *J. Stat. Phys.* 88.1 (July 1997), pp. 487–511. ISSN: 1572-9613. DOI: 10.1007/BF02508481.

[Sun17] G. Sun. "Fidelity susceptibility study of quantum long-range antiferromagnetic Ising chain." In: *Phys. Rev. A* 96 (4 Oct. 2017), p. 043621. DOI: 10.1103/PhysRevA.96.043621.

[Sut71] B. Sutherland. "Quantum Many-Body Problem in One Dimension: Ground State." In: *J. Math. Phys.* 12.2 (1971), pp. 246–250. DOI: 10.1063/1.1665584. eprint: https://doi.org/10.1063/1.1665584.

[Suz71] M. Suzuki. "Relationship among Exactly Soluble Models of Critical Phenomena. I*): 2D Ising Model, Dimer Problem and the Generalized XY-Model." In: *Prog. Theor. Phys* 46.5 (Nov. 1971), pp. 1337–1359. ISSN: 0033-068X. DOI: 10.1143/PTP.46.1337. eprint: http://oup.prod.sis.lan/ptp/article-pdf/46/5/1337/5268367/46-5-1337.pdf.

[Suz76] M. Suzuki. "Relationship between d-Dimensional Quantal Spin Systems and (d+1)-Dimensional Ising Systems: Equivalence, Critical Exponents and Systematic Approximants of the Partition Function and Spin Correlations." In: *Prog. Theor. Phys* 56.5 (1976), pp. 1454–1469. DOI: 10.1143/PTP.56.1454.

[SIC12] S. Suzuki, J. Inoue, and B. K. Chakrabarti. *Quantum Ising phases and transitions in transverse Ising models*. Vol. 862. Springer, 2012.

[Tak77] M. Takahashi. "Half-filled Hubbard model at low temperature." In: *J. Phys. C: Solid State Physics* 10.8 (1977), p. 1289. DOI: 10.1088/0022-3719/10/8/031.

[Tro59] H. F. Trotter. "On the Product of Semi-Groups of Operators." In: *Proc. Am. Math. Soc.* 10.4 (1959), pp. 545–551. ISSN: 00029939, 10886826. DOI: 10.2307/2033649.

[TW05] M. Troyer and U.-J. Wiese. "Computational Complexity and Fundamental Limitations to Fermionic Quantum Monte Carlo Simulations." In: *Phys. Rev. Lett.* 94 (17 May 2005), p. 170201. DOI: 10.1103/PhysRevLett.94.170201.

[Vai+18] V. D. Vaidya et al. "Tunable-Range, Photon-Mediated Atomic Interactions in Multimode Cavity QED." In: *Phys. Rev. X* 8 (1 Jan. 2018), p. 011002. DOI: 10.1103/PhysRevX.8.011002.

[Van+18] L. Vanderstraeten et al. "Quasiparticles in Quantum Spin Chains with Long-Range Interactions." In: *Phys. Rev. Lett.* 121 (9 Aug. 2018), p. 090603. DOI: 10.1103/PhysRevLett.121.090603.

[VMC08] F Verstraete, V. Murg, and J.I. Cirac. "Matrix product states, projected entangled pair states, and variational renormalization group methods for quantum spin systems." In: *Advances in Physics* 57.2 (July 2008). arXiv:0907.2796, pp. 143–224. DOI: 10.1080/14789940801912366. eprint: https://doi.org/10.1080/14789940801912366.

[VHF15] S. Vijay, J. Haah, and L. Fu. "A new kind of topological quantum order: A dimensional hierarchy of quasiparticles built from stationary excitations." In: *Phys. Rev. B* 92 (23 Dec. 2015), p. 235136. DOI: 10.1103/PhysRevB.92.235136.

[Vod+15] Davide Vodola et al. "Long-range Ising and Kitaev models: phases, correlations and edge modes." In: *New J. Phys.* 18.1 (Dec. 2015), p. 015001. DOI: 10.1088/1367-2630/18/1/015001.

[WZZ97] Y.G Wang, W.L Zhong, and P.L Zhang. "Ferroelectric films described by transverse ising model with long-range interactions." In: *Solid State Commun.* 101.11 (1997), pp. 807–810. ISSN: 0038-1098. DOI: https://doi.org/10.1016/S0038-1098(96)00730-2.

[Wan+17] Yan-Cheng Wang et al. "Caution on emergent continuous symmetry: A Monte Carlo investigation of the transverse-field frustrated Ising model on the triangular and honeycomb lattices." In: *Phys. Rev. B* 96 (11 Sept. 2017), p. 115160. DOI: 10.1103/PhysRevB.96.115160.

[WIH12] H. Watanabe, N. Ito, and C.-K. Hu. "Phase diagram and universality of the Lennard-Jones gas-liquid system." In: *J. Chem. Phys.* 136.20 (2012), p. 204102. DOI: 10.1063/1.4720089. eprint: https://doi.org/10.1063/1.4720089.

[Weg94] F. J. Wegner. "Flow-equations for Hamiltonians." In: *Ann. Phys. (Leipzig)* 506.2 (Jan. 1994), pp. 77–91. ISSN: 1521-3889. DOI: 10.1002/andp.19945060203.

[Weg01] F. J. Wegner. "Flow equations for Hamiltonians." In: *Phys. Rep.* 348.1 (2001). Renormalization group theory in the new millennium. II, pp. 77–89. ISSN: 0370-1573. DOI: 10.1016/S0370-1573(00)00136-8.

[WR73] F. J. Wegner and E. K. Riedel. "Logarithmic corrections to the molecular-field behavior of critical and tricritical systems." In: *Phys. Rev. B* 7.1 (1973), p. 248. DOI: 10.1103/PhysRevB.7.248.

[WOH94] Z. Weihong, J. Oitmaa, and C. J. Hamer. "Series expansions for the 3D transverse Ising model at T=0." In: *J. Phys. A* 27.16 (1994), p. 5425. DOI: 10.1088/0305-4470/27/16/010.

[Whi92] S. R. White. "Density matrix formulation for quantum renormalization groups." In: *Phys. Rev. Lett.* 69 (19 Nov. 1992), pp. 2863–2866. DOI: 10.1103/PhysRevLett.69.2863.

[WJ28] E. P. Wigner and P. Jordan. "Über das Paulische Äquivalenzverbot." In: *Z. Phys* 47 (1928), p. 631.

[Wil72] Kenneth G. Wilson. "Feynman-Graph Expansion for Critical Exponents." In: *Phys. Rev. Lett.* 28 (9 Feb. 1972), pp. 548–551. DOI: 10.1103/PhysRevLett.28.548.

[Wor+13] M. van den Worm et al. "Relaxation timescales and decay of correlations in a long-range interacting quantum simulator." In: *New J. Phys.* 15.8 (2013), p. 083007. DOI: 10.1088/1367-2630/15/8/083007.

[Wyn56] P. Wynn. "On a device for computing the e_m (S_n) transformation." In: *Math. Tables Other Aids Comput.* (1956), pp. 91–96.

[Yan77] A. Yanase. "Correlation index of the Ising model with a transverse field." In: *J. Phys. Soc. Jpn.* 42.6 (1977), pp. 1816–1818. DOI: 10.1143/JPSJ.42.1816.

[YJZ19] F. Yang, S.-J. Jiang, and F. Zhou. "Achieving continuously tunable critical exponents for long-range spin systems simulated with trapped ions." In: *Phys. Rev. A* 99 (1 Jan. 2019), p. 012119. DOI: 10.1103/PhysRevA.99.012119.

[YS11] H. Y. Yang and K. P. Schmidt. "Effective models for gapped phases of strongly correlated quantum lattice models." In: *Europhys. Lett.* 94.1 (Apr. 2011), p. 17004. DOI: 10.1209/0295-5075/94/17004.

[ZOH94] W. Zheng, J Oitmaa, and C. J. Hamer. "Series expansions for the 3D transverse Ising model at T=0." In: *J. Phys. A* 27.16 (Aug. 1994), pp. 5425–5444. DOI: 10.1088/0305-4470/27/16/010.

ACKNOWLEDGMENTS

Zum Abschluss möchte ich mich noch bei einigen Menschen für ihre Unterstützung bedanken. Danke an Kai für das Angebot diese Arbeit in deiner Arbeitsgruppe zu schreiben, für die vielen Diskussionen, deine persönliche Nähe zu deinen Mitarbeitern und deine Begeisterung für die Physik und auch für Themen über die Physik hinaus. Ich hoffe, dass dir die politischen Themen in Zukunft nicht über den Kopf wachsen und du stets noch die Zeit findest, selbst die Kreide in die Hand zu nehmen und an der Tafel über ein Problem nachzudenken.

Vielen Dank auch an den Rest der Gruppe, die in den vielen Gruppentreffen stets gute Ideen und Diskussionen lieferte und auch außerhalb des Unialltags für eine abwechslungsreiche Zeit sorgte. Danke an Caro für das Korrekturlesen der Einleitung.

Danke auch an Sebastian, dass du mich dazu inspiriert hast den Schritt zu den Monte-Carlo-Methoden zu wagen und für deine Unterstützung bei der Entwicklung der Methode.

Für die vielen langen Kaffeepausen, Spiele- und Kochabende und Diskussionen über und auch fernab der Physik und das freundschaftliche Klima bedanke ich mich bei der gesamten Theorie 1. Insbesondere möchte ich auch Ingrid danken, die stets alle bürokratischen Hürden für uns alle geebnet hat.

Auf die Unterstützung meiner Familie konnte ich mich stets verlassen. Danke, dass ihr so seid, wie ihr seid!

Als wichtigste Person möchte ich mich auch bei dir, Larissa, für deine stete Unterstützung bedanken. Wenn es einmal stressig wurde, hast du mir Vieles abgenommen und mir immer alle Freiräume gelassen. Danke.